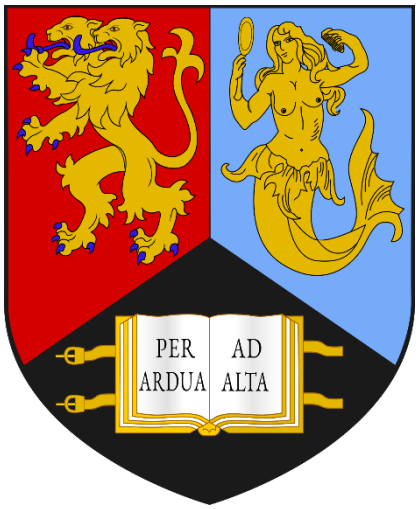

UNIVERSITY OF BIRMINGHAM

Novel Electrode Materials and Educational Resources for Li-/Na-ion Batteries

by

Elizabeth Helen Driscoll

A thesis submitted to
The University of Birmingham
for the degree of
Doctor of Philosophy

The School of Chemistry
College of Engineering and Physical Sciences
The University of Birmingham
July 2022

Abstract

This thesis describes a breadth of novel materials for Li- and Na-ion batteries, before considering novel educational resources to explain characteristics and operation of these types of battery.

Initial focus is given towards high power Nb containing anodes for fast charge Li-ion battery application, from the synthesis and characterisation of these materials towards fabrication of suitable coatings for electrochemical testing. Niobium-based containing electrodes have increased in interest due to their inherent stability at high charging rates, while also having significantly higher gravimetric capacities. In particular this body of work will highlight novel materials: $Nb_{22}CuO_{56}$ and $Nb_9Ti_{1.5}W_{1.5}O_{30}$ (monoclinic C2/m), and their respective performance in a half coin cell architecture. The motivation of Cu doping is towards improved electrical conductivity, while doping with Ti and W (usually doped separately) has the opportunity to deliver performance similar to W-doped systems while reducing the overall cost. Consideration towards optimising the latter material is highlighted, with the identification of phase transformation noted upon ball-milling these materials. Towards ease of recycling and reducing the overall toxicity of cell manufacture, methodologies towards producing electrodes utilising water-based 'green' binders is considered for $Nb_9Ti_{1.5}W_{1.5}O_{30}$ using the conventional CMC/SBR dual binder system, before exploring the use of iota-carrageenan – as an alternative to PVDF.

The latter part of this thesis will then explore a range sulfate-based Na-ion cathode materials. Building on prior work of the established ion-size relationship influencing

structure preference of alluaudite-type and bimetallic sulfate systems, mixed-metal substitution is considered to exploit this relationship further to mitigate the use of toxic dopants (i.e. selenate). The discovery of a novel Na-Ti-SO_4-OH system (the first of its kind) is also highlighted within this section.

The final part of this work will describe a series of engaging educational resources to explore and aid the understanding of Li-ion batteries – most notably the development and impact of 'Battery Jenga' will be highlighted, which stands as the first resource to effectively explore the operation of this type of battery, while remaining accessible and hands-on to a range of different audiences.

Personal Acknowledgements

To say the past four to five years of study and research have been challenging would be an understatement. I wanted to do a PhD to push myself and to be able to develop my scientific thinking. At the start of the programme, when a diagram of a rollercoaster was shown to describe this degree – they certainly weren't joking. It has been challenging. I have certainly wanted to quit many times: thank you to the floor 5 post docs for the support to keep going!

First off I want to thank Prof. Peter Slater, or as I cheekily say Le Peter when I had a question. I am so grateful for Pete's support and friendship over the years, his insight and expertise is simply phenomenal! But also Pete – I am sorry for the amount of times you've seen me cry over the years! Thank you for putting up with me and being a source of the creativity for all our outreach work – we've achieved a heck of a lot! I would also like to thank my second supervisor Prof. Paul Anderson for always being a voice of reason. Also Prof. Frank Berry has truly been the smile and life mentor I needed at some dark times – thank you for your friendship Frank, just sorry I never got useful Fe samples to you.

I'd also like to thank my big sister – Dr Laura Driscoll – a source of inspiration and a fantastic scientist. If you see Driscoll *et al.* cited, it's not a self-citation, just Driscoll the elder published some good work that I followed on from. I have loved having the chance to work with my big sister (tell teenager me that ha!), but it has been truly brilliant to be able to talk shop, think things through and of course have a spare pair of hands to help me change cylinders or sort out messy tube furnaces.

Dr Tzu-Yu (Evin/babe) Chen, one of my closest friendships formed during Masters and PhD. Evin, again another incredible scientist, and I am so grateful for all your help (thank you TOPAS Queen), support, guidance and snacks (kinder bueno yes!).

At the time of writing this thesis, I had joined Prof. Emma Kendrick's group – Energy Materials Group over in the School of Metallurgy and Materials at the University. Trying to juggle writing a thesis and being a "grown-up" post-(work in progress)doc, wasn't something I anticipated, after the challenges of my year industry a few years prior. A special thank you to Emma for being an amazing battery guru. Dr Scott Gorman for teaching me the initial ways of coin cell fabrication. Learning a new area within the

battery sector and forming friendships in this group has been so refreshing! I'd like to thank Dr. Rob Sommerville in particular – his energy has certainly helped me through writing this thesis. And pictures of his cat Lola.

Thank you to the researchers from Slater Group and Floor 5, in particular: Abbey, Josh, Bo, Beth & Deano, Antony, Abu S and Abu M. Also Dr Ruth Patchett for setting me on this outreach path.

On the side of PhD, I was fortunate to join the RSC Solid State Chemistry committee and through the ECR, I have met some amazing individuals – thanks guys for the encouragement for finishing.

I'd like to also thank Dr Jo Douglas-Harris. Jo was assigned as my mentor through the RSC and has really supported me in this transition – finishing PhD and figuring out what is next. Our conversations and Jo's perspective have helped me enormously.

A huge thank you to my partner in crime James. As much as he is a diva, James has been very supportive of me pursuing this PhD (I know he's secretly hoping to be a house husband if I make some good dollar). James has seen me at the lowest, but has kept the constant supplies of tea and hot water bottles in helping me write this piece. At one point he did ask whether I had finished a few months ago and whether I was just milking it… if only.

Thank you to my family for your support and love – particularly at my lowest back in February 2020. A year later, my little Nephew arrived into the world, with the push to finish PhD, he has bought a new perspective to life and bought so much joy. Thank you Charlie Bear – maybe in twenty years, your two Aunties might have convinced you to go down the Chemistry path, but maybe one that involves more money.

To make doing a PhD equally more challenging, the water tank on the roof in the School of Chemistry decided to flood the building back in May 2018. This apparently wasn't enough of a delay, COVID-19 pandemic also had a significant factor – but all I can say is I tried my best.

Thank you to Prof. Jan Skakle (University of Aberdeen) and Dr Pooja Goddard (Loughborough University) for their input in finalising this thesis.

For Buba, Mum and Dad.

Abbreviations

AM	Active Material
B	Binder
BSE	Back scatter electron
CB	Carbon Black
cif	Crystallographic Information File
CMC	Sodium carboxymethyl cellulose
CNT	Carbon nanotubes
CV	Constant Voltage
DTA	Differential Thermal Analysis
EXAFS	Extended X-ray Absorption Fine Structure
EDX/EDS	Energy-dispersive X-ray Spectroscopy
GSAS	General Structure and Analysis System (Unit Cell refinement software)
LCO	Lithium cobalt oxide
LMO	Lithium manganese oxide (spinel)
LTO	Lithium titanate – $Li_4Ti_5O_{12}$
NCA	Lithium Nickel Cobalt Aluminium Oxide
NMC	Lithium Nickel Manganese Cobalt Oxide
NiBs	Sodium-ion Batteries
OCV	Open circuit voltage
PVDF	Polyvinylidene fluoride
SE	Secondary electron
SEI	Solid electrolyte interface

SEM	Scanning electron microscopy
SHE	Standard Hydrogen Electrode
SOP	Standard Operating Procedure
TGA	Thermogravimetric analysis
TOPAS	Crystallographic Profile fitting software
TNO	Titanium niobite - $TiNb_2O_7$
Wt %	Weight percentage
XANES	X-ray absorption near edge structure

Publications

Results from within this thesis have already or are expected to be published. In the instances where the results chapters comprise of published work, this will be made explicit at the start of each chapter.

The following research within this thesis, which has been published:

- E. H. Driscoll *et al.*, "Na-ion batteries: positive electrode materials" Encyclopedia of Inorganic and Bioinorganic Chemistry, 2019.
- E. H. Driscoll *et al.*, "The importance of ionic radii in determining the structure obtained for sodium transition metal sulfates: Tuning structure through transition metal and selenate doping", *Journal of Solid State Chemistry*, 2020, **282**, 121080.
- E. H. Driscoll *et al.*, "The Building Blocks of Battery Technology: Using modified tower block games set to explain and aid the understanding of rechargeable Li-ion batteries", *J. Chem. Educ.* 2020, 97, 8, 2231–2237.

The following (working) paper titles are expected from this thesis, as a whole or as a contribution:

- E. H. Driscoll *et al.*, "Novel Sodium Titanium Hydroxy Sulfate Material", unpublished work.
- L. L. Driscoll, E. H. Driscoll *et al.*, "Ball milling electrode materials: utilization of pressure phenomena to obtain next generation electrode materials", unpublished work.
- E. H. Driscoll *et al.*, "Novel high power Li-ion anode: $Nb_9Ti_{1.5}W_{1.5}O_{30}$", unpublished work.
- E. H. Driscoll *et al.*, "Recharging Battery Education and Engagement: Synthesis, Manufacturing, and Recycling – extended battery outreach resources", unpublished work.

Table of Contents

Chapter 1: An Introduction to Li- and Na-ion batteries

Over the course of this doctoral programme from commencement of studies in 2017, Li-ion batteries have remained a hot and important topic – such that the increased interest for electrification for the automotive industry has had its own media "thermal" runaway, with the dream of purchasing electric vehicles becoming more of a reality, evidenced by the increased visibility in society.

This chapter will form an introduction to Li-ion batteries and its lesser known sibling Na-ion. It will cover the initial discovery over 30 years ago (now as of 2019, a Nobel Prize winning discovery) to understanding the fundamentals of battery operation. This will then be extended to exploring the common materials for both cathode and anode chemistries in both Li-/Na-ion, before considering the latest materials to come into the spotlight as well as areas of increased interest.

Figure 1. 1: Chapter abstract representing 'towards an electric future' which involves decarbonising the transport network through electrification, and considering alternative Li-ion technologies, such as Na-ion. Both technologies and the (intercalation) chemistries and electrodes will be discussed.

1.1 Background

The modern life-style, compared to the pre-industrial period, has been dependent on the use of fossil fuels, whether it is for the heating of homes or for the transport network, the consumption of these finite resources has been a driving cause towards the green house effect and thus, can be correlated to the adverse and extreme weather conditions associated with climate change.

Efforts towards mitigating climate change effects and the global temperature rises (limiting increase to 1.5 °C) are now being reflected in policy makers' mandates with the push towards Net Zero emissions.[1] One such UK government policy involves the end of sales of new petrol and diesel cars by 2030, in addition to a commitment for all cars to be fully zero emissions capable.[1] The move towards electric vehicles (EV) will not only benefit climate targets, but has the added advantage of improving air quality in urban areas. Thus towards an electric future, understanding the Li-ion technology and developments from a chemist's perspective is paramount, in addition to how Na-ion batteries can be sought as an alternative for infrastructure energy storage.

1.2 Battery Operation: Li- and Na-ion

A battery is an electrochemical cell which produces an electric current via a chemical reaction.[2] Although the term battery nominally signifies multiple cells, the term is often loosely used to describe a single cell. There are two types of batteries: non-rechargeable (primary) and rechargeable (secondary); Li- and Na-ion being examples of the latter. While the name (non)-rechargeable distinguishes nominally the differences in operation, all electrochemical cells consist of two electrodes: termed anode and cathode, with an electrolyte. Note within battery research, in particular, to the

rechargeable types, the electrodes are defined based upon the redox reactions happening upon discharge. This nomenclature will be continued throughout and explored further within section **1.6 Educational Resources** on **p46**.

Upon charging a rechargeable Li-/Na-ion battery, an electron is shuttled from the cathode to the anode through an external circuit, whilst the counter positive-ion (Li^+ or Na^+) transverses the electrolyte to intercalate into the anode material (**Figure 1. 2**). The reverse process occurs on discharging, whereby the electron in the external circuit is used for work before re-entering the cathode material (**Figure 1. 2**).[3] This mechanism described has led to this type of battery being termed 'rocking chair' where the electrodes operate via (de)intercalation reactions.

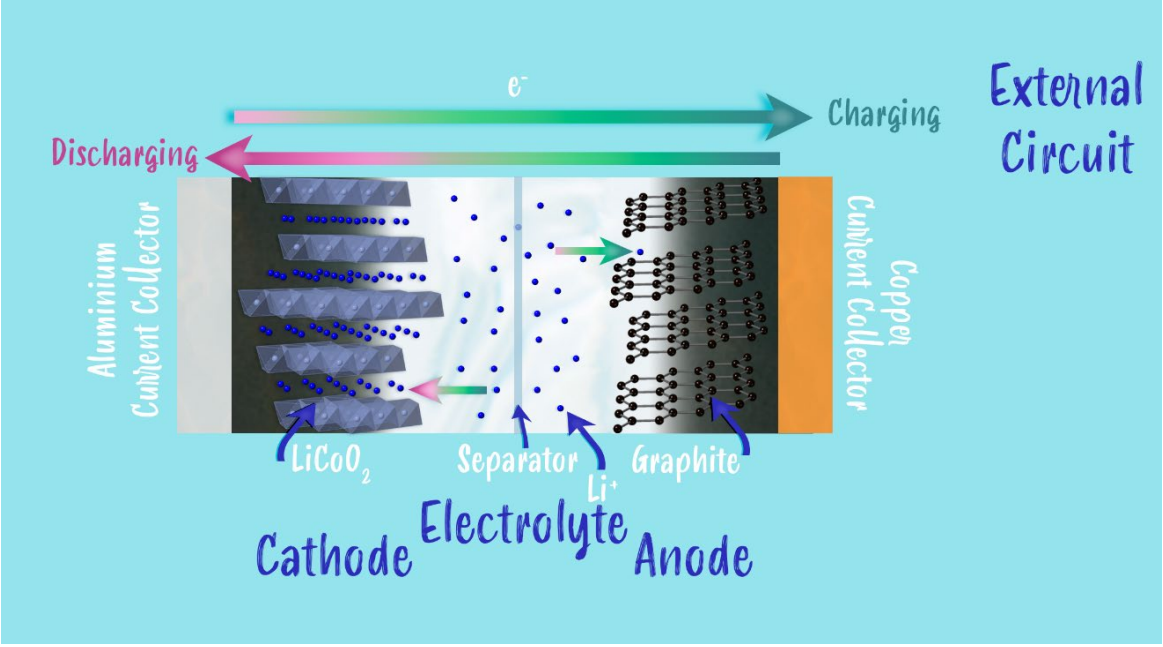

Figure 1. 2: Diagram depicting the movement of charges upon charging (arrows pointing to right) and discharging (arrows pointing to left).

A key characteristic of this type of electrode material in Li-/Na-ion batteries is the ability to act as intercalation host structures, such that they contain empty channels or layers capable of reversibly accommodating the ions, in addition to a mixed-valence species in the host framework to accept and release electrons.[4] Both the cathode and anode material must have the ability to (de)intercalate ions, without major structural changes, in addition to demonstrating high ionic and electronic conduction. To prevent short-circuiting of the cell, the electrolyte requires a negligible electronic conduction but a high ionic conduction. Within cell fabrication, a physical barrier – known as a separator is also included, to prevent short circuiting through direct physical contact (see **Figure 2. 9** for a coin cell set-up).

One less obvious feature is the requirement for the chemical potentials of the anode (μ_A) and cathode (μ_C) to be within the electrolyte's thermodynamic stability window (E_g), unless a solid-electrolyte-interface (SEI) is formed within the device to give a protective passivation layer. Without the condition of $\mu_A - \mu_C \leq E_g$ or the formation of an SEI, the cathode can oxidise the electrolyte or alternatively the anode can reduce the electrolyte, thus potentially damaging this component.[3] A schematic demonstrating the different energy levels of the three components is shown in **Figure 1. 3.** The band gap of the electrolyte is between the highest occupied molecular orbital (HOMO; valence band) and the lowest unoccupied molecular orbital (LUMO; conduction band).

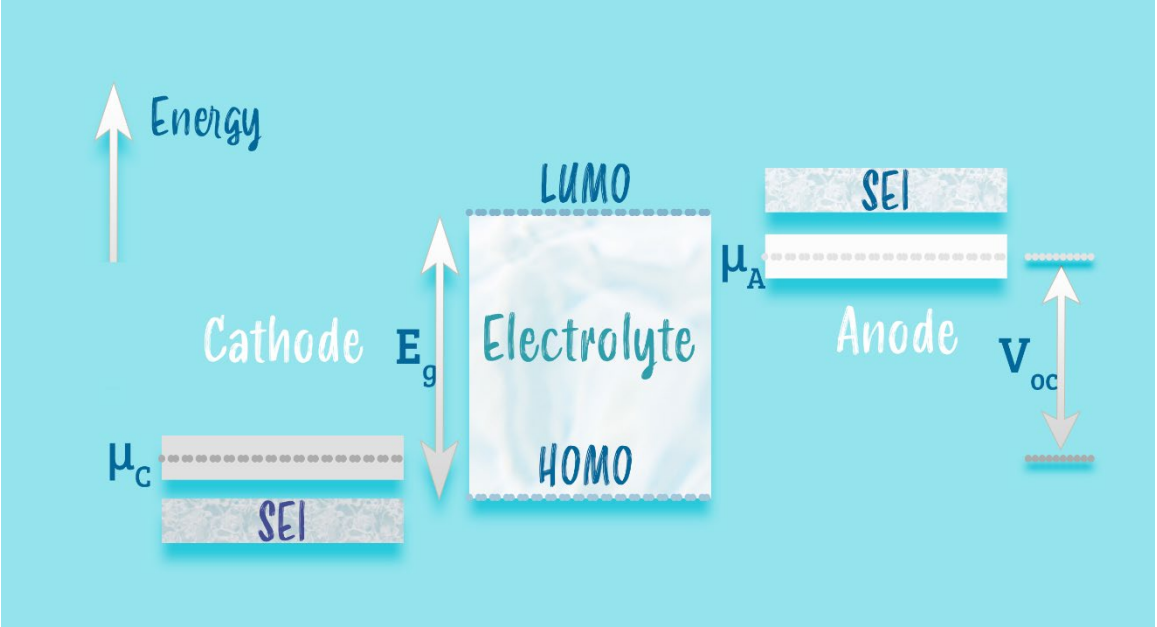

Figure 1. 3: Band diagram of the associated energy levels of the electrodes and electrolyte within the thermodynamic stability window or outside in the form of SEI.

An initial factor in determining the effectiveness and performance of a battery is the energy density, which is often deduced collectively by the Li-/Na-ion storage capacity and the discharging potential of the cell.

The theoretical energy density of a battery cell is given by the product of the theoretical capacity and open-circuit voltage (**Equation 1. 1**). The capacity (Λ), depending on the application specifics, can be quantified as charge transfer per unit weight (specific/gravimetric capacity; A h g^{-1}) or as charge transfer per unit volume (A h cm^{-3}). The difference in the chemical potentials of the electrodes over the magnitude of electron charge, between the anode and cathode affords the open-circuit voltage (V_{oc}) (**Equation 1. 2**). **Figure 1. 4** shows numerous electrode materials at respective potentials to lithium metal and in short shows the varying V_{oc} between the electrode materials (i.e. the difference).

Equation 1. 1: Determination of the theoretical energy density of a battery.

$$E = \Lambda V_{oc}$$

Equation 1. 2: Determination of the open-circuit voltage from the corresponding chemical potentials of both electrodes.

$$eV_{oc} = \mu_A - \mu_C$$

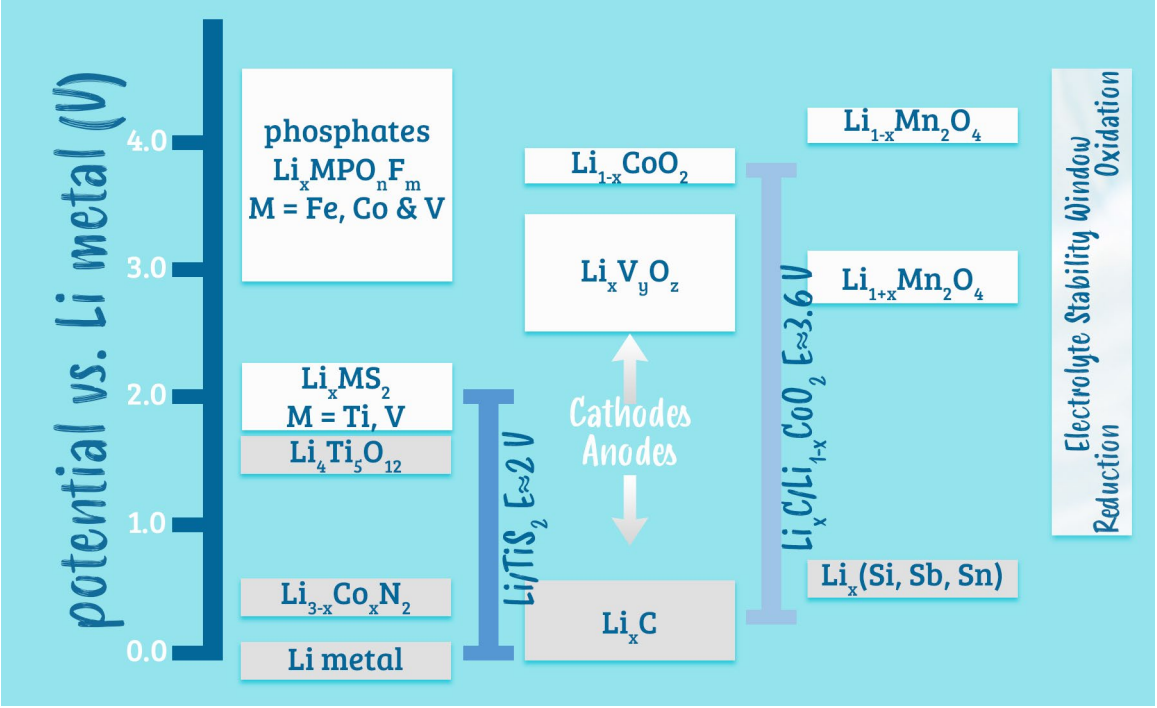

Figure 1. 4: Voltage ranges for various cathode and anode combinations. The difference between the two electrodes is the cell voltage. Figure adapted from P. M. Woodward, P. Karen, J. S. O. Evans and T. Vogt, Solid State Materials Chemistry, Cambridge University Press, Cambridge, 2021.[5]

To compare the various existing rechargeable technologies, an energy density plot considering both the gravimetric and volumetric contributions of the active materials can be plotted (**Figure 1. 5**), which visually describes the importance of Li-ion batteries being a lead technology in high energy density, low weight and volume technology. Future alkali technologies: Na-ion and K-ion are included in addition.

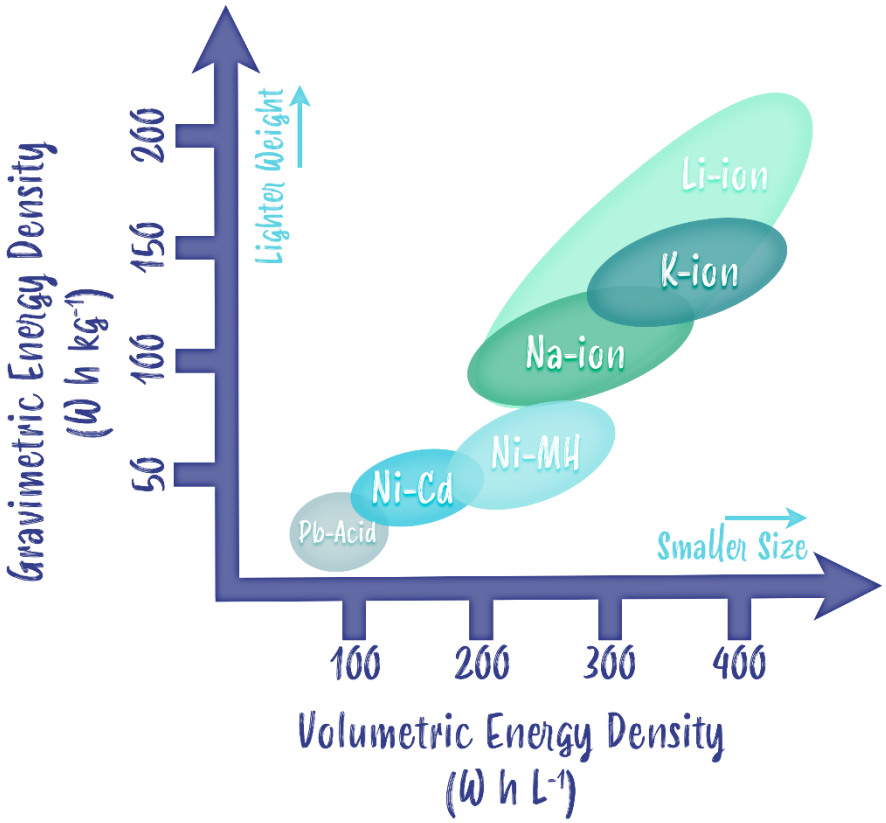

Figure 1. 5: Energy densities of commercial batteries, with the addition of alkali metal intercalation batteries. Schematic adapted from El Kharbachi et al., J. Alloys Compd., 2020, 817, 153261. [6]

1.3 Lithium-ion Chemistries

1.3.1 Li-ion Cathodes

1.3.1.1 Oxides

Layered oxide materials of the form $LiMO_2$ (M = Co, Ni and Mn) with the rocksalt structure, have witnessed widespread and successful commercialization, most notably the cathode material $LiCoO_2$ (LCO). Developments upon this archetypal LiB material has seen alternative transition metals, either fully replacing the Co, or partially substituting, in this composition. These materials will be considered in turn, focusing on performance and the design strategy thereafter.

1.3.1.1.1 $LiCoO_2$ (LCO)

LCO was initially prepared by Goodenough *at al.* in the 1980's and demonstrated an open-circuit voltage of ca. 4.0 V against Li metal, which is associated with the redox couple of Co^{3+}/Co^{4+}.[7] The predecessors of this technology, were nominally sulfide based ($LiTiS_2$; 2 V achieved against lithium metal[8]) – while these paved the way for layered intercalation structures, the move towards oxide based materials allows for a greater accessible voltage window (**Figure 1. 6**). In the 1990's, this material gained further attention with SONY successfully producing a Li-ion battery, through use of this material in conjunction with a carbon anode, which has witnessed widespread commercialization.[9]

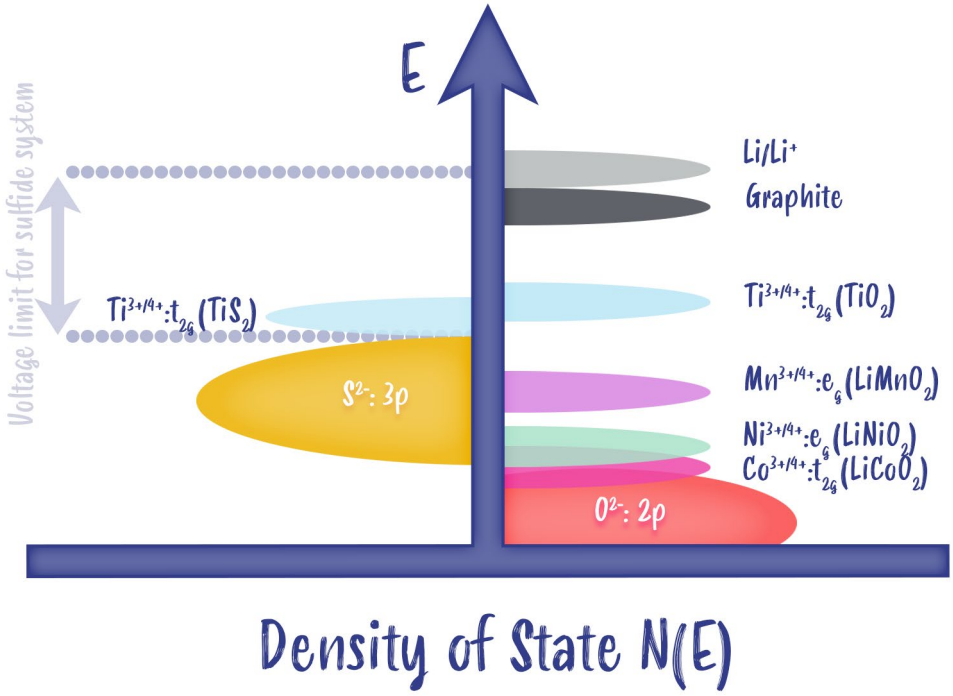

Figure 1. 6: Band diagram representing the relative redox energies of $M^{3+}/^{4+}$ (M = Mn, Co, Ni, Ti) in relation to anions (S^{-2} and O^{2-}). Schematic adapted from A. Manthiram, Nat Commun 11, 1550 (2020).[10]

LCO has the α-$NaFeO_2$ rocksalt structure, where alternating layers (111) consist of ordered Li^+ and Co^{3+} octahedra (**Figure 1. 7**) within a cubic closed-pack array of oxide ions (i.e. ABC stacking) – which is termed an O3 structure. This nomenclature[11] used extensively in the oxide literature is used to describe how the layers stack and quite commonly it is with reference to O3 and P2 structures (**Figure 1. 8**). The letter corresponds to the co-ordination of the lithium (sodium for NiBs oxide structures) in the layered structure (O referring to octahedral; P referring to prismatic). The number refers to the number of MO_2 layers required to form the structure, and equally the stacking within the oxygen sub-lattice; O3 as described previously being ABC, while P2-type materials stack AABB. The inclusion of ' following the co-ordination distinction refers to distortion within the MO_2 layers.

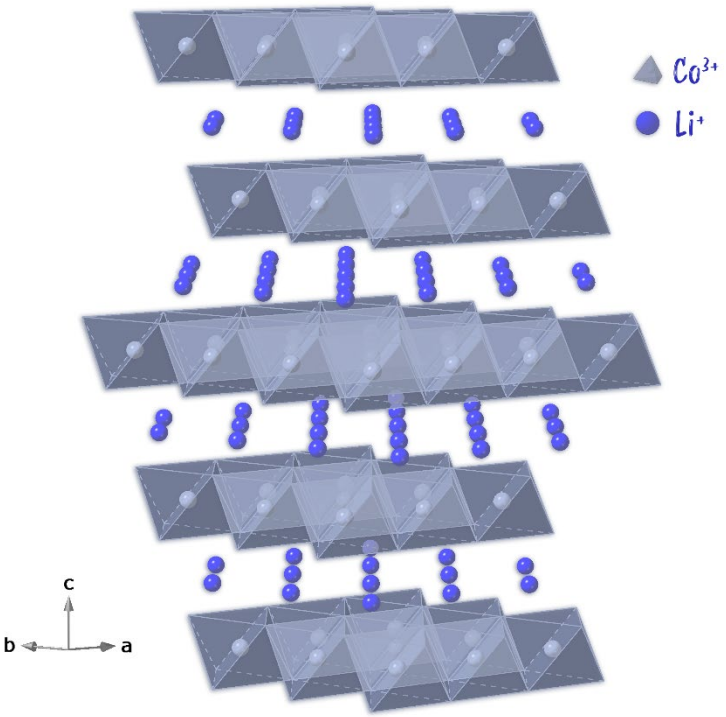

Figure 1. 7: Crystal structure of $LiCoO_2$.

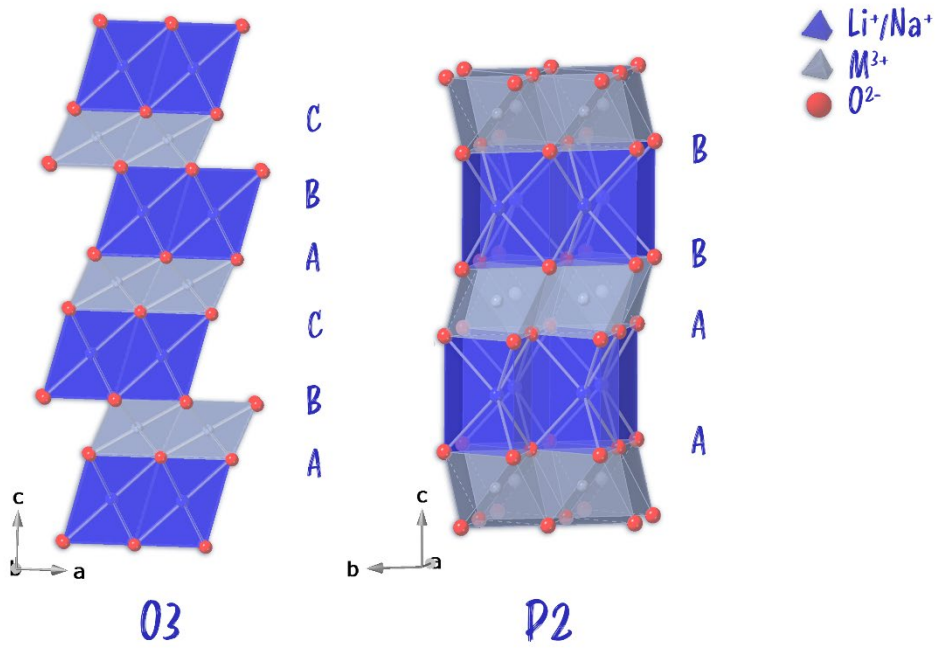

Figure 1. 8: Differentiation of O3 and P2 stacking. Schematic adapted from Driscoll et al., Na-Ion Batteries: Positive Electrode Materials in Encyclopedia of Inorganic and Bioinorganic Chemistry, R. A. Scott (Ed.), Wiley, 2019, doi:10.1002/9781119951438.eibc2686.[12]

The theoretical capacity of this material is calculated to be 273.8 mA h g^{-1}, however due to safety concerns only ½ mole of Li can be extracted per formula unit, resulting in the actual measurable capacity to be approximately 140 mA h g^{-1}. This limitation is the result of the band overlap seen for $Co^{3+/4+}$ t_{2g} and O^{2-} p-orbital (**Figure 1. 6**), such that with increasing hole (i.e. electron vacancies) generation through oxidation and electron promotion to the anode (Li/Li^+ metal or graphite) band, oxygen can be evolved from the lattice[13] and thus is a major safety concern given contact with the highly flammable liquid electrolyte.

Other drawbacks of this material consist of capacity fade at high current cycling, in addition to high toxicity and cost associated with the use of cobalt. From an ethical standpoint, there are also serious concerns regarding the sourcing of cobalt – the Democratic Republic of Congo (DRC) being the largest producer, has received significant attention regarding child labour and modern slavery in its 'Artisanal and Small-scale Mining (ASM)' industry.[14] In lieu of this, cathode chemistries have been developed which have no or limited Co use.

1.3.1.1.2 $LiNiO_2$ (LNO)

$LiNiO_2$ is isostructural with LCO. Although a promising candidate (theoretical capacity of 275 mA h g^{-1}), this material is sensitive to the synthesis route and in particular the mixing of Ni into the Li sheets results in electrochemical inactivity, through the Li diffusion pathways becoming blocked[15,16]. The re-introduction of Co (e.g. 20% substitution) into LNO affords added structural stability, however, the material

remains sensitive to moisture in ambient conditions and proves tricky to handle during manufacturing.

1.3.1.1.3 $LiNi_{0.8}Co_{0.15}Al0_{.05}O_2$ (NCA)

To further improve the stability of the LNO beyond Co substitution, Al substitution proves a fortuitous material known as NCA. While Co limits the degree of cationic mixing, the Al improves the thermal stability and electrochemical performance.[17]

1.3.1.1.4 $LiMnO_2$

The Mn equivalent of LCO and LNO has been proposed as a potential cathode candidate, due to Mn's high natural abundance and low toxicity, however, this system's limitation is a known phase change to a more stable spinel structure ($LiMn_2O_4$; LMO) where manganese is present in both +3 and +4 oxidations states.[18] The phase change corresponds to the migration of Mn from octahedral sites within the MO_2 layers, via a tetrahedral site, into an octahedral site within the Li^+ layer.[10] The structure and electrochemical performance of $LiMn_2O_4$ (LMO) will be discussed in section **1.3.1.1.6** on **p14**.

1.3.1.1.5 $Li(Ni_xMn_yCo_z)O_2$ (x+y+z =1; NMC)

While retaining the focus on layered cathode systems, multiple compositions (**Table 1. 1**) have been developed with the triple transition metal system containing Ni, Mn and Co and often denoted with NMC (not as common but it is sometimes written as NCM). NMC-type materials were created to take advantage of the characteristic chemical and structural stability of these three metals, in addition to considering

abundance and environmental issues. Through synthesis of this material, the oxidation of Mn^{3+} to Mn^{4+} through the reduction of Ni^{3+} to Ni^{2+}, results in Ni^{2+}serving as a structural stabilizer without involvement in the redox processes during (dis)charging of the material.[10] In terms of chemical stability, when considering the band structure (**Figure 1. 6**) oxidation of the $Mn^{3+/4+}$ doesn't afford the release of oxygen from within the cell, however, as mentioned above can suffer structural instability through migration of the ions from different octahedral sites.

With respect to the NMC chemistries, lower Ni contents (NMC-111/-532/-622) are currently used commercially, however this is expected to be superseded by Ni-rich cathodes.[19] The pursuit towards NMC 811 and beyond mitigates Co usage, while obtaining higher capacities, although moisture instability inhibits ease of manufacture, commonly needing coatings to be used.

Table 1. 1: Variety of NMC compositions with their specific capacities. NMC 111 up to NMC 811 capacities have been obtained from a supplier, while the higher Ni content NMC capacities are obtained from the literature.

Nomenclature	Chemical Formula	Capacity (mA h g^{-1})	Ref.
NMC 111	$LiNi_{0.33}Mn_{0.33}Co_{0.33}O_2$	154.8	20
NMC 532	$LiNi_{0.5}Mn_{0.3}Co_{0.2}O_2$	187	
NMC 622	$LiNi_{0.6}Mn_{0.2}Co_{0.2}O_2$	175.8	
NMC 811	$LiNi_{0.8}Mn_{0.1}Co_{0.1}O_2$	203.4	
NMC 955	$LiNi_{0.9}Mn_{0.05}Co_{0.05}O_2$	221	21
	$LiNi_{0.95}Mn_{0.025}Co_{0.025}O_2$	230	

1.3.1.1.6 $LiMn_2O_4$ (LMO)

The spinel structure of $LiMn_2O_4$ has been shown to cycle reversibly[22] although due to the presence of the Mn^{3+} ion, a Jahn-Teller distortion decreases the performance of the cathode on cycling with a phase change from a cubic to a tetragonal spinel.[23] The doping of mono- and multi-valent cations onto the manganese site has been shown to improve the capacity retention by keeping the average oxidation state of manganese above +3.5.[24] The crystal structure of $LiMn_2O_4$ is shown in (**Figure 1. 9**) which shows Mn ions to occupy the layer in between alternate layers of the oxides in addition to ions being present within the lithium layer.

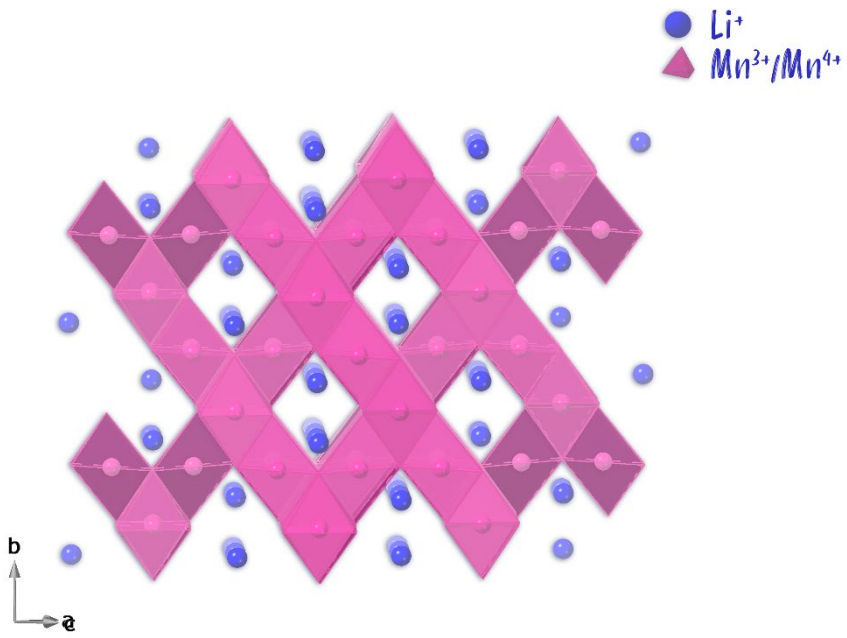

Figure 1. 9: Crystal structure of LMO.

1.3.1.2 Polyanions

The use of polyanions (XO_4/XO_3) offers the advantage of influencing the energy of redox couples through an inductive effect. The counterion within the polyanion, often in general denoted by X, has the ability to withdraw electron density within the metal – polyanion framework through the M – O – X connection from the adjacent M – O bond. Through this inductive effect, the overall covalency is reduced, resulting in reduced band overlap with increasing ionicity, and hence the energy of the M^{2+}/M^{3+} redox couple is reduced, as shown in **Figure 1. 10**. The XO_4/XO_3 group is used to define SO_4^{2-},PO_4^{3-}, SiO_4^{4-} and BO_3^{3-}. The sulfate unit is found to show the greatest inductive effect, in contrast to the silicate unit with the lowest. The phosphate and borates are intermediate between these two limits.

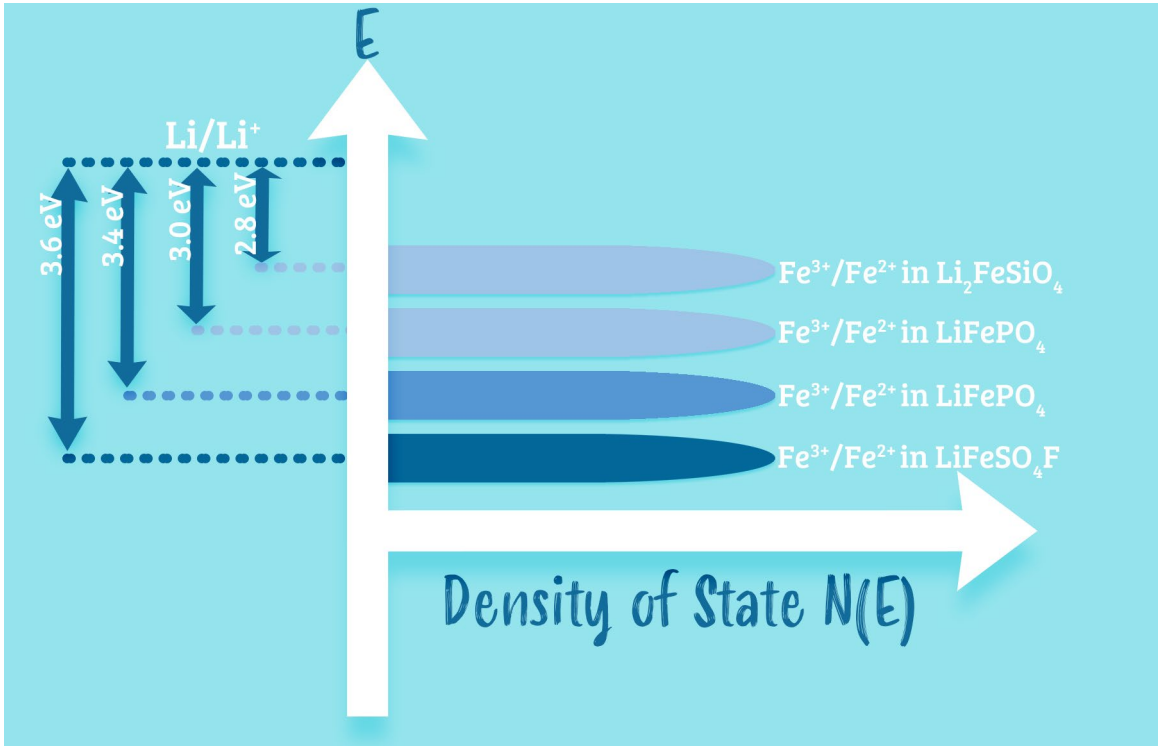

Figure 1. 10: Effect of the Fe redox couple with different polyanion groups. Diagram adapted from Barpanda et al. Trans. Indian Ceram. Soc., 2015, 74, 191–194 .[25]

1.3.1.2.1 $LiFePO_4$ (LFP)

Work by Goodenough *et al.* led to the proposal of $LiFePO_4$ as a potential cathode material with a voltage of 3.5 V against Li.[26] Reversible extraction of lithium from the composition was demonstrated, utilizing the Fe^{2+}/Fe^{3+} redox couple, in addition to the insertion of Li into $FePO_4$.[26] This material is an inexpensive, non-toxic and a safe option due to the full delithiated product $FePO_4$ being stable. LFP is reported to have an olivine structure – a hexagonal analogue to the spinel structure – often denoted M_2XO_4. Within the hexagonal closed-packed oxide array, one eighth of the tetrahedral sites are occupied by the X ions, whilst half of the octahedral sites are occupied by the M ions.[4] The crystal structure of LFP is shown in **Figure 1. 11.** The olivine structure crystallizes in preference to spinel with the presence of certain small X ions such as B^{3+}, Si^{+4} and P^{+5}.[26]

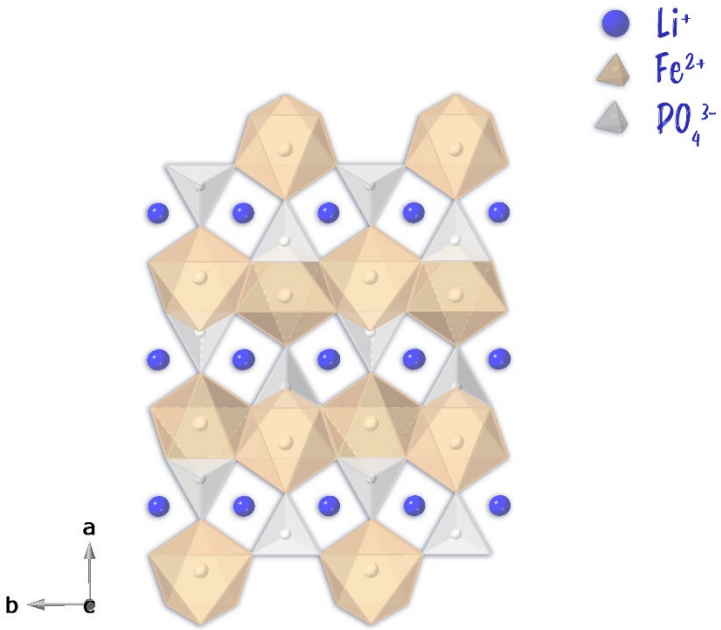

Figure 1. 11: Crystal structure of LFP.

1.3.2 Li-ion Anodes

1.3.2.1 Lithium Metal

As previously noted within the cathode literature, lithium metal has been a common anode to pair against. Being the lightest and most electropositive element (-3.04 V against SHE), this anode provides a foundation for light weight, high energy dense batteries with a theoretical capacity of 3,862 mA h g^{-1}. However, notably inefficient cycling with the use of organic electrolytes, due to the formation of a passivating layer (SEI) which consequently modifies the charge transfer reaction mechanism and continual growth of this layer, with consumption of lithium (low Coulombic efficiency), increases the impedance of the electrode.[27] The limitation of this electrode resides with issues surrounding safety. When considering high power applications, such as for electric vehicle use, high (dis)charge rates[28] are required to meet consumer expectations and use. With the use of lithium metal anodes and high current rates, the lithium plating can become non-uniform resulting in the formation of dendrites. Large dendrite growth can effectively cause bridging of the two electrodes, through piercing the separator, such that a large current can now pass and heat is generated rapidly[29] – a considerable and severe safety risk with the involvement of a flammable liquid electrolyte.

1.3.2.2 Graphite

Current anode technology often consists of a graphite-based (**Figure 1. 12**) electrode, due to its favourable properties: high capacity (372 mA h g^{-1}), low working voltage potential and low cost, within Li-ion battery architecture. The draw back with graphite, however, is the poor stability in high (dis)charging operation conditions, while maintaining long term stability and energy density. An unwanted characteristic relates back to the formation of dendritic lithium on the electrode, where upon fast charging Li plating can occur leading to the potential for the dendrite effect bridging between the two electrodes – thus resulting in a short circuit.

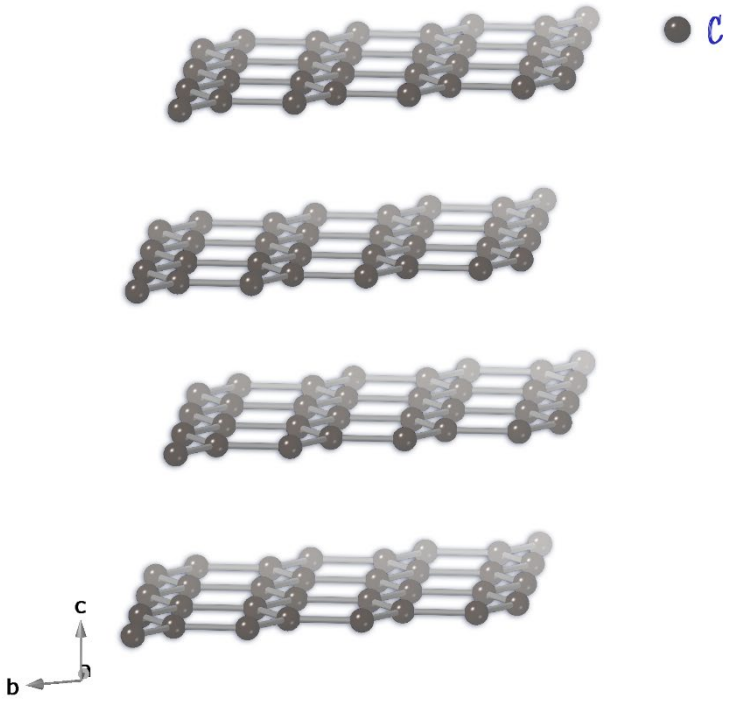

Figure 1. 12: Crystal structure of graphite.

1.3.2.3 $Li_4Ti_5O_{12}$ (LTO)

The spinel of lithium titanate (**Figure 1. 13**) is an alternative to graphite, and has the capability to withstand fast charge with good reversibility. The limitation comes in the form of a lower energy density, through the operating voltage being ca. 1.5 V[30], rather ca. 0 V for graphite vs Li/Li^+, in addition to having a maximum capacity of 175 mA h g^{-1}. The inherent safety and rate capability is the result of the high average voltage, such that there is no risk of Li dendrites or substantial lithium loss due to SEI formation.

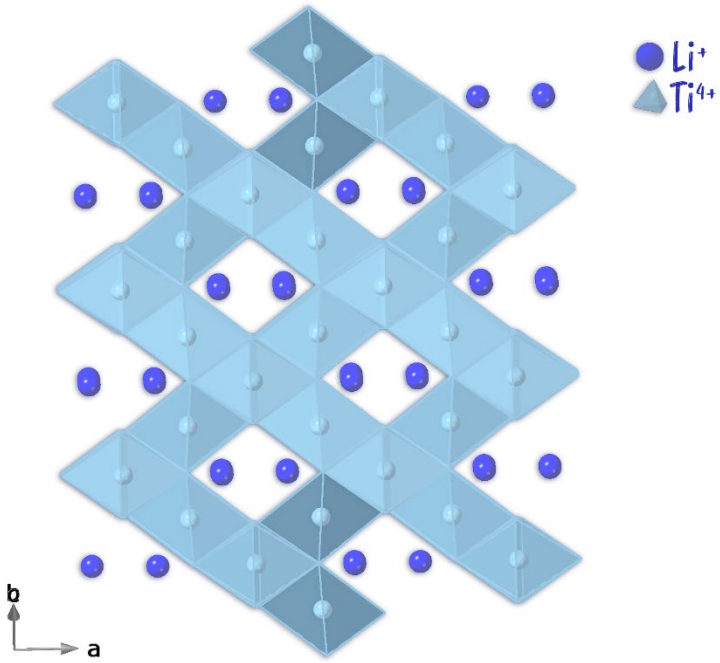

Figure 1. 13: Crystal structure of LTO.

1.3.2.4 Nb_2O_5 Polymorphs

Niobium containing oxides have recently been proposed for fast charge applications, with good stability at the high charge rates, with the observed capacities found to be much higher than LTO.

Of interest (and the simplest) has been Nb_2O_5 – however multiple polymorphs exist and thus have shown varying cell performance. Rather than the conventional Greek-letter denotation for naming polymorphs, Schäfer *et al.* (following on notation from Brauer's[31] classification) classified Nb_2O_5 based on the temperature at which the phases are obtained at: TT, T, M and H (from the German of Tief-Tief (TT), Tief (T), Medium (M) and Hoch (H) meaning low-low, low, medium and high).[32,33] Other polymorphs of Nb_2O_5 are named based-on the morphology of the particles, which again derives from German translation and definitions: B (leaves/plates), N (needles) and R (prisms).[33]

As reiterated by Nico *et al.*, with the numerous polymorphs existing for this system, long-standing confusion and misconceptions of these systems are still prevalent nearly half a century upon the initial body of work.[33] Nominally within the literature, the intermediate polymorphs such as T (orthorhombic) and M (tetragonal) are sometimes confused, in addition to the notation of M-Nb_2O_5 being used by some groups to describe the monoclinic H-Nb_2O_5[34]. While the polymorph may be misnamed, further variations are noted in cell performance[34] and quite often originate from the synthesis conditions[35,36].

Within the literature, there appears to be no golden ticket polymorph of Nb_2O_5 to use – such that the material isn't consistently good at both low and high current densities; although high capacities at high current densities is highly preferable given the desired application for high power use. Hu *et al.* found M-Nb_2O_5 (tetragonal) to have the greatest discharge capacity at higher current densities (5 A g^{-1}) compared to the other polymorphs (T (orthorhombic)-, TT (pseudohexagonal)-, and H (monoclinic) - Nb_2O_5).[37] At lower current density (0.1 A g^{-1}), M- and H-Nb_2O_5 out-perform T- and TT-polymorphs. Grittith *et al.* found at very low current density (20 mA g^{-1}), the H-Nb_2O_5 to be superior in the capacity, however with increasing current densities (rate) the capacity of this polymorph beyond 100 mA g^{-1} up to 2 A g^{-1} decreases significantly in capacity, and instead all other 3 polymorphs considered (B (monoclinic)-, T- and TT-) have greater capacities – with T-Nb_2O_5 having the highest.[38]

Li et *al.* considered the amorphous polymorph, however at a current density of 50 mA g^{-1} the order of highest capacities returned TT>T>a.[39] With the varying differences in capacity values at the different rates, it is therefore important to have tests which considered low and high current densities.

To attempt to see correlation within the literature, where values have been given with the current densities, these have been tabulated in **Table 1. 2**.

Table 1. 2: The determined specific capacities and the corresponding applied current densities for each polymorph of Nb_2O_5 described within the literature.

Polymorph	Crystal Symmetry	Capacity (mA h g^{-1})	Applied Current Density (mA g^{-1})	Reference
a	Amorphous	149	50	39
TT	Pseudohexagonal	191	50	39
		112.2	100	37
		165	200	38
		19.3	5000	37
T	Orthorhombic	152	50	39
		117.3	100	37
		160	200	38
		33.2	5000	37
M	Tetragonal	162.3	100	37
		121.6	5000	37
H	Monoclinic	151.8	100	37
		175	20	38
		151.8	100	37
		67.8	5000	37
B	Monoclinic	20	20	38

1.3.2.5 Wadsley-Roth Structures

The following systems to be discussed for high power applications will largely be Wadsley-Roth block structures which are oxygen-deficient derivatives of the ReO_3 crystal structure (i.e perovskite-type with no A-site cation occupancy; **Figure 1. 14**), and commonly form for compositions of NbO_2-Nb_2O_5[40], TiO_2-Nb_2O_5[40] and WO_3-Nb_2O_5[41]. The blocks are defined by the shear planes which exist within the structure to compensate for the oxygen off-stoichiometry (**Figure 1. 15**), such that the blocks are connected through octahedra that have been rotated from corner- to edge-sharing (**Figure 1. 16**).[42] The blocks themselves can be defined by $n \times m$.

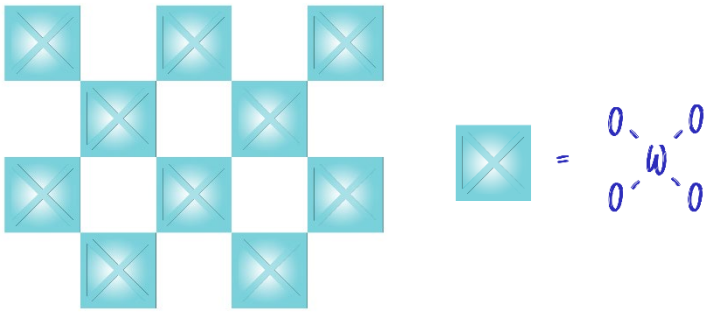

Figure 1. 14: Schematic representing corner-sharing blocks of WO_6 octahedra. Adapted from A. R. West, Solid State Chemistry and its applications, John Wiley & Sons Ltd, Chichester, 2014.

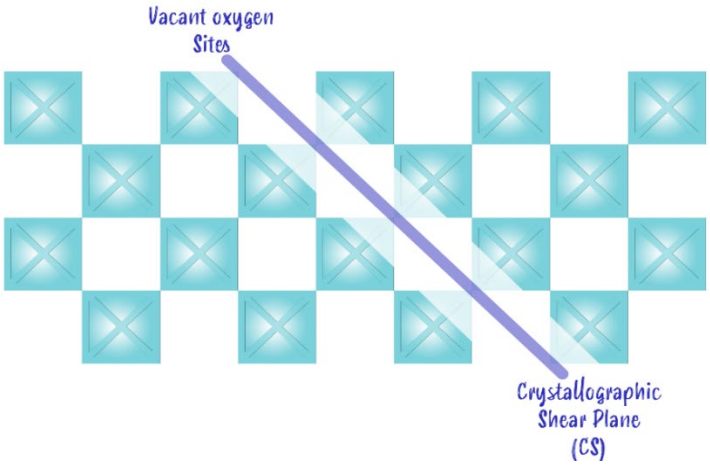

Figure 1. 15: Block structure with a crystallographic shear plane present with vacant oxygen sites. Adapted from A. R. West, Solid State Chemistry and its applications, John Wiley & Sons Ltd, Chichester, 2014.

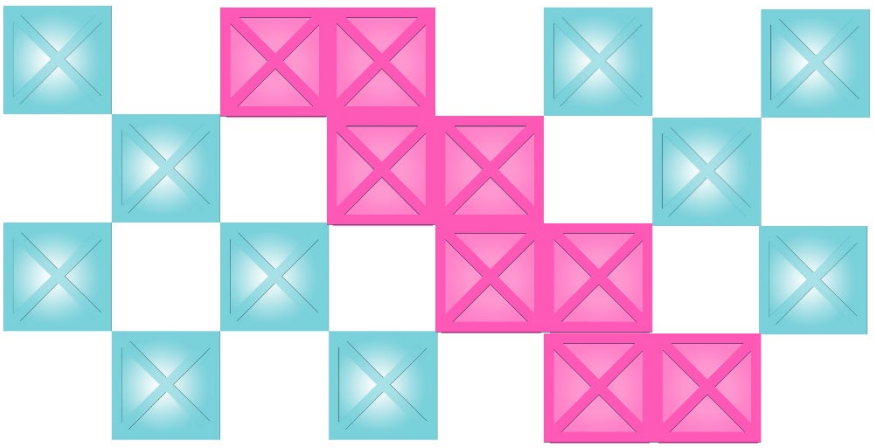

Figure 1. 16: Formation of Wadsley-Roth block structures, where the octahedra have rotated to form blocks of edge sharing to compensate for the oxygen deficiency along the CS plane – these are represented with the pink blocks. Adapted from A. R. West, Solid State Chemistry and its applications, John Wiley & Sons Ltd, Chichester, 2014.

1.3.2.6 Titanium Niobate Systems

Ti-Nb-O systems such as $TiNb_2O_7$ (TNO), $TiNb_{24}O_{62}$ and $Ti_2Nb_{10}O_{29}$ have been demonstrated as alternatives to LTO, which operate in a similar voltage window, however are advantageous as higher capacities are achievable due to the multi redox couples accessible with Nb.

1.3.2.6.1 $TiNb_2O_7$ (TNO)

The TNO crystal structure is considered to be the first block/Wadsley-Roth phase, such that the phase is found to consist of 3 x 3 blocks, as shown in **Figure 1. 17**. Although it was initially thought that the Ti and Nb were randomly distributed across the 5 crystallographic distinct positions, Rietveld refinement using Neutron data found

preference for the Nb to occupy the central corner-shared octahedra, while Ti had preference for the edge-shared octahedra.[43]

The theoretical capacity of TNO was determined to be 387.6 mA h g^{-1}, based upon multiple metal redox couples of: Ti^{4+}/Ti^{3+}, Nb^{5+}/Nb^{4+} and Nb^{4+}/Nb^{3+} occurring.[44] The renewed interest in this material by Goodenough *et al.* found the performance to be ca. 200 mA h g^{-1} and between ca. 80-100 mA h g^{-1} at C/10 and 2 C respectively.[44] Improvements in performance were found through the doping of Ti and carbon coating the material. As reviewed by Aghamohammadi *et al.*, a wide variation of performances are noted for this material, with synthesis route and particle morphology contributing to these differences.[45]

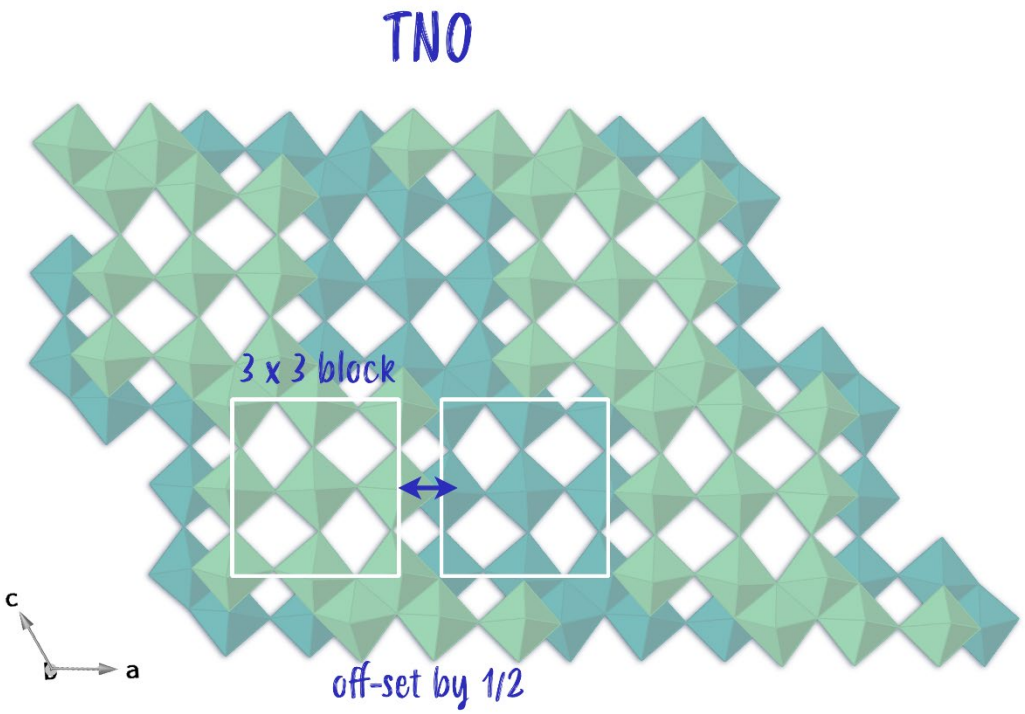

Figure 1. 17: Crystal structure of $TiNb_2O_7$ (TNO). The contrast of the octahedra is to enable clearer depiction of the 3 x 3 block. To simplify the diagram, the oxygens have been omitted.

1.3.2.6.2 $Ti_2Nb_{10}O_{29}$

The related system, $Ti_2Nb_{10}O_{29}$, is a 3 x 4 block structure (**Figure 1. 18**). This material has a theoretical capacity of 395.5 mA h g^{-1}. The discharge capacities determined by Wu *et al.*, at 0.1 C, 0.5 C, 1 C and 10 C were found to be 247, 221, 221 and 130 mA h g^{-1} (where the authors have determined 1 C to be based upon 22 Li^+ inserted into 1 formula unit in 1 hr).[46]

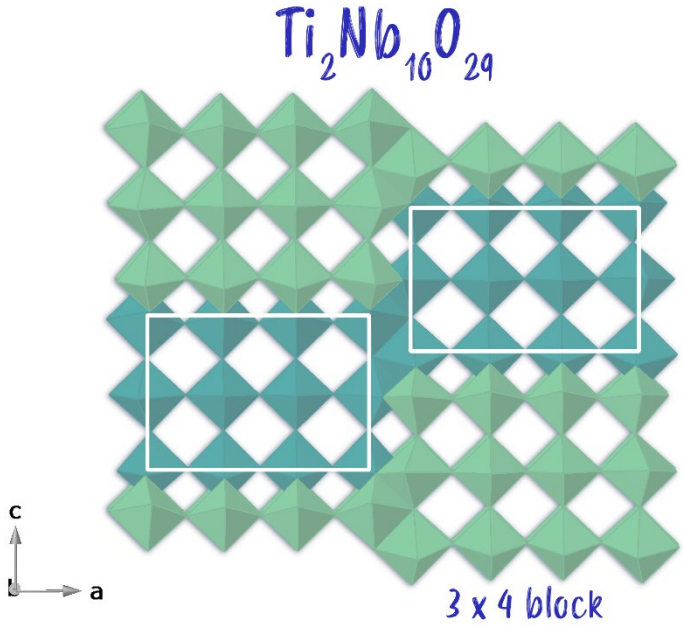

Figure 1. 18: Crystal structure of $Ti_2Nb_{10}O_{29}$. The contrast of the octahedra is to enable clearer depiction of the 3 x 4 block. To simplify the diagram, the oxygens have been omitted.

1.3.2.6.3 $TiNb_{24}O_{62}$

Within the Ti-Nb-O known family, $TiNb_{24}O_{62}$ (**Figure 1. 19**) has the highest theoretical capacity of 402 mA h g^{-1}. Yang *et al.* have investigated this material, and assuming 1 C to be equivalent to the theoretical capacity (representative of 45 Li^+ inserted into 1 formula unit), determined the specific capacity to be 296 and 181 mA h g^{-1} at 0.1 C and 20 C, respectively, for the porous material (their microspheres returned lower capacities at these ratings).[47]

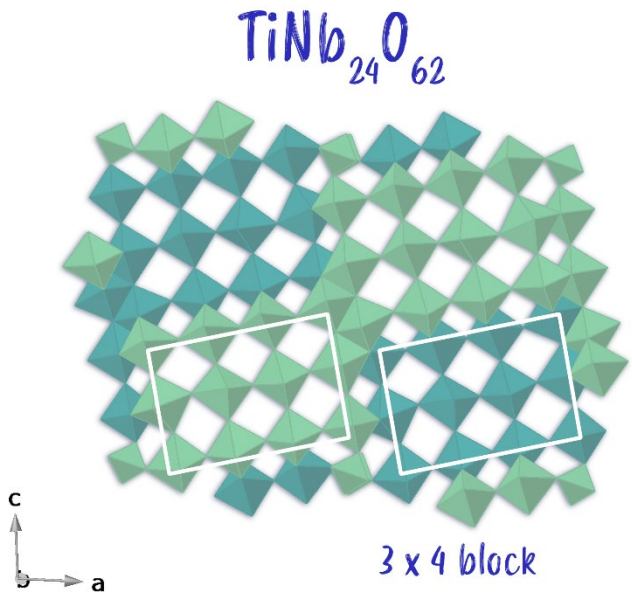

Figure 1. 19: Crystal structure of $TiNb_{24}O_{62}$. The contrast of the octahedra is to enable clearer depiction of the 3 x 4 block. To simplify the diagram, the oxygens have been omitted.

1.3.2.7 Tungsten Niobate Systems

In keeping with a Nb-based system, Nb-W-O systems have been of interest. Considerable work by Griffith *et al.* has investigated these types of systems, in particular $Nb_{16}W_5O_{55}$ (**Figure 1. 20**) and $Nb_{18}W_{16}O_{93}$, which have respective theoretical capacities of 302 and 228 mA h g^{-1}. $Nb_{18}W_{16}O_{93}$ crystal system could not be found in the ICSD database, however, recent reports suggest it to be a non-existent phase and instead draws similarities quite close to known $Nb_8W_9O_{47}$ and $Nb_7W_{10}O_{47.5}$ systems (i.e. $(Nb,W)_{34}O_{94}$).[48]

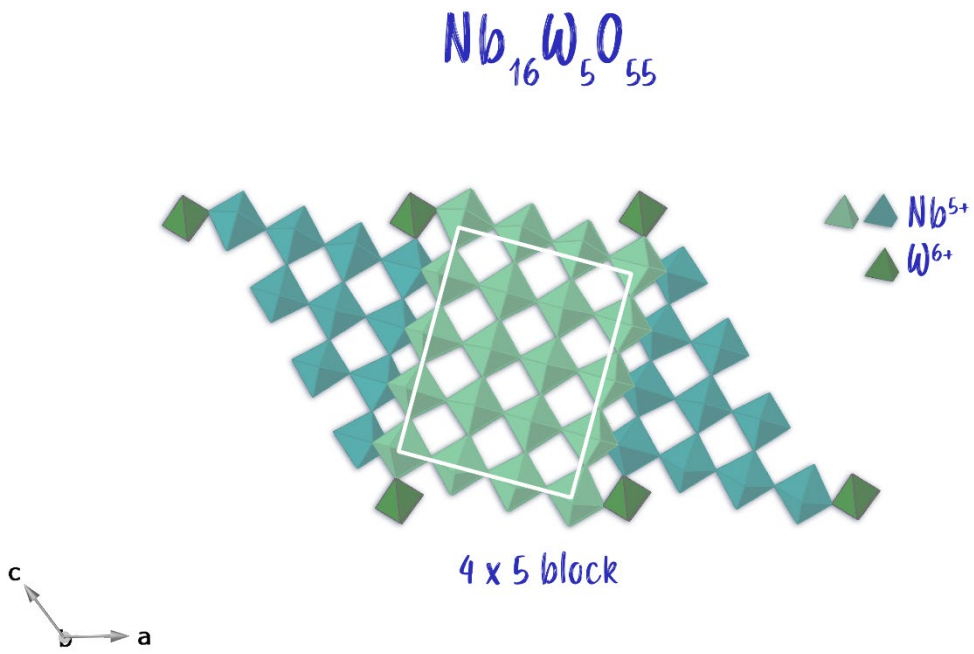

Figure 1. 20: Crystal structure of $Nb_{16}W_5O_{55}$. The contrast of the octahedra is to enable clearer depiction of the 4 x 5 block. To simplify the diagram, the oxygens have been omitted.

For ease of comparison, the resulting capacities achieved at set C-rates (defined within the experimental chapter in section **2.2.5.1.2 C-rate**)/current densities have been tabulated (**Table 1. 3**).[49] Where only a C-rate was given within the publication, the current density is denoted with a * to highlight it has been determined from the values

that have been given. In the instances where the capacity hasn't been quantified, this was estimated from the galvanostatic data that were presented within the publication (from the voltage window of 3 V to 1 V). In actuality, the capacities achieved at C/5 were similar with 225 mA h g^{-1} for both materials and likely it is the Nb being the dominate redox active material.

Table 1. 3: Achieved capacities of Nb-W-O systems, with the associated C-rate/current density applied. [49]

Formula	Theoretical Capacity (mA h g^{-1})	C-rate applied	Current Density Applied (mA g^{-1})	Capacity (mA h g^{-1})
$Nb_{16}W_5O_{55}$	343	C/5	34.3	225
		5C	857.5*	171
		20C	3,430*	148
		60C	10,300	125*
$Nb_{18}W_{16}O_{93}$	228	C/5	29.8*	225*
		20C	2,980*	150
		60C	8,940*	105
		100C	14,900	70

In the work by Griffith *et al.*, the electrode coatings were stated as being 2.1 mg, with the disc diameter being 1.27 cm. In the related patent application of $Nb_{16}W_5O_{55}$, the practical capacity was stated as being 171.3 mA h g^{-1} – lower than the publication claims – this apparent difference can likely be attributed to the electrode coating where within the patent the electrode masses (without the current collector as before) is higher in

the range 6.3 – 7.87 mg.[50] Nominally when pursuing high power applications, thin electrodes are preferred, however in commercial applications thicker electrodes are desired. Given such changes with electrode thickness the differences in literature values should be treated with caution when evaluating material performance. The electrode design approach will be considered within the experimental chapter and re-iterates the importance of this difference (see section **2.2.3 p66**).

1.3.2.8 Niobate Summary

With the multitude of varying compositions of W-/Ti-Nb, for ease of correlation between metal ratio and structure – two further plots have been produced. **Figure 1. 21** shows the ternary plot of all 3 metals in the variety of compositions previously mentioned in this section, while **Figure 1. 22** considers the materials through crystal density and oxygen stoichiometry to relate structure preference/block-size to oxygen content. Considering the information in both figures, when doping with W into Nb_2O_5, a structure changeover occurs from a 4 x 5 Wadsley-Roth block structure ($Nb_{16}W_5O_{55}$) to a tungsten-bronze structure of $Nb_{18}W_{16}O_{93}$, correlating to an increase in the proportion of W from 24% up to 47%. And hence supports previous claims of $Nb_{18}W_{16}O_{93}$ to be a tungsten bronze structure related to $Nb_8W_9O_{47}$ and $Nb_7W_{10}O_{47.5}$ systems (i.e. $(Nb,W)_{34}O_{94}$),[48] rather than a standalone Wadsley-Roth block structure. The change in block size relating to oxygen content is easily visualised in **Figure 1. 22**, whereby smaller blocks correlate to increase oxygen vacancies and hence the formation of greater defects in the form of glide planes.

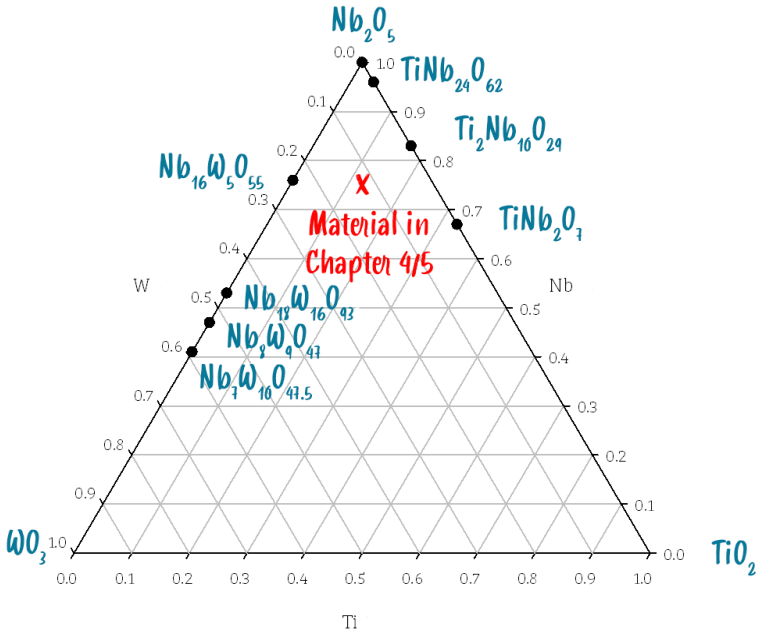

Figure 1. 21: Ternary plot showing the proportion of each metal (Nb/Ti/W) within the structures mentioned in this section ($MO_{2.5}$). The novel material discussed in Chapters 4 and 5 has also been added.

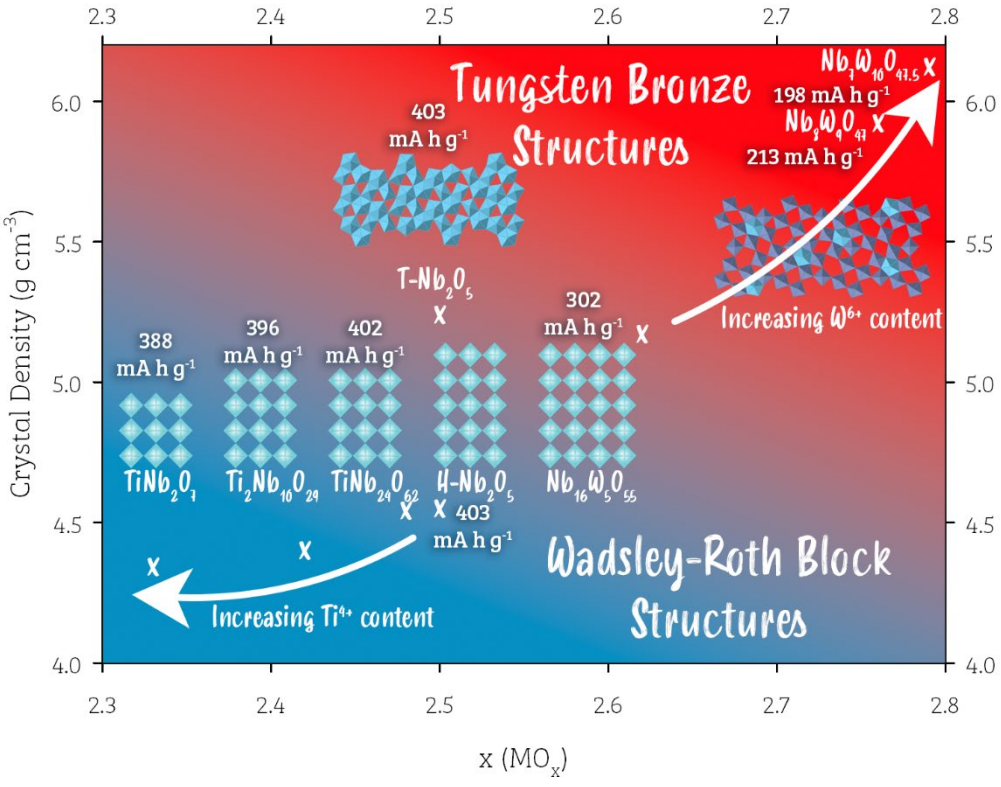

Figure 1. 22: Plot of oxygen content in (MO_x) vs. the crystal density (g cm^{-3}) for all the niobate materials mentioned within this section. Two separate regions on the plot have been denoted with Wadsley-Roth Block structures (with the visual of aid of block size) and Tungsten-Bronze structures. The theoretical gravimetric capacities for all materials have been added – this is based upon Ti^{4+}/Ti^{3+}, Nb^{5+}/Nb^{4+}, Nb^{4+}/Nb^{3+}, and W^{6+}/W^{5+}.

1.4 Alternative Technologies: Na-ion Chemistries

Na-ion batteries (NiBs) in recent years have witnessed a renaissance as a potential technology for large scale storage grid applications. Although this type of battery was initially investigated in parallel to the Li-ion in the 80's[51–54], Li-ion proved more favourable due to the resulting higher energy density and ease of manufacture. However, in recent years, interest in NiBs has been renewed to seek an alternative to Li-ion, where cost is a more important factor than weight or performance[55]. In particular there are concerns regarding abundance (lithium, as of 2020 is regarded as a critical material, joining Co, natural graphite, P on the list)[56] and environmental implications of sourcing lithium (through hard rock and salt brines)[57]. Thus with sodium's higher natural abundance[12,58], this technology can be advantageous in specific applications. Furthermore common commercial Na-ion cathodes do not contain Co.

1.4.1 Na-ion Cathodes

There are many parallels of the materials investigated for use in Na-ion batteries, as to the Li equivalent: from layered metal oxides to polyanion systems.

1.4.1.1 Oxides

Drawing comparison to the archetypal Li-ion layered oxide cathodes, there are a range of layered Na_xMO_2 materials (M = Mn, Ni, Fe, Co, Cr, Sn and Ti) covered extensively in the literature and it is important to reiterate these systems follow the same co-ordination nomenclature stated previously under section **1.3.1.1.1 $LiCoO_2$ (LCO)** regarding O- and P-type structures. Typically O3 materials have a Na content, x, closer to 1 while the P-type structures can vary extensively of $x < 1$.[12] Transitions of On and Pm

(n and m are the number denotation referring to the number of MO_2 layers required to form the structure) where n ≠ m, cannot be easily converted due to the high energy barrier through the necessity of bonds breakage.

While the Na-ion oxide literature is quite extensive, only a few of these systems will be highlighted here on – a comprehensive table of these materials can be found in reference [12].

1.4.1.1.1 Na_xCoO_2

Analogous to archetypal LCO, the sodium equivalent is known, however, during the cycling of this material phase structure transitions can occur which inhibits performance; Ceder *et al.* has investigated the transitions from the starting structure O3-type[59], while Delmas *et al.* the P2-type[60]. Given the ethics surrounding the sourcing of Co as mentioned previously, the search for a cathode material which is environmentally friendly and low-cost would be more beneficial.

1.4.1.1.2 α-$NaFeO_2$

The related α-$NaFeO_2$ has gained interest due its composite metal ions being of high abundance. The material has been shown to exhibit a flat voltage plateau at 3.3 V vs Na metal, with a reversible capacity of 85 mA h g^{-1}.[61]

1.4.1.2 Prussian-Blue and -White Materials

Towards the pursuit of open frameworks, Prussian blue ($KFe_2(CN)_6$)[62] and its associated analogues have come under the spotlight for Na-ion cathode applications. Prussian blue has a cubic framework, where the Fe^{2+} and Fe^{3+} occupy alternate corners within the cell, but are bridged by the cyano $(C{\equiv}N)^-$ ligand where high spin Fe^{2+} co-ordinates to the C atoms and the low spin Fe^{3+} to the N atoms.[62] In general, Prussian-blue analogues can be described with the formula of $Na_xM[Fe(CN)_6]_y.nH_2O$ ($0 \leq x \leq 2, 0 \leq y \leq 1$), where M = Mn, Fe, Co, Ni and Zn, and can be synthesized via a low temperature aqueous route. Goodenough *et al.* showed good reversibility on discharging the Prussian blue material (70 mA h g^{-1} at C/20) vs. Na – however noted poor Coulombic efficiency initially which has been attributed to crystalline water within the material, which is unlikely to be completely removed.[62] The related structure, Prussian White, $Na_{2-x}Fe_2(CN)_6).yH_2O$ has also shown promise as a Na-ion cathode material, achieving a capacity of 140 mA h g^{-1} at 1 C when tested against Na/Na^+.[63]

1.4.1.3 Polyanions

1.4.1.3.1 Phosphate-Based Cathodes

1.4.1.3.2 Maricite and Olivine ($NaFePO_4$)

Drawing parallels towards the Li-ion cathode research, the equivalent Na-analogue of LFP can be synthesized (the olivine structure), however, $NaFePO_4$ does exhibit an additional crystal phase: the thermodynamically stable maricite[64] structure – both structures are shown in **Figure 1. 23**. The apparent differences in structures resides around the connectivity of the FeO_6 units to the PO_4 tetrahedra. Within the maricite form, the Fe octahedra is edge-sharing with the PO_4 units, such that there are no cationic channels. In contrast, and as shown previously with the LFP structure, the olivine structure results in the Fe octahedra being corner-shared to the PO_4 units – allowing for an open 3D network and as such, a 1D sodium diffusion channel. Hence, from a structural perspective, the electrochemical inactivity of the maricite phase can be attributed to the trapping of Na^+ within in the structure and as such resulting in no redox behaviour.[65] However, the olivine equivalent electrochemical results have been reported through the use of nano-sized $FePO_4$ for the (de)intercalation of Na, delivering a capacity of 142 mA h g^{-1} after the first cycle and retaining 95% of capacity, although the charge rate for this result is significantly slow in comparison to commercial cathodes at C/20.[66] Other synthesis methods for this phase have resulted in low capacities.

Due to the apparent unfavourable nature of synthesizing olivine $NaFePO_4$ directly, electrochemical insertion of Na into $FePO_4$ is implemented to prepare the phase, but

unlike the Li-analogue, upon charging, an intermediate composition of lower Na content, $Na_{0.7}FePO_4$, forms.[64]

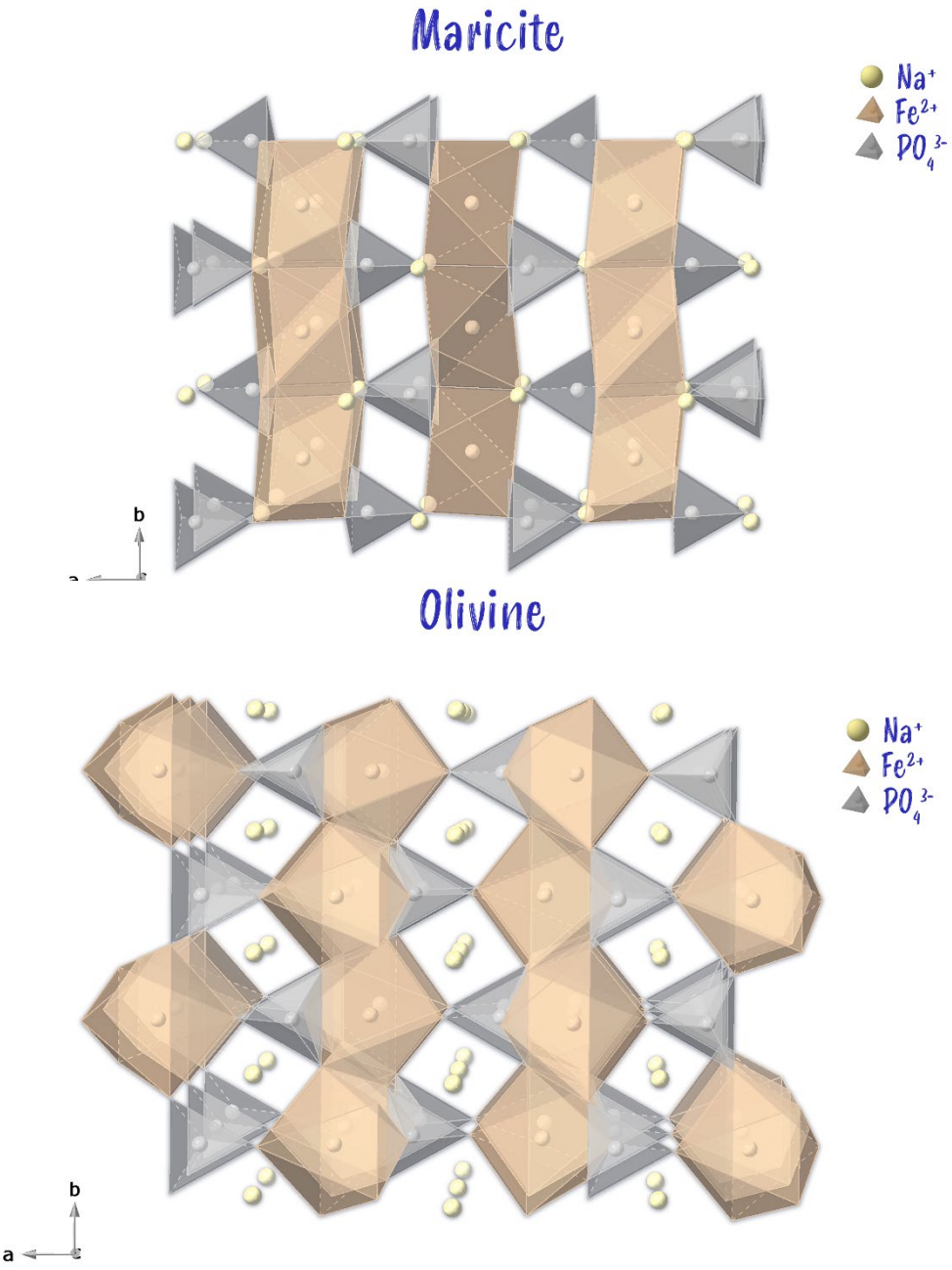

Figure 1. 23: The two crystal phases of $NaFePO_4$: maricite (top) and olivine (bottom).

1.4.1.3.2.1 Nasicon-Type Materials

The NASICON structure (**Figure 1. 24**) – an abbreviation of **Na** superionic **con**ductor – originates from initial compositions for solid electrolytes which demonstrated high ionic conductivity[67]. The general formulae of NASICON systems is given by $A_yM_2(XO_4)_3$ ($0 \leq y \leq 4$), where A constitutes alkali- and alkaline-metal ions, with the M relating to a multivalent transition metal ion, while the polyanion substitute has the possibility to be a phosphate (PO_4^{3-}), silicate (SiO_4^{4-}) or sulfate (SO_4^{2-}) group.

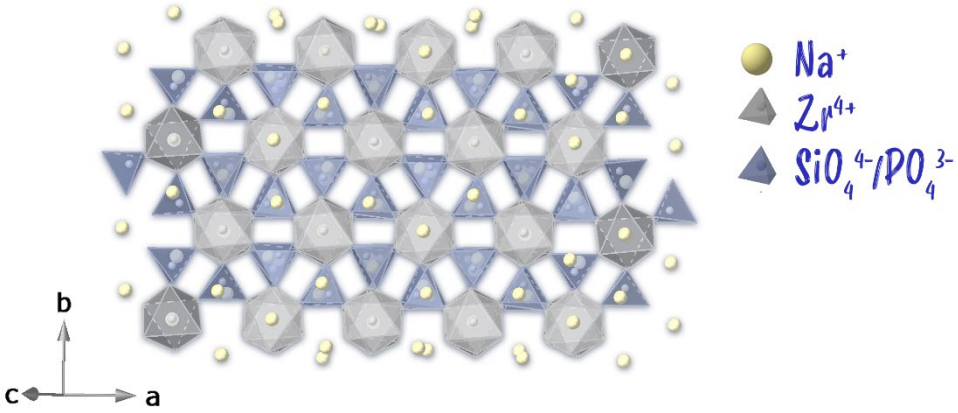

Figure 1. 24: Crystal structure of a NASICON material.

$Na_3V_2(PO_4)_3$ and a related phosphate fluoride $Na_3V_2(PO_4)_2F_3$ are NASICON structures of interest for NiBs. The former material, when cycled between 2.7 – 3.8 V returns a charge and discharge capacity of 98.6 and 93 mA h g^{-1} at C/20, respectively.[68] The initial work on the phosphate fluoride returned a capacity ca. 120 mA h g^{-1} from cycling between 3.0 to 4.6 V.[69] $Na_3Ti_2(PO_4)_3$ has also been reported for NiBs use.[70]

1.4.1.3.3 Sulfate Systems

1.4.1.3.3.1 Alluaudite

Of particular interest, in recent years, has been the alluaudite structure after reports of the highest Fe^{2+}/Fe^{3+} redox couple observed for a sulfate system, $Na_2Fe_2(SO_4)_3$, which had a potential of 3.8 V against Na metal.[71] The alluaudite structure is an open 3D framework with the general formula of $AA'BM_2(XO_4)_3$, where the A sites are partially occupied with Na^+, while the B and M sites are the transition metal ion sites. It is a 3D framework structure (**Figure 1. 25**), where the 3D network forms from 2D sheets of MO_6 octahedral units bonded to the XO_4 tetrahedral units, with these 2D sheets connected via the tetrahedral units.

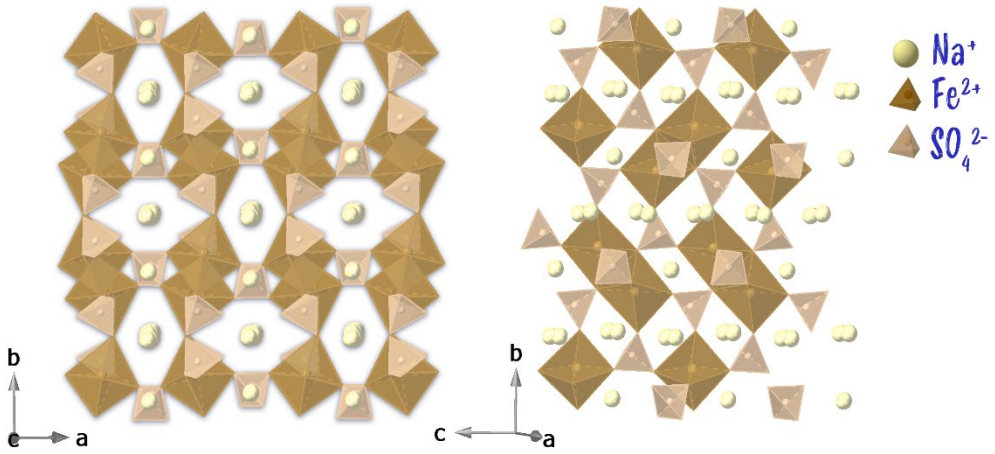

Figure 1. 25: Crystal structure of $Na_{2.5}Fe_{1.75}(SO_4)_3$ which adopts the alluaudite-type structure. The left image shows clearly the network of the octahedra and tetrahedra, while the right image shows the edge-sharing of the Fe octahedra.

Further studies showed that "$Na_2Fe_2(SO_4)_3$" had a tendency to form off-stoichiometric systems i.e. $Na_{2+2x}Fe_{2-x}(SO_4)_3$ with a secondary impurity phase of vanthoffite $Na_6Fe(SO_4)_4$ observed for the ideal "$Na_2Fe_2(SO_4)_3$" composition.[72] Further work has also shown similar

non-stoichiometric behaviour for the Mn[73] and Co[74] analogue phases. It is worth noting, that the alluaudite structure is not limited to the inclusion of the sulfate substituent alone, with molybdate[75,76] and numerous phosphate-based[12-26] systems having also been studied for NiB cathode applications. Furthermore, mixed polyanion systems have also been investigated; e.g. sulfate doping onto the phosphate site in $Na_xFe_y(PO_4)_{3-z}(SO_4)_z$ to tune the voltage.[92]

1.4.1.3.3.2 Bimetallic Sulfates

Another group of materials that has attracted recent interest as potential battery materials are the 2-1-2 bimetallic sulfates, $Na_2M(SO_4)_2$ (M = divalent cation)[93]. The structure of these materials consist of two distorted transition metal octahedra (hence the naming of these as bimetallic sulfates) which are bridged together through a sulfate tetrahedron (shown in **Figure 1. 26**).[93] The crystal structure of these phases is exemplified by $Na_2Co(SO_4)_2$ in **Figure 1. 26**. These systems are typically formed from dehydration of their equivalent tetrahydrate phases, $Na_2M(SO_4)_2.4H_2O$ (M = Co, Fe), with the Fe-analogue being shown to be electrochemically active and to return a voltage of ca. 3.3 V vs Na/Na^+.[94] Nevertheless, the difficulty in synthesising this Fe system is shown by previous studies by Barpanda *et al.* who were unable to synthesise this 2-1-2 phase from dehydration of the dihydrate, $Na_2Fe(SO_4)_2.2H_2O$.[95]

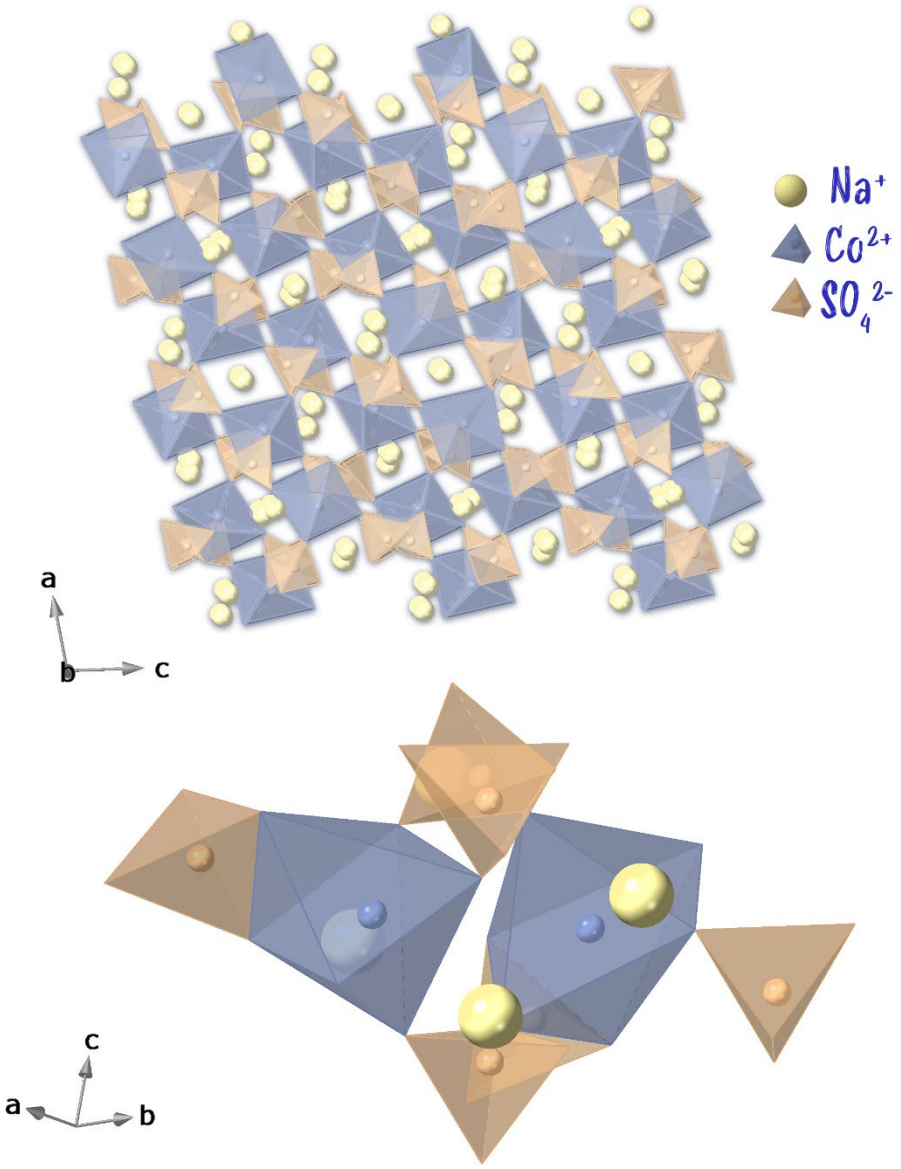

Figure 1. 26: Crystal structure of the bimetallic sulfate 2-1-2 system, $Na_2Co(SO_4)_2$ (top), with the bottom image showing the bridging of the Co octahedra with the sulfate tetrahedra.

1.4.1.3.3.3 Alluaudite – Bimetallic Size Relationship

In prior work, the effect of selenate doping in $Na_2M(SO_4)_2.2H_2O$ (M= Mn, Co, Ni) was investigated, and the products formed on dehydrating these systems examined.[96] This work showed that, for the simple sulfate systems, the 2-1-2 structure was observed for smaller divalent transition metals ions (Co and Ni), while the larger divalent transition metal ions (Mn, Fe) led to the formation of an alluaudite-phase, along with some Na rich impurities (due to the higher Na content in the precursor; 2:1 Na:M, compared to a ratio closer to 1:1 expected for alluaudite). The results from selenate doping led to some interesting observations. While all attempts to dehydrate the $Na_2Fe(SO_4)_{2-y}(SeO_4)_y.2H_2O$ phases resulted in amorphous products (attributed to a redox side reaction between the Fe and the selenate), the dehydration of the Mn, Co, Ni samples were all successful and showed the formation of a high Na content alluaudite phase, $Na_3M_{1.5}(SO_4)_{3-z}(SeO_4)_z$ (M=Mn, Co, Ni), with the amount of selenate needed to obtain a phase-pure alluaudite phase increasing as the size of the transition metal decreased.[96] Significantly, this led to the first report of a Ni-based alluaudite sulfate-selenate phase, as well as higher Na contents than previously achieved in prior sulfate-based alluaudite structure studies. The crystal structure changeover from 2-1-2 to the alluaudite on selenate doping is thought to be related to the spatial requirements for the larger selenate compared to sulfate. In the 2-1-2 structure, as previously mentioned, each metal octahedron has one edge-sharing linkage to a tetrahedron while there is corner-sharing to the rest of the tetrahedra. For the alluaudite structure, considering the bonding interactions of each metal octahedron to the tetrahedra alone, all 6 tetrahedra are corner-sharing to the metal octahedron. The corner-sharing means that the larger selenate units are positioned further away in the alluaudite than the 2-1-2 structure, thus favouring the alluaudite structure on selenate doping. These features also account for the structure

changeover in the simple sulfate systems on changing the transition metal, with larger transition metals favouring the alluaudite structure.

Through consideration of the level of selenate content that was required to stabilise the alluaudite phase, an ion size relationship (sum of M^{2+} radius and average S^{6+}/Se^{6+} radius) was proposed to dictate which structure (2-1-2 or alluaudite) was formed (Figure 1. 27).

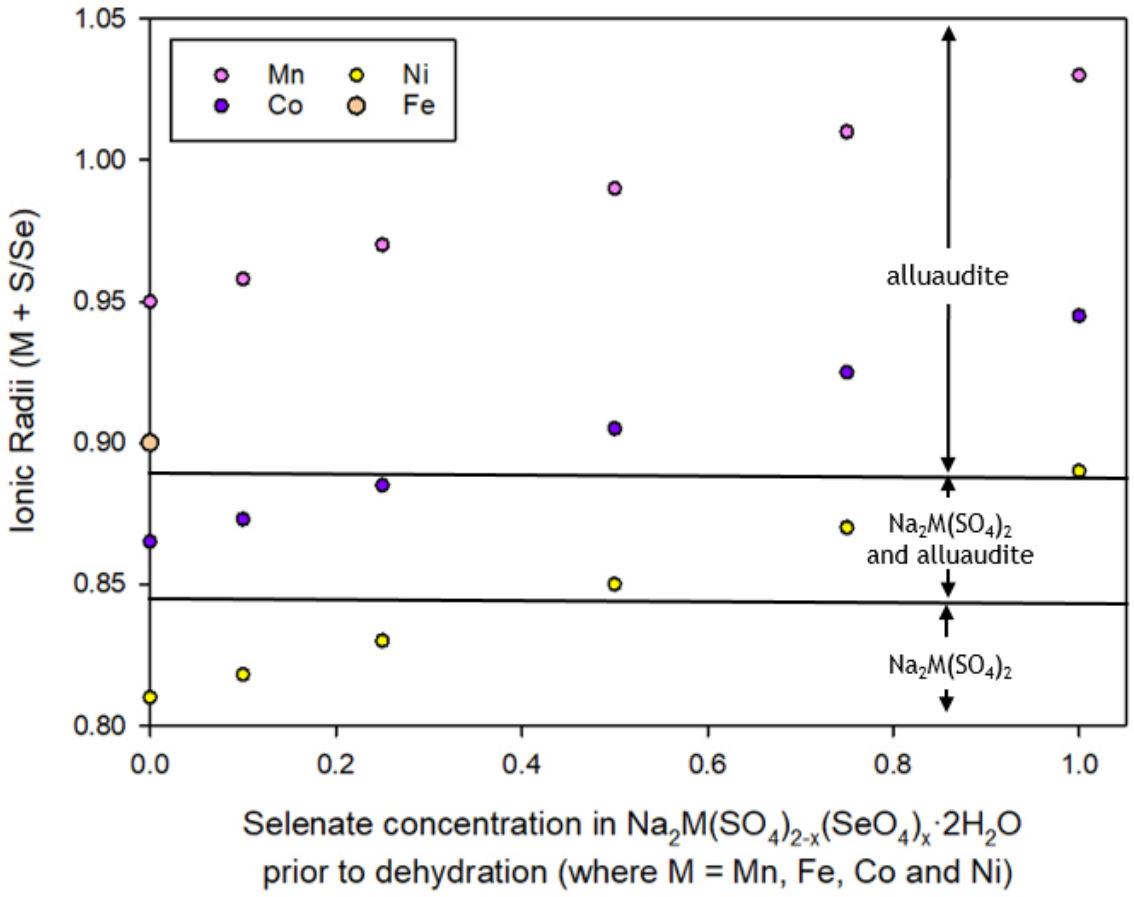

*Figure 1. 27: Plot of sum of the ionic radii of M and the weighted average ionic radius of S/Se (where M = Mn, Fe, Co and Ni) vs selenate content in the starting dihydrate. Note only the undoped (no selenate) Fe phase resulted in a crystalline product after dehydration, therefore only one data point is available for this series. Reproduced with permission from the Journal Solid State Chemistry, 2018, **258**, 64–71.*

1.4.2 Na-ion Anodes

While it is quite easy to see connections between Li- and Na-ion cathode materials, unfortunately the use of graphite as a Li-ion anode, is not a direct technology transfer for Na-ion anodes. The lack of Na intercalation into graphite is often wrongly attributed to sizing differences, however, given that the larger K^+ ion is able to successfully intercalate into the graphite, this is not the case for Na.[97] The inability to intercalate is attributed to the weakening ionic bonding from Cs to Na, which results in the formation energy of NaC_6 to be positive. Li is an exception to this trend given the covalent interactions in the graphene framework which result in the formation energy to be negative, and thus favourable.[97] Hence, non-graphitizable carbon called 'hard carbons' are employed as the anode in Na-ion batteries.

1.4.2.1 Hard Carbons

The popular name attributed to hard carbon originates from earlier literature and patent use, in which the carbonaceous material was defined by its mechanical hardness, although a more modern definition relates to the material's inability to transform to a graphitizable form above 3000°C.[98] Hard carbons are a promising candidate for use as a Na-ion anode, due to their high storage capacity (300 mA h g^{-1})[99], cycling stability, low working potential (0.15 V vs Na/Na^+) and environmental benignity, such that they can be produced from renewable bio-sources and are cheap.

In understanding the intercalation mechanism, the "house of cards" model developed by Dahn *et al.* has been proposed.[100,101] This model can be broken into two aspects – understanding the structure of the carbons[101] (which a topic by itself, is a contentious

one given the complexity of the structure and numerous reports in efforts to define one[98]) and the intercalation mechanism of Li[102,103] and Na[103].

1.5 Other Components within the Battery

1.5.1 Electrolyte

While the focus has primarily been on the electrode materials thus far, which determines the cell voltage, capacity and energy output of the cell, the electrolyte plays an important role. The electronic and ionic characteristics and electrolyte stability window have already been covered in 1.2 Battery Operation: Li- and Na-ion, however the electrolyte also determines the rate at which energy can be accepted or released.[17] For use in Li-ion and Na-ion batteries, the respective alkali-metal salt is dissolved in a non-aqueous solvent – due to the decomposition of water above 1.23 V vs Li/Li^+. The solvent used to dissolve the salts, requires a high dielectric constant to enable fast ion transport, while being polar in nature to dissolve the salts.[17]

Like most aspects of a battery, the electrolyte composition is dependent on application.

1.5.1.1 Solvents

The most commonly used solvent is ethylene carbonate (EC) and is commonly mixed with dimethyl carbonate (DMC). Typically, the electrolytes consist of mixtures to allow for the multiple properties required as an electrolyte. The ratio of EC/DMC is nominally 50 vol% and can be stable up to voltages of 5 V.[17]

1.5.1.2 Salts

The salt selected needs to have the following requirements: completely dissolvable within the solvent, high purity, high transference number, not be susceptible to forming solvated crystal phases with the solvent, and for the anion ligand to be stable within highly oxidative/reductive environments.

$LiPF_6$ is often the salt of choice, as it has a good balance of these properties, however, the drawbacks relate to the equilibrium shown in **Equation 1. 3**, where gaseous PF_5 is in equilibrium with $LiPF_6$, along with the potential of HF formation if exposed to moisture.

Equation 1. 3: Equilibrium of $LiPF_6$.

$$LiPF_{6\,(s)} \leftrightarrow LiF_{(s)} + PF_{5\,(g)}$$

For Na-ion batteries, the equivalent $NaPF_6$ can also be utilised, as well as $NaClO_4$. [104]

1.5.2 Separator

A none active component in cells is the separator material, which provides a physical barrier between the electrodes, and its main role is to hold a large amount of electrolyte – thus the material must be an insulating porous material. Given the separator has no role within the cell chemistry, to limit the overall mass and volume of the non-active components of the cell as a whole, the separator needs to be as a light and thin as possible.[17] Within this thesis, glass fibre separators were used.

1.6 Educational Resources

While fundamental and laboratory scientific research will always have a necessity towards pushing the frontiers of knowledge, and in particular to this field, enabling batteries to see their fruition towards Net-Zero and mitigating the effects of climate change, the communication aspects of this work has an equal importance in conveying technology operation to consumers and inspiring the next generation. This section will provide a basis to battery education and engagement resources currently adopted.

The key to understanding battery operation relies on understanding the redox processes and the electrochemistry at play. When teaching this area – specifically the electrochemistry - multiple applications can be tied to these fundamental principles[105], however, this topic is more than often associated with being a troublesome area to teach[106]. This issue is attributed to taught misconceptions which are formed either from misinterpretation or over generalization to inappropriate situations.[107] Multiple surveys to assess the drawbacks and misconceptions for this area have been conducted, in addition to the use of a cognitive conflict approach, for both teachers[108] and students[107,109], respectively, in efforts to understand how to improve the teaching of this area.

To support learning and be engaging, hands-on demonstrations are often used. The most commonly used activity employs lemon-/potato cells[110], which are useful for introducing the concept of electrode potentials, electrical circuits and a non-rechargeable battery (Figure 1. 28). The basics of this demonstration involves piercing a zinc-containing nail and a copper coin into either a lemon or potato. Crocodile clips

and wires are attached to each metal and connected to a voltmeter. An LED can be connected, but usually only lights with multiple 'cells' in series.

It is difficult to not mention efforts by Prof. Saiful Islam in his efforts of battery engagement with this activity, with the lemon battery's cameo in the 2016 Royal Institution Christmas Lectures and more recently achieving a Guinness World Record, in collaboration with the Royal Society of Chemistry to achieve a battery delivering 2,307.8 V (with a current of 0.84 mA).[111,112] Hence, without a doubt this practical is well established and can be used as a practical and safe demonstration.

Figure 1. 28: Photograph depicting the set-up of a single lemon(-electrolyte) battery, which is connected to a multimeter.

However, the role of each component can often be confused, such that the copper coin is wrongly termed as a working electrode. When considering the electrode potentials and the states of the metals (**Table 1. 4**), the favourable reaction would be $Zn_{(S)} + 2H^+_{(aq)} \rightarrow Zn^{2+}_{(aq)} + H_{2(g)}$ to produce a voltage of + 0.76 V. The difference in voltage observed (i.e. greater than +0.76 V) can be attributed to the over potential of the cell.

Table 1. 4: Reduction half equations of interest for the lemon-electrolyte batteries.

Reduction Half Equation	Reduction Potential (V)
$Cu^{2+}_{(aq)} + 2e^- \rightarrow Cu_{(s)}$	+0.34
$Zn^{2+}_{(aq)} + 2e^- \rightarrow Zn_{(s)}$	-0.76
$2H^+_{(aq)} + 2e^- \rightarrow H_{2(g)}$	0

Under the definition of an electrode having the ability to conduct electricity, the copper coin is classed as an electrode (which should be more appropriately termed current collector) but sometimes can be wrongly classed as the redox active material within the cell. This confusion may stem from the similarities of this cell (voltaic pile) and the Daniell Cell – where the overall reaction is $Zn_{(S)} + Cu^{2+}_{(aq)} \rightarrow Zn^{2+}_{(aq)} + Cu_{(s)}$ producing a voltage of 1.1 V.

An added advantage of this demonstration and other approaches, however, is the tactile nature, which can be made visually and audio stimulating, with a connection to a musical birthday card[110] or with a connected LED[113] or a clock[114]. In addition, quite often these demonstrations make use of classroom based tools or use available household

products[115]. Hence these activities in general are suited for a wide range of students, including those who are either visually impaired or deaf.[110]

Although a good-hands on activity to introduce key aspects of batteries, these demonstrations cannot explain how rechargeable batteries work and additionally, often leads to a misconception that the lemon or the potato are solely the powerhouse behind the circuit. Within the literature, efforts to explain and elaborate on the chemistry of the Li-ion battery appear to be limited to degree level, requiring specialist equipment and hazardous materials.[116–119]

With the current UK policy direction towards Net Zero and limiting the sale of new internal combustion engines by 2030, the electrification of infrastructure is becoming more apparent and thus the switch visualised by consumers, there needs to be more open sources which communicate the technology they are buying into. Currently the UK chemistry curriculum is limited to solely two lines on Li-ion batteries (discussed in **Chapter 7**), and so more needs to be done to raise this awareness. In March 2021, Sir Patrick Vallance (Government Chief Scientific Adviser) was asked a similar themed question regarding communicating the communication of greener technologies – in short the initial answer sought to say this relevant science question was more for the communication team.[120]

A month later, the Royal Society of Chemistry published part 1 of "Green shoots: A sustainable chemistry curriculum for a sustainable planet". One key finding found "educators and young people think that climate change and sustainability should be priorities for the chemistry curriculum" and for actions towards providing educational

resources related to climate change and sustainability, in addition to calls for improvements for the chemistry curriculum.[121] These actions emphasize calls from myself and Prof. Peter Slater to "Recharge Battery Education and Engagement" efforts to start the conversation on the use of sustainable energy technologies.

1.7 Project Aims

This project will cover a multitude of areas from Li-ion anodes to Na-ion cathodes, before considering educational resources available to explore this type of battery technology.

The project will initially consider two novel niobium doped oxides as Li-ion anodes for high power applications, involving the development of procedures for coating formulation and electrochemical testing, before considering alternative green binder systems to mitigate the use of PVDF.

Following on from prior work regarding the structure-size relationship of alluaudite – bimetallic sulfate structures, further consideration towards metal doping will be investigated, to mitigate the use of selenate – a toxic substance – which resulted in the first known Ni-based alluaudite for Na-ion cathode application.

The final aspect of this project will consider how Li-ion battery technology is currently communicated and the development of resources to support learning and understanding of this type battery, which is widely available to consumers.

1.8 References

1 H. M. Government, Net Zero Strategy: Build Back Greener, https://www.gov.uk/government/publications/net-zero-strategy, (accessed 25 July 2022).

2 E. A. Smart, Lesley E. , Moore, *Solid State Chemistry: An Introduction*, CRC Press, Boca Raton, 3rd edn., 2005.

3 J. B. Goodenough and Y. Kim, *Chem. Mater.*, 2010, **22**, 587–603.

4 A. R. West, *Solid State Chemistry and Its Applications*, John Wiley & Sons, Chichester, 2nd edn., 2012.

5 P. M. Woodward, K. Pavel, J. S. O. Evans and V. Thomas, *Solid State Materials Chemistry*, Cambridge University Press, Cambridge, 2021.

6 A. El Kharbachi, O. Zavorotynska, M. Latroche, F. Cuevas, V. Yartys and M. Fichtner, *J. Alloys Compd.*, 2020, **817**, 153261.

7 K. Mizushima, P. C. Jones, P. J. Wiseman and J. B. Goodenough, *Mater. Res. Bull.*, 1980, **15**, 783–789.

8 M. S. Whittingham, *Science*, 1976, **192**, 1126–1127.

9 Y. Nishi, H. Azuma, A. Omaru, *Non Aqueous Electrolyte Cell*, US Patent 4959281A, 1990.

10 A. Manthiram, *Nat. Commun.*, 2020, **11**, 1550.

11 C. Delmas, C. Fouassier and P. Hagenmuller, *Phys. B+C*, 1980, **99**, 81–85.

12 E. H. Driscoll, L. L. Driscoll and P. R. Slater, *Na-Ion Batteries: Positive Electrode Materials in Encyclopedia of Inorganic and Bioinorganic Chemistry*, ed. R. A. Scott, Wiley, 2019, pp. 1–14.

13 R. V. Chebiam, A. M. Kannan, F. Prado and A. Manthiram, *Electrochem. commun.*, 2001, **3**, 624–627.

14 The Faraday Institution, Building a Responsible Cobalt Supply Chain, https://faraday.ac.uk/wp-content/uploads/2020/05/Insight-cobalt-supply-chain1.pdf, (accessed 25 July 2022).

15 J. R. Dahn, U. von Sacken and C. A. Michal, *Solid State Ionics*, 1990, **44**, 87–97.

16 T. Ohzuku, A. Ueda and M. Nagayama, *J. Electrochem. Soc.*, 1993, **140**, 1862.

17 H. Berg, *Batteries for Electric Vehicles: Materials and Electrochemistry*, Cambridge University Press, Cambridge, 2015.

18 A. R. Armstrong, A. D. Robertson, R. Gitzendanner and P. G. Bruce, *J. Solid State Chem.*, 1999, **145**, 549–556.

19 The Faraday Institution, Lithium, Cobalt and Nickel: The Gold Rush of the 21st Century,https://faraday.ac.uk/wp-content/uploads/2020/12/Faraday_Insights_6_Updated_Dec2020.pdf, (accessed 30 May 2022).

20 Targray NMC Powder for Battery Manufacturers, https://www.targray.com/li-ion-battery/cathode-materials/nmc, (accessed 21 May 2022).

21 C. S. Yoon, M. H. Choi, B.-B. Lim, E.-J. Lee and Y.-K. Sun, *J. Electrochem. Soc.*, 2015, **162**, A2483–A2489.
22 J.-M. Tarascon, E. Wang, F. K. Shokoohi, W. R. McKinnon and S. Colson, *J. Electrochem. Soc.*, 1991, **138**, 2859–2864.
23 J.-M. Tarascon, W.-R. Mckinnon, F. Coowar, T. N. Bowmer, G. Amatucci and D. Guyomard, 1994, **141**, 1421–1431.
24 R. J. Gummow, A. de Kock and M. M. Thackeray, *Solid State Ionics*, 1994, **69**, 59–67.
25 D. Dwibedi and P. Barpanda, *Trans. Indian Ceram. Soc.*, 2015, **74**, 191–194.
26 A. K. Padhi, K. S. Nanjundaswamy and J. B. Goodenough, *J. Electrochem. Soc.*, 1997, **144**, 1188–1194.
27 D. . Fauteux and R. . Koksbang, *J. Appl. Electrochem.*, 1993, **23**, 1–10.
28 M. J. Lain and E. Kendrick, *J. Power Sources*, 2021, **493**, 229690.
29 Q. Wang, B. Liu, Y. Shen, J. Wu, Z. Zhao, C. Zhong and W. Hu, *Adv. Sci.*, 2021, **8**, 2101111.
30 T. F. Yi, L. J. Jiang, J. Shu, C. B. Yue, R. S. Zhu and H. Bin Qiao, *J. Phys. Chem. Solids*, 2010, **71**, 1236–1242.
31 G. Brauer, *Zeitschrift fur Anorg. und Allg. Chemie*, 1941, **248**, 1–31.
32 H. Schafer, R. Gruehn and F. Schulte, *Angew. Chemie - Int. Ed.* , DOI:https://doi.org/10.1002/anie.196600401.
33 C. Nico, T. Monteiro and M. P. F. Graça, *Prog. Mater. Sci.*, 2016, 80, 1–37.
34 J. Liao, R. Tan, Z. Kuang, C. Cui, Z. Wei, X. Deng, Z. Yan, Y. Feng, F. Li, C. Wang and J. Ma, *Chinese Chem. Lett.*, 2018, **29**, 1785–1790.
35 M. Lübke, A. Sumboja, I. D. Johnson, D. J. L. Brett, P. R. Shearing, Z. Liu and J. A. Darr, *Electrochim. Acta*, 2016, **192**, 363–369.
36 E. C. Wheeler-Jones, M. J. Loveridge and R. I. Walton, *Electrochim. Acta*, 2021, **392**, 138964.
37 Z. Hu, Q. He, Z. Liu, X. Liu, M. Qin, B. Wen, W. Shi, Y. Zhao, Q. Li and L. Mai, *Sci. Bull.*, 2020, **65**, 1154–1162.
38 K. J. Griffith, A. C. Forse, J. M. Griffin and C. P. Grey, *J. Am. Chem. Soc.*, 2016, **138**, 8888–8899.
39 S. Li, Q. Xu, E. Uchaker, X. Cao and G. Cao, *CrystEngComm*, 2016, **18**, 2532–2540.
40 R. Roth, B. Gatehouse and A. Wadsley, *Naturwissenschaften*, 1964, **51**, 262–263.
41 R. Roth and A. Wadsley, *Acta Crystallogr.*, 1965, **19**, 26–32.
42 T. Yuan, L. Soule, B. Zhao, J. Zou, J. Yang, M. Liu and S. Zheng, *Energy Fuels*, 2020, **34**, 13321–13334.
43 K. J. Griffith, Y. Harada, S. Egusa, R. M. Ribas, R. S. Monteiro, R. B. Von Dreele, A. K. Cheetham, R. J. Cava, C. P. Grey and J. B. Goodenough, *Chem. Mater.*, 2021, **33**, 4–18.
44 J.-T. Han, Y.-H. Huang and J. B. Goodenough, *Chem. Mater.*, 2011, **23**, 2027–2029.
45 H. Aghamohammadi, N. Hassanzadeh and R. Eslami-Farsani, *J. Alloys Compd.*, 2022, **911**, 165117.
46 X. Wu, J. Miao, W. Han, Y. S. Hu, D. Chen, J. S. Lee, J. Kim and L. Chen, *Electrochem.*

commun., 2012, **25**, 39–42.
47 C. Yang, S. Deng, C. Lin, S. Lin, Y. Chen, J. Li and H. Wu, *Nanoscale*, 2016, **8**, 18792–18799.
48 M. Wörle and F. Krumeich, *Zeitschrift fur Anorg. und Allg. Chemie*, 2021, **647**, 98–106.
49 K. J. Griffith, K. M. Wiaderek, G. Cibin, L. E. Marbella and C. P. Grey, *Nature*, 2018, **559**, 556–563.
50 S. Shivareddy, C. P. Grey, Electrode Composition, GB Patent (pending) GB1914983, 2019.
51 C. Delmas, J.-J. Braconnier and P. Fouassier, Claude Hagenmuller, *Solid State Ionics*, 1981, **3–4**, 165–169.
52 A. Maazaz, C. Delmas and P. Hagenmuller, *J. Incl. Phenom.*, 1983, **1**, 45–51.
53 A. Mendiboure, C. Delmas and P. Hagenmuller, *J. Solid State Chem.*, 1985, **57**, 323–331.
54 C. Delmas, F. Cherkaoui, A. Nadiri and P. Hagenmuller, *Mater. Res. Bull.*, 1987, **22**, 631–639.
55 The Faraday Institution: NEXGENNA – SODIUM-ION BATTERIES, https://www.faraday.ac.uk/research/beyond-lithium-ion/sodium-ion-batteries/, (accessed 30 October 2021).
56 European Commission, *Critical Raw Materials Resilience: Charting a Path towards greater Security and Sustainability*, 2020.
57 C. Early, The new 'gold rush' for green lithium, https://www.bbc.com/future/article/20201124-how-geothermal-lithium-could-revolutionise-green-energy, (accessed 17 May 2022).
58 S. Roberts and E. Kendrick, *Nanotechnol. Sci. Appl.*, 2018, **11**, 23–33.
59 Y. Lei, X. Li, L. Liu and G. Ceder, *Chem. Mater.*, 2014, **26**, 5288–5296.
60 R. Berthelot, D. Carlier and C. Delmas, *Nat. Mater.*, 2011, **10**, 74–80.
61 J. Zhao, L. Zhao, N. Dimov, S. Okada and T. Nishida, *J. Electrochem. Soc.*, 2013, **160**, A3077–A3081.
62 Y. Lu, L. Wang, J. Cheng and J. B. Goodenough, *Chem. Commun.*, 2012, **48**, 6544–6546.
63 M. J. Piernas-Muñoz, E. Castillo-Martínez, O. Bondarchuk, M. Armand and T. Rojo, *J. Power Sources*, 2016, **324**, 766–773.
64 P. Moreau, D. Guyomard, J. Gaubicher and F. Boucher, *Chem. Mater.*, 2010, **22**, 4126–4128.
65 B. L. Ellis, W. R. M. Makahnouk, Y. Makimura, K. Toghill and L. F. Nazar, *Nat. Mater.*, 2007, **6**, 749–753.
66 J. Kim, D.-H. Seo, H. Kim, I. Park, J.-K. Yoo, S. K. Jung, Y.-U. Park, W. A. Goddard and K. Kang, *Energy Environ. Sci.*, 2015, **8**, 540–545.
67 J. B. Goodenough, H. Y.-P. Hong and J. A. Kafalas, *Mater. Res. Bull.*, 1976, **11**, 203–220.
68 Z. Jian, L. Zhao, H. Pan, Y. S. Hu, H. Li, W. Chen and L. Chen, *Electrochem. commun.*, 2012, **14**, 86–89.
69 R. K. B. Gover, A. Bryan, P. Burns and J. Barker, *Solid State Ionics*, 2006, **177**, 1495–1500.
70 P. Senguttuvan, G. Rousse, M. E. Arroyo y de Dompablo, H. Vezin, J.-M. Tarascon and M. R. Palacín, *J. Am. Chem. Soc.*, 2013, **135**, 3897–3903.

71 P. Barpanda, G. Oyama, S.-I. Nishimura, S.-C. Chung and A. Yamada, *Nat. Commun.*, 2014, **5**, 4358.
72 G. Oyama, S.-I. Nishimura, Y. Suzuki, M. Okubo and A. Yamada, *ChemElectroChem*, 2015, **2**, 1019–1023.
73 D. Dwibedi, R. B. Araujo, S. Chakraborty, P. P. Shanbogh, N. G. Sundaram, R. Ahuja and P. Barpanda, *J. Mater. Chem. A*, 2015, **3**, 18564–18571.
74 D. Dwibedi, R. Gond, A. Dayamani, R. B. Araujo, S. Chakraborty, R. Ahuja and P. Barpanda, *Dalt. Trans.*, 2017, **46**, 55–63.
75 J. Gao, P. Zhao and K. Feng, *Chem. Mater.*, 2017, **29**, 940–944.
76 A. V. Serdtsev, S. F. Solodovnikov and N. I. Medvedeva, *Mater. Today Commun.*, 2020, **22**, 100925.
77 K. Trad, D. Carlier, L. Croguennec, A. Wattiaux, M. Ben Amara and C. Delmas, *Inorg. Chem.*, 2010, **49**, 10378–10389.
78 K. Trad, D. Carlier, L. Croguennec, A. Wattiaux, M. Ben Amara and C. Delmas, *Chem. Mater.*, 2010, **22**, 5554–5562.
79 S. Liu, L. Chen, Y. Zhao, M. Wen and X. Lian, *J. Electroanal. Chem.*, 2019, **832**, 121–128.
80 P. Zhang, K. Yang, L. Song, H. J. Feng and J. Gao, *J. Alloys Compd.*, 2019, **783**, 409–415.
81 D. Dwibedi, R. Gond and P. Barpanda, *Chem. Mater.*, 2019, **31**, 7501–7509.
82 A. E. Chamryga, M. Nowagiel and T. K. Pietrzak, *J. Non. Cryst. Solids*, 2019, **526**, 119721.
83 R. Essehli, H. Ben Yahia, R. Amin, F. El-Mellouhi and I. Belharouak, *Energy Storage Mater.*, 2020, **24**, 343–350.
84 R. Essehli, I. Belharouak, H. Ben Yahia, K. Maher, A. Abouimrane, B. Orayech, S. Calder, X. L. Zhou, Z. Zhou and Y. Sun, *Dalt. Trans.*, 2015, **44**, 7881–7886.
85 W. Huang, B. Li, F. Saleem, X. Wu and J. Li, *Chem. Eur. J.*, 2015, **21**, 851–860.
86 D. Harbaoui and M. M. S. Sanad, *Inorg. Chem.*, 2017, **56**, 13051–13061.
87 D. Liu and G. T. R. Palmore, *ACS Sustain. Chem. Eng.*, 2017, **5**, 5766–5771.
88 J. Kim, H. Kim and S. Myung, *J. Mater. Chem. A*, 2017, **5**, 22334–22340.
89 W. M, X. Liu, Y. Zhao, S. Liu, H. Liu, Y. Dong, Q. Kuang and Q. Fan, *J. Solid State Electrochem.*, 2018, **22**, 891–898.
90 K. Trad, A. Castets, A. Wattiaux, C. Delmas, M. Ben Amara and D. Carlier, *J. Solid State Chem.*, 2018, **265**, 12–17.
91 K. Walczak, A. Kulka and J. Molenda, *Solid State Sci.*, 2019, **87**, 21–26.
92 J. Lu, S. Nishimura and A. Yamada, *Chem. Mater.*, 2017, **29**, 3597–3602.
93 A. M. Fry, O. T. Sweeney, W. Adam Phelan, N. Drichko, M. A. Siegler and T. M. McQueen, *J. Solid State Chem.*, 2015, **222**, 129–135.
94 M. Reynaud, G. Rousse, A. M. Abakumov, M. T. Sougrati, G. Van Tendeloo, J.-N. J.-N. Chotard and J.-M. J.-M. Tarascon, *J. Mater. Chem. A*, 2014, **2**, 2671–2680.
95 P. Barpanda, G. Oyama, C. D. Ling and A. Yamada, *Chem. Mater.*, 2014, **26**, 1297–1299.
96 L. L. Driscoll, E. Kendrick, K. S. Knight, A. J. Wright and P. R. Slater, *J. Solid State Chem.*, 2018, **258**, 64–71.

97 H. Moriwake, A. Kuwabara, C. A. J. Fisher and Y. Ikuhara, *RSC Adv.*, 2017, **7**, 36550–36554.
98 X. Dou, I. Hasa, D. Saurel, C. Vaalma, L. Wu, D. Buchholz, D. Bresser, S. Komaba and S. Passerini, *Mater. Today*, 2019, **23**, 87–104.
99 D. A. Stevens and J. R. Dahn, *J. Electrochem. Soc.*, 2000, **147**, 1271.
100 Y. Liu, J. S. Xue, T. Zheng and J. R. Dahn, Carbon, 1996, 34, 193–200.
101 J. R. Dahn, W. Xing and Y. Gao, Carbon N. Y., 1997, 35, 825–830.
102 J. R. Dahn, T. Zheng, Y. Liu and J. S. Xue, Science, 1995, 270, 590–593.
103 D. A. Stevens and J. R. Dahn, *J. Electrochem. Soc.*, 2001, **148**, A803.
104 F. Wei, Q. Zhang, P. Zhang, W. Tian, K. Dai, L. Zhang, J. Mao and G. Shao, *J. Electrochem. Soc.*, 2021, **168**, 050524.
105 R. I. Perkins, *J. Chem. Educ.*, 1985, **62**, 1018–1019.
106 A. R. Özkaya, *J. Chem. Educ.*, 2002, **79**, 735–738.
107 M. J. Sanger and T. J. Greenbowe, *J. Chem. Educ.*, 1997, **74**, 819–823.
108 D. Cheung, *Chem. Educ. Res. Pract.*, 2011, **12**, 228–237.
109 M. Nias, *Int. J. Sci. Educ.*, 2002, **24**, 425–439.
110 S. G. Cady, *J. Chem. Educ.*, 2014, **91**, 1675–1678.
111 Saiful Islam, https://www.rigb.org/explore-science/explore/person/saiful-islam, (accessed 30 May 2022).
112 Highest voltage from a fruit battery, https://www.guinnessworldrecords.com/world-records/108028-highest-voltage-from-a-fruit-battery#:~:text=The highest voltage from a,a power of 1.94 Watts., (accessed 30 May 2022).
113 P. O. Eggen and B. Skaugrud, *J. Chem. Educ.*, 2015, **92**, 1053–1055.
114 T. M. Letcher and A. W. Sonemann, *J. Chem. Educ.*, 1992, **69**, 157–158.
115 M. A. Parkes, T. Chen, B. Wu, V. Yufit and G. J. Offer, *J. Chem. Educ.*, 2016, **93**, 681–686.
116 R. S. Treptow, *J. Chem. Educ.*, 2003, **80**, 1015–1020.
117 P. Coppo, *J. Chem. Educ.*, 2017, **94**, 1174–1178.
118 K. Schmidt-Rohr, *J. Chem. Educ.*, 2018, **95**, 1801–1810.
119 F. D. R. Maharaj, W. Wu, Y. Zhou, L. T. Schwanz and M. P. Marshak, *J. Chem. Educ.*, 2019, **96**, 3014–3017.
120 Royal Society of Biology, Sir Patrick Vallance | Voice of the Future 2021 | Royal Society of Biology, https://www.youtube.com/watch?v=Gbs0kXAYaD0&list=PLxu6ICEq35Pf2wrWJLOdOazP2h0r-f2dm&index=3, (accessed 30 June 2022).
121 Royal Society of Chemistry: Green shoots : A sustainable chemistry curriculum for a sustainable planet, https://www.rsc.org/new-perspectives/sustainability/a-sustainable-chemistry-curriculum/, (accessed 30 June 2022).

Chapter 2: Experimental Methods & Techniques

Within this chapter, the experimental methods used within this thesis will be explored, from the basis of synthetic routes implemented, to understanding the fundamentals and basic principles of the characterisation techniques used.[1–5] For coin cell fabrication – a baseline example of ink formulation and coating procedure will be given, however within the results chapter, a more detailed method is provided and efforts discussed therein.

Figure 2. 1: Graphical abstract representing experimental methods (with a sketch of Prof. Peter Slater's lab space) - where samples are initially prepared in powder form, characterised before coin cell fabrication.

2.1 Synthetic Routes

2.1.1 Solid State

The most common and simplest synthesis method is the namesake "solid state" or ceramic method as it is more formally known. Stoichiometric amounts of solid precursors are dispensed, thoroughly ground together within an agate pestle and mortar, before firing to high temperatures (i.e. 500 up to 1200 °C) in an alumina crucible (provided the material won't react with this type of crucible e.g. lithium-garnet based materials – other inert crucibles are available). The typical procedure involves an intermittent grinding step before re-firing.

Although this synthesis method is energy intensive, it is a way to assess feasibility of formation of new materials. The materials aren't heated beyond their melting temperatures, which ensures the reaction takes place within the solid state. As such, the reaction relies on the diffusion of ions (dictated by operation temperature) to the surface to allow the reaction to take place. Ensuring powders are thoroughly mixed, and reducing particle size, can reduce diffusion length of ions, and in addition, the intermediate grinding step can aid the creation of new reaction interfaces. In determining heating parameters, it is often by trial and error to find suitable reaction conditions. PXRD (section 2.3.1 on p77) is commonly used to assess the stage of the reaction.

2.1.2 Wet Chemical Methods: Dissolution and Precipitation

While the solid state process is quite energy intensive, alternative wet chemical methods can be implemented to afford lower energy consumption, through atomic/molecular level of mixing within solution. Of focus for this body of work is the dissolution and

precipitation method. Other methods, such as sol-gel and the Pechini method work on a similar principle, admittedly with different reagents criteria, but are not relevant to this thesis.

In the dissolution and precipitation method, reagents are dispensed and dissolved into solution. The reaction mixture is heated and stirred with a magnetic bead to ensure all materials are dissolved and thorough mixing takes places. The reaction mixture is then removed from the hot plate, with the stirrer bar subsequently removed, before being placed into a pre-heated oven to evaporate the water overnight. The remaining precipitate is then collected and ground up in a pestle and mortar, before heating in an alumina crucible.

2.2 Electrochemical Testing: Preparation and Procedures

In order to assess the application of these materials, ink formulations and battery fabrication and electrochemical testing are required. Nominally this would be after full characterisation of the system, however, given batteries can be dismantled to deduce changes upon cycling – the characterisation techniques will be covered after this topic.

2.2.1 Coating Formulations

As mentioned in the introduction, Li-ion batteries consist of 2 electrodes and an electrolyte (normally liquid). In order to produce the two electrodes from the powders, a composite electrode is produced through the mixing of the electrochemically active material (AM), with a conductive additive (CB) and a binder (B). The conductive additive, typically graphite and/or carbon black, is added into the mixture to aid the overall electronic conductivity of the electrode. The binder system is introduced to hold all the

materials together and to help adhesion to the current collector. The most common of these materials are polyvinylidene fluoride (PVDF) or polytetrafluoroethylene (PTFE or Teflon™)[5]. An example of the make up of a composite electrode is shown in Figure 2. 2, where the electronic conductive pathways are shown.

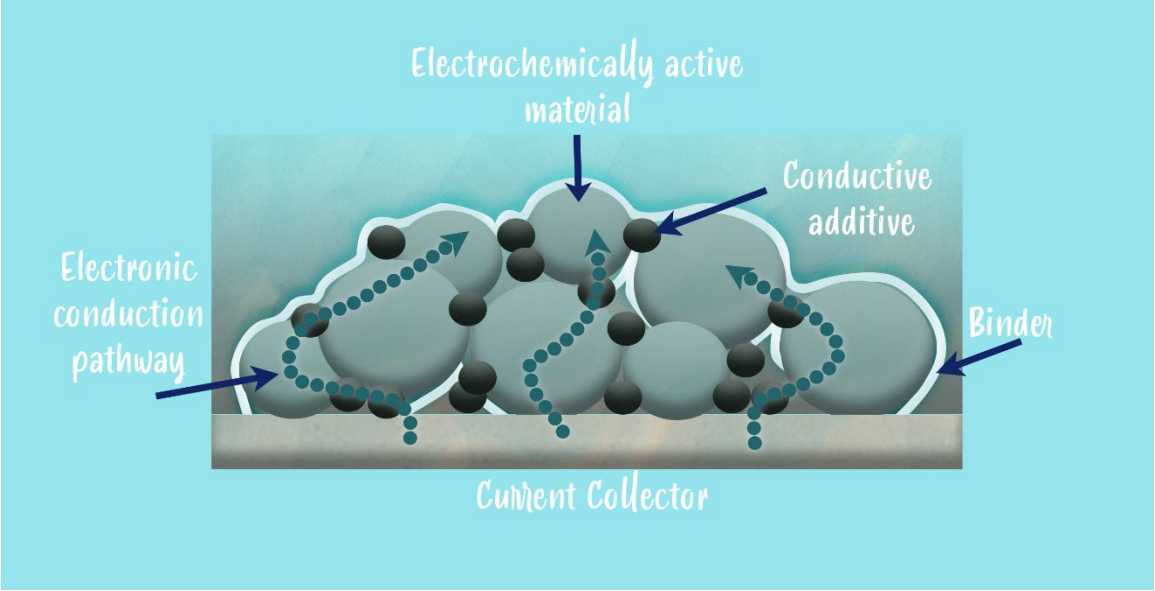

Figure 2. 2: Graphic depicting the make up of a composite electrode with the electrochemical active material mixed with a conductive additive and binder. Suggested electronic conduction pathways are shown in the green arrows. Figure adapted from H. Berg, Batteries for Electric Vehicles: Materials and Electrochemistry, Cambridge University Press, Cambridge, 2015.[4]

With respect to the ionic conduction pathways, typically electrode materials are in powder form before ink formulation, and hence will result in a porous electrode. This quality thus means an improvement in the ionic conduction pathway of lithium ions, compared to dense a solid electrode, given the electrolyte can permeate through the electrode coating. The difference in types of electrodes (solid and porous) with respect to ionic conduction is shown in Figure 2. 3.

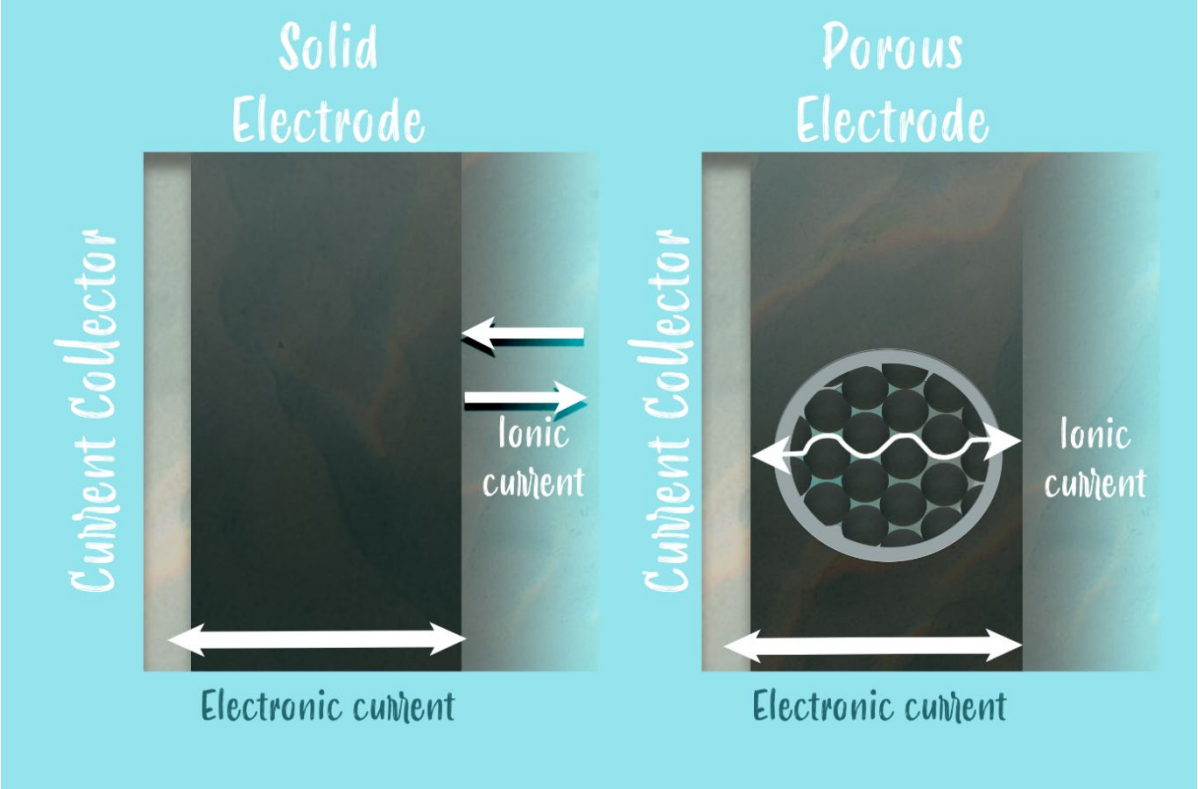

Figure 2. 3: Graphic illustrating the difference in electrolyte penetration, given the different qualities of the electrode materials: solid and porous, which can influence the ionic conduction. Adapted from M. Root, The TAB Battery Book: An In-Depth Guide to Construction, Design and use, The McGraw-Hill Companies, New York, 2011.[5]

To form a composite electrode, the powder has to be formulated into an ink ready for coating. The selected binder system will dictate the solvent to be used. In the use of PVDF (chemical formula shown in **Figure 2. 4**), N-Methyl-2-pyrrolidone (NMP) is the common solvent of choice – however, there are safety concerns with this solvent, due to the substances well-known teratogen, sensitizer and toxic nature.

In light of this, safer and green binder systems can be used in ink formulations, such as sodium carboxymethyl cellulose (CMC; **Figure 2. 5**) and styrene-butadiene rubber (SBR; **Figure 2. 6**), but are more commonly used for anode materials, such as for the

formulation of a graphite ink. This is due to the instability of common cathode materials towards water.

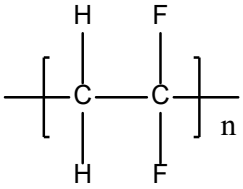

Figure 2. 4: Monomer unit of poly-vinylidene fluoride (PVDF).

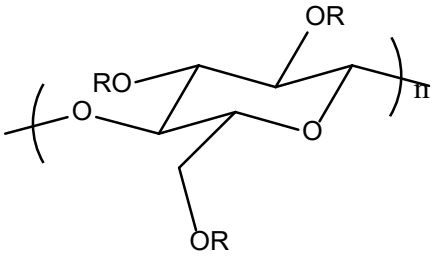

$R = H \text{ or } CH_2CO_2Na$

Figure 2. 5: Monomer unit of the polymer sodium carboxymethyl cellulose.

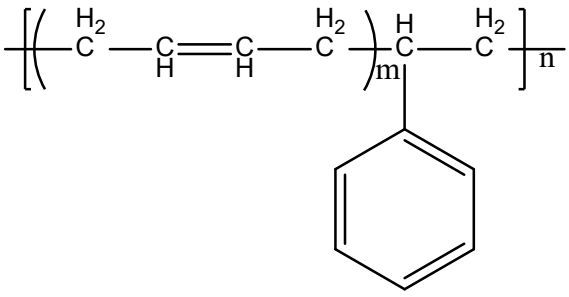

Figure 2. 6: Monomer unit of the polymer styrene-butadiene rubber.

A typical coating formulation of AM:B:CB is 80:10:10, however it is becoming more common place for there to be a higher proportion of AM, i.e. 90:5:5.

To produce the electrode coating, the formulated ink is deposited onto a coater and drawn down onto the current collector (held in place with vacuum). The thickness of the (wet) coating can be pre-set with the bar height (Figure 2. 7).

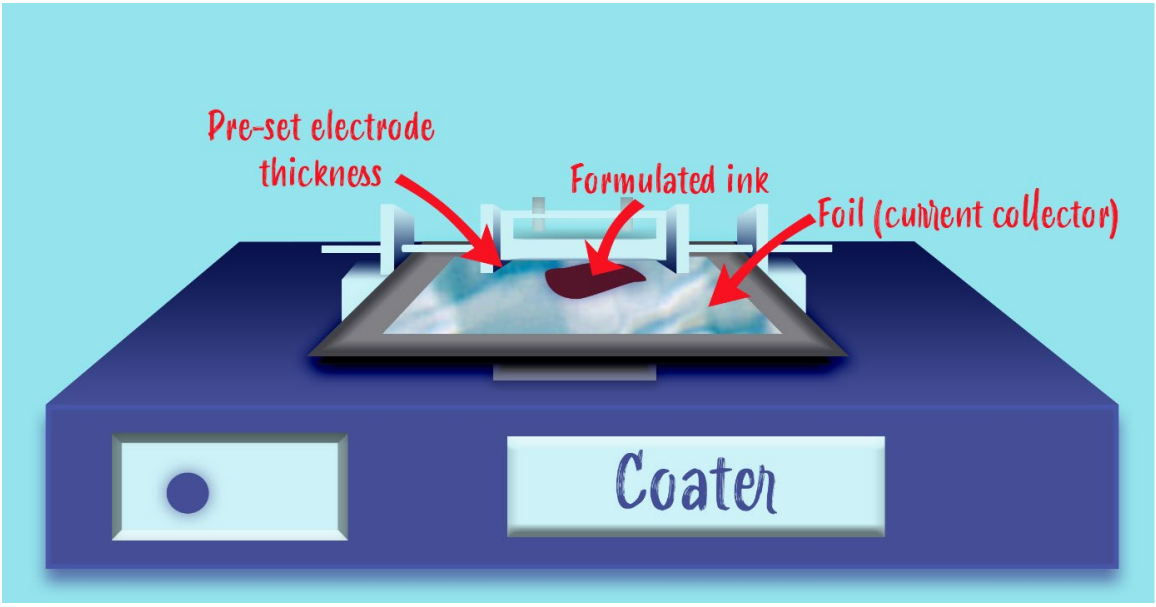

Figure 2. 7: Graphic showing the electrode coater and how the bar can be adjusted for a desired thickness, when the formulated ink is deposited onto the current collector.

The current collector material depends ultimately on the operating voltage of the electrodes. Typically, cathode materials make use of an aluminium current collector, while graphite coatings for anodes make use of a copper current collector. The use of copper in this scenario is the result of this electrode's low operating voltage, in which lithium and aluminium alloying would take place below 0.5 V if an aluminium current collector was in use. Thus, for higher potential anodes, such as LTO, an aluminium current collector can be used. The benefits of using aluminium foils over copper are through the former being of higher natural abundance and lower weight, which would

impact the cost and the gravimetric capacities of these devices. Due to the novelty of these materials undergoing testing in this thesis, as a starting point, the anodes were deposited on to a copper current collector – future work would consider the use of aluminium.

The coated electrode is initially placed onto a hot plate (80°C) to remove the solvent – if NMP is in use this should be done under extraction. The electrode is then placed overnight under vacuum at 110°C.

2.2.2 Calendering[6]

Before cell assembly, the electrodes should be calendered – this process involves feeding the electrode between two stainless steel rollers to compact the electrode to a certain thickness to produce a porosity between 30 – 40%, as shown in **Figure 2. 8**.

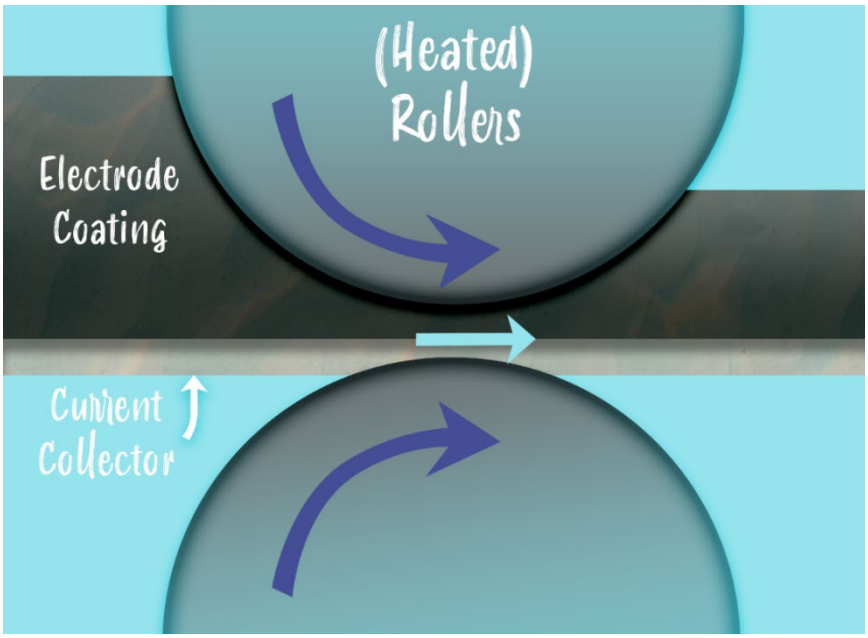

Figure 2. 8: Schematic demonstrating the process of calendering, where by the coated electrode is passed through the rollers (temperature of rollers dependent on binder system). This process reduces the porosity of the coating, as shown by the reduced thickness of the electrode coating after passing through the rollers.

Uncalendered electrodes typically tend to be ~ 70% porosity. The process can be enhanced through heating the rollers to: 80°C for PVDF-based electrodes and 30°C for CMC/SBR (this is related to the softening temperature of the binder).

Calendering has a substantial effect on pore structure of the electrode, and hence can affect electrochemical performance through the electrolyte wetting and charge transfer reactions during cycling.

2.2.2.1 Bulk Density and Porosity

To assess the reduction of the porosity of the coating, the bulk density of the active material is required. To determine this value, the formula unit mass and cell volume are required, as illustrated by Equations 2. 1 - 2. 3.

Equation 2. 1: Determination of formula unit mass.

$$Formula\ unit\ mass\ (g\ mol^{-1}) = Z\ (formula\ units\ per\ volume) \times RMM\ (g\ mol^{-1})$$

Equation 2. 2: Conversion of cell volume from Ångstroms to cm³.

$$Cell\ volume\ (cm^3) = volume\ (\text{Å})\ \times 10^{-24}$$

Equation 2. 3: Determination of theoretical density.

$$Theoretical\ Density\ (g\ cm^{-3}) = \frac{Formula\ unit\ mass\ (g\ mol^{-1})}{Cell\ volume\ (cm^3) \times N_A(mol^{-1})}$$

The overall porosity is determined through comparing the electrode coating's actual density to the theoretical density (as previously calculated) – as shown by Equations 2. 4 - 2. 6.

Equation 2. 4: Determination of the density of the electrode, from the coat weight and the thickness of the coating.

$$Electrode\ Density\ (mg\ cm^{-3}) = \frac{Coat\ weight\ (mg\ cm^{-2})}{Thickness\ of\ coating\ (cm)}$$

Equation 2. 5: The coat weight can be calculated from the mass and area of the electrode coating.

$$Coat\ weight\ (mg\ cm^{-2}) = \frac{Mass\ of\ coating\ (mg)}{Area\ of\ electrode\ (cm^2)}$$

Equation 2. 6: Porosity of the coating is determined from the electrode density and the theoretical density of the coating.

$$Porosity = 1 - \left(\frac{Electrode\ Density\ (g\ cm^{-3})}{Theoretical\ Density\ (g\ cm^{-3})} \times 100\right)$$

2.2.3 Application Characteristics: High Energy or High Power

Although cell design hasn't been considered within this thesis (given a standard procedure for electrode coatings being used for ease of comparison), it is important for there to be an awareness of cell design with respect to application – high energy or high power. While these electrodes are porous and the electrolyte can saturate the available pores, the thickness and surface area of the coating can have a considerable effect on (dis)charging rates, the resistance and power output. To achieve high power output,

electrodes ideally need to be thin to limit resistance through the reduction in electronic conduction pathways.

2.2.3.1 Tap Density

The tap density is approximately the inverse of porosity and is used as a control parameter in cell manufacturing. This value can indicate whether a material's application is more suited to energy or power performance. A high tap density will provide high energy, and a low tap density invariably be high power. In order to measure the tap density, powders were weighed and then loaded into a volumetric measuring cylinder and placed onto a Quantachrome Instrument AUTOTAP. The tap density can then be calculated from these values.

2.2.4 Coin Cell Assembly

2.2.4.1 Li-Half Cell

The AM electrode was cut to size (12 mm) before assembly. The AM – Li metal coin cells were assembled in an argon-filled glovebox. Steel 2032 cases were used, with a single 1 mm stainless steel spacer for compression. The lithium metal electrode was prepared from a dispensed fraction of lithium ribbon, where the surface was scratched using a stainless steel spatula (to remove the tarnished surface and leave a shiny and rough texture) before being cut to size (12.7 mm), ready for assembly. The electrolyte was 1.0 M $LiPF_6$ in 50:50 (v/v) ethylene carbonate and dimethyl carbonate – two 50 µL

additions were made during assembly. The separator, glass fibre, was cut to size (14.3 mm). The coin cell was constructed as illustrated in Figure 2. 9.

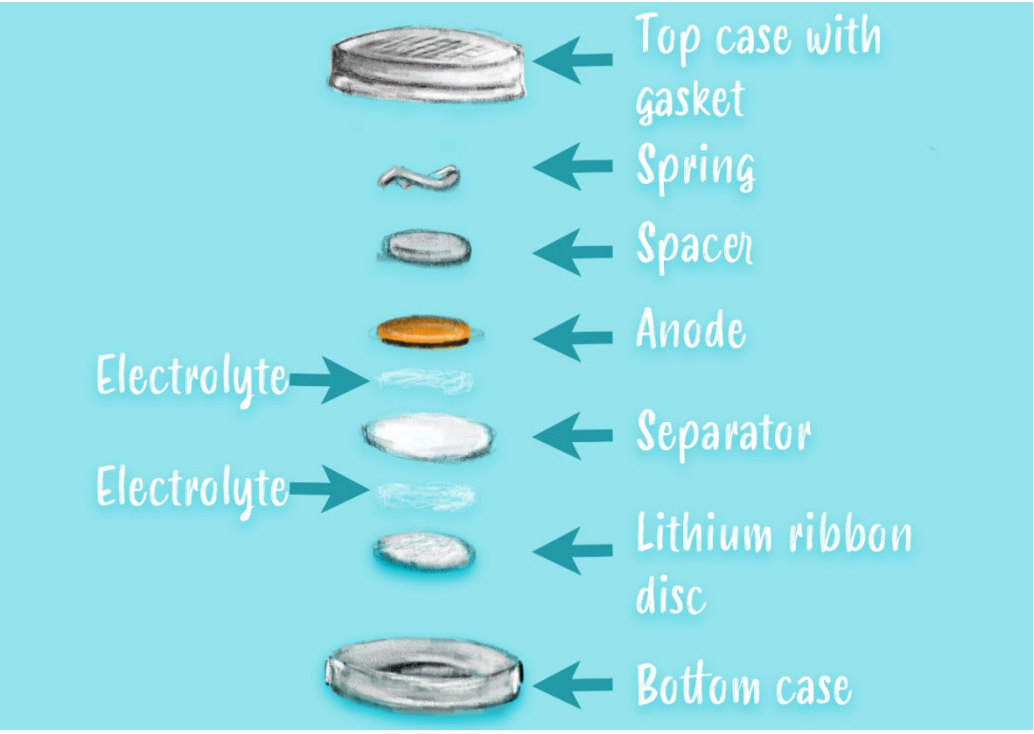

Figure 2. 9: Diagram depicting the pieces which make up a Li half coin cell. In the instance of producing a full cell, the lithium ribbon disc is replaced with a cathode electrode.

2.2.4.2 Full Cell

The main difference in the fabrication of full coin cells, involves the change of the Li metal (previously behaving as the positive electrode) to an actual cathode material (NMC 532 in this scenario). To balance the electrodes, the anode electrode was cut to 12 mm (same as previous), however the cathode electrode (previously 12.7 mm for Li) was cut to 11 mm. This reduction essentially allows a greater area for the lithium to insert within the anode electrode on charging. The further alteration involved the use of 2 spacers (1 mm thickness each), instead of a single spacer as seen previously. The amount of spacers used for this will be commented on when discussing these results,

and is to account for the initial thickness change from lithium metal to the cathode electrode, so as to retain a similar compression within the coin cell.

In the preparation of the full cells, the coatings of both electrodes require the capacity (mA h cm^{-2}; determination shown by equations **Equation 2. 7 - 2. 8**) to be balanced. In the fabrication of full cells of NMC 532-$Nb_9Ti_{1.5}W_{1.5}O_{30}$, to balance effectively, the NMC 532 electrodes were required to be cut to a diameter of 11 mm with the target capacity of 1 mA h cm^{-2}, while the anode would need to be 12 mm in diameter with the aim of 1.1 mA h cm^{-2}, such that the ratio of cathode to anode is 1 : 1.1 in terms of the capacity (mA h cm^{-2}).

Equation 2. 7: Determination of active mass per unit area.

$$\frac{Total\ Electrode\ Mass\ (g)\ \times \%\ of\ AM}{\pi(radius\ of\ electrode\ disc, cm)^2} = x\ (g\ cm^{-2})$$

Equation 2. 8: Determination of area capacity from the gravimetric capacity.

$$Capacity\ (mA\ h\ g^{-1}) \times x\ (g\ cm^{-2}) = x\ Capacity\ (mA\ h\ cm^{-2})$$

2.2.5 Electrochemical Testing

2.2.5.1 Galvanostatic Cycling

This mode of testing involves applying a constant current (galvanostatic) and measuring the voltage response.

2.2.5.1.1 Base Testing Procedure

As standard, the electrochemical properties were measured using a BioLogic BCS805 battery tester in galvanostatic mode between 3.0 V and 1.0 V, unless explicitly stated in later testing studies within this thesis.

2.2.5.1.2 C-rate

C-rate is a measure of the (dis)charge rate relative to the maximum cell capacity. This term can be described with notation of $\frac{1}{n}$ C, such that n = 1 hour, which would be defined as 1 C and thus equates to the cell requiring 1 hour to be fully (dis)charged. In the instances of (dis)charging being less than an hour, such as 30 mins (n = $\frac{1}{2}$), this would be represented by 2 C. In contrast, if the battery requires 20 hours to charge, this is denoted by C/20.

2.2.5.1.3 Determining Applied Current Ratings

There are two methods to determine the current to apply to coin cells. Quite often, if the amount of Li insertion is known, method 1 is followed. If not, method 2 is advisable. Within this body of work, nominally method 1 was used initially, although it was found that the total amount of Li insertion exceeded initial prediction. With this, the legends for all the electrochemical testing data includes the current density (mA g^{-1}), the applied current (mA) and the active mass of the electrode.

2.2.5.1.3.1 Method 1

To determine the C-rate through this method, mathematical quantities listed in **Table 2. 1** are used. Firstly, the no. of lithium ions expected to be removed from the

cathode material are determined (which equates to the no. of lithium ions to be intercalated into the anode material), which in turn provides the no. of moles of electrons within this process. This worked example makes use of archetypal $LiCoO_2$ and the first step is highlighted in **Equation 2. 9. Equation 2. 10 - 2. 12** show the work through of converting the no. of moles of electrons to the total charge per mole of the reaction, before undergoing a series of unit conversions to obtain the final units of mA h g^{-1}. Based upon the active mass of the material and C-rate, a current to apply to the cell can be determined (**Equation 2. 13 - 2. 14**).

Table 2. 1: Mathematical quantities and symbols used in the determination of current loading.

Symbol	Definition	Physical Quantity	Unit
N	no. of moles		Mol
q_e	Charge of an electron	1.602×10^{-19}	C
N_A	Avogadro's number	6.0223×10^{-19}	mol^{-1}
F	Faraday's constant	$96,485$	C mol^{-1}
RMM	Relative Molecular Mass		g mol^{-1}

Equation 2. 9: Total moles (n) of electrons removed on charging

$$LiCoO_2 \rightarrow Li^+ + e^- + CoO_2$$

$$n = 1$$

Equation 2. 10: Determining the total charge per mole of the reaction

$$C\ mol^{-1} = nF = nN_A q_e$$

$$C\ mol^{-1} = 1 \times 96,485$$

Equation 2. 11: Conversion of units to C g^{-1} from C mol^{-1}

$$C\ g^{-1} = \frac{\mathrm{nF}}{\mathrm{RMM}} = \frac{C}{mol} \times \frac{mol}{g}$$

Equation 2. 12: Conversion of units to mA h g^{-1} (equivalent to A h kg^{-1})

$$mA\ h\ g^{-1} = \frac{\mathrm{nF}}{\mathrm{RMM}} \times \frac{1000}{3600}$$

Equation 2. 13: Conversion of units to mA h, through multiplying through with the active mass.

$$mA\ h = mA\ h\ g^{-1} \times AM\ (g)$$

Equation 2. 14: Determination of mA to apply, through the division of time (hours) of the expected charging (lithiation step if half-cell).

$$mA = \frac{mA\ h}{h}$$

It is important to note that, using this method to deduce the constant current for the electrochemical procedure is only advisable if the amount of lithiation intercalation is known and provided with the given electrode mass, otherwise the calculated C-rating would be invalid. See **Table 2. 2** where the approximate C-rating is related to mA g^{-1} (Method 2).

2.2.5.1.3.2 Method 2

Ideally, the current density mA g^{-1} should be used as a base unit for the constant current determination. The table below outlines the mA h g^{-1} relation to the approximate C-rating (assuming the electrode has a specific capacity of 200 mA h g^{-1}). If for example, the active mass of the electrode was found to be 3.92 mg and an approximate C-rating

of C/20 was required for the initial formation cycling, a current value of ± 39.2 μA would be applied.

Table 2. 2: Series of mA g^{-1} values to provide an approximate C-rating, traditionally used in method 1, assuming a capacity of 200 mA h g^{-1}.

mA g^{-1}	Approximate C-rating
10	C/20
20	C/10
40	C/5
100	C/2
200	1 C
400	2 C
600	3 C
1000	5 C
2000	10 C
4000	20 C
6000	30 C
10,000	50 C

Where the assumed capacity varies from this estimate, the applied current may be altered to reflect a set time of (de)lithiation (**Equation 2. 15**). For example, if the capacity of the electrode was 300 mA h g^{-1}, applying a current density of 10 mA g^{-1} would result in the (de)lithiation to take longer than 20 hours.

Equation 2. 15: Conversion of specific (gravimetric) capacity to current density.

$$\frac{mA\ h\ g^{-1}}{h} = mA\ g^{-1}$$

2.2.5.1.4 Advanced Testing Procedures

After the initial electrochemical testing studies, more advanced testing was conducted with the following technique settings applied.

2.2.5.1.4.1 Formation Cycling

Towards the latter end of the cell performance testing, formation cycling, as discussed in **Electrochemical Testing: Method 2**, made use of an applied current density of 10 mA g^{-1}. A constant voltage step was incorporated through the condition of the voltage to be held at the lower limit for 3 hours or until the current rate reached 40% of its value originally applied. A rest of 10 minutes between each cycle was also incorporated. Formation cycling in the more advanced testing (after the initial trials making use of **Electrochemical Testing: Method 1**) was set for a maximum of 3 cycles to allow for conditioning of the cell, before either asymmetric studies or the long-term constant current cycling.

2.2.5.1.4.2 Asymmetric Cycling

In this type of study, most commonly, the lithiation step was constantly increased in current rate, while the delithiation step remained fixed at an equivalent C/5 rate. Where the delithiation step is instead increased, while the lithiation rate is kept constant, this will be stated. As before, the constant voltage step was applied through the current to be held at the lower voltage until it reached 40% of the original value. As the (de)lithiation time was gradually increased, the time condition, in conjuction with the

current breakdown, was set at 40% of duration of lithiation. Before each cycle a rest of 20 minutes was applied.

2.2.5.1.4.3 Long term – constant current cycling

An approximate "3C-3C" rating was applied to both the lithiation and delithiation steps. The current was based upon the use of 600 mA g^{-1} (**Table 2. 2**). While **Table 2. 2** makes the assumption of the capacity to be 200 mA g^{-1}, when investigating a novel material, a constant current density (mA g^{-1}) can allow for ease of comparison.

On the lithiation step (for a lithium half-coin cell), to apply a constant voltage, the limit of holding the cell at the lower voltage was set based on two conditions: a maximum duration of 20 minutes or to a breakdown of current of 40% of the original current applied, whichever occurred first. Between each cycle, a 2 minute rest time was applied to the cell.

2.2.5.2 Determining the Average Voltage

To determine the average voltage, the integral of the voltage (V) and capacity ($Q \quad - Q \quad$) (mA h g^{-1}) is first determined (**Figure 2. 10**), which is then divided by the capacity achieved for that particular step (**Equation 2. 16**).

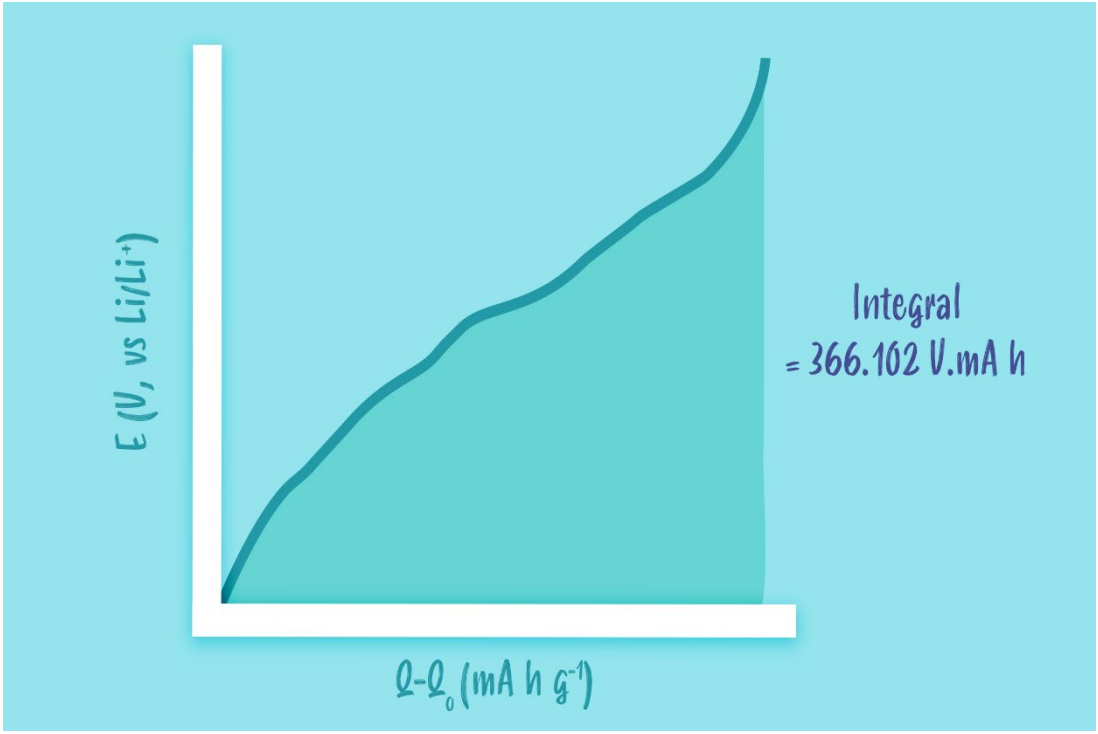

Figure 2. 10: Plot of voltage E (V vs Li/Li^+) vs Q-Q_0 (mA h g^{-1}) where the integral has been calculated.

Equation 2. 16: Example of determining the average voltage from a voltage - capacity profile.

$$\frac{366.102\ V\ mA\ h\ g^{-1}}{249\ mA\ h\ g^{-1}} = 1.47\ V$$

2.3 Characterization Techniques

2.3.1 X-ray Diffraction

X-ray diffraction is a powerful and important technique within solid-state chemistry, to elucidate sample composition and phase purity of crystalline materials. Before exploring the experimental set-up and fundamentals behind this technique, the basics behind crystal structures need to be explored first.

2.3.1.1 The Unit Cell

The initial building block for crystallography and crystalline materials revolves around the importance of defining the unit cell. The unit cell itself is the smallest, simplest and repeatable form which shows the full symmetry.

To define a unit cell, 6 (unit cell) parameters are required – the dimensions to form the basis of the cell (a, b, c) and the associated angles (α , β , γ), defined in units of Ångstroms (Å; 1×10^{-10} m) and degrees (°), respectively (**Figure 2. 11**).

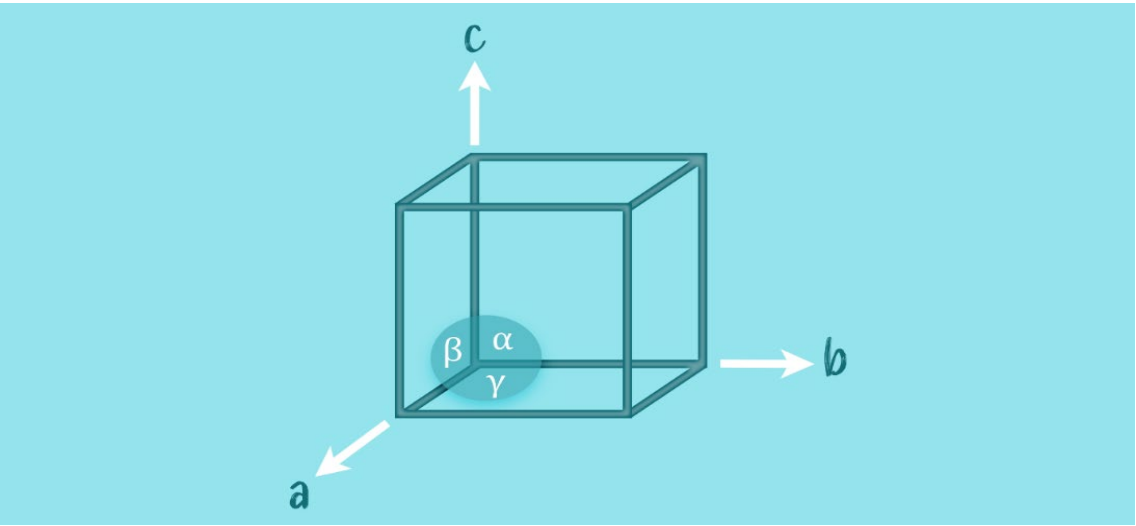

Figure 2. 11: Graphic illustrating the dimensions and angles required to form the basis of a unit cell. Figure adapted from L. L. Driscoll, PhD Thesis, University of Birmingham, 2016.[1]

Building upon the unit cell to produce an extended crystal structure through translational symmetry, a crystal lattice can be deduced of the repeatable units of the unit cells to form a spatial pattern of equal and equally oriented surroundings (quantified as individual lattice points; **Figure 2. 12**). A motif, which could be described as a small group of atoms, can be applied to each lattice point.

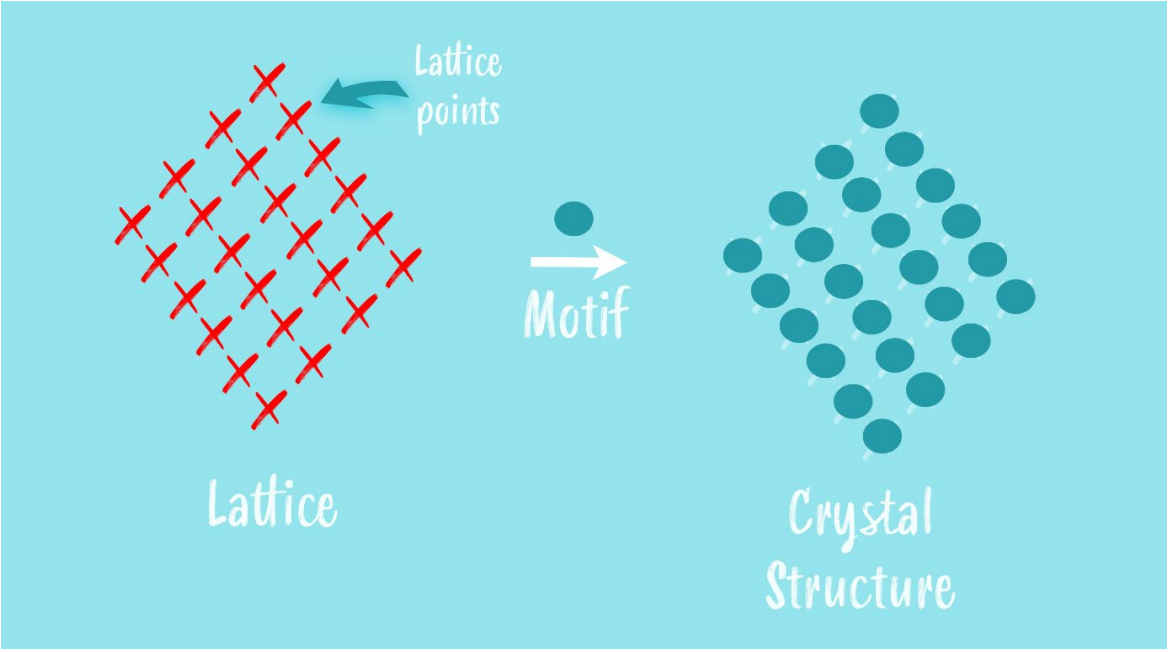

Figure 2. 12: Using the building blocks of lattice points within a unit cell to generate a lattice, which forms the basis of a crystal structure with the application of a motif onto these sites. Figure adapted from P. M. Woodward, P. Karen, J. S. O. Evans and T. Vogt, Solid State Materials Chemistry, Cambridge University Press, Cambridge, 2021.[7]

2.3.1.2 Crystal Systems

In considering the variability in the dimensions and angles of a unit cell, 7 crystal systems can be deduced – with different symmetry elements (**Table 2. 3**).

Table 2. 3: The characteristics of seven crystal systems.

Unit Cell Dimensions	Crystal System	Symmetry Elements
$a = b = c;\ \alpha = \beta = \gamma = 90°$	Cubic	Four three-fold axis
$a = b = c;\ \alpha = \beta = \gamma \neq 90°$	Trigonal	One three-fold axis
$a = b \neq c;\ \alpha = \beta = 90°, \gamma = 120°$	Hexagonal	One six-fold axis
$a = b \neq c;\ \alpha = \beta = \gamma = 90°$	Tetragonal	One four-fold axis
$a \neq b \neq c;\ \alpha = \beta = \gamma = 90°$	Orthorhombic	Three perpendicular two-fold axis
$a \neq b \neq c;\ \alpha = \gamma = 90°, \beta \neq 90°$	Monoclinic	One two-fold axis
$a \neq b \neq c;\ \alpha \neq \beta \neq \gamma \neq 90°$	Triclinic	None or an inversion centre

2.3.1.3 Bravais Lattice

On top of 7 crystal systems, four lattice types can be deduced with the differing centring. Essentially all lattice types are primitive in nature (i.e. lattice points existing at each corner of the unit cell) but with additional points present for centring. The description of each lattice type is given in **Table 2. 4** and are visually represented in **Figure 2. 13**.

Table 2. 4: Four different lattice types, due to space filling, and the associated notation and description for each.

Lattice Type	Notation	Description
Primitive	P	Lattice point at each corner
Body-centred	I	Lattice point at each corner, with one in the centre of the unit cell
Face-centre	F	Lattice point at each corner, with lattice points in each face of the unit cell
Base-centre	A, B, C	Lattice point at each corner, in addition to a pair of points within the centre of a face. For example, C-centring would have a pair of points in the ab face.

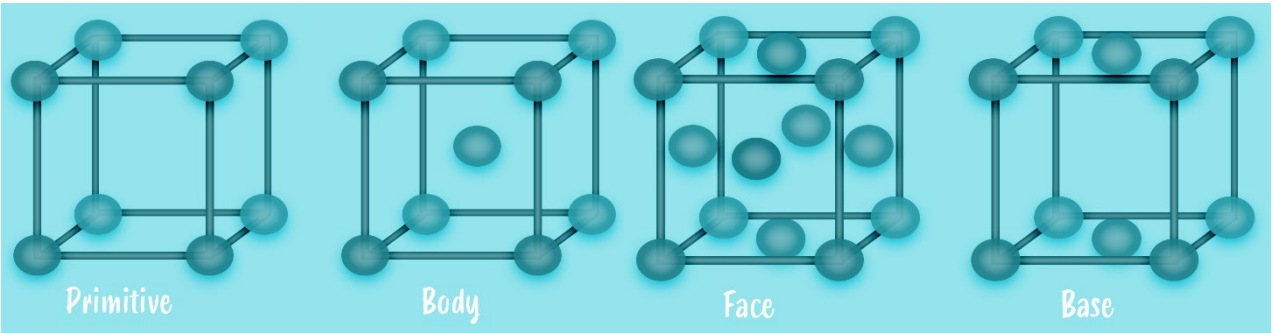

Figure 2. 13: Visual representation of the four lattice types. Figure adapted from L. L. Driscoll, PhD Thesis, University of Birmingham, 2016.[1]

Combining the 7 crystal systems and the 4 lattice types, generates 14 unique unit cell types – formally known as Bravais lattices. Through combining these lattice points with point groups (deduced from symmetry elements), 230 three-dimensional space groups can be determined. Thus, the space group, an important factor in crystallography describes the full symmetry of the crystal system.

2.3.1.4 Miller Indices

To support the visualisation and description of the crystal system, lattice planes can be described with Miller indices – a combination of 3 numbers denoted in the form of (hkl). It is important to note here that lattice planes are an imaginary concept to provide a reference grid of the unit cell, with respect to shape and dimensions. This does not necessarily mean a lattice plane will coincide with a layer of atoms.

Miller indices, after selecting an origin in the crystal system (and labelling the unit dimensions accordingly i.e. a, b and c), are determined from the reciprocal where the lattice plane of interest intersects on the 3 axes. For example, if the plane intersects the a-axis at 1, while running parallel to the other axes, the reciprocal of 1, ∞, ∞ would represent (100) plane. **Figure 2. 14** shows a visual representation of miller indices (100), (110) and (111).

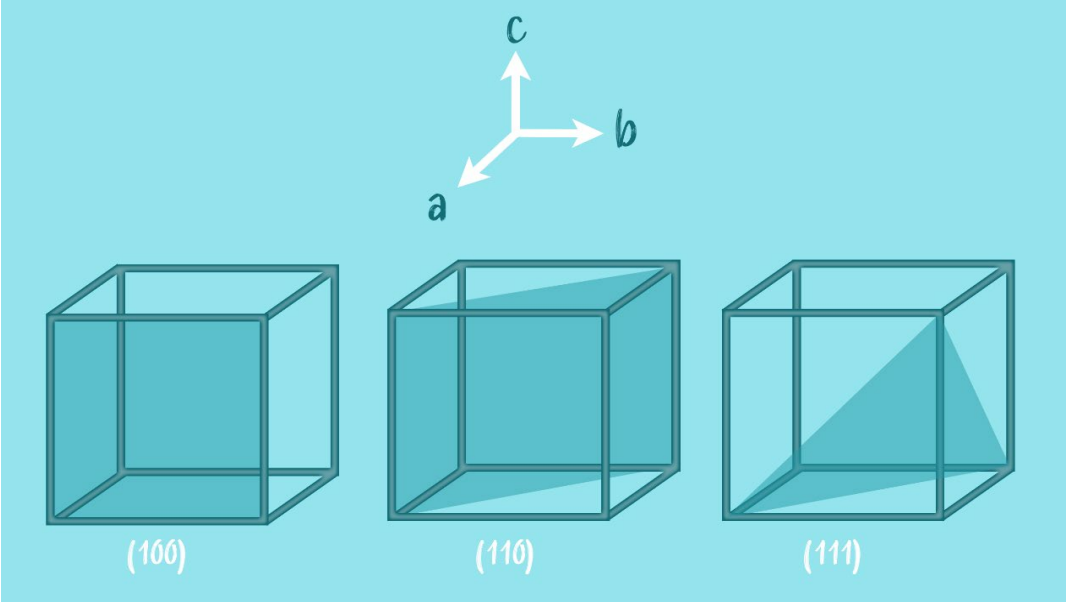

Figure 2. 14: Miller indices (100), (110) and (111) represented by the plane they intersecting, based upon the lattice vectors a, b and c. Figure adapted from L. L. Driscoll, PhD Thesis, University of Birmingham, 2016.[1]

The d-spacing of these particular (hkl) values can be determined from the unit cell parameters for orthogonal crystal systems, as shown in **Equation 2. 17**. This equation becomes more complex if the angles are not all 90° (i.e. hexagonal, monoclinic and triclinic systems).

Equation 2. 17: Determination of d-spacing of a particular (hkl) from the unit cell parameters of an orthogonal (cubic, tetragonal and orthorhombic) crystal system.

$$\frac{1}{{d_{hkl}}^2} = \frac{h^2}{a^2} + \frac{k^2}{b^2} + \frac{l^2}{c^2}$$

2.3.1.5 Generation and Diffraction of X-rays

X-rays generated within a laboratory setting, are produced via a beam of electrons accelerated to ca. 30 - 40 kV and allowed to hit a metal target, such as Cu. The incident electrons have sufficient energy to ionise the inner electrons within the metal's 1s orbital (referred to as the K shell). With an electron vacancy now present in the inner shell, electrons in the outer shells (2p or 3p) drop down to this energy level, in the process of doing so emitting X-radiation. Due to the nature of the energy levels being discrete, the transition energies have fixed values and hence the resulting spectrum is characteristic of the metal as such – and thus a fixed number of monochromatic wavelengths can be generated. A second component of the resulting spectrum to note is a broad spectrum consisting of white radiation – which is generated from high energy electrons being slowed or stopped from the collision with the lost energy converted to electromagnetic radiation.

Returning to the monochromatic wavelengths, the associated transition of the 2p → 1s is termed $K\alpha$, with an associated weighted average wavelength of 1.5418 Å, while the transition of 3p → 1s is termed $K\beta$ and has a wavelength of 1.3922 Å. The former and more intense wavelength occurs more frequently than the latter and is used within diffraction experiments.

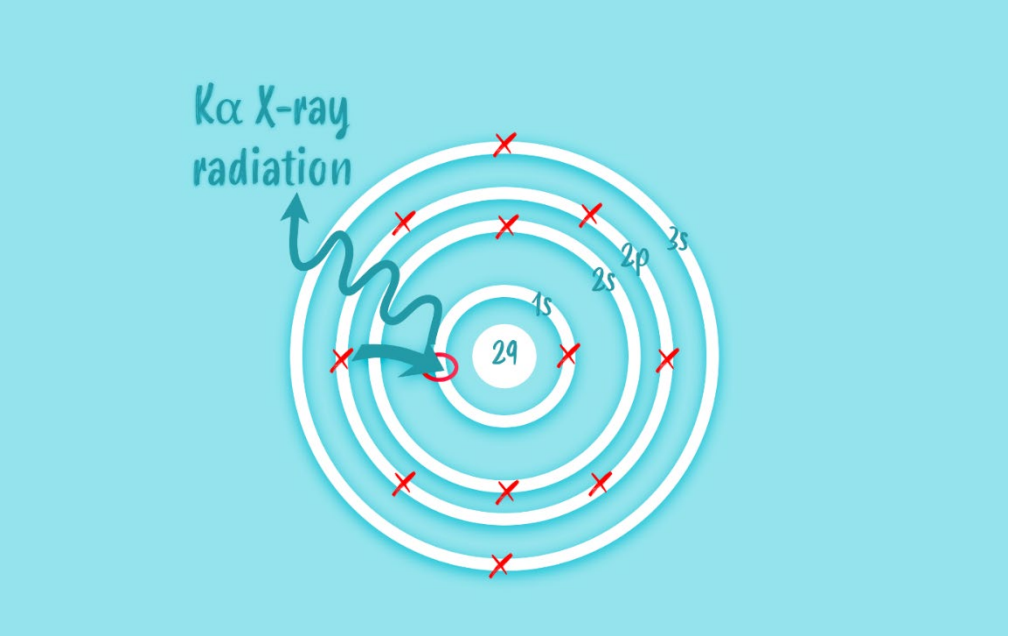

Figure 2. 15: Repesentation of the formation of Kα X-ray radiation, through the de-excitation process of a 2p electron to the electron vacancy within the core shell. This process results in the emission of energy. Figure adapted from A. R. West, Solid State Chemistry and its applications, John Wiley & Sons Ltd, Chichester, 2014.[2]

The $K\alpha$ peak is in fact a doublet, due to the two possible spin states arising from the total angular moment, *j*, given by the orbital quantum number, *l*, and the spin quantum number, *s*:

$$j = l \pm s$$

For a p orbital, the orbital quantum number is equivalent to 1, while the spin quantum number is ½. From the total angular momentum, two possible transitions can be deduced:

$$2p_{\frac{1}{2}} \rightarrow 1s_{\frac{1}{2}}\ (K\alpha_1) \text{ and } 2p_{\frac{3}{2}} \rightarrow 1s_{\frac{1}{2}}\ (K\alpha_2)$$

The associated wavelengths of $K\alpha_1$ and $K\alpha_2$ are found to be: 1.54041 Å and 1.54433 Å, respectively.

To remove unwanted radiation ($K\beta$) and generate monochromatic radiation for experiments, a filter can be used to absorb undesirable wavelengths. For example, with the use of Cu radiation, a sheet of Ni foil is used. The higher energy of $K\beta$ emission can effectively ionise the Ni 1s (1.488 Å) and thus the undesirable $K\beta$ can be effectively absorbed (in addition to white radiation), while $K\alpha$ cannot – as shown in **Figure 2. 16**. The atomic number of the element in the filter is generally one or two less than that of the target material.

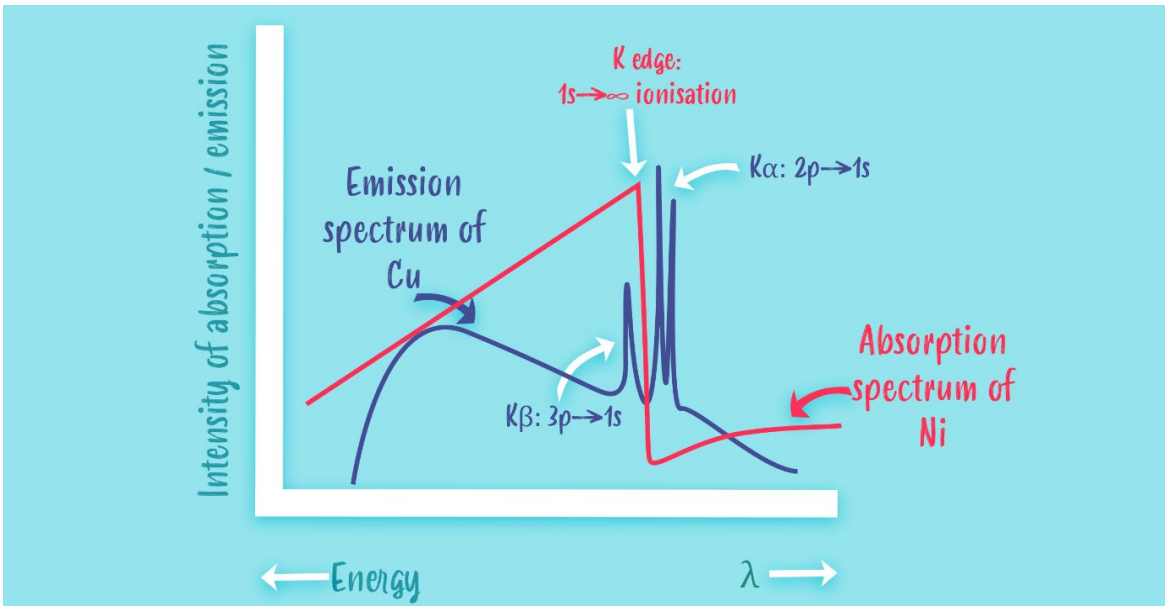

Figure 2. 16: Schematic showing the emission of $K\alpha$ and $K\beta$ radiation, with the addition of a Ni filter to remove the latter emission source. Figure adapted from A. R. West, Solid State Chemistry and its applications, John Wiley & Sons Ltd, Chichester, 2014.[2]

Alternatively, a crystal monochromator can be used, such that a single wavelength is selected and used. To achieve this, the crystal monochromator is oriented in a specific way to allow $K\alpha$ radiation to be diffracted only.

2.3.1.6 Bragg's Law

The Bragg approach considers crystals to consist of layers or planes (the description originating from the definition of unit cells and explored previously when considering Miller indices). The atoms within these planes reflect incident radiation at an angle equivalent to the angle of incidence. Radiation can be transmitted further into the crystal and be subsequently reflected by succeeding planes. The derivation of Bragg's law is where two rays of incident radiation are shown to be reflected, however the second beam interacting with plane B has to travel a further distance of **xyz** for both rays to remain in-phase, which is equivalent to an integral number, n, of wavelengths to prevent destructive interference (**Figure 2. 17**).

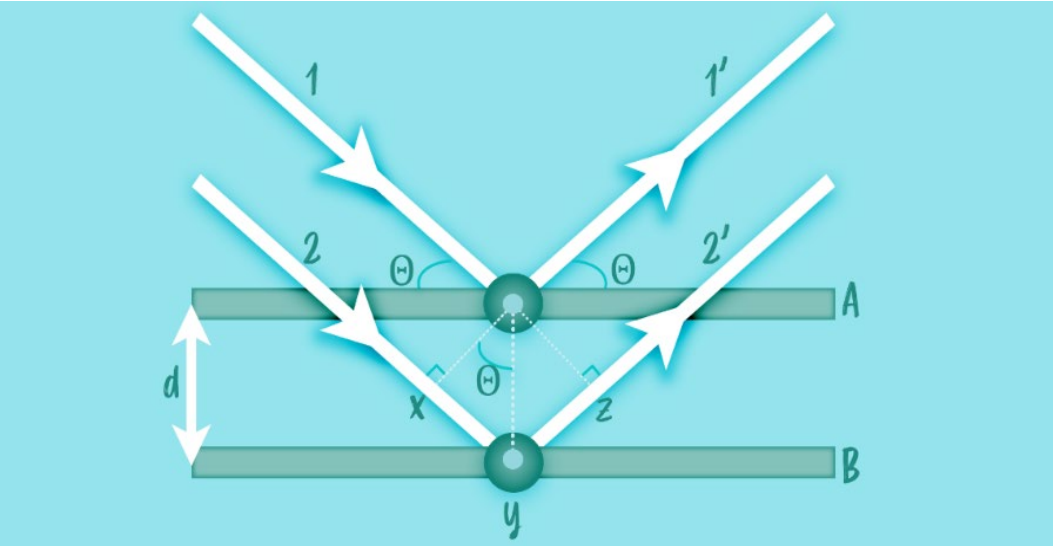

Figure 2. 17: Diagram depicting the reflection of light from different planes in a crystal, which is the principle behind Bragg's Law. Figure adapted from A. R. West, Solid State Chemistry and its applications, John Wiley & Sons Ltd, Chichester, 2014.[2]

Thus the Bragg equation can be derived and results in the expression shown in **Equation 2. 18.** The experimentally obtained **2θ** values with the Bragg equation can

allow for the determination of d-spacing values, which can be used to calculate unit cell parameters. The unique XRD pattern produced may be inferred as being a fingerprint of the composition of a particular crystal system.

Equation 2. 18: Bragg equation.

$$n\lambda = 2d_{hkl} \sin \theta_{hkl}$$

2.3.1.7 Powder X-ray Diffraction

X-ray diffraction and Bragg's law is not solely limited to the use of single crystals, polycrystalline powders which contain a very large number of small crystals - known as crystallites – orientated randomly to one another are able to generate a pattern using powder X-ray diffraction (PXRD). With a large number of crystallites present in the sample, upon irradiation there is a high probability that some planes within the material should possess the Bragg angle required for diffraction. The diffracted beams can be detected through a movable detector and the data collected on a computer.

From each of the lattice planes, the diffracted radiation will give rise to the surface of a cone –this is the result of the random orientation of the powder and no restriction upon Bragg's law with respect to the crystallite's angular orientation. Through the intersection of the diffraction cones by the detector, a trace of the respective intensity is recorded as a function of 2θ (**Figure 2. 18**).

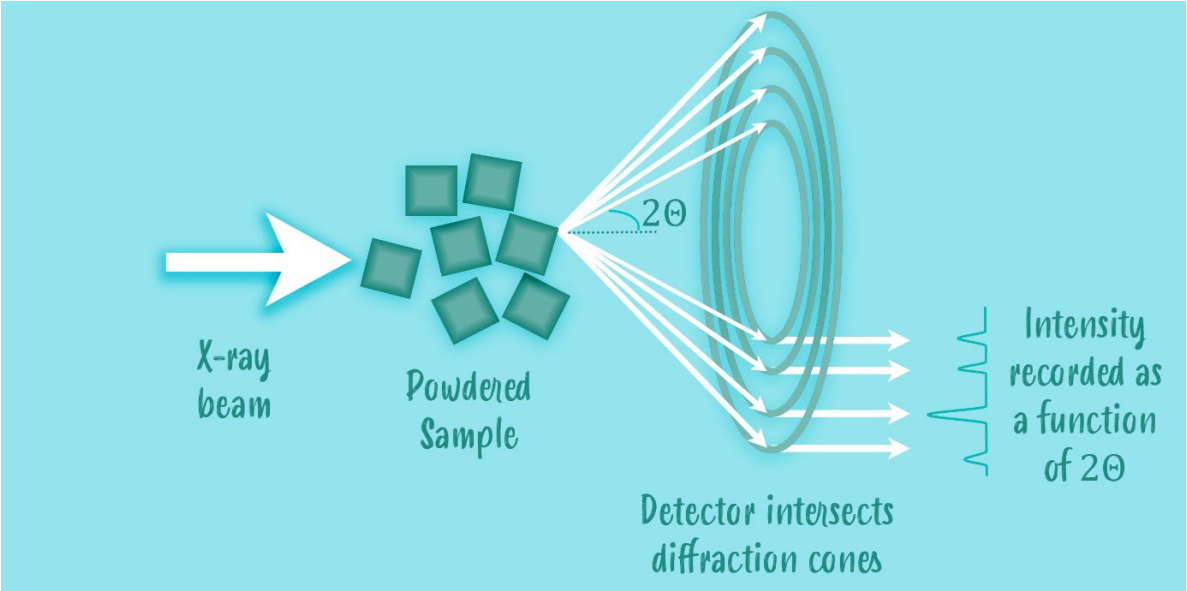

Figure 2. 18: Formation of a cone of diffracted radiation of a crystalline powder sample. Figure adapted from L. L. Driscoll, PhD Thesis, University of Birmingham, 2016.[1]

2.3.1.8 Peak position

The peak position is dictated by Bragg's law, and hence any changes in d-spacing of the crystal system will affect 2θ. This general observation is useful when inferring whether a doping study has been successful. For example, substitution of a larger ion in a place of a small ion, will result in a greater d-spacing, which is observed through the pattern shifting to lower 2θ. However care must be taken, for example, if all peaks are shifted consistently by the same value of 2θ, this would instead suggest a sample preparation or instrumental factor is at play.

2.3.1.9 Peak Intensity

Given X-rays are scattered by the electrons of atoms within the unit cell – a proportionality of increasing atomic number (Z) will result in a greater number of scattering events, and hence an increase in intensity. The effectiveness of an atom's

ability to scatter electrons is given by a scattering factor (f_0). The scattering factor is not only defined by Z, but by the Bragg angle - as 2θ increases, the scattering factor reduces to the finite size of atoms such that X-rays scattered from different parts of an atom can give some destructive interference.

The summation of all scattering events by all the atoms within the unit cell, in a given direction of a hkl reflection, is known as a structure factor (F_{hkl}) which is dependent on the atomic position and the scattering factor. The intensity is propositional to the square of the structure factor, where j represents the atoms within the cell (Equation 2. 19).

Equation 2. 19: Proportionality of intensity to the square of the structure factor.

$$I_{hkl} \propto |F_{hkl}|^2 = \sum_j (f_j \cos \delta_j)^2 + \sum_j (f_j \sin \delta_j)^2$$

The phase difference, δ, is determined from the fractional co-ordinations, x, y and z, and the indices of reflection, relative to the origin. Note, π is given in radians (Equation 2. 20).

Equation 2. 20: Determination of phase difference.

$$\delta_j = 2\pi(hx + ky + lz)$$

Knowing whether reflections are in phase or not, is a powerful tool in predicting the occurrence of a peak from constructive interference. Systematic absences arise from destructive interference, when the diffracted beams are out of phase (λ/2 or π) and if

they are of the same amplitude (determined by the scattering factor). Systematic absences can be predicted based-upon Bravais lattices (**Table 2. 5**).

Table 2. 5: Systematic absences for Bravais lattices.

Lattice Type	Notation	Systematic Absences
Primitive	P	All hkl values are observed
Body-centred	I	The total value of h+k+l must be always even. Odd values are absent.
Face-centre	F	Values of hkl must be either all odd or all even. 0 is regarded a positive value.
Base-centre	A, B, C	Total values of k+l must always be even.

Other translational symmetry elements present such as screw-axes, glides planes will give additional systematic absences (**Figure 2. 19**).

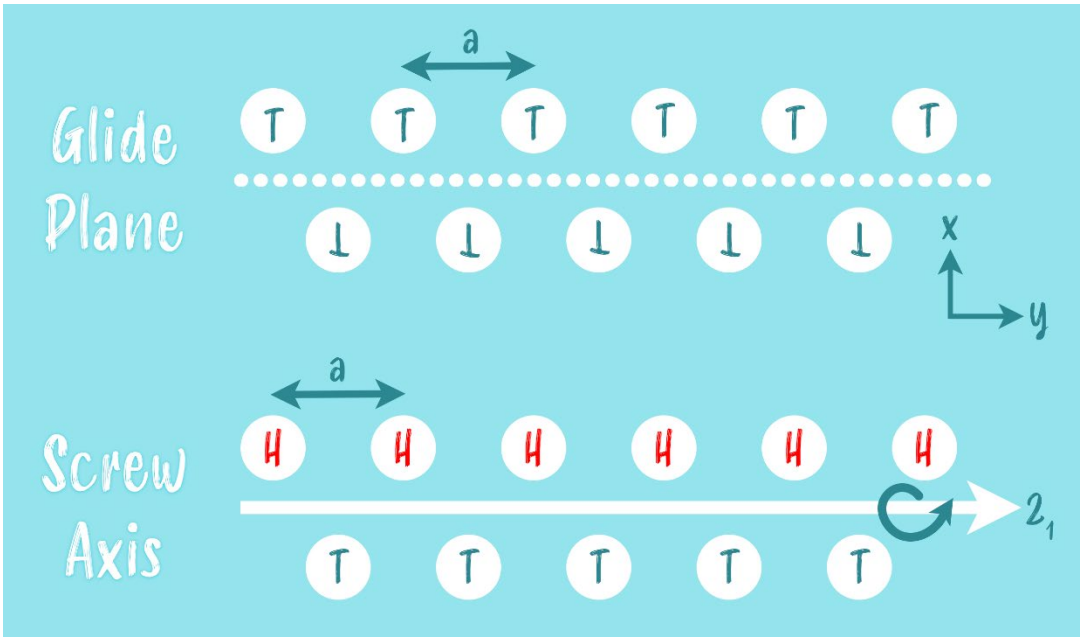

Figure 2. 19: Diagram illustrating other translational symmetry elements such as screw axes and glide planes, based upon the use of a coin with heads (H) and tails (T). Figure adapted from A. R. West, Solid State Chemistry and its applications, John Wiley & Sons Ltd, Chichester, 2014. [2]

2.3.1.10 Peak Shape

The resulting peak shape can be affected by two factors: instrumental set-up and the sample itself. Of the instrumental factors: alignment, configuration of the diffraction slits and the radiation source (i.e. not fully monochromatic) can influence the resulting peak shape. Sample factors of particle size, structural defects and microstrain broadening can influence the resulting peak shape too.

2.3.1.11 Diffractometers

Multiple diffractometers were used throughout the course of this body of work. With each PXRD data set, the radiation source in use is defined within the associated caption. Initial measurements for phase purity checks were typically conducted in the range of 10 – 50/60 ° (2θ) at a step size of ca. 0.02°. In the instance of higher quality data collection required for refinements, samples were ran for longer durations up to a higher 2θ limit of 90° or above (2θ). Powdered samples were prepared on standard holders with silicon low background wafers, with a smooth flat surface. In the instance of investigating (dismantled/pristine) electrodes, a small amount of Vaseline was dispensed onto the low background holder before placing and flattening the electrode to the surface.

Samples containing Fe, Co and Ni were examined using a Bruker D2 instrument, to mitigate fluorescence typically observed with the use of a Cu X-ray source.

Diffractometer	Geometry	Radiation	Filter/Monochromator
Bruker D8	Reflection	Cu $K\alpha_1/K\alpha_2$	Filter (Ni)
Bruker D2	Reflection	Co $K\alpha_1/K\alpha_2$	Filter (Fe)
PANalytical Empyrean	Reflection	Cu $K\alpha_1/K\alpha_2$	Filter (Ni)

2.3.1.12 Pawley Fit

As a precursor to a full Rietveld refinement (discussed in detail in the next section) – a Pawley fit[8] is an effective fitting technique, which allows observed peaks to be fitted without a full structural model (i.e. no atomic positions and structure factors), but the fit to be constrained against size and symmetry of the unit cell. By running a Pawley fit, the unit cell of a system can be quickly obtained.

2.3.1.13 Rietveld Refinement

The Rietveld refinement, named after its developer Hugo Rietveld, allows powder samples to be structurally characterized. Originally developed for Neutron Diffraction (which won't be discussed in this thesis) it was subsequently transferred across for the use of XRD.

To start a Rietveld refinement a structural model is required – in which the following parameters are needed: symmetry of the proposed unit cell, unit cell parameters, atomic positions and occupancies. The model, using a least squares method, can then be used to generate a calculated powder XRD of the system under investigation, with the sequential variation in parameters aiming to reduce the difference of the calculated and experimentally observed pattern.

The progression of the refinement can be monitored with residual, M, which accounts for the difference between the observed and calculated patterns. This value should decrease as the refinement progresses.

Equation 2. 21: Residual accounts for the difference of observed and calculated patterns.

$$M = \sum_i w_i (I_i^{exp} - I_i^{calc})^2 \text{, where } w_i = \frac{1}{I_i^{exp}}$$

Equation 2. 22: Determination of the calculated pattern.

$$I_i^{calc} = \left[S \sum_{hkl} L_{hkl} |F_{hkl}|^2 \phi(2\theta_i - 2\theta_{hkl}) P_{hkl} A \right] + bkg_i$$

Symbol	Definition
$S = S_F \frac{f_j}{V_j^2}$	Scale factor, which is influenced by the Rietveld generic scale factor, the intensity of the beam, the phase volume fraction and the phase cell volume.
L_{hkl}	Lorentz-Polarization and multiplicity factor
$\|F_{hkl}\|^2$	Structure factor for (hkl) reflection (see 2.3.1.9)
A	Absorption factor
P_{hkl}	Preferred orientation function
$\Phi(2\theta_i - 2\theta_{hkl})$	Profile shape function. Alternative functions can be substituted into the equation depending on the nature of the sample
bkg_i	The background intensity at the i^{th} step

There are three methods to monitor the progression of the refinement: inspecting the fit, reviewing the statistical factors and the resultant crystal structure.

While refining the structural model, a visual inspection of the fit is easy to access through the generation of a difference plot of the calculated and observed intensities, as a function of 2θ (**Figure 2. 20**).

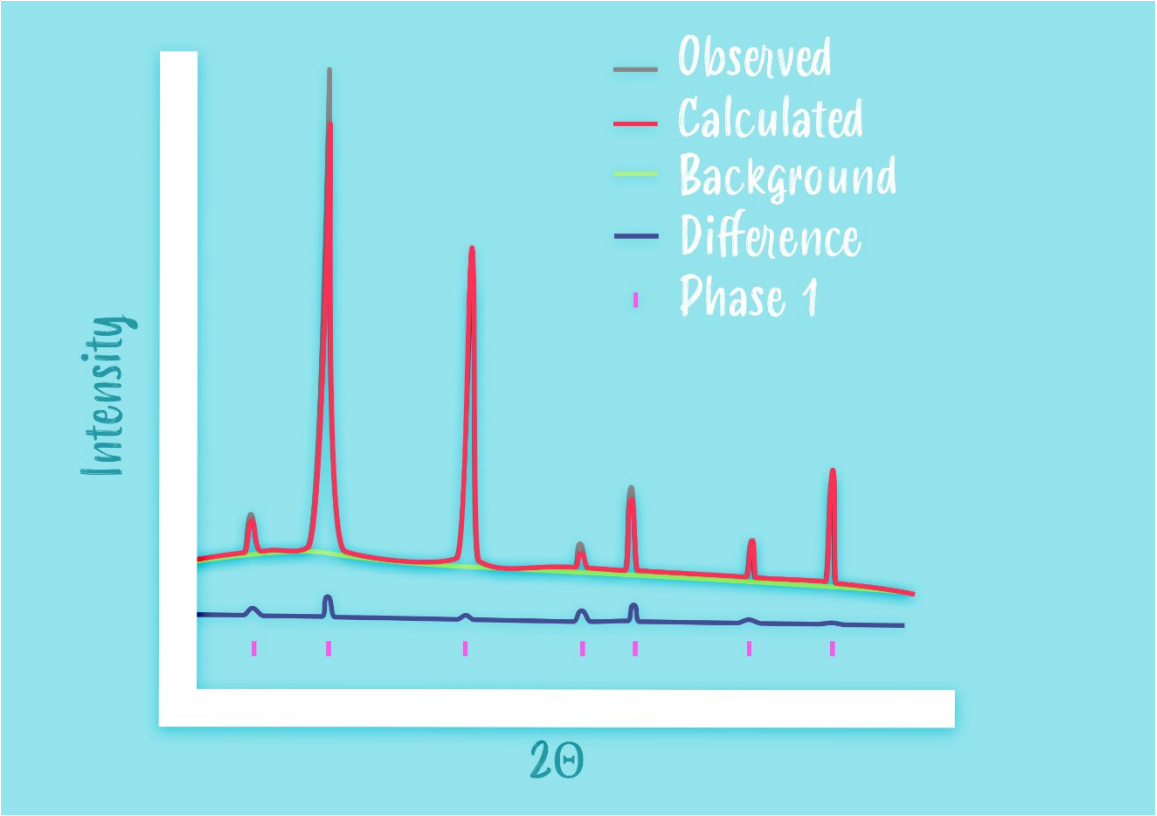

Figure 2. 20: Graphic illustrating a difference plot that could be produced on the refinement programme GSAS.

The second method to monitor the progression is through the statistical R-factors (Equation 2. 23 Equation 2. 25).

Equation 2. 23: The profile factor (R_p).

$$R_p = \frac{\sum \left| I_i^{exp} - I_i^{calc} \right|}{\sum I_i^{exp}}$$

Equation 2. 24: The weighted profile factor (R_{wp}).

$$R_{wp} = \sqrt{\frac{\Sigma_{i=1}^{N} \left[w_i \left(I_i^{exp} - I_i^{calc} \right) \right]^2}{\Sigma_{i=1}^{N} \left[w_i I_i^{exp} \right]^2}}$$

$$w_i = \frac{1}{\sqrt{I_i^{exp}}}$$

Equation 2. 25: R-expected (Rexp) where is N is the number of points and P the number of parameters.

$$R_{exp} = \sqrt{\frac{N - P}{\Sigma_{i=1}^{N} \left[w_i I_i^{exp} \right]^2}}$$

Of the three R-factors, the R_{wp} is considered the best to evaluate the progression of the refinement, due to the numerator consisting of the residual (Equation 2. 21) which as previously stated should decrease as the refinement progresses.

The number of parameters used in the refinement can affect the fit (such as background, peak type and peak shape etc.). The number of parameters is accounted for in the deduction of R_{exp} (Equation 2. 25) which is the lowest obtainable value of R_{wp}.

Taking R-factors, R_{exp} and R_{wp}, a final parameter to evaluate the fit can be used – χ^2 (**Equation 2. 26**). Ideally this value should be 1, however, given the R_{wp} parameter relationship to the background function, caution is required since R_{exp} will be strongly influenced by the quality of the collected data.

Equation 2. 26: Determination of χ^2.

$$\chi^2 = \left(\frac{R_{wp}}{R_{exp}}\right)^2$$

The final method involves inspecting the crystal model. Through the use of GSAS or TOPAS, a crystallographic information file (CIF) can be generated, which can be opened into software such as CrystalMaker© to inspect the generated crystal model. It is important the crystal model is considered, as the refinement programme may generate a fit which is statistically a good fit, but make little chemical sense.

2.3.2 X-ray Absorption Techniques

In the same way that atoms give rise to characteristic X-ray emission spectra, the same is true for X-ray absorption spectra. This technique, as the absorption edge (wavelength) is tuned to the particular elements under investigation, can give greater detail beyond diffraction techniques helping to deduce the local structure around each element, rather than an average of all the elements present.

Two techniques are commonly used to monitor the region of absorption edges: X-ray absorption near edge structure (XANES) and extended X-ray absorption fine structure (EXAFS) – the regions these techniques apply to are shown in Figure 2. 21. The former technique observes fine structure associated with the inner shell transitions. The chemical environment of the atoms play a vital part in the exact peak positions, from oxidation state to the surrounding ligands. The latter, EXAFS, examines a much larger region from the absorption edge to higher energies up to 1 keV and can be described as in-situ electron diffraction, as the X-radiation is absorbed by a bound electron within the core shell and ejected as a photoelectron, which can provide information regarding interatomic distances, co-ordination number and thermal parameters.

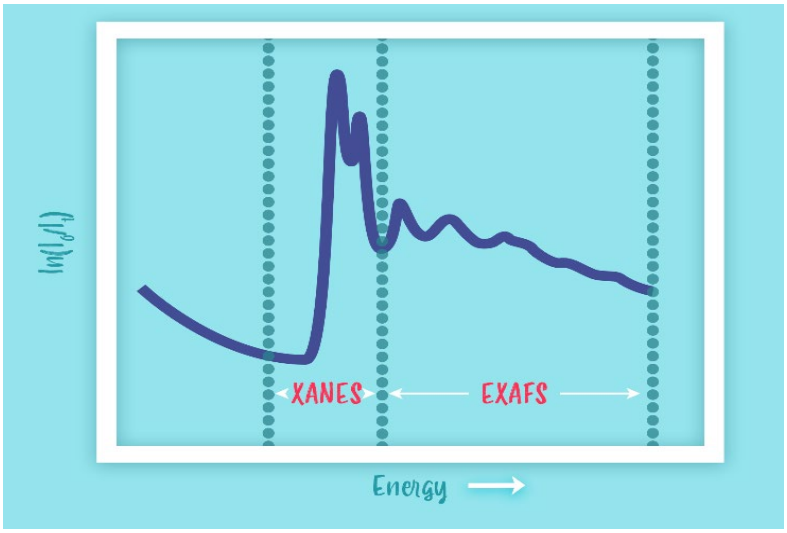

Figure 2. 21: An X-ray absorption spectrum defining the XANES and EXAFS regions. Figure adapted from D. L. Burnett, PhD Thesis, University of Warwick, 2016.[9]

2.3.2.1.1 Sample Preparation

Following advice from Dr Giannantonio Cibin (Diamond Lightsource) concerning the difficulty in measuring Ti based samples, an initial ratio of the material under investigation was mixed with cellulose. The remaining sample masses were determined to ensure the Ti content were the same, respective of the relative molecular mass. Each material was thoroughly mixed with 50 mg of Avicel® cellulose and pelletised (13 mm). Samples were then submitted to Diamond Lightsource Ltd Energy Materials Block Allocation Group SP14239 for data collection.

2.3.3 Thermal Analysis Techniques: TGA and DTA

Thermal analysis techniques, such as thermogravimetric analysis (TGA) and differential thermal analysis (DTA), enables physical and chemical properties of a sample to be measured against temperature. Both measurements can be run simultaneously.

TGA measurements involve recording the mass differences as a function of temperature or time (**Figure 2. 22**), which can provide details of any mass loss (e.g. water, oxygen, CO_2 loss) from the sample.

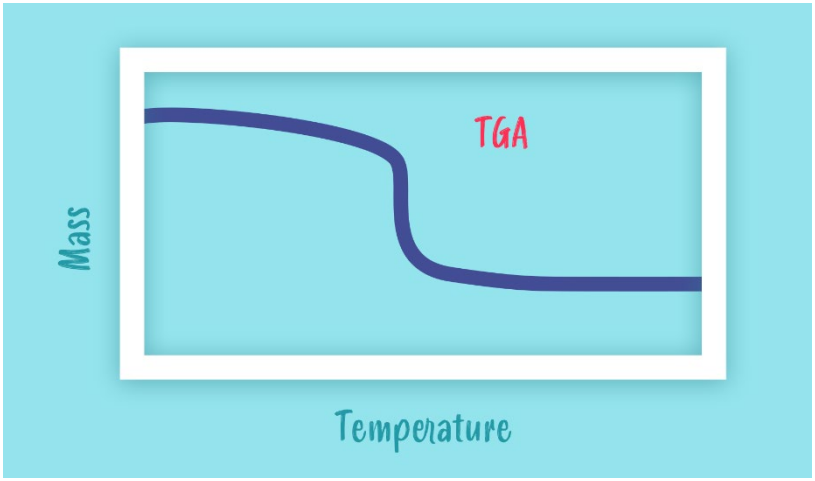

Figure 2. 22: Schematic of a TGA plot showing mass loss with respect to temperature. Figure adapted from A. R. West, Solid State Chemistry and its applications, John Wiley & Sons Ltd, Chichester, 2014.[2]

DTA measurements involve the comparison of the sample's crucible temperature to that of the reference crucible, which can provide details of thermal events taking place, such as: change in crystal structure, melting, and decomposition. If the temperature of the sample lags behind the reference, this would signify an endothermic event, while an

exothermic event is visible from the sample's temperature leading on the reference (Figure 2. 23).

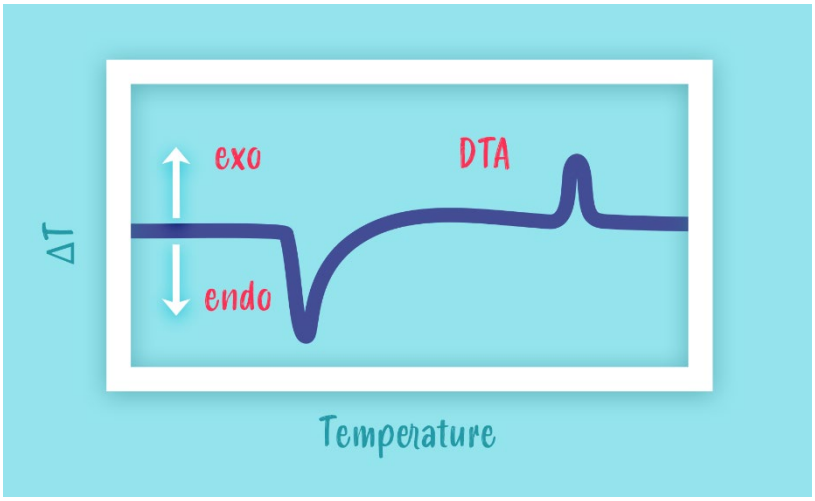

Figure 2. 23: Schematic of a DTA trace with the direction marked on for an exothermic and endothermic response. Figure adapted from A. R. West, Solid State Chemistry and its applications, John Wiley & Sons Ltd, United Kingdom, 2014.[2]

Thermal analysis may also be supported by the use of a quadrupole mass spectrometer (MS), where evolved gases from the sample are transformed into positively charged ions, which are then accelerated using an electric field and distinguished as a function of their m/z ratio.

The set up in use for this work, made use of a Netzsch STA 449 F1 Jupiter thermogravimetric analyser (under a nitrogen atmosphere) coupled with a Netzsch 403C mass spectrometer (m/z value set at a maximum at 150) to help identify mass losses during the study. An empty alumina crucible is first run under the desired experimental conditions to provide a suitable correction for the sample's measurement. In the instance of the sample measurement, typically 20 – 30 mg of sample is loaded

into the empty crucible. In both cases (correction and sample run), the crucible is first placed into the furnace chamber which is evacuated under vacuum before refilling the chamber with the desired atmosphere. The programme for the analyser is then set to gradually ramp up (5-10°C min^{-1}) to a desired final temperature. At this point isothermal steps and controlled cooling steps can be applied.

2.3.4 Electron Microscopy

2.3.4.1 Scanning Electron Microscopy (SEM)

The use of a scanning electron microscope is a powerful tool in providing surface, topography and morphological insights into powders or solid (based-films), such as electrode coatings.

In using this technique, electrons from an electron gun are accelerated between 5-50 kV and concentrated onto a small region of the sample (50 - 500 Å), with a penetration depth of up to 1 µm. The principle set-up of an SEM is shown in **Figure 2. 24**.

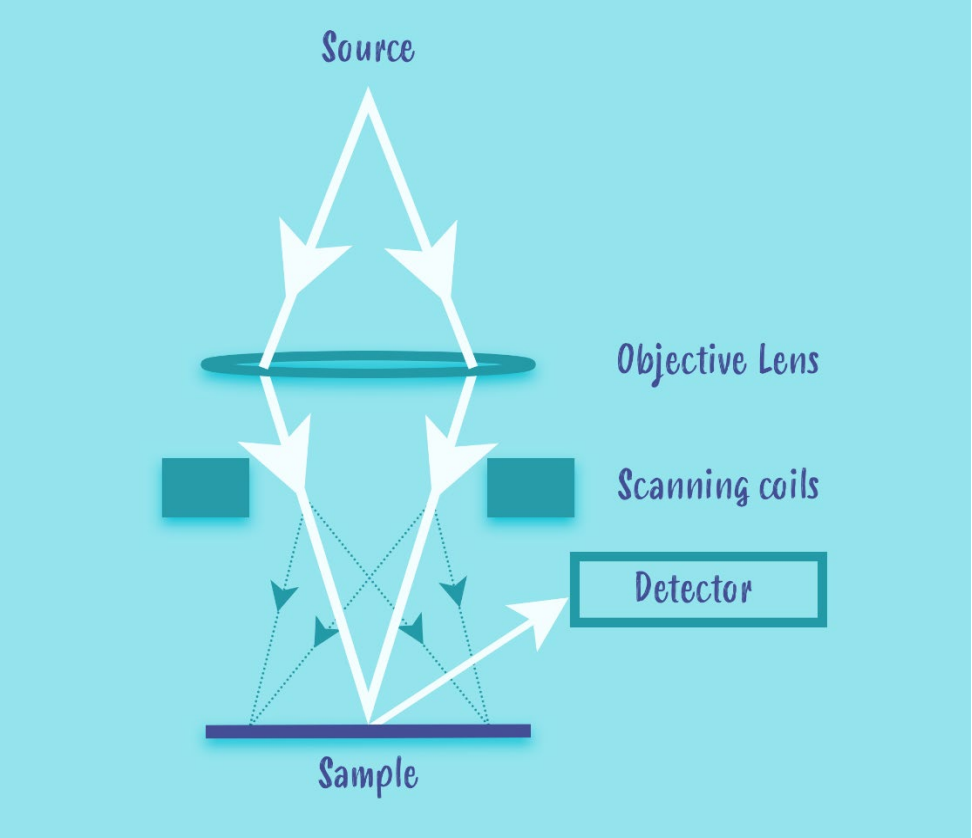

Figure 2. 24. Set-up of a SEM. Figure adapted from A. R. West, Solid State Chemistry and its applications, John Wiley & Sons Ltd, United Kingdom, 2014.[2]

The SEM can be run in two modes: secondary ionised electrons (typically denoted SE for secondary electron image) or in back-scattered electron (BSE) mode. Both measurements offer different insights into the material, given the two modes are of differing energies and hence the escape depth for the electrons are different. The collection of SE image is the result of inelastic scattering and can image the surface (shallower depth, due to being lower energy). Back-scattered electrons are able to escape from a thicker region of the sample, given no further secondary collisions after the initial event. Electrons which penetrate beyond this limit are unable to escape from the sample, given the loss of energy to lattice vibrations.

The penetration and escape depths of SE and BSE are illustrated in **Figure 2. 25**.

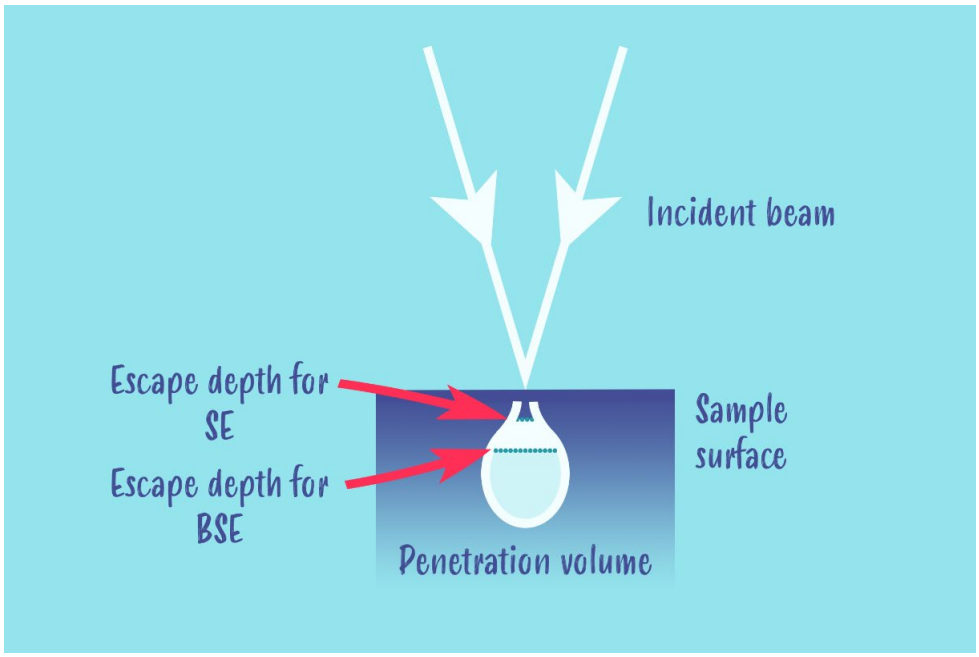

Figure 2. 25: Penetration and escape depths in SEM of SE and BSE. Figure adapted from A. R. West, Solid State Chemistry and its applications, John Wiley & Sons Ltd, United Kingdom, 2014.[2]

2.3.4.2 Energy-dispersive X-ray Spectroscopy (EDX/EDS)

Energy-dispersive X-ray Spectroscopy often denoted as EDX/EDS can support qualitative studies on elements present within the sample. Through the bombardment of electrons onto the surface, during the use of SEM, X-ray emission spectra is generated – the energies/wavelengths detected can thus determine the presence of the elements within the sample. Quantitative studies are possible given suitable calibration.

Within this body of work, a Hitachi tabletop Microscopes TM4000Plus II was used with an Oxford Instruments EDS using AZtec software for elemental analysis.

A small amount of powdered material or cut electrode discs were placed onto a conductive carbon disc and adhered to the sample holder. The sample holder would then be placed into the instruments evacuation chamber to vacuum the sample down – to enable the electron gun to be switched on. Typically the vacuum would be held at a moderate level. To collect surface information, the electrons would be set to be accelerated to 5 kV, while elemental analysis would require 15 kV. Images of the detector set in SE and BSE were both conducted.

2.4 Experimental Methods and Techniques Summary

To relate all methodology and technique practices mentioned within this chapter, to the subsequent results chapter, Figure 2. 26 and Figure 2. 27, highlight step-by-step methods of synthesis and characterisation (applicable to all chapters) and cell fabrication and testing (for materials testing for battery application), respectively.

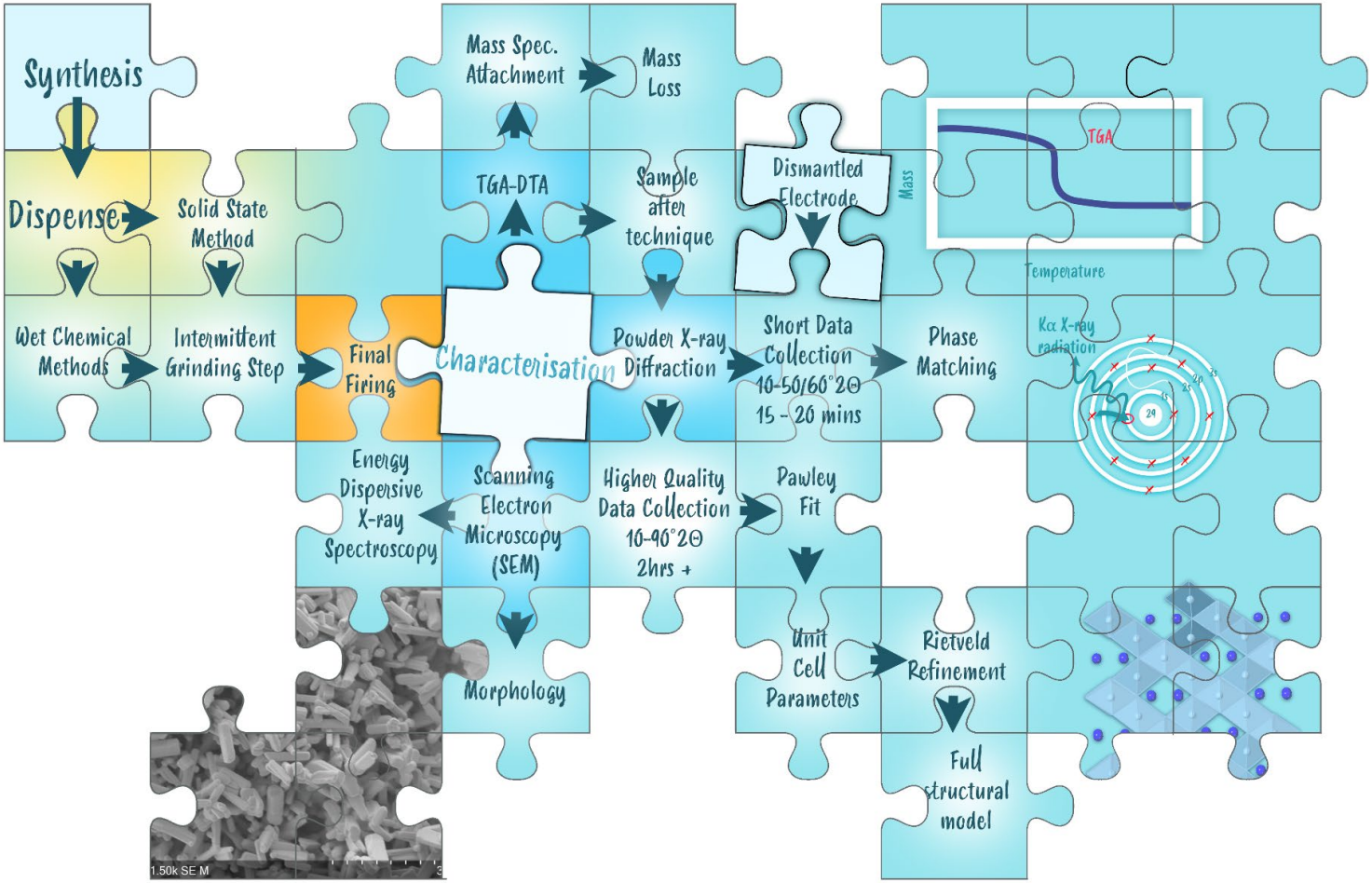

Figure 2. 26: Flow chart of processing stages from synthesis to characterisation, in the form of a jig-saw puzzle. The flow-chart highlights key stages for both areas and the techniques applied. This process visible here forms the basis of the material synthesis and characterisation within the results chapters.

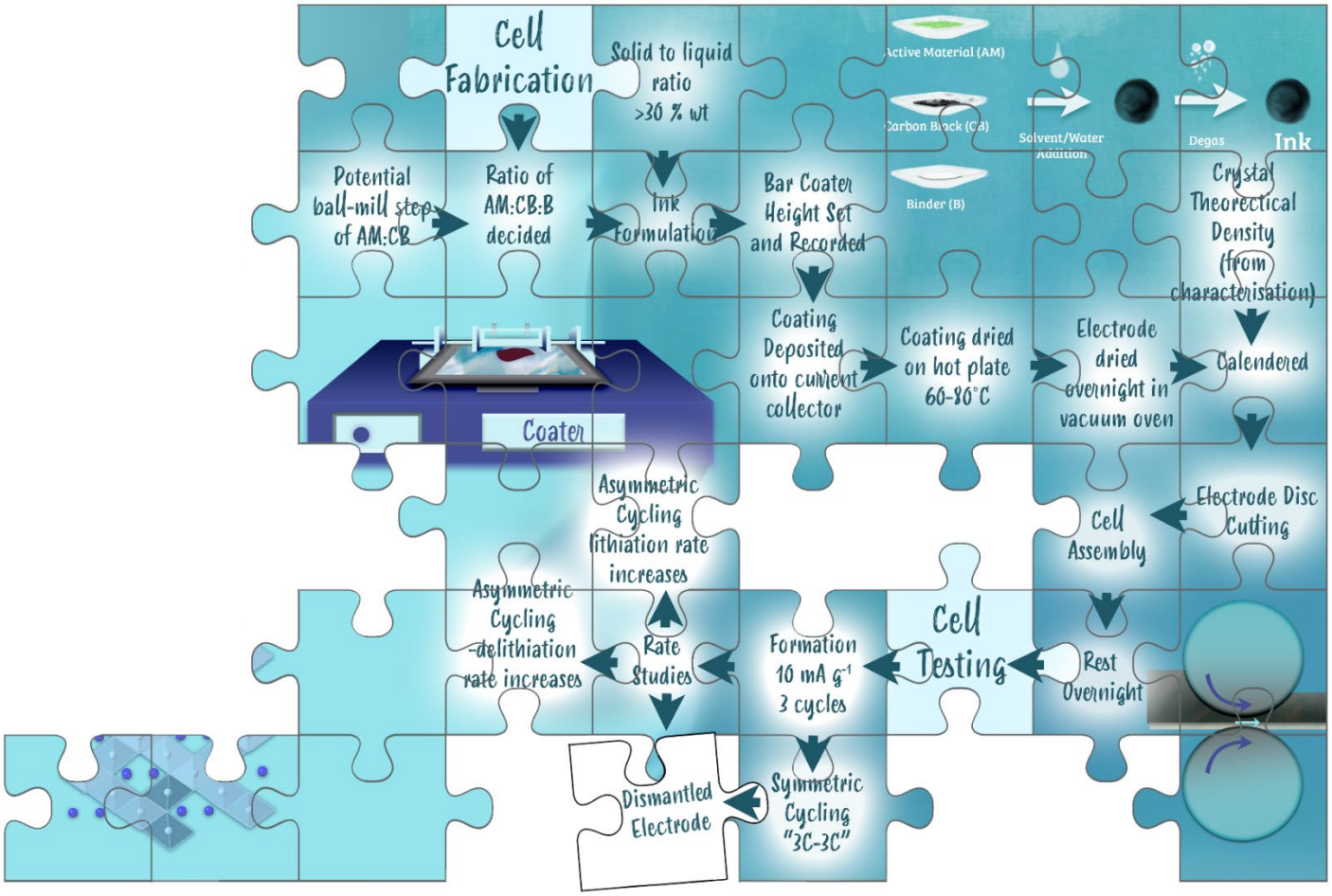

Figure 2. 27: Flow chart representative of the stages involved in cell fabrication and testing, in the form of a jig-saw puzzle. The step-by-step process will apply to Chapters 3 to 5 whereby these materials have been tested to evaluate their electrochemical performance nominally in Li half coin cell architecture.

2.5 References

1 L. L. Driscoll, University of Birmingham, 2016.

2 A. R. West, *Solid State Chemistry and Its Applications*, John Wiley & Sons, Chichester, 2nd edn., 2012.

3 E. A. Smart, Lesley E. , Moore, *Solid State Chemistry: An Introduction*, CRC Press, Boca Raton, 3rd edn., 2005.

4 H. Berg, *Batteries for Electric Vehicles: Materials and Electrochemistry*, Cambridge University Press, Cambridge, 2015.

5 M. Root, *The TAB Battery Book: An In-Depth Guide to Construction, Design, And Use*, The McGraw-Hill Companies, New York, 2011.

6 D. Ledwoch, University College London, 2021.

7 P. M. Woodward, K. Pavel, J. S. O. Evans and V. Thomas, *Solid State Materials Chemistry*, Cambridge University Press, Cambridge, 2021.

8 J. S. O. Evans, Pawley Fitting, https://community.dur.ac.uk/john.evans/topas_workshop/tutorial_tio2pawley.htm, (accessed 5 May 2022).

9 D. L. Burnett, University of Warwick, 2016.

Chapter 3: Synthesis, characterization and application of novel Nb-based anode materials: Cu doping

In this chapter, a novel Cu doped Nb_2O_5 with the formula $Nb_{22}CuO_{56}$ was prepared for potential applications as a high-power Li-ion anode. The novel system of $Nb_{22}CuO_{56}$ was originally identified by P. R. Slater (University of Birmingham, UK) through his detailed doping studies into Nb_2O_5. The material was passed onto E. H. Driscoll for investigations into its electrochemical performance. Efforts to enhance the electronic conductivity of this material will consider ex-solution synthesis techniques. Structural characterisation of this material will be explored, before consideration of its electrochemical performance. Before considering the results of these mixtures, it is important that there is an awareness of the baseline presented by the undoped Nb_2O_5 material already reported (using these coating and testing conditions), both from a structural and a morphological perspective, and any consequential changes that may occur at higher temperatures.

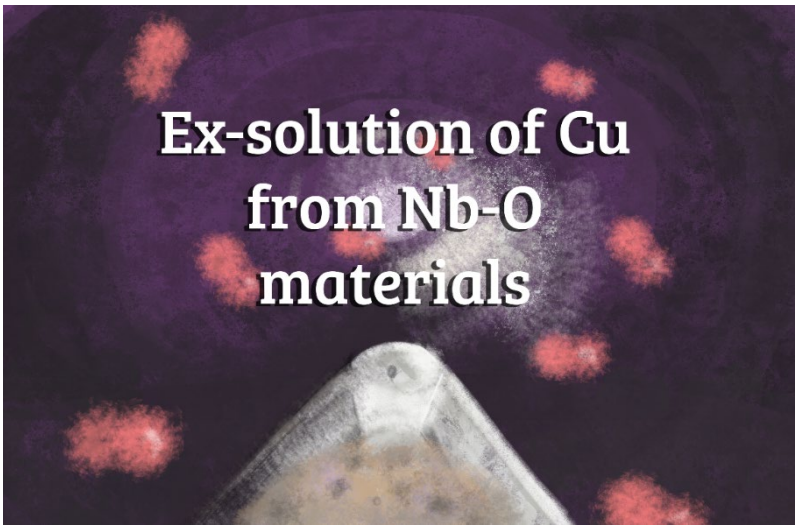

Figure 3. 1: Graphical abstract showing a visualization of the ex-solution of Cu from the Nb-Cu-O material, heating within a tube furnace with a hydrogen atmosphere – this system is the primary focus of this chapter.

3.1 Background: Context and Aims

To current knowledge, only one Cu-doped niobium oxide system has been reported within the literature – $Cu_2Nb_{34}O_{87}$ - and a series of studies have been performed on this phase with respect to morphological design to improve performance as a high power Li-anode.[1–3] $Cu_2Nb_{34}O_{87}$ is a member of the Wadsley-Roth block structures, with the same crystal structure as $Ti_2Nb_{10}O_{29}$ (3 x 4 block structure).

The interest in this material stems from its high theoretical capacity which is greater than graphite, 400 mA h g^{-1} vs. 372 mA h g^{-1}, based upon Nb's redox couples of Nb^{5+}/Nb^{4+} and Nb^{4+}/Nb^{3+}. First papers on this system, prepared via a solid state method, reported reversible capacities of 281, 259, 240, 212 and 184 mA h g^{-1} for C-rates of 0.5, 1, 2, 5 and 10 C from cycling between 0.8 to 3.0 V vs Li metal, with an electrode coating consisting of AM:CB:B ratio of 65:25:10. No current densities were provided in this publication to associate against the determined C-rates. This material has been cited to be more highly conducting compared to undoped Nb_2O_5 due to the Cu^{2+} valence electrons.[1] Further work investigated improvements via engineering the morphology to "inverse opal", enabling the delivery of slightly higher capacities such that at 10 C (equivalent to 4 A g^{-1}) a reversible capacity of 199 mA h g^{-1} was achieved.[2] The mass loading was reported to be ca. 1.0 mg cm^{-2}.

Given the lack of transparency and details regarding coating methodology and electrochemical testing, this section will consider the initial work within cell testing novel Nb oxide materials, in particular the $Nb_{22}CuO_{56}$. The decision to dope Nb_2O_5 with Cu stems from the concept of improving the overall conductivity of the material through ex-solution work – which will be considered in this section.

3.2 Experimental

3.2.1 Synthesis of Active Material

The niobium copper oxide materials were prepared through weighing stoichiometric amounts of Nb_2O_5 and CuO, which were ground together using an agate pestle and mortar. The mixture was then be heated up to 850°C/12hrs/5°C min^{-1} within an alumina crucible, and after intermittent grinding at room temperature, was re-heated up to 1150°C/12hrs/5°C min^{-1}.

As-purchased Nb_2O_5 (T-Nb_2O_5; orthorhombic phase; labelled as bottle sample in this work: supplied by Alfa Aesar, 99.9% metals basis) was heated up to 850°C/12hrs/5°C min^{-1} within an alumina crucible, and after intermittent grinding at room temperature, was re-heated up to 1100°C/12hrs/5°C min^{-1} to obtain the parent H-Nb_2O_5 polymorph structure.

The sample purity and structure determination were evaluated using powder X-ray diffraction. Structure refinements were carried out using the TOPAS suite of programs to determine unit cell parameters through a Pawley fit, before conducting a Rietveld refinement to confirm the structural model for this system.

3.2.2 Coating Methods

The basis of the coating methodologies and terminology discussed in this section are previously covered in section 2.2.1 Coating Formulations on p58.

3.2.2.1 Method 1

The electrode ink coating was prepared with an AM:CB:B mass ratio of 80:10:10 using a Thinky Mixer (model ARE-250). The initial step involved mechanochemical mixing of the AM and CB together for a total time of 30 mins at 350 rpm, using a Fritsch planetary ball mill (Pulverisette 7).

The binder - polyvinylidene difluoride (PVDF) - was mixed with N-methyl pyrrolidone (NMP) initially for 5 mins/1300 rpm, before additions of the Super P carbon black and the active material (previously ball milled together) with subsequent additions of NMP to produce a slurry (10 mins/1300 rpm for each step). To degas the mixture, a final mix of 3 mins/1800 rpm was performed. The resulting slurry was cast onto copper foil using a draw-down coater, where the bar height was set to 200 μm. The resulting coating was dried for up to 2 hours at 80°C before being transferred for overnight drying in a vacuum oven pre-set at 110°C.

3.2.2.2 Method 2

The electrode ink coating was prepared with an AM:CB:B ratio of 80:10:10 using a Thinky Mixer. The binder - polyvinylidene difluoride (PVDF) - was mixed with N-methyl pyrrolidone (NMP) initially for 5 mins/1300 rpm, before separate additions of the SuperP carbon black and the active material with subsequent additions of NMP to produce a slurry (10 mins/1300 rpm for each step). To degas the mixture, a final mix of 3 mins/1800 rpm was performed. The resulting slurry was cast onto copper foil using a draw-down coater, where the bar height was set to 200 μm. The resulting coating was

dried for up to 2 hours at 80°C before being transferred for overnight drying in a vacuum oven pre-set at 110°C.

The main difference between these methods relates to when the CB is added to the mixture. In method 1, CB is combined with the AM before coating in a ball mill step, while method 2, the CB addition has its own step – the sequence of the additions of the solids is shown in **Figure 3. 2.**

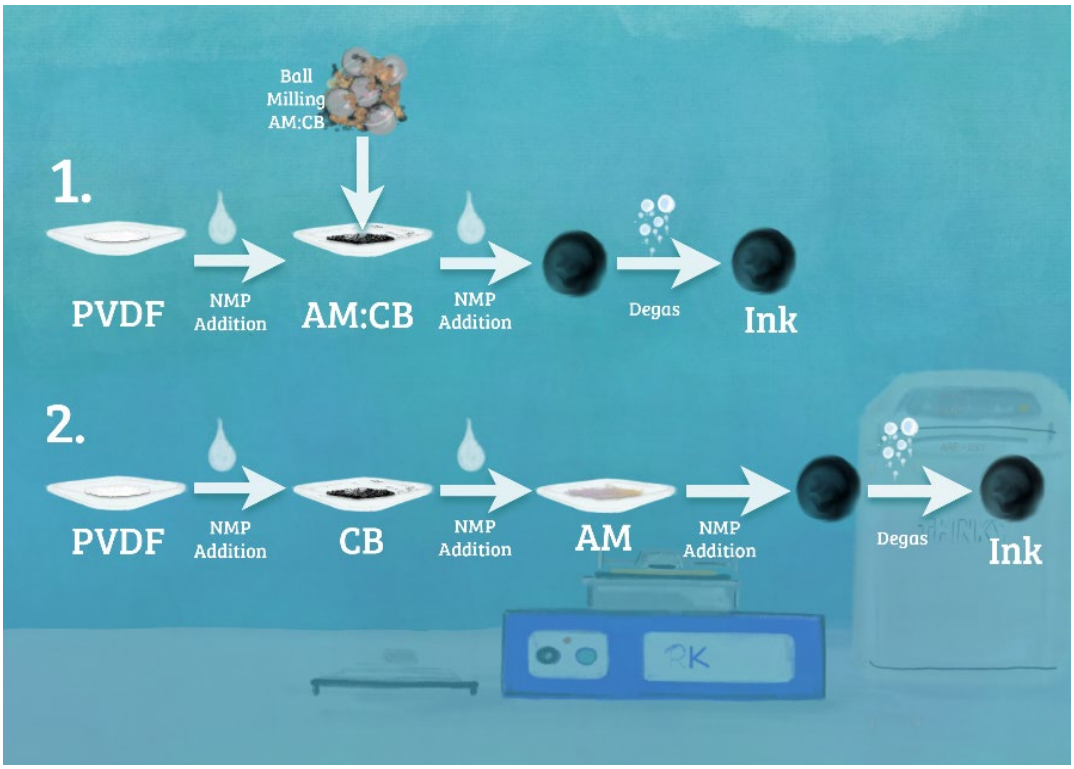

Figure 3. 2: Representation of the coating process described with methods 1 and 2 with the order of solid additions.

This system was considered in parallel to the $Nb_9Ti_{1.5}W_{1.5}O_{30}$ (material discussed in a later **Chapter 4**) – thus some of the learning curves experienced in that chapter (and discussed in more depth), were equally experienced within this body of work.

Unless explicitly stated towards the latter end of this chapter, it should be assumed the electrodes were uncalendared and the additional processing step is implemented when considering optimisation processes.

3.2.3 Coin Cell Assembly

3.2.3.1 Li-Half Cell

The AM electrode was cut to size (12 mm) before assembly. The AM – Li metal coin cells were assembled in an argon-filled glovebox. Steel 2032 cases were used, with a single 1 mm stainless steel spacer for compression. The lithium metal electrode was prepared from a dispensed fraction of lithium ribbon, where the surface was scratched using a stainless steel spatula (to remove the tarnished surface and leave a shiny and rough texture) before being cut to size (12.7 mm), ready for assembly. The electrolyte was 1.0 M $LiPF_6$ in 50:50 (v/v) ethylene carbonate and dimethyl carbonate – two 50 µL additions were made during assembly. The separator, glass fibre, was cut to size (14.3 mm).

3.2.4 Electrochemical Testing

As standard, the electrochemical properties were measured using a BioLogic BCS805 battery tester in galvanostatic mode between 3.0 V and 1.0 V, unless explicitly stated in later testing studies within this chapter.

3.3 Results and Discussion

3.3.1 H-Nb_2O_5

3.3.1.1 Characterisation

Before discussing the results of the novel copper doped niobium oxide, undoped H-Nb_2O_5 was investigated as a baseline material – this benchmarking is particularly important given the amount of variation in performance reported within the niobate literature. The Nb_2O_5 precursor taken from the bottle (Niobium (V) oxide, Alfa Aesar 99.9% trace metal basis) was present in the low temperature phase (T-Nb_2O_5; orthorhombic) and upon heating to 1150°C, transforms to the H-Nb_2O_5 system (monoclinic), as shown with **Figure 3. 3**. The unit cell parameters, refined through Pawley fit, of both these polymorphs are presented in **Table 3. 1.** The crystal structure of these two polymorphs are represented in **Figure 3. 4**. The T-Nb_2O_5 structure is composed of highly distorted octahedral and pentagonal bipyramidal Nb-O sites, while the H-Nb_2O_5 phase consists of ReO_3-like blocks of octahedra and adopts one of the Wadsley-Roth family of crystallographic shear structures.[4]

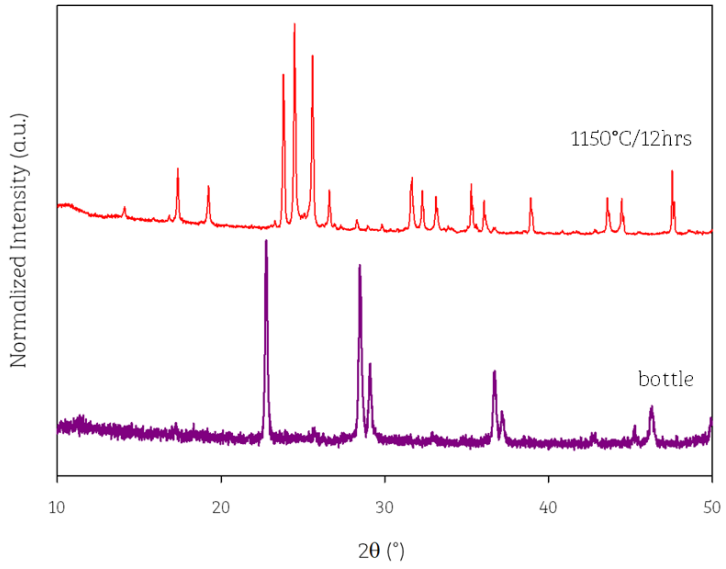

Figure 3. 3: XRD patterns of Nb_2O_5 from the bottle and the sample after heating to 1150°C/12hrs/5°C min^{-1} (Cu Kα).

Table 3. 1: Unit cell paramters of polymorphs T- and H- Nb_2O_5 of the bottle and synthesized sample, respectively, compared to reference values.

Composition	Crystal Symmetry	a (Å)	b (Å)	c (Å)	β (°)	Cell Volume (Å^3)	Reference
T-Nb_2O_5	Orthorhombic	6.220(2)	29.254(7)	3.948(2)	90.0	718.3(5)	
Reference	P b a m	6.175(1)	29.175(4)	3.930(1)	90.0	708.012	5
H-Nb_2O_5	Monoclinic	21.166(7)	3.8229(9)	19.148(5)	118.03(1)	1367.7(7)	
Reference	P2	21.1600	3.8220	19.3500	119.83	1357.561	6

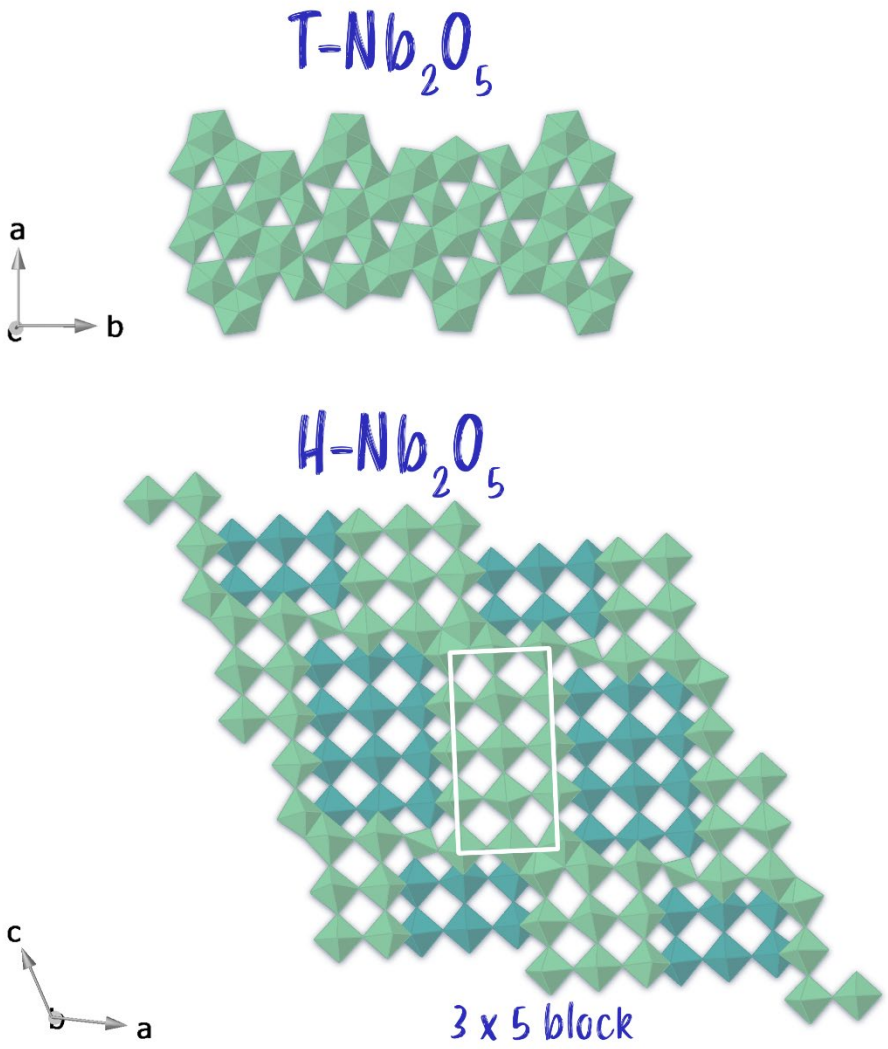

Figure 3. 4: Crystal structures of T- and H-Nb_2O_5 phases (3 x 5 block structure), top and bottom respectively. The Nb is represented by the polyhedral; for simplicity the oxygens have been omitted.

SEM images were collected for both polymorphs (**Figure 3. 5**), where rod-like character is shown for both samples, however the low temperature phase shows more of the particles are agglomerated together.

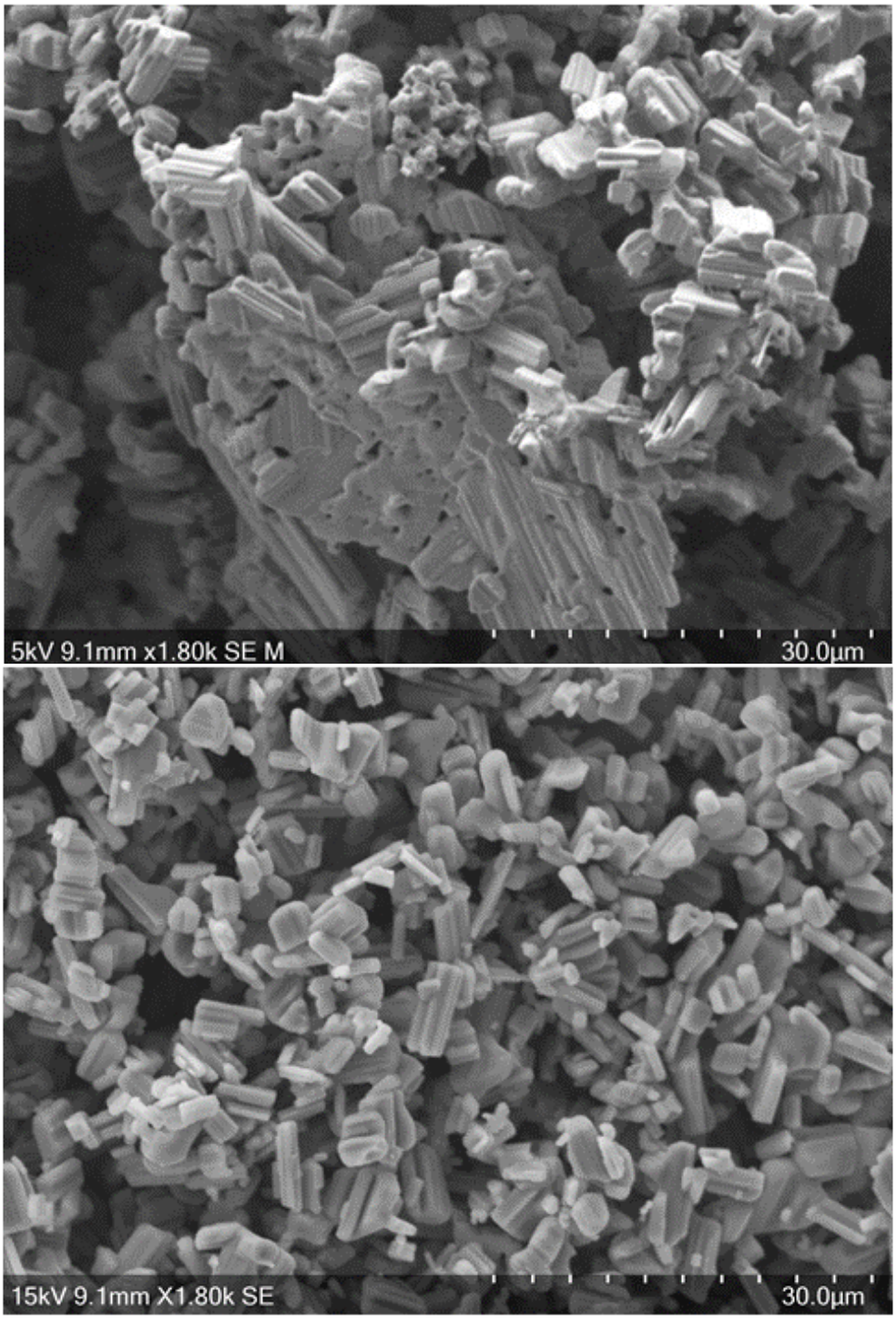

Figure 3. 5: SEM images of Nb_2O_5 from the bottle (top) and the sample heated 1150°C (bottom).

3.3.1.2 Electrochemical Performance

The higher temperature phase was coated using the procedure described previously in **Coating Methods: Method 2** and fabricated into a Li half-coin cell. The cell was only subjected to initial formation cycling at 10 mA g^{-1} (total of 7 cycles[†]) with the data for the initial 5 (de)lithiation cycles presented in **Figure 3. 6**. The initial specific capacity for lithiation and delithiation was found to be 243.2 mA h g^{-1} and 239.4 mA h g^{-1}, respectively – greater than the theoretical capacity of ca. 202 mA h g^{-1}, assuming only the Nb^{5+}/Nb^{4+} redox couple, thus indicating a further redox process of the Nb (i.e. Nb^{4+}/Nb^{3+}) is taking place. The average voltage was determined from the initial 3 formation cycles, where upon lithiation and delithiation was found to be 1.528(8) and 1.60(2) V, respectively. The corresponding differential capacity plot derived from the delithiation/lithiation profiles is shown in **Figure 3. 7**. Reversible peaks are visible at approximately 2.03, 1.68, 1.41 and 1.20 V, signifying redox processes, and are similar in value to those reported by Griffith *et al.*[4] for this phase. The higher voltage peaks are likely indicative of the Nb^{5+}/Nb^{4+}, while 1.41 and 1.20 V are attributed to the Nb^{4+}/Nb^{3+} redox couple, however the peaks themselves simply provide information towards phase changes within the structure upon cycling.

[†] The cell was set to cycle for longer, however due to a cell tester-computer fault the procedure stopped sooner than expected.

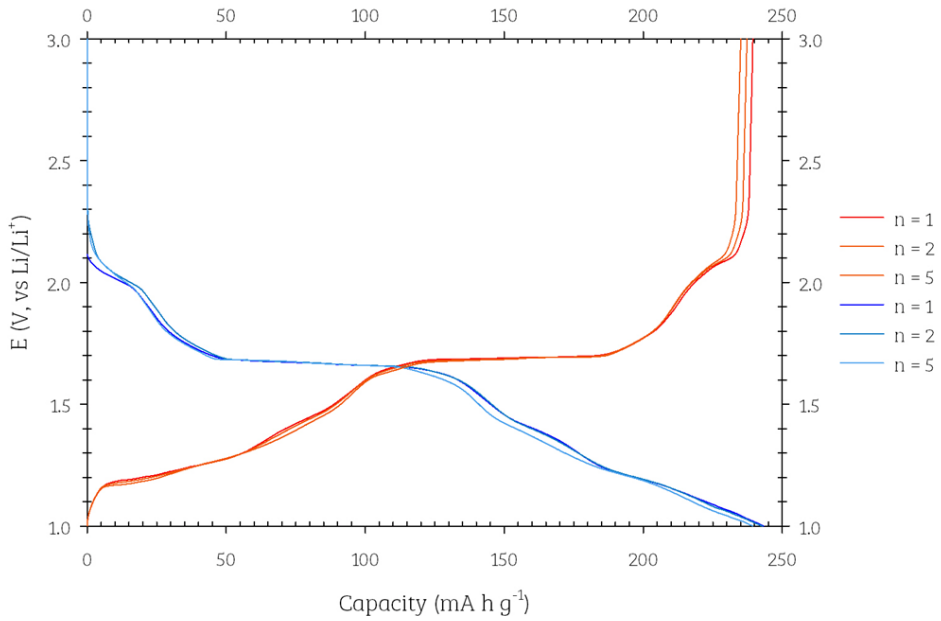

Figure 3. 6: Galvanostatic discharge-charge curves of H-Nb_2O_5 from 3.0 V to 1.0 V at a rate of 10 mA g^{-1}.

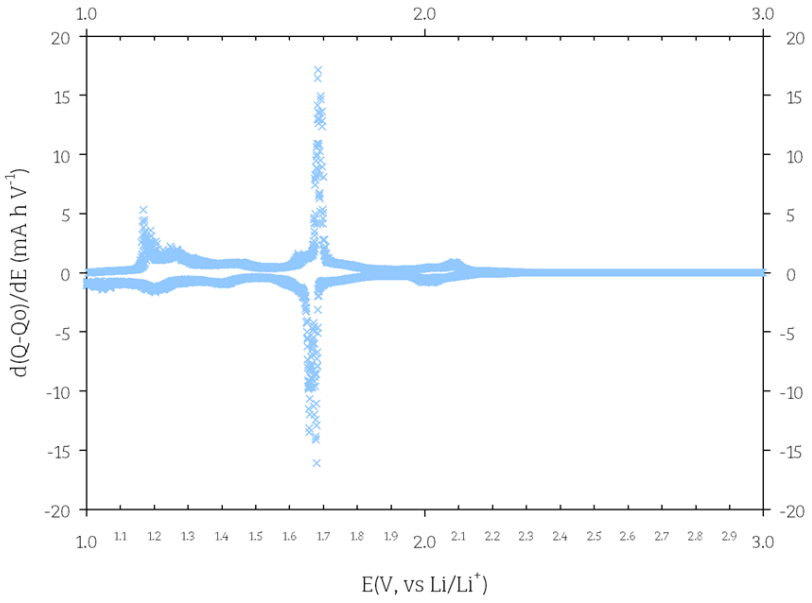

Figure 3. 7: Differential scanning calorimetry (DSC) plots derived from the galvanostatic discharge/charge profile of H-Nb_2O_5 at a rate corresponding to 10 mA g^{-1}.

3.3.1.3 Post-Mortem Cell Analysis

The cell was dismantled and the electrode analysed by X-ray diffraction: no visible changes in phase from the pristine material were observed **(Figure 3. 8)**. Through a Pawley fit, the unit cell parameters were deduced (**Table 3. 2**) and show a small decrease in cell volume for the dismantled electrode. This is probably related to residual Li in the H-Nb_2O_5 phase for the latter. In addition the SEM images of the dismantled electrode show the retention of the rod-like character (**Figure 3. 9**).

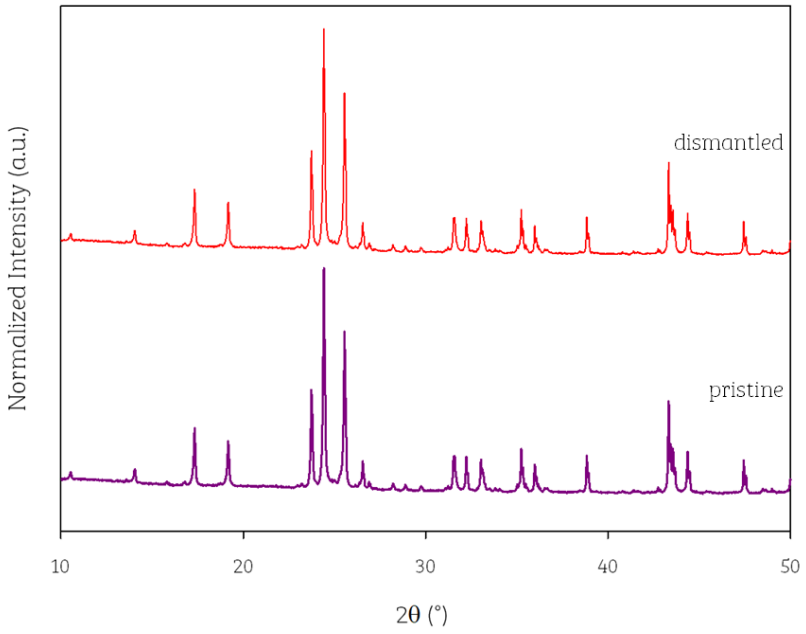

Figure 3. 8: Resulting XRD patterns comparing the H-Nb_2O_5 powder, labelled pristine, to the electrode film (coating including the Cu foil) from the dismantled cell (Cu Kα).

Table 3. 2: Unit cell parameters of H-Nb_2O_5 after cycling in a Li half cell.

Composition	a (Å)	b (Å)	c (Å)	β (°)	Cell Volume (Å^3)
Dismantled	21.160(2)	3.8122(2)	19.126(1)	118.124(7)	1360.7(2)
Pristine	21.166(7)	3.8229(9)	19.148(5)	118.03(1)	1367.7(7)

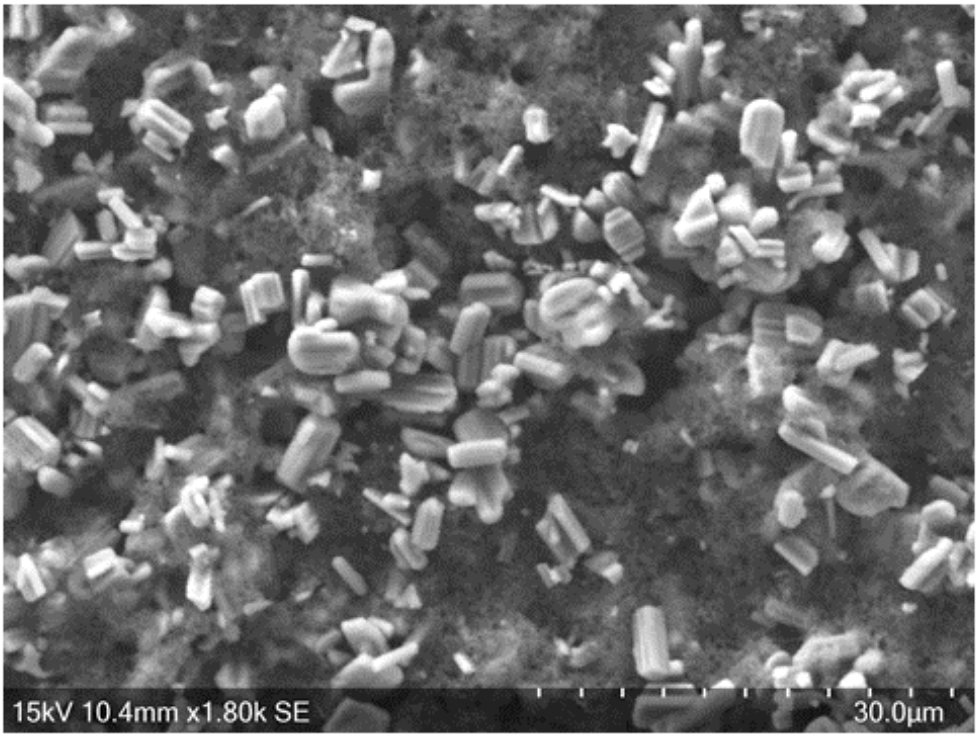

Figure 3. 9: SEM image of the dismantled cell – showing the H-Nb_2O_5 cell.

This initial study allows for a direct comparison in terms of the methodology used in fabricating cells, and to quantify the differences in the specific capacity of the doped niobates, which will be considered next.

3.3.2 $Nb_{22}CuO_{56}$: pristine and ex-solution studies

The novel system of $Nb_{22}CuO_{56}$ was originally identified by P. R. Slater (University of Birmingham, UK) through his detailed doping studies into Nb_2O_5. The material was passed onto E. H. Driscoll for investigations into its electrochemical performance. In addition to examination of the parent phase, heating of the phase in H_2 was performed to try to ex-solve Cu and so to form conducting particles on the surface to improve the overall electron conductivity.

3.3.2.1 Characterisation

3.3.2.1.1 Basic Phase Information

The system was first characterised with PXRD and the resulting patterns of this phase is presented **Figure 3. 10**, alongside H-Nb_2O_5 for comparison. For consideration towards improved conductivity, the equivalent ex-solution $Nb_{22}CuO_{56}$ (prepared via under H_2 treatment at 700°C to be denoted in text as X-$Nb_{22}CuO_{56}$) was also initially characterised through this method.

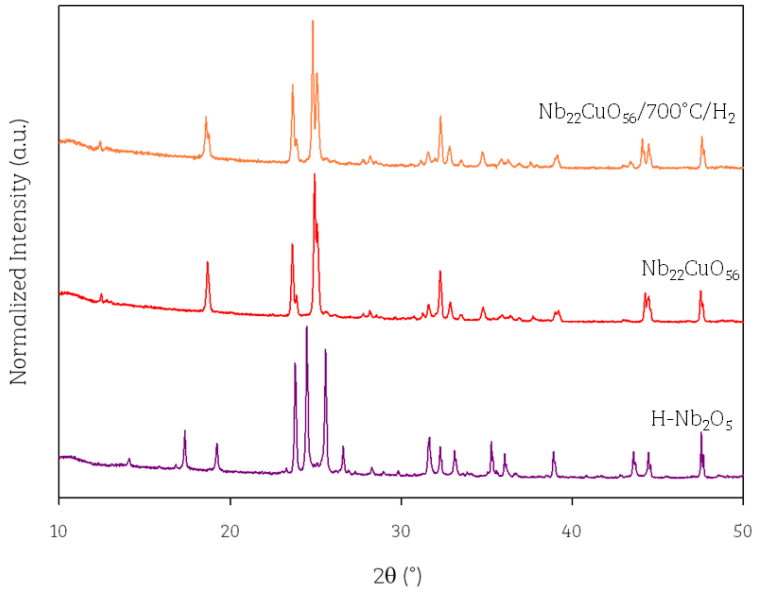

Figure 3. 10: Resulting XRD pattern of novel system $Nb_{22}CuO_{56}$ and ex-solved system, compared to H-Nb_2O_5.

Of current literature and related crystal systems in the ICSD database, the phase could not be matched – although using indexing the closest links were with a monoclinic system. With the support and expertise of Dr Tzu-Yu Chen, the samples were Pawley fitted as part of the TOPAS suite, for the pristine and X- $Nb_{22}CuO_{56}$, as shown **Figure 3. 11** and **Figure 3. 12**, respectively, using the space group C2 (monoclinic) and

the corresponding unit cell parameters deduced (**Table 3. 3**). This Pawley fit suggested that the material was phase pure.

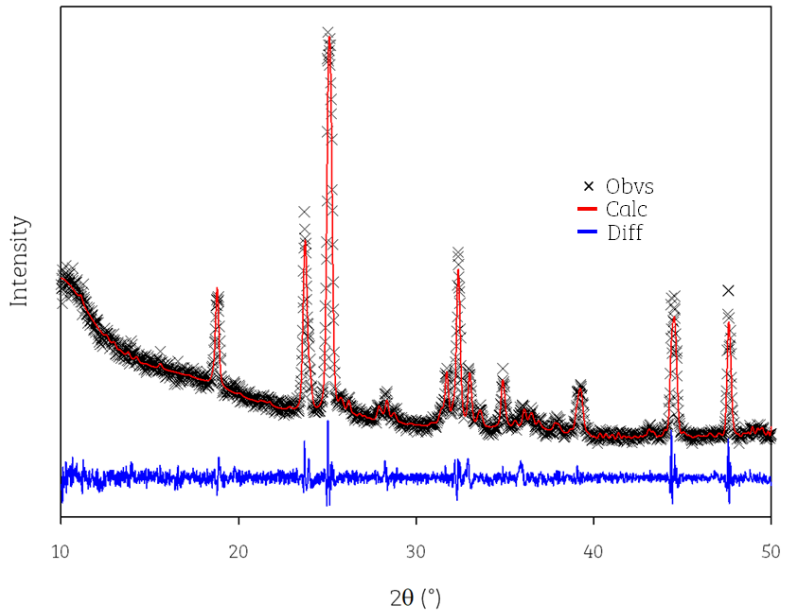

Figure 3. 11: Observed, calculated and difference XRD profiles for $Nb_{22}CuO_{56}$ (R_{wp} – 9.01%, R_p – 5.35%) (Cu Kα) through a Pawley fit on TOPAS, using C2 as the phase's space group.

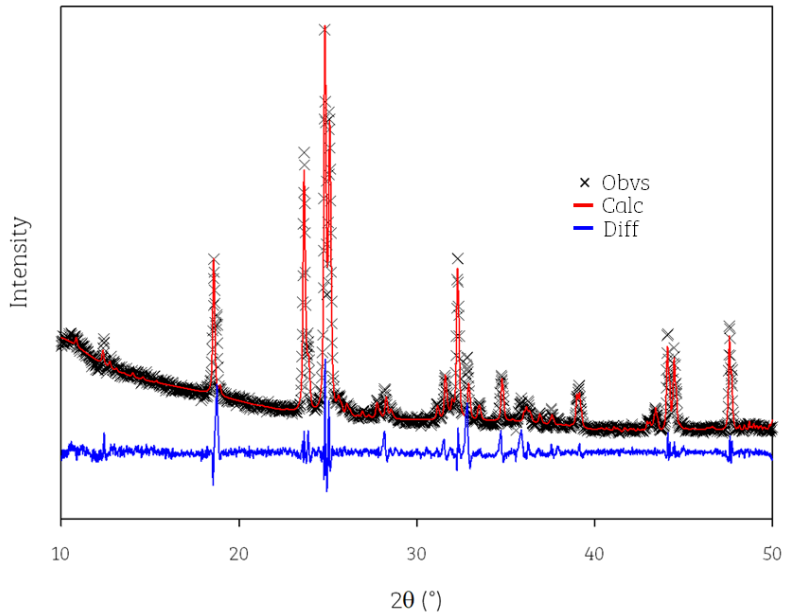

Figure 3. 12: Observed, calculated and difference XRD profiles for $Nb_{22}CuO_{56}/H_2$ (R_{wp} – 9.48%, R_p – 6.21%) (Cu Kα) through a Pawley fit on TOPAS, using C2 as the phase's space group.

Table 3. 3: Unit cell parameters of $Nb_{22}CuO_{56}$ and the H_2 treated sample, in comparison to the H-Nb_2O_5.

Composition	Crystal Symmetry	a (Å)	b (Å)	c (Å)	β (°)	Cell Volume (Å^3)
H-Nb_2O_5	Monoclinic P2	21.166(7)	3.8229(9)	19.148(5)	118.03(1)	1367.7(7)
$Nb_{22}CuO_{56}$	Monoclinic C2	29.93(1)	3.846(2)	21.14(1)	95.56(2)	2423(2)
$Nb_{22}CuO_{56}/H_2$	Monoclinic C2	29.640(5)	3.8194(5)	20.957(5)	95.447(7)	2361.7(7)

3.3.2.1.2 Structural Model

Developing upon the initial Pawley fits, a cif was identified and obtained by Dr Tzu-Yu Chen (via the equivalent Japanese Crystal Database) – $Na_{0.77}Nb_{1.88}Fe_{0.038}O_{4.808}$, a monoclinic cell (C2/m symmetry) with unit cell parameters of a, b, c, β and cell volume: 28.5622 Å, 3.8331 Å, 17.5383 Å, 125.096° and 1571.026 Å^3 respectively.

With this further information, Pawley fits were re-ran for $Nb_{22}CuO_{56}$ and X-$Nb_{22}CuO_{56}$ with symmetry of C2/m, and are shown in **Figure 3. 13** and **Figure 3. 14**, respectively. The deduced unit cell parameters are given in **Table 3. 4.**

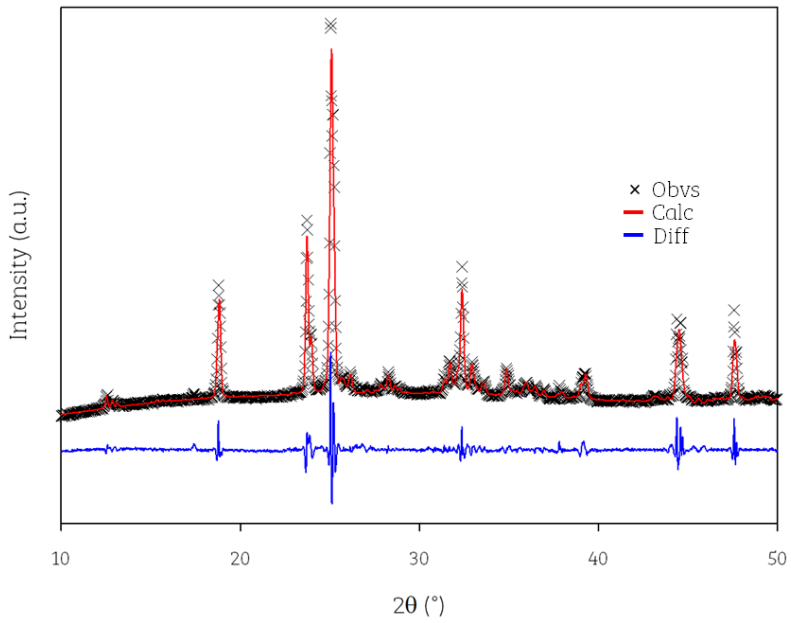

Figure 3. 13: Observed, calculated and difference XRD profiles for $Nb_{22}CuO_{56}$ (R_{wp} – 3.42 %, R_p – 2.04%) (Cu Kα) through a Pawley fit on TOPAS, using C2/m as the phase's space group.

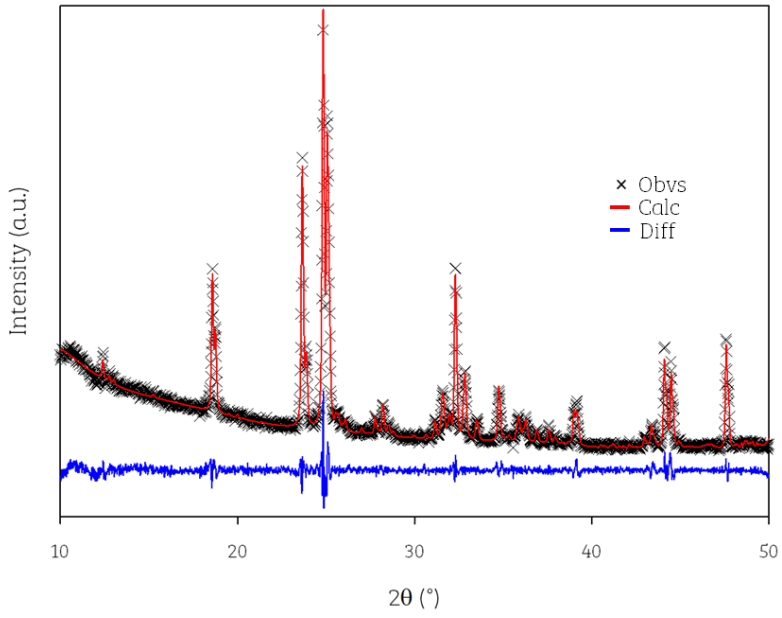

Figure 3. 14: Observed, calculated and difference XRD profiles for X-$Nb_{22}CuO_{56}$ (R_{wp} – 5.70 %, R_p – 4.36 %) (Cu Kα) through a Pawley fit on TOPAS, using C2/m as the phase's space group.

Table 3. 4: Unit cell parameters of $Nb_{22}CuO_{56}$ and the H_2 treated sample from running a Pawley fit with C2/m symmetry.

Composition	Crystal Symmetry	a (Å)	b (Å)	c (Å)	β (°)	Cell Volume (Å^3)
H-Nb_2O_5	Monoclinic P2	21.166(7)	3.8229(9)	19.148(5)	118.03(1)	1367.7(7)
$Nb_{22}CuO_{56}$	Monoclinic C2/m	28.612 (8)	3.8360 (8)	17.560 (5)	125.00 (2)	1578.8 (8)
X- $Nb_{22}CuO_{56}$	Monoclinic C2/m	28.545 (2)	3.8249 (3)	17.577 (1)	125.034 (6)	1571.3 (2)

Using the TOPAS software, the parameters deduced from the Pawley fit were used for the Rietveld refinement, albeit the background function was reset. The refinement considered the refinement of the x and z co-ordinates, before refining the occupancies (with min. and max. limits set at 0 and 1 respectively) along with the atomic displacement parameters. The temperature factors from the original .cif used were also refined. The resulting crystal structure is shown in **Figure 3. 15**. The corresponding fit and the resulting structural parameters are given in **Figure 3. 16** and **Table 3. 5** respectively. It is noticeable that there are still intensity mismatches, which suggests further complexities within the structure. In this respect it is quite challenging with these Nb oxide structures to deduce a good structural fit, given the complexity of these materials and the potential for intergrowth structures or other structural faults within. This future work requires more detailed studies including TEM studies to confirm the 4 x 4 block size of the structural model. Given the Nb2 site has the lowest occupancy, it is likely the Cu^{2+} ion has preference for this site.

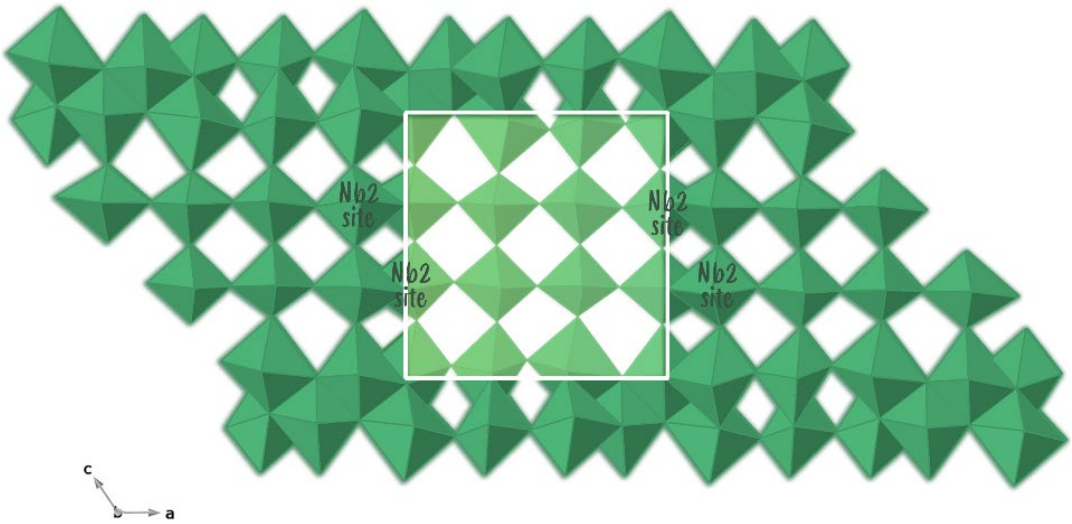

Figure 3. 15: Crystal structure of $Nb_{22}CuO_{56}$ – the (4 x 4) block is highlighted in a lighter green – with the Nb2 site labelled, in reference to Cu doping within the structure (due to reduced occupancy value from the refinement).

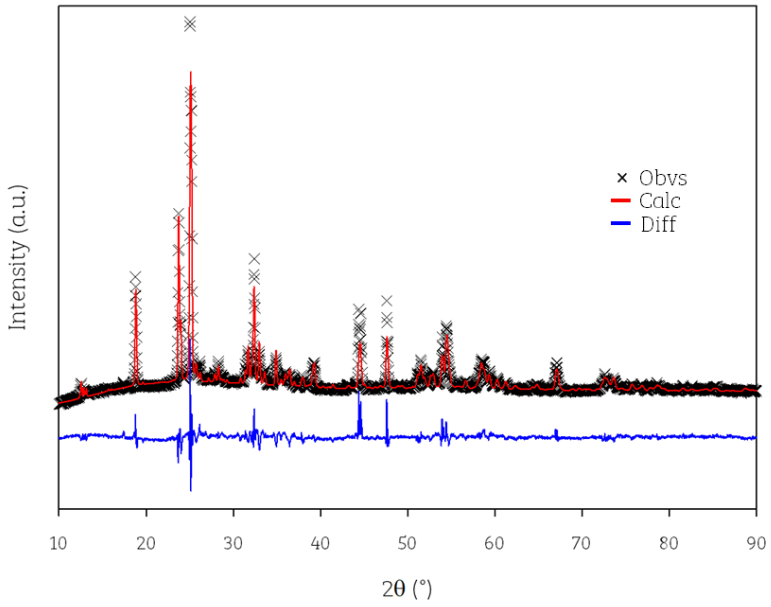

Figure 3. 16: Observed, calculated and difference XRD profiles for $Nb_{22}CuO_{56}$ (R_{wp} – 4.34 %, R_p – 2.9%) (Cu Kα) through a Rietveld refinement on TOPAS, using the model of Na-Nb-Fe-O.

Table 3. 5: Structural parameters and coordinates for $Nb_{22}CuO_{56}$. Cell parameters: a = 28.587 (1) Å, b = 3.8356 (1) Å, c = 17.5491 (1) Å, β = 125.145 (5) °. Cell volume = 1573.4 (2) Å^3. R_{wp} = 4.34% and R_p 2.9%

Atom Type	Multiplicity	Wyckoff Letter and Site Symmetry	x	y	Z	Occ
Nb1	4	i m	0.155 (1)	0	0.095 (2)	0.98 (5)
Nb2	4	i m	0.251 (2)	0	0.366 (3)	0.81 (6)
Nb3	4	i m	0.290 (2)	0	0.010 (2)	0.90 (6)
Nb4	4	i m	0.344 (1)	0	0.633 (2)	0.89 (5)
Nb5	4	i m	0.386 (2)	0	0.368 (3)	0.94 (9)
Nb6	4	i m	0.429 (1)	0	0.109 (2)	0.85 (5)
Nb7	4	i m	0.521 (1)	0	0.371 (3)	0.98 (9)
Nb8	4	i m	0.564 (1)	0	0.098 (2)	0.92 (4)
O1	4	i m	0.028 (5)	0	0.369 (9)	1.0 (2)
O2	4	i m	0.062 (9)	0	0.08 (1)	0.4 (1)
O3	4	i m	0.110 (6)	0	0.643 (9)	1.0 (2)
O4	4	i m	0.167 (9)	0	0.37 (1)	1.0 (2)
O5	4	i m	0.212 (6)	0	0.24 (1)	0.9 (3)
O6	4	i m	0.218 (6)	0	0.097 (9)	1.0 (3)
O7	4	i m	0.265 (6)	0	0.652 (8)	0.9 (2)
O8	4	i m	0.299 (5)	0	0.504 (9)	1.0 (2)
O9	4	i m	0.32 (1)	0	0.37 (2)	1.0 (3)
O10	4	i m	0.344 (8)	0	0.24 (1)	1.0 (3)
O11	4	i m	0.35 (2)	0	0.12 (3)	0.7 (4)
O12	4	i m	0.430 (7)	0	0.50 (1)	1.0 (2)
O13	4	i m	0.45 (1)	0	0.36 (1)	1.0 (2)
O14	4	i m	0.489 (3)	0	0.069 (6)	0.9 (2)
O15	4	i m	0.485 (8)	0	0.27 (1)	0.9 (3)
O16	4	i m	0.586 (9)	0	0.36 (1)	1.0 (3)
O17	4	i m	0.615 (6)	0	0.24 (1)	0.9 (2)
O18	4	i m	0.64 (2)	0	0.05 (3)	0.2 (2)
O19	4	i m	0.780 (5)	0	0.078 (8)	1.0 (2)
O20	4	i m	0.905 (6)	0	0.0872 (9)	1.0 (2)

3.3.2.1.3 Morphology

The $Nb_{22}CuO_{56}$ material was found to consist of rod-like particles (**Figure 3. 17**). However, the main focus of this preliminary work was to consider improvements of performance through the *ex*-solution of Cu from the structure – the confirmation of the *ex*-solution is shown by the formation of spherical particles now visible on the rods (**Figure 3. 18**), which from the EDS map correlates with Cu (**Figure 3. 19**). An intermediate heating step of 400°C/H_2 has also been included in this figure which also showed Cu *ex*-solution (a pristine sample was used in this trial and was not consequently heated further to higher temperatures).

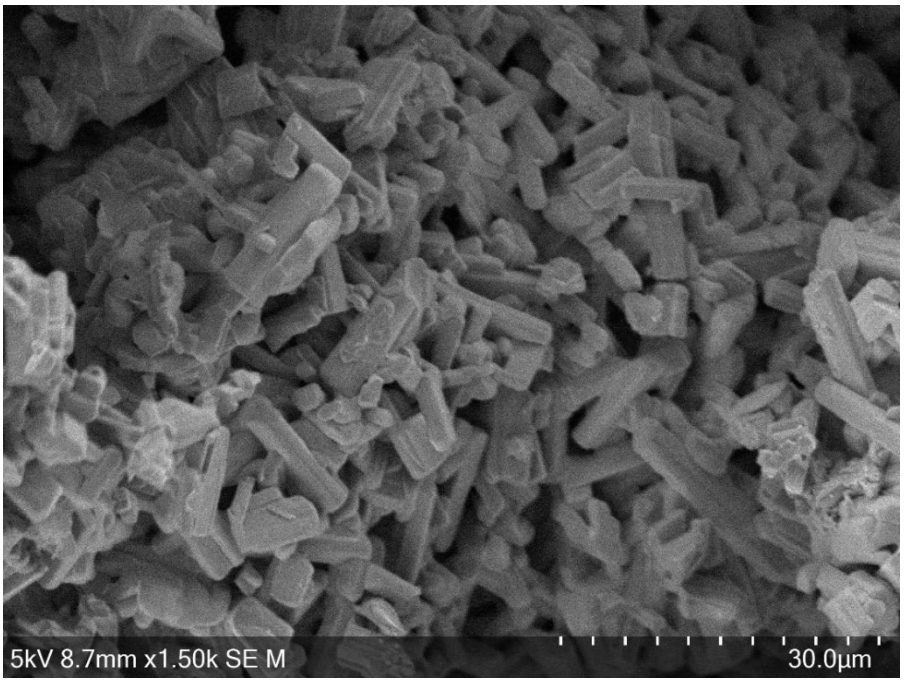

Figure 3. 17: SEM image of the as prepared $Nb_{22}CuO_{56}$.

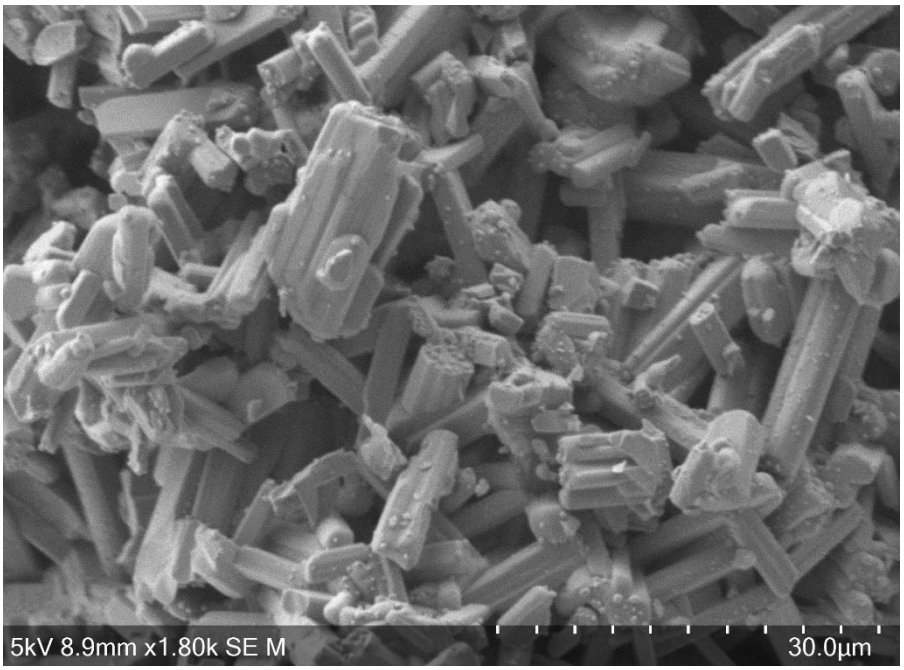

Figure 3. 18: SEM image of the as prepared $Nb_{22}CuO_{56}$ heated to 700°C under a H_2 atmosphere.

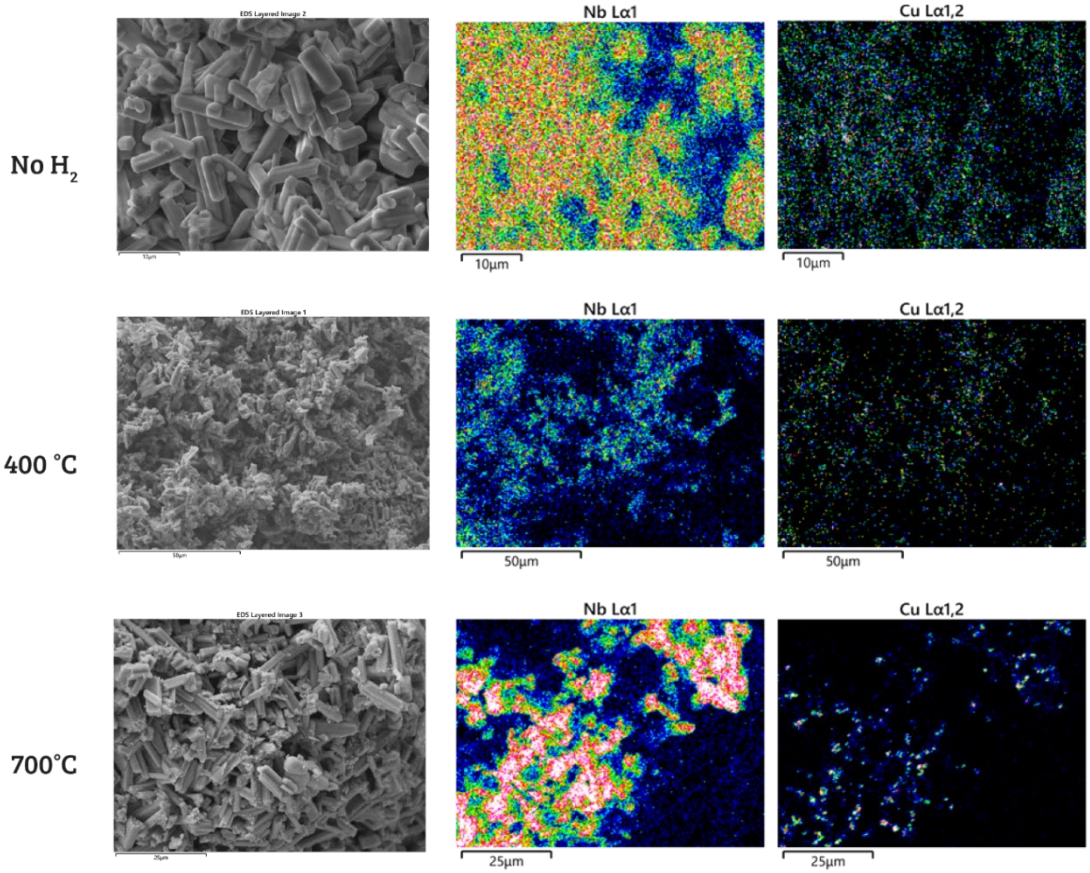

Figure 3. 19: SEM-EDS maps of the $Nb_{22}CuO_{56}$ top) pristine, middle) 400°C/H_2 and bottom) 700°C/H_2 of Nb and Cu.

3.3.2.2 Electrochemical Performance

The initial cell testing work made use of electrodes fabricated via **Coating Methods: Method 1**, and due to the preliminary nature of this study, the electrodes were uncalendered.

The initial testing for the X-$Nb_{22}CuO_{56}$ (H_2/700 °C) (RMM: 3003. 45 g mol^{-1}) followed the **2.2.5 Electrochemical Testing: Method 1** on **p70**. The cells were set to cycle at a C/20 rate which assumed all 22 Nb ions to be involved in the following redox couple Nb^{5+}/Nb^{4+} - this is equivalent to applying a current density of 9.83(2) mA g^{-1} for the initial formation steps. One of these cells is highlighted in **Figure 3. 20**. The selected voltage limits of 3.0 V and 0.8 V were initially selected based on prior reports on $Cu_2Nb_{34}O_{87}$.[1]

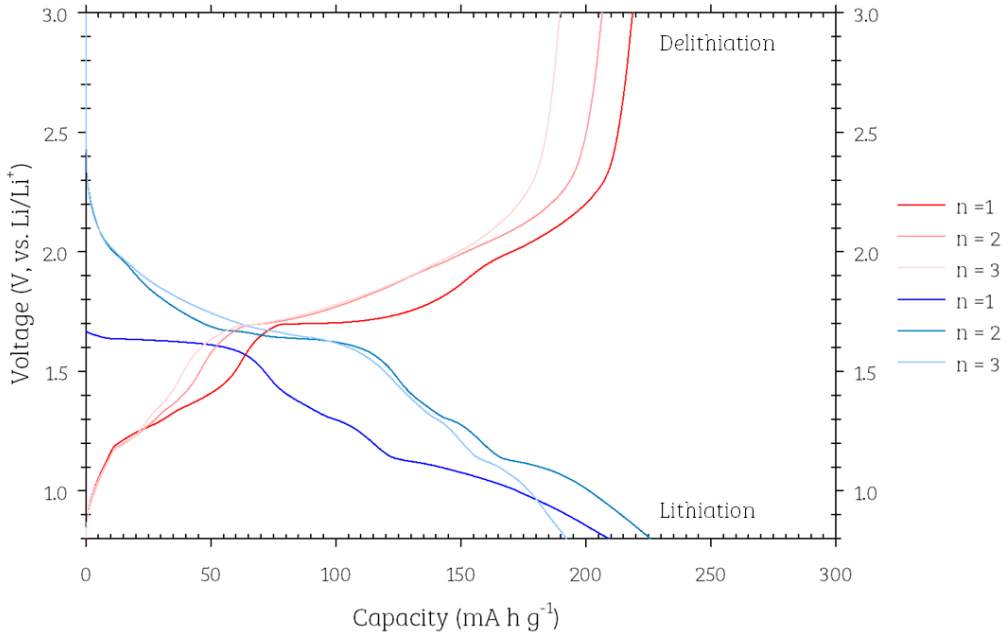

Figure 3. 20: Galvanostatic discharge-charge curves of X-$Nb_{22}CuO_{56}$ (H_2/700 °C) vs. Li metal.

The corresponding differential scanning calorimetry (DSC) plot is shown in **Figure 3. 21**, which allows for ease of identification to phase changes occurring during cycling. There appears to be multiple reversible curves however the most distinct are 1.66/1.72 V.

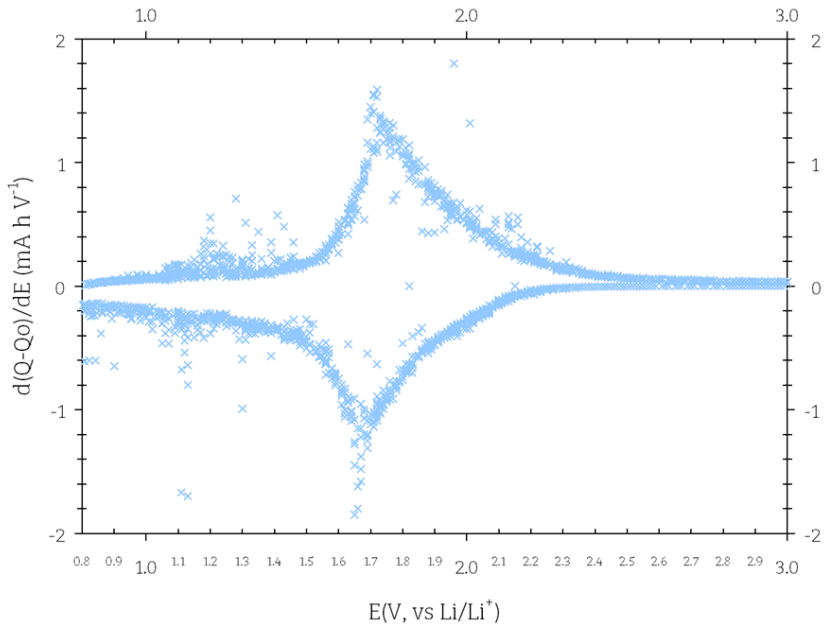

Figure 3. 21: Differential scanning calorimetry (DSC) plot derived from the galvanostatic discharge/charge profile of X-$Nb_{22}CuO_{56}$ (H_2/700 °C) vs. Li metal at a rate corresponding to 9.85 mA g^{-1}.

To consider the impact of the ex-solution of the Cu, the pristine material was also tested using the same coating and testing methodology however with the lower voltage limit adjusted from 0.8 V to 1.0 V (as lowering the voltage below 1.0 V can lead to some SEI formation). The resulting galvanostatic discharge-charge curves are plotted in **Figure 3. 22**, and shows an initial capacity to be greater than X-$Nb_{22}CuO_{56}$ (despite the higher lower-voltage cut off). In addition, the initial OCV on lithiation n=1 shown in **Figure 3. 20** (which is lower than the pristine $Nb_{22}CuO_{56}$, shown in **Figure 3. 22**) is likely the effect of the ex-solution step reducing the Nb^{5+} ions too, not only the Cu^{2+}.

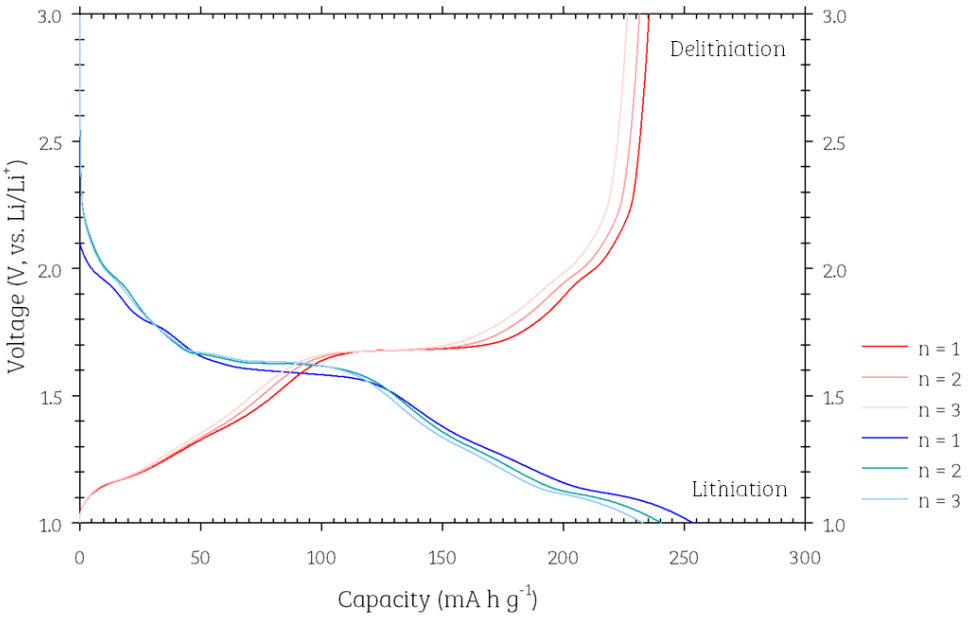

Figure 3. 22: Galvanostatic discharge-charge curves of $Nb_{22}CuO_{56}$ vs. Li metal, with a current density of 9.75 mA g^{-1} applied.

The associated DSC plot is shown in **Figure 3. 23** and it is quite evident the reversible peaks are more distinct in the pristine sample than the X-$Nb_{22}CuO_{56}$, with reversible peaks identified at 1.97 V, 1.67V, 1.63 V, 1.5 V, 1.30 V, 1.12 V – the trace itself exhibits similarities to the H-Nb_2O_5 DSC, although not a direct match, but this can be attributed to structural differences in block sizes.

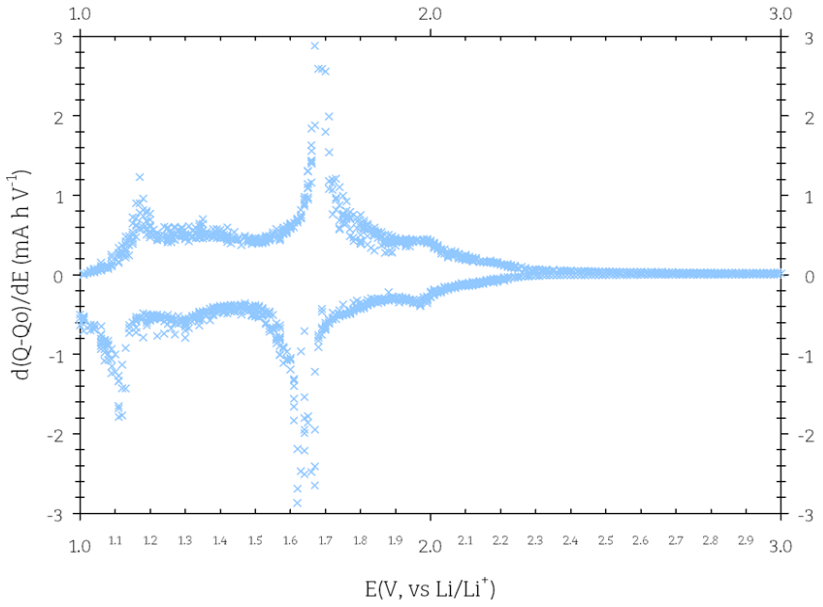

Figure 3. 23: Differential scanning calorimetry (DSC) plot derived from the galvanostatic discharge/charge profile of $Nb_{22}CuO_{56}$ vs. Li metal at a rate corresponding to 9.75 mA g^{-1}

To compare the effect of the ex-solution of the Cu from the material, the average values of the 2 cells of X-$Nb_{22}CuO_{56}$ were compared against the 3 cells of the $Nb_{22}CuO_{56}$ (**Figure 3. 24**). Towards the latter end of this project, the fabrication of 3 cells became the norm – to allow for repeats and to mitigate against cell failure events.

The X- $Nb_{22}CuO_{56}$ samples were cycled at ca. 10 mA g^{-1} for 20 cycles – the initial cycles show quite a variation in values, but beyond the 5th cycle the cells appear to become more stable given the reduced error of the 2 cells. The average initial capacity was found to be 233 (23) and 217 (2) mA h g^{-1} for lithiation and delithiation, respectively. Only the first three cycles of the pristine $Nb_{22}CuO_{56}$ have been plotted – cell failure seems to have occurred soon after, although it wasn't clear whether there is the fault of the testing equipment (which is likely probable given all cells failed in a similar time period). The pristine $Nb_{22}CuO_{56}$ shows a reduced range of the obtained capacities, in addition to

reaching a higher capacity – 240(33) and 207 (59) mA h g^{-1} for lithiation and delithiation, respectively. Thus it can be suggested the ex-solution of Cu is negatively impacting the performance of the material, such that introducing the reduction synthesis step may actually be reducing the Nb^{5+} in addition to the Cu^{2+}, and hence impacting the structure and electrochemical performance.

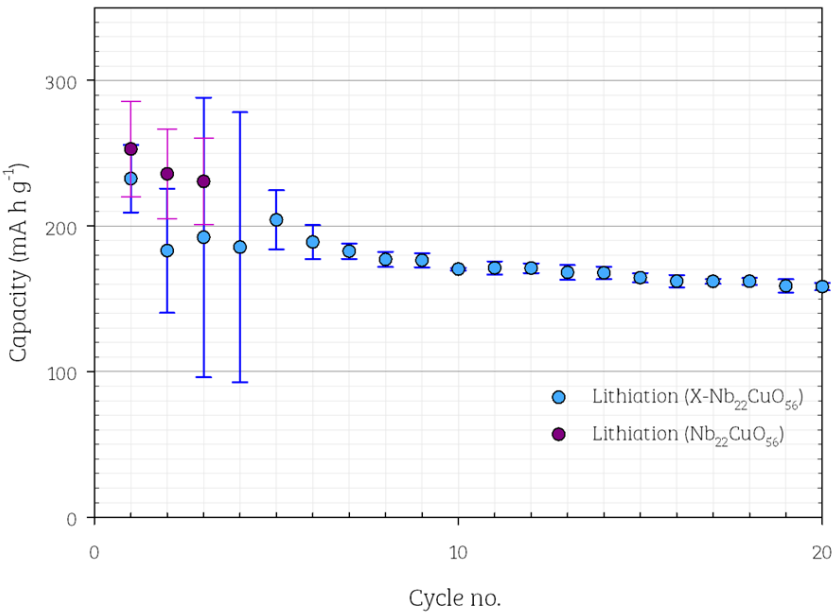

Figure 3. 24: Comparison of the average lithiation capacity of the $Nb_{22}CuO_{56}$ (purple) and X-$Nb_{22}CuO_{56}$ (blue) over a series of cycles at ca. 10 mA g^{-1}.

Given the variation in the DSC plots of the pristine and X- $Nb_{22}CuO_{56}$ samples, albeit more distinct reversible curves in the former, an investigation to further understand any phase changes was conducted corresponding to these curves – nominally examining whether there was any suggestion of metallic Cu forming during cycling as shown for the X- $Nb_{22}CuO_{56}$. The resulting SEM images are presented in the **Chapter 9: Appendix** on **p312,** but in short, no distinct evidence of metallic Cu on the surface is apparent.

3.3.3 Advanced Testing of $Nb_{22}CuO_{56}$

Given the reduction step having an unfavourable influence towards the electrochemical performance, focus was switched to the pristine $Nb_{22}CuO_{56}$ material. The following section will discuss the advanced testing applied to this material, with the use of 3.2.2 Coating Methods: Method 2 on p111. The reasoning behind the variation in coating methods is discussed in more detail in Chapter 4 with the study on $Nb_9Ti_{1.5}W_{1.5}O_{30}$ and given that these materials were considered at the same time, naturally more attention was given to the doped Ti and W system due to its improved performance.

3.3.3.1 Tap Density

Using Quantachrome Instrument AUTOTAP and applying a series of 500 taps to the sample, the sample's tap density was found to be 1.08 g cm^{-3}.

Based upon the thickness and mass of the electrode disc (excluding the current collector foil), the initial density of the electrode coating was determined to be 0.83 g cm^{-3}, and using the theoretical density (3.87 g cm^{-3}; see . within the appendix for the full determination) the initial porosity was found to be ca. 79% (as prepared coatings typically have a porosity of 70%). Reviewing the thickness data for these electrodes the porosity was only reduced to 75% (ideally porosity with calendaring should be to 30-40%). Thus, the following set of data can be viewed as a bench mark in considering the alternative coating method (2.2.1 Coating Formulations: Method 2 on p58), rather than viewing this as performance with calendering.

3.3.3.2 Formation Cycling

From previous DSC analysis (**Figure 3. 23**), no redox processes are observed above 2.5 V, with this in mind, the voltage limits were amended for the cells to cycle between 1 V and the new upper limit of 2.5 V. On formation cycling (10 mA g^{-1}), the lithiation and delithiation capacities, were found on average to be 239 ± 45 and 209 ± 18 mA h g^{-1}, respectively, as shown in **Table 3. 6**. Thus there is an initial first cycle loss of ca. 13% (based upon the averages).

Table 3. 6: Specific capacities of the four cells ($Nb_{22}CuO_{56}$ vs Li metal) with initial formation cycling at 10 mA g^{-1}.

Cell/ Electrode No.	Mass (mg)	Process	OCV (V)	Capacity (mA h g^{-1})		
				1	2	3
1	4.08	Lithiation	2.69	276	204	192
		Delithiation		209	197	189
2	3.92	Lithiation	1.99	265	220	208
		Delithiation		228	212	204
3	4.48	Lithiation	2.59	271	202	190
		Delithiation		208	194	186
4	3.92	Lithiation	2.62	346	256	233
		Delithiation		240	223	211

3.3.3.3 Long term – constant current cycling

Cells (electrode no.) 1 and 2, after formation cycling were set to cycle for 500 further times, as shown in **Figure 3. 25,** at a higher rate of 600 mA g^{-1} (full description of testing procedure *see* **2.2.5.1.4 Advanced Testing Procedures**). At this higher rate a lower capacity of ca. 109 mA h g^{-1} was observed. After 500 cycles, both cells had a capacity

retention (lithiation) 60.0 (3) %. Note - the initial cycle is marked as cycle 0, rather than 1. By the end of cycling, the capacity rention was ca. 60% and delivering a lithiation capacity between 64-66 mA g^{-1}.

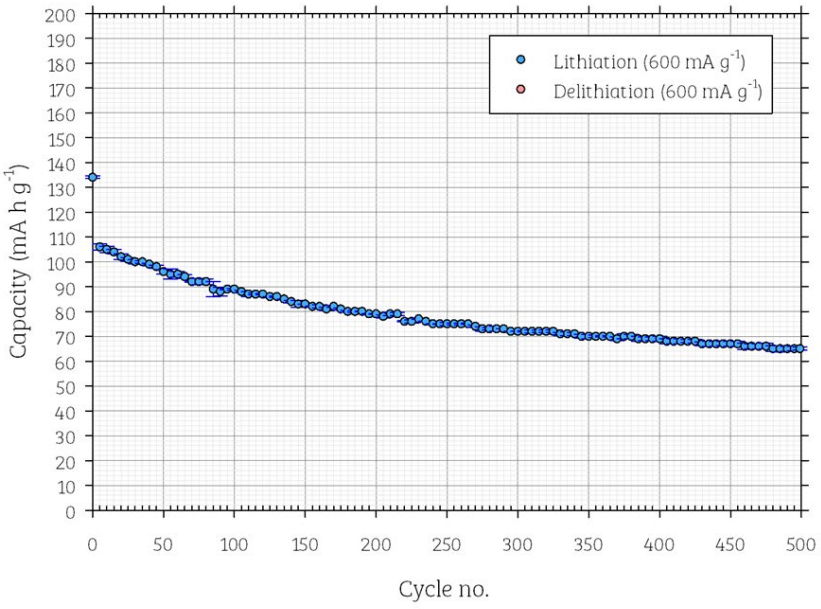

Figure 3. 25: The average specific capacities of $Nb_{22}CuO_{56}$ vs. Li metal, between limits of 2.5 V to 1 V, using electrodes 1 and 2, at a capacity of 600 mA g^{-1} over 500 cycles, with error bars included.

Table 3. 7: Resulting lithiation capacities of electrodes 1 and 2 ($Nb_{22}CuO_{56}$ vs Li metal; Figure 3. 25), which underwent continuous cycling at 600 mA g^{-1} for 500 cycles.

Electrode No.	Mass (mg)	Lithiation Capacity (mA h g^{-1})		Capacity
		1	500	Retention (%)
1	4.08	109.3	66.1	60.3
2	3.92	108.1	64.6	59.7

3.3.3.4 Asymmetric Cycling (Lithiation Rate Increasing)

The second test applied to half of the conditioned cells (no. 3 and 4) involved asymmetric cycling between the limits 1 V to 2.5 V, where the delithiation rate was kept constant at approximately 100 mA g^{-1}. The lithiation rate was gradually increased from: 20 mA g^{-1} up to 4 A g^{-1} with 5 cycles at each rate. This style of testing is supposed to mimic application conditions such that the lithiation (i.e. charging if in a full cell architecture) would cope with the consumers' demands of high charge rates. The resulting data are plotted in **Figure 3. 26** and tabulated in **Table 3. 8**. At the higher current densities (4 A g^{-1}) the material returned a low lithiation capacity of 30 (6) mA h g^{-1}, with a capacity retention of 30%. The material returned on a linear trajectory when the current density was reduced back to 20 mA g^{-1}.

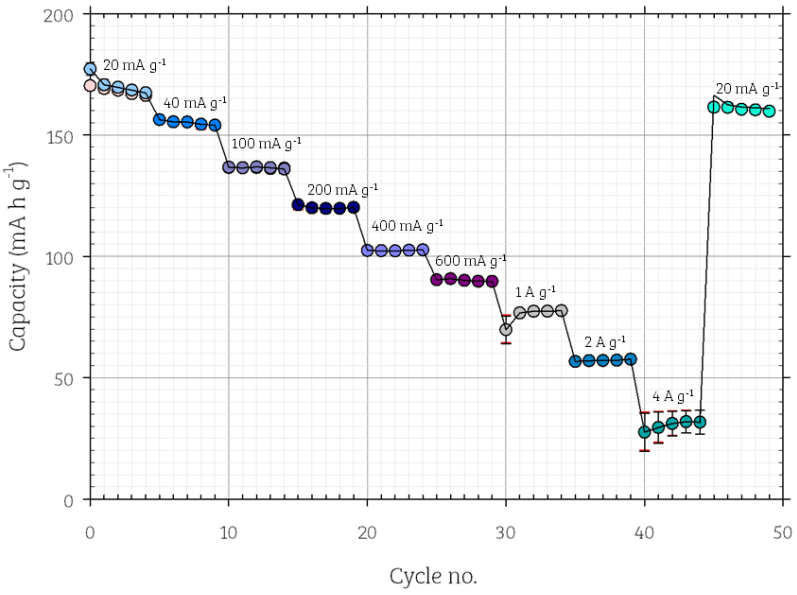

Figure 3. 26: Average specific capacities of electrodes 3 and 4 ($Nb_{22}CuO_{56}$ vs Li metal) at each charging step. Black error bars are for lithiation, red are for the delihiation.

Table 3. 8: Average specific capacities of the cell data plotted ($Nb_{22}CuO_{56}$ vs Li metal; Figure 3. 26) with the capacity retention determined from the average value at 20 mA g^{-1} for both lithiation and delithiation.

Lithiation Current Density (mA g^{-1})	Capacity (mA h g^{-1})		Capacity Retention (%)	
	Lithiation	Delithiation	Lithiation	Delithiation
20	171 (4)	168 (2)	100	100
40	155 (1)	155 (1)	91	92
100	137 (1)	136.4 (9)	80	81
200	120 (2)	120 (2)	70	71
400	102 (1)	102 (1)	60	61
600	90.1 (6)	90.1 (6)	53	54
1000	76 (4)	76 (4)	44	45
2000	57.1 (6)	57.2 (6)	33	34
4000	30 (6)	31 (6)	18	18
20	162 (3)	161 (2)	95	96

3.4 Conclusions

Given the differences in the numerous literature reports of Nb_2O_5 polymorphs and their respective electrochemical performance, the developed coating and testing methodology within this thesis was used to benchmark H-Nb_2O_5, to allow for ease of comparison of the novel doped materials, both within this chapter and the next. Applying a current density of 10 mA g^{-1}, returned an initial specific capacity for lithiation and delithiation of 243.2 and 239.4 mA h g^{-1}, respectively. The average voltage was found to be 1.528(8) and 1.60(2) V (across the first 3 formation cycles, for lithiation and delithiation respectively). The reversible redox peaks identified agreed with previous literature reports. Considering the initial capacity values, it would appear the Nb^{5+}/Nb^{4+} is taking place in full, while there are additional Nb^{4+}/Nb^{3+} redox processes occurring too – but not in full (this is given by the theoretical capacity for one redox process alone delivering ca. 200 mA h g^{-1}).

To our current knowledge, $Nb_{22}CuO_{56}$ is only the second niobium copper oxide to have been assessed for high power Li-ion anode applications. The material itself was originally indexed with C2 symmetry, before the discovery of a suitable cell ($Na_{0.77}Nb_{1.88}Fe_{0.038}O_{4.808}$) with C2/m symmetry which allowed for a full Rietveld refinement. This allowed fitting of the data albeit with some intensity mismatched and so further studies (e.g. TEM) are required to validate the structure.

In order to try to improve the conductivity of the overall material, $Nb_{22}CuO_{56}$ was heated under H_2 to produce metallic Cu nanoparticles – denoted X-$Nb_{22}CuO_{56}$ within this work – and was confirmed by the SEM. Nevertheless the preliminary studies showed the pristine $Nb_{22}CuO_{56}$ to have a higher average capacity than the X-$Nb_{22}CuO_{56}$, and thus

work on the ex-solved sample was ceased. Conducting advanced testing on the pristine material, using coating method 2, led to improved performance (239 ± 45 and 209 ± 18 mA h g^{-1} for lithiation and delithiation respectively, while cycling at 10 mA g^{-1}) – similar to the benchmark values for the H-Nb_2O_5. Unfortunately, during advanced testing, the material delivered less than satisfactory performance at the higher current densities, but was able to return on its linear trajectory at the lower ratings. Nevertheless the electrode porosity was high, which may be hindering performance at high rates (due to inadequate particle contact and hence conductivity). So further work is warranted to try to improve the performance.

3.5 Future Work

While advances have been made in developing coating and testing methodology, as well as deducing a possible structural model for this material, further work is still required. TEM studies and the collection of higher quality data will be necessary to confirm the structure.

While the electrochemistry was preliminary, further optimisation is still required with the coatings – such that ensuring the electrodes are calendered to lower porosities, which would improve the conduction pathways of the materials. While the advanced testing considered the change in lithiation current densities, it would be paramount to consider it for the delithiation step too, while keeping lithiation rates constant, as performed for the $Nb_9Ti_{1.5}W_{1.5}O_{30}$ (**Chapter 4**, *see* **p177**).

3.6 References

1 L. Yang, X. Zhu, X. Li, X. Zhao, K. Pei, W. You, X. Li, Y. Chen, C. Lin and R. Che, *Adv. Energy Mater.*, 2019, **9**, 1902174.

2 X. Zhu, G. Liang, Q. Fu, R. Li, Y. Chen, Y. Bi, D. Pan, R. Das, C. Lin and Z. Guo, *Chem. Commun.*, 2020, **56**, 7321–7324.

3 X. Cai, H. Yan, Z. Yang, J. Zhang, H. Yu, L. Zhang and J. Shu, *Ceram. Int.*, 2021, **47**, 24511–24518.

4 K. J. Griffith, A. C. Forse, J. M. Griffin and C. P. Grey, *J. Am. Chem. Soc.*, 2016, **138**, 8888–8899.

5 K. K. and S. Tamura, *Acta Crystallogr.*, 1975, **B31**, 673–677.

6 B. M. Gatehouse and A. D. Wadsley, *Acta Crystallogr.*, 1964, **17**, 1545–1554.

Chapter 4: Synthesis, characterization and application of novel Nb-based anode materials: Ti and W doping

In this chapter, a novel titanium and tungsten doped niobium oxide system has been investigated for its potential use as a Li-ion battery anode in high power applications. Within this body of work, the effects on the electrochemical performance of variation in the coating procedures and particle morphology have been considered, with the ultimate investigation of full cell performance evaluation of the anode against an established layered metal oxide cathode material. The baseline presented by H-Nb_2O_5 using methods discussed in the thesis are covered in the previous results chapter.

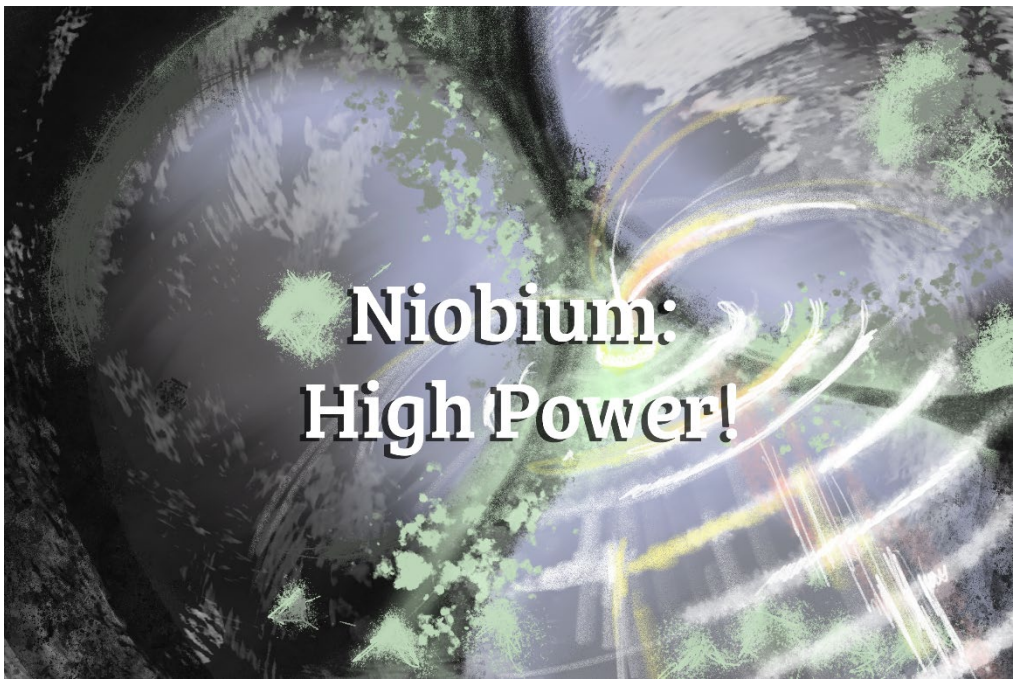

Figure 4. 1: Chapter abstract representing one aspect of this whereby phase transformations occurred with high speed ball milling.

4.1 Background: Context and Aims

In the continued pursuit of Li-ion anodes capable of delivering high charging and discharging rates, while maintaining high capacities, and without compromising safety, has resulted in developments replacing graphite with $Li_4Ti_5O_{12}$ (LTO) and thereafter, Nb-based systems such as $TiNb_2O_7$ (TNO). The latter offer greater capacities than LTO, leading to increased interest in finding new Nb-O based materials suited for high power applications.

While Griffith *et al.* has found exemplary performance with $Nb_{16}W_5O_{55}$ and $Nb_{18}W_{16}O_{93}$ Wadsley-Roth systems[1], this results chapter will consider a novel material, initially discovered by P. R. Slater (University of Birmingham, UK) through his research towards novel Nb systems doped with Ti-Mo/W. This chapter and subsequent chapter (Chapter 5) will focus on the detailed characterisation of a Ti-W-Nb-O system, where the formula was suggested to be $Nb_9Ti_{1.5}W_{1.5}O_{30}$ – and is the same crystal phase as the $Nb_{22}CuO_{56}$ previously discussed.

Therefore the aim of this aspect of the project can be simplified to the following: the characterisation of the material, followed by the development of coating methodologies and electrochemical performance strategies to initially offer a benchmark before considering opportunities to optimise. The development of the methods will allow for a baseline protocol to be followed in subsequent work.

4.2 Experimental

4.2.1 Synthesis of Active Material

4.2.1.1 Anode Active Material

The niobium titanium tungsten oxide materials were prepared through weighing stoichiometric amounts of Nb_2O_5, TiO_2 (anatase) and WO_3, which were then ground together using an agate pestle and mortar. The mixture was then heated up to 850°C/12hrs/5°C min^{-1} within an alumina crucible, and after intermittent grinding at room temperature, was re-heated up to 1100°C/12hrs/5°C min^{-1}.

The sample purity and structure determination were evaluated using powder X-ray diffraction. Structure refinements were carried out using the TOPAS suite of programs to determine unit cell parameters through a Pawley fit.

4.2.1.2 Cathode Active Material

To test the anode material in a full cell architecture, the cathode material NMC 532 was used in conjunction. The NMC 532 was prepared in house through the following method: The amounts were based on synthesizing 4 g of $Ni_{0.5}Mn_{0.3}Co_{0.2}(OH)_2$ (NMC 532$(OH)_2$); appropriate equimolar amounts of $NiSO_4.6H_2O$, $MnSO_4.H_2O$ and $CoSO_4.7H_2O$ were dissolved in 50 mL of water. After 1-2 hours of mixing at 75°C, NaOH was added to increase the pH of the solution to 11 and to precipitate out the NMC 532$(OH)_2$. The resulting mixture was stirred for a further hour before filtration in a Buchner funnel with washing with ca. 50 mL water. The resultant (wet) brown mass on the filter paper was left to dry overnight in a drying oven pre-set at 60°C for 48 hours. The collected dry black hydroxide phase was ground and a stoichiometric amount of $LiOH.H_2O$ was added

to the mixture. The sample was then fired under O_2 to 800°C/12hrs/5°C min^{-1}. The sample purity and structure determination were evaluated using powder X-ray diffraction.

Other NMC materials could have been selected for the initial full cell proof of concept. While there are moves towards higher Ni content cathodes (beyond NMC 811 up to NMC955), this material was selected due to being commercially known, in addition to increased stability in comparison to NMC 811.

4.2.2 Coating Methods

Within the coating methodology, the components: active mass (AM), carbon black (CB) and binder (B) are abbreviated. The AM represents $Nb_9Ti_{1.5}W_{1.5}O_{30}$, while the CB within this section makes use of a SuperP carbon black and B: PVDF.

4.2.2.1 Method 1

The electrode ink coating was prepared with an AM:CB:B mass ratio of 80:10:10 using a Thinky Mixer (model ARE-250). The initial step involved mechanochemical mixing of the AM and CB together for a total time of 30 mins at 350 rpm, using a Fritsch planetary ball mill.

The binder - polyvinylidene difluoride (PVDF) - was mixed with N-methyl pyrrolidone (NMP) initially for 5 mins/1300 rpm, before additions of the Super P carbon black and the active material with subsequent additions of NMP to produce a slurry (10 mins/1300 rpm for each step). To degas the mixture, a final mix of 3 mins/1800 rpm was performed. The resulting slurry was cast onto copper foil using a draw-down coater, where the bar

height was set to 200 µm. The resulting coating was dried for up to 2 hours at 80°C before being transferred for overnight drying in a vacuum oven pre-set at 110°C.

4.2.2.2 Method 2

The electrode ink coating was prepared with an AM:CB:B ratio of 80:10:10 using a Thinky Mixer. The binder - polyvinylidene difluoride (PVDF) - was mixed with N-methyl pyrrolidone (NMP) initially for 5 mins/1300 rpm, before additions of the SuperP carbon black and the active material with subsequent additions of NMP to produce a slurry (10 mins/1300 rpm for each step). To degas the mixture, a final mix of 3 mins/1800 rpm was performed. The resulting slurry was cast onto copper foil using a draw-down coater, where the bar height was set to 200 µm. The resulting coating was dried for up to 2 hours at 80°C before being transferred for overnight drying in a vacuum oven pre-set at 110°C.

The main difference between these methods relates to when the CB is added to the mixture. In method 1, CB is combined with the AM before coating in a ball mill step, while method 2, the CB addition has its own step – the sequence of the additions of the solids is shown in Figure 4. 2.

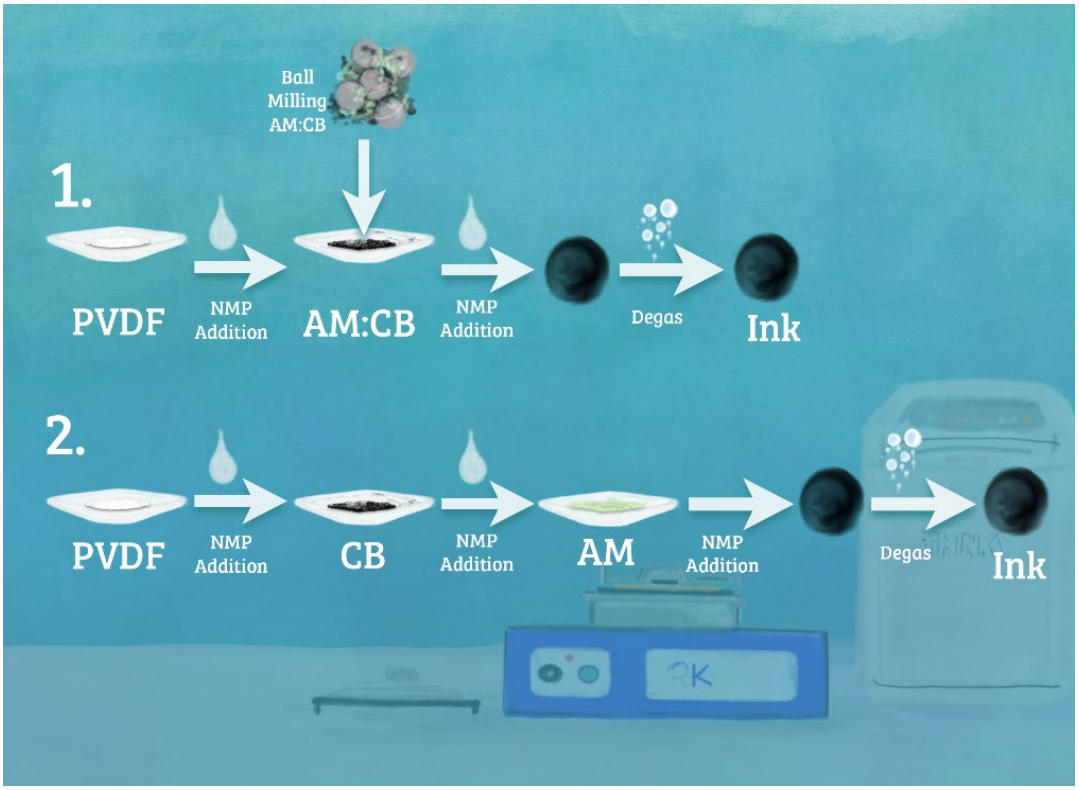

Figure 4. 2: Representation of the coating process described with methods 1 and 2 with the order of solid additions.

Unless explicitly stated, it should be assumed the electrodes are uncalendered.

4.2.3 Electrochemical Testing

As standard, the electrochemical properties were measured using a BioLogic BCS805 battery tester in galvanostatic mode between 3.0 V and 1.0 V, unless explicitly stated in later testing studies within this chapter. The testing procedures are outlined in 2.2.5 Electrochemical Testing.

4.3 Results and Discussion

4.3.1 $Nb_9Ti_{1.5}W_{1.5}O_{30}$

Based upon previous research by P. R. Slater (University of Birmingham, UK) a Nb-Ti-Mo-O system was identified through co-doping (Ti and Mo) in place of Nb. Further doping studies considered the use of W in place of Mo, to retain overall charge balance. Through variation of composition, the phase pure material was suggested to be $Nb_9Ti_{1.5}W_{1.5}O_{30}$. The inclusion of Ti in place of W is a cost effective strategy, if electrochemical performance remains consistent with the established W-Nb-O materials.

4.3.1.1 Characterisation

The system was first characterised with PXRD and the resulting pattern of this system is presented **Figure 4. 3**, alongside H-Nb_2O_5 for comparison. The $Nb_9Ti_{1.5}W_{1.5}O_{30}$ system is present as the same phase as the Cu-doped system formerly mentioned, and using TOPAS a Pawley fit was ran using C2/m symmetry. The fit shows the material to be phase pure (**Figure 4. 4**) and the corresponding unit cell parameters are shown in **Table 4. 1**.

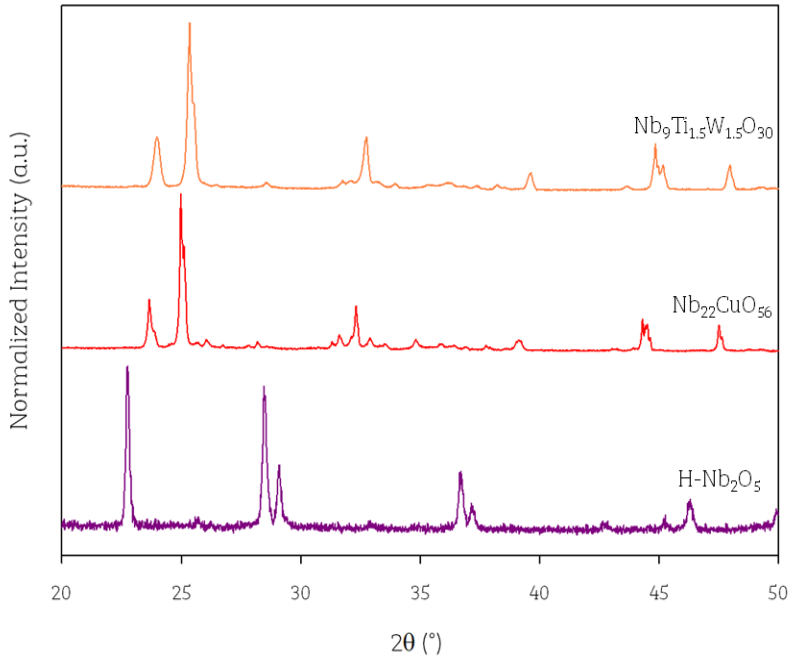

Figure 4. 3: Resulting XRD pattern of novel system $Nb_9Ti_{1.5}W_{1.5}O_{30}$ compared to H-Nb_2O_5 and $Nb_{22}CuO_{56}$ (material explored in Chapter 3).

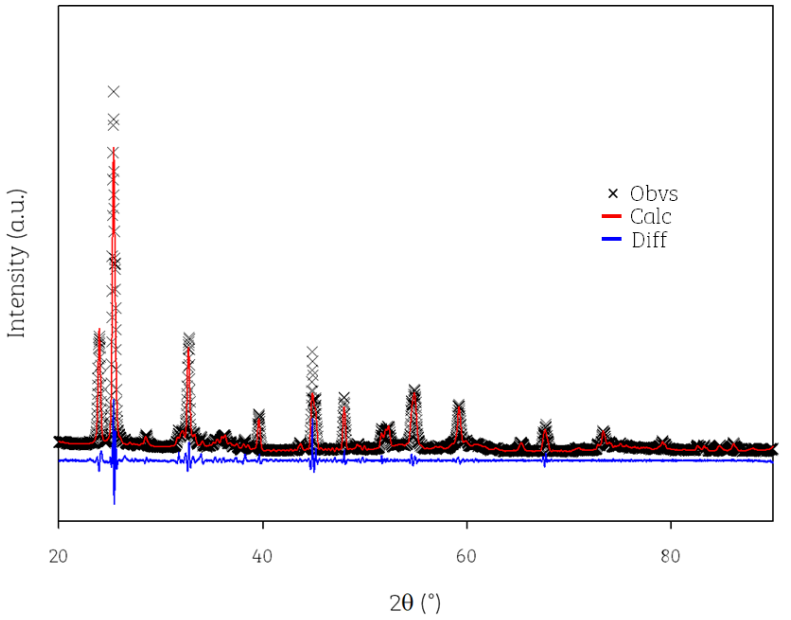

Figure 4. 4: Observed, calculated and difference XRD profiles for $Nb_9Ti_{1.5}W_{1.5}O_{30}$ (R_{wp} – 7.87 %, R_p – 5.67%) (Cu Kα) – using C2/m symmetry.

Table 4. 1: Unit cell parameters of $Nb_9Ti_{1.5}W_{1.5}O_{30}$ compared to H-Nb_2O_5.

Composition	Crystal Symmetry	a (Å)	b (Å)	c (Å)	β (°)	Cell Volume (Å^3)
H-Nb_2O_5	Monoclinic P2	21.166 (7)	3.8229 (9)	19.148(5)	118.03(1)	1367.7(7)
$Nb_9Ti_{1.5}W_{1.5}O_{30}$	Monoclinic C2/m	28.43 (1)	3.814 (2)	17.265 (6)	125.23 (1)	1530 (1)

To determine the full atomic arrangement of this system, future work will involve the use of TEM[2] and single crystal measurements. Full structural determination of these materials, from PXRD, is quite challenging given the structures of these phases, incidents of preferred orientation and the potential of intergrowths within the structure. At this current stage, the confirmation of the phase purity and unit cell parameters is satisfactory to quantify the materials success as a novel anode. Further optimisation and understanding of the intercalation mechanism will require this greater level of detail, and in respect modelling studies would be of interest once the full structure has been elucidated.

SEM images of the material were also taken and the rod-like character shown previously for the Nb-O phases is observed too for the Nb-Ti-W-O system (**Figure 4. 5**). Using ImageJ software to estimate particle size, particles were found to be ca. 9.032 $\pm$ 2.363 μm and 1.782 $\pm$ 0.743 μm, for the long and short sides, respectively, although it should be noted that there is evidently a variation in sizes.

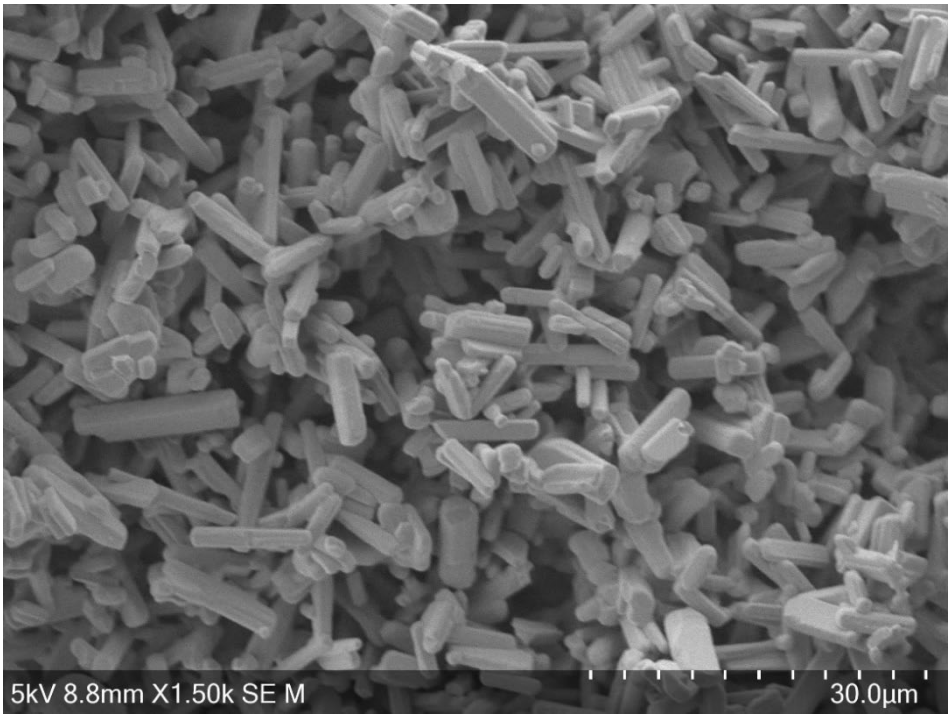

Figure 4. 5: SEM image of pristine $Nb_9Ti_{1.5}W_{1.5}O_{30}$.

4.3.1.2 Electrochemical Performance

The cells were initially set to cycle at a rate of C/20 (**2.2.5 Electrochemical Testing: Method 1**), based on $Nb_9Ti_{1.5}W_{1.5}O_{30}$ (RMM: 1663.7356 g mol^{-1}) having a theoretical capacity of 144.96 mA h g^{-1} with the Nb^{5+}/Nb^{4+} redox only considered initially. The experimental capacity on the initial charging step was instead found to be 233.22 mA h g^{-1}, reflecting an equivalent amount of 14.48 lithium ions (/electrons) inserted into this material upon lithiation supporting involvement of Ti and W also in the redox processes (**Figure 4. 6**). As stated before (and with hindsight), this method should only be used if the amount of lithium intercalation is known, such that applying a current of 0.036 mA, where the electrode's active mass is 5.04 mg would return an applied capacity of 7.24 mA g^{-1}; and thus a greater observed higher specific capacity and a longer duration of (de)lithiation for one cycle (ca. 65 hours in total instead of the expected 40 hours). The

average voltage for the first 3 formation cycles were found to be 1.529(6) V for lithiation and 1.592(2) V for delithiation – similar in value to the H-Nb_2O_5 material.

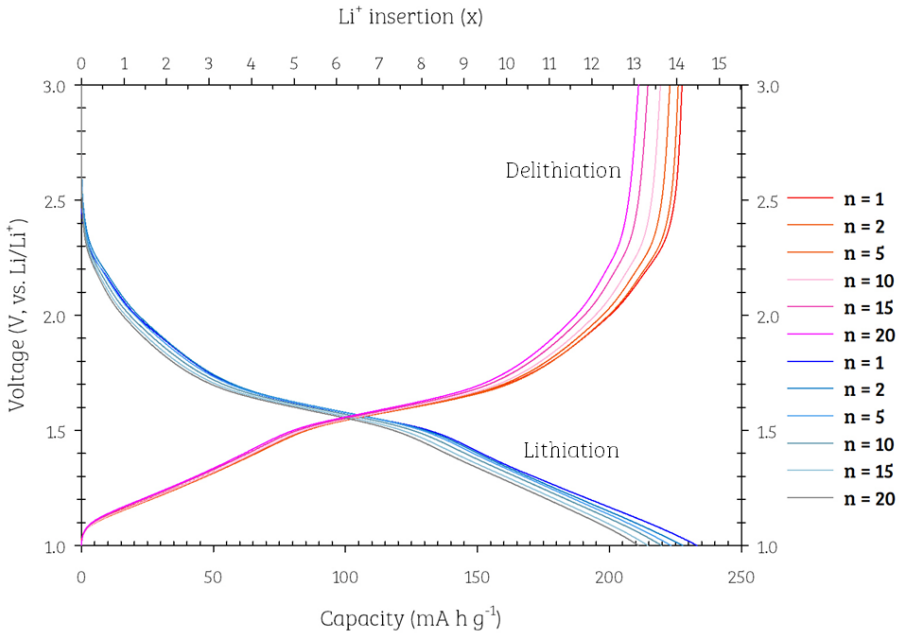

Figure 4. 6: Galvanostatic discharge-charge curves of $Nb_9Ti_{1.5}W_{1.5}O_{30}$ vs. Li metal.

After cycling the cell for a total of 20 cycles, the cell was further investigated with a series of varying charging rates to see how well the cell's capacity would be retained at these steps (**Figure 4. 7**).

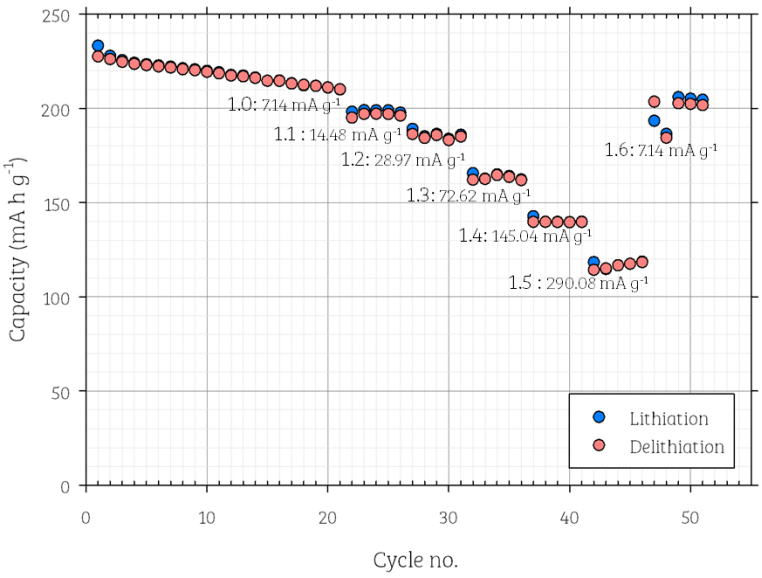

*Figure 4. 7: Capacity value vs cycle no. for $Nb_9Ti_{1.5}W_{1.5}O_{30}$ vs. Li metal in a half cell architecture for (de)lithiation. Tabulated values are presented in the **Appendix 9.2** on **p316**.*

The current applied was determined with the following C-ratings (C/10, C/5, C/2, 1C, 2C and C/20) based upon (**2.2.5 Electrochemical Testing: Method 1**), but have been back corrected using **2.2.5 Electrochemical Testing: Method 2**– values for both methods are shown in **Table 4. 2**. The actual time for lithiation for each has also been included too. As shown by the table, using method 1 when the amount of lithium insertion is unknown will result in incorrect current determination and thus the wrong C-ratings. The equivalent C-ratings through method 2 of determining the mA g^{-1} closely resembles the actual time it took to lithiate – although there is greater variation at the higher applied currents. It is best practice to quote mA g^{-1} at varying charging rates to be able to compare data easily, rather than relying on assumption of the theoretical capacity.

From this initial study, the material shows good potential with a capacity of ca. 118 mA h g^{-1} (290 mA g^{-1}; < 30 mins lithiation time) and of the small cycles ran at each

charging variation, the capacity loss is low (when considering the second cycle to the last cycle). In addition, returning to the slower rate, the returned capacity in Step 1.6: 7.14 mA g^{-1} appears to be following a linear decrease from the initial 20 cycles in Step 1.0: 7.14 mA g^{-1}, thus cycling at the higher rates has not damaged the cell. Thus, this is promising for an unoptimized material.

Table 4. 2: The variation in C-ratings from using Electrochemical Testing: Methods 1 and 2, compared to the actual C-rate determined by the lithiation process for the first 3 cycles of each step.

Step	1.0	1.1	1.2	1.3	1.4	1.5	1.6
Initial Assumed C-rating (Method 1)	C/20	C/10	C/5	C/2	1 C	2 C	C/20
Lithiation Time	32.0 hrs	13.7 hrs	6.4 hrs	2.3 hrs	58.2 mins	24.1 mins	27.2 hrs
Actual C-rate	C/32	C/13.7	C/6.4	C/2.3	1C	2.4C	C/27.2
Applied mA g^{-1}	7.14	14.48	28.97	72.62	145.04	290.08	7.14
Equivalent C-rate (assuming capacity of 233 mA h g^{-1})	C/33	C/16	C/8	C/3	C/1.6	1.24C	C/33
Expected Lithiation Time	32.7 hrs	16.1 hrs	8 hrs	3.2 hrs	1 hr 36 mins	48 mins	32.7 hrs

Reversible curves from DSC are present at: 2.21, 1.95, 1.58, 1.34 and 1.12 V (**Figure 4. 8**).

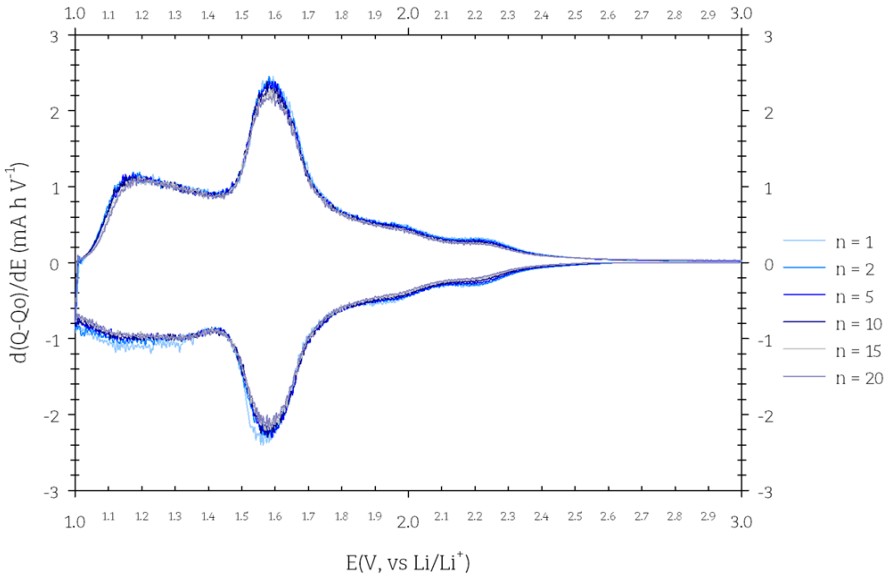

Figure 4. 8: Differential scanning calorimetry (DSC) plot derived from the galvanostatic discharge/charge profile of $Nb_9Ti_{1.5}W_{1.5}O_{30}$ at a rate corresponding to 7.14 mA g^{-1}.

4.3.2 Optimising Processing Route

In an attempt to optimise the coating of the material, altering the material additions was considered. Where previously the AM and CB were ball-milled together before coating, instead this route considered sequential additions of each component (**Coating Methods: Method 2**). Further fabrication route processing and optimisation is described in **Chapter 5**. As before, the prepared coatings were assembled into a Li half-coin cell and tested. The galvanostatic discharge-charge curves of this have been plotted in **Figure 4. 9**. The initial lithiation cycle has a specific capacity of 213.41 mA h g^{-1} – lower than the other lithiation cycles and the previous cell (**Figure 4. 6**). From reviewing the data, initial lithiation (for n = 1) of this cell took 22 hours compared to 25 hours on the next cycle (n = 2). The starting OCV on the initial cycle for this cell was 1.92 V, where the initial study (**Figure 4. 6**) the OCV was 2.46 V.

The lower starting OCV voltage would consequently result in a reduced lithiation time when lithiating to 1 V and hence the specific capacity would be less. Omitting cycle 1 from consideration, the obtained capacity values of the second cycle to the twentieth have been compared of this cell to three cells ran on the same testing procedure (i.e. current applied determined by **2.2.5 Electrochemical Testing: Method 1**). When focusing on the second cycle, a specific capacity of 242.72 mA h g^{-1} is returned – greater than all 3 former cells at 230(3) mA h g^{-1}. The capacity retention at formation is also found to be greater with method 2 at 95.4 % than 92.1(1)%.

While both sets of cells, with varying coating procedure, made use of the same testing methodology to determine the current to apply (i.e. method 1), the determined capacity mA g^{-1} is greater for method 2 cells (9.63 mA g^{-1}) than 7.41 mA g^{-1} for method 1 cells. With a slightly greater capacity, the lithiation time would be shorter, however yet the specific capacity returned is still greater in coating method 2 cells. Thus, coating method 2, was deemed to be the best method and will be used throughout the rest of this chapter.

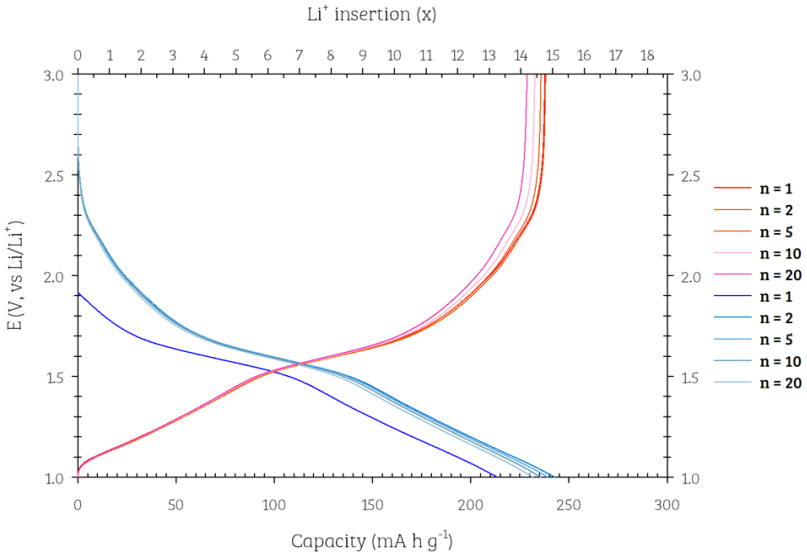

Figure 4. 9: Galvanostatic discharge-charge curves of $Nb_9Ti_{1.5}W_{1.5}O_{30}$ vs. Li metal, where the Nb material has been prepared through coating method 2, at a rate of 9.63 mA g^{-1}.

Table 4. 3: Specific capacities obtained from $Nb_9Ti_{1.5}W_{1.5}O_{30}$ vs. Li metal cells through varying the coating method procedure.

Coating Method	Cell no.	Applied Current (mA)	AM (mg)	mA g^{-1}	Capacity on lithiation step (mA h g^{-1})			Capacity Retention (%) n = 2→20
					1	2	20	
1	1	0.034	4.72	7.20	236.99	230.16	211.84	92.0
	2	0.036	5.04	7.14	233.22	227.81	209.99	92.2
	3	0.037	5.12	7.22	235.76	232.90	214.51	92.1
2	1[†]	0.047	4.88	9.63	213.41	242.72	231.55	95.4

[†] Only one cell was fabricated and fully cycled to the same procedure previously. The lack of lab access (COVID-19) and available channels at this time of work, with the multitude of chemistries to trial has limited the initial attempts of reproducibility. However this coating method and the resulting capacities are consistent with the specific capacities which have been obtained and shown later in this chapter.

4.3.3 Optimising Particle Size

4.3.3.1 $Nb_9Ti_{1.5}W_{1.5}O_{30}$ – 700 rpm

The next factor in optimising performance considered particle size – the aim was to reduce particle size to improve particle coating distribution, as well as reduce lithium diffusion pathways (to enhance high rate performance). The first trial involved ball milling the powder at 700 rpm for 2 hours. The resulting powder was examined by SEM, as shown in **Figure 4. 10** and compared to the as prepared powder. There is a stark contrast in morphology, where the rod-like character is replaced with larger agglomerates and covered haphazardly with smaller "fluffy" fractions. With this change in morphology, a surprising change in phase was also observed in the resulting PXRD patterns (**Figure 4. 11**), where the powder now exists in an orthorhombic symmetry resembling T-Nb_2O_5. Notably, there are no TiO_2 or WO_3 impurities, thus it is assumed both doped metals remain within the T-phase. Broadening of the peaks is intuitive of particle size becoming smaller – which is demonstrated by the "fluffy" fractions observed in the SEM.

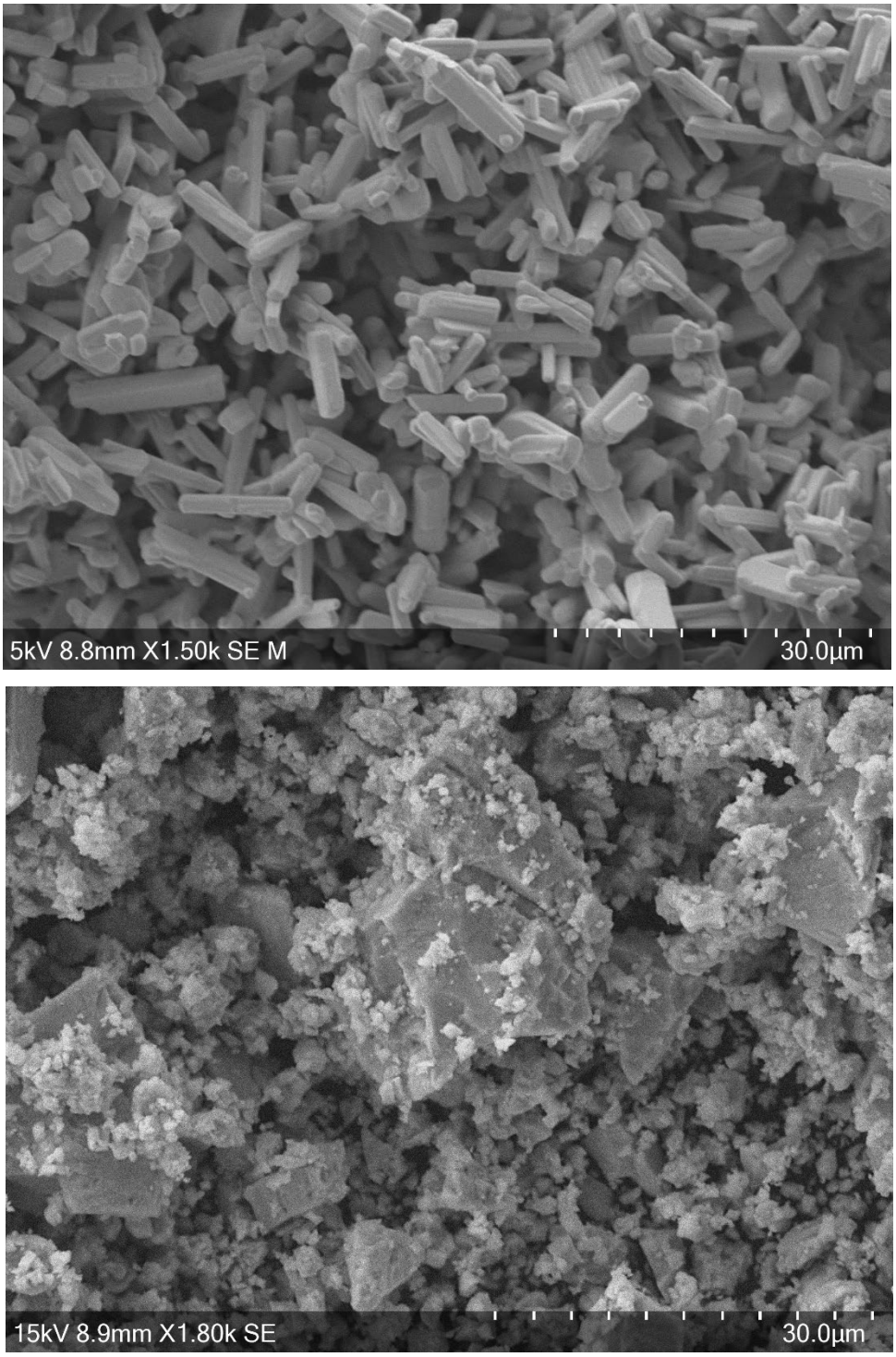

Figure 4. 10: SEM images of the as prepared $Nb_9Ti_{1.5}W_{1.5}O_{30}$ (top) and the powder after ball milling for 2 hrs at 700 rpm (bottom).

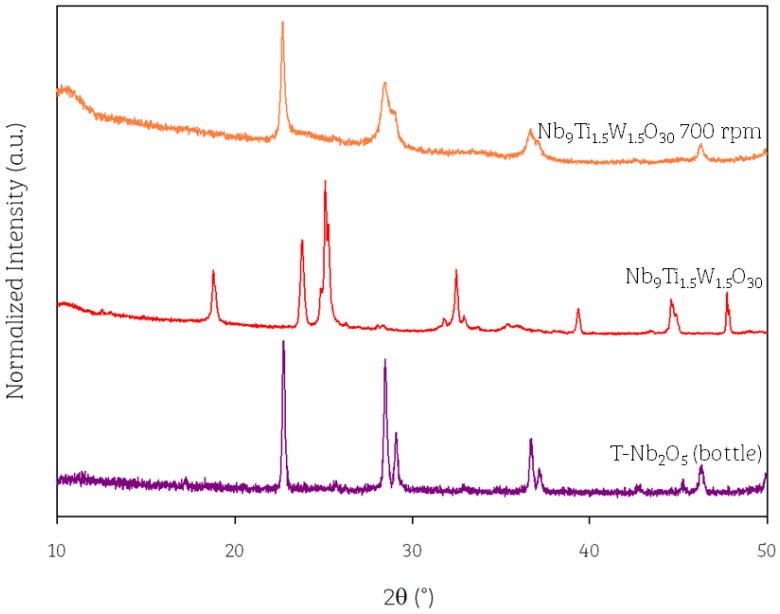

Figure 4. 11: XRD patterns from bottom to top of: T-Nb_2O_5 (orthorhombic phase; from bottle), $Nb_9Ti_{1.5}W_{1.5}O_{30}$ as prepared and the sample after ball milling at 700 rpm 2hrs (Cu Ka).

4.3.3.2 $Nb_9Ti_{1.}5W1_{.5}O_{30}$ – 350 rpm

Another portion of the as prepared $Nb_9Ti_{1.5}W_{1.5}O_{30}$ was ball milled at a lower rpm to attempt to maintain the original phase. Ball milling for 15 mins at 350 rpm, resulted in the morphology to change to "fluffy" more spherical particles (**Figure 4. 12**). This time the sample did not undergo a phase change (**Figure 4. 13**). When considering the peak intensities, it would seem this additional ball mill step has reduced the level of preferred orientation, and hence the peak at 23.8° **2θ** shows a reduction in the intensity.

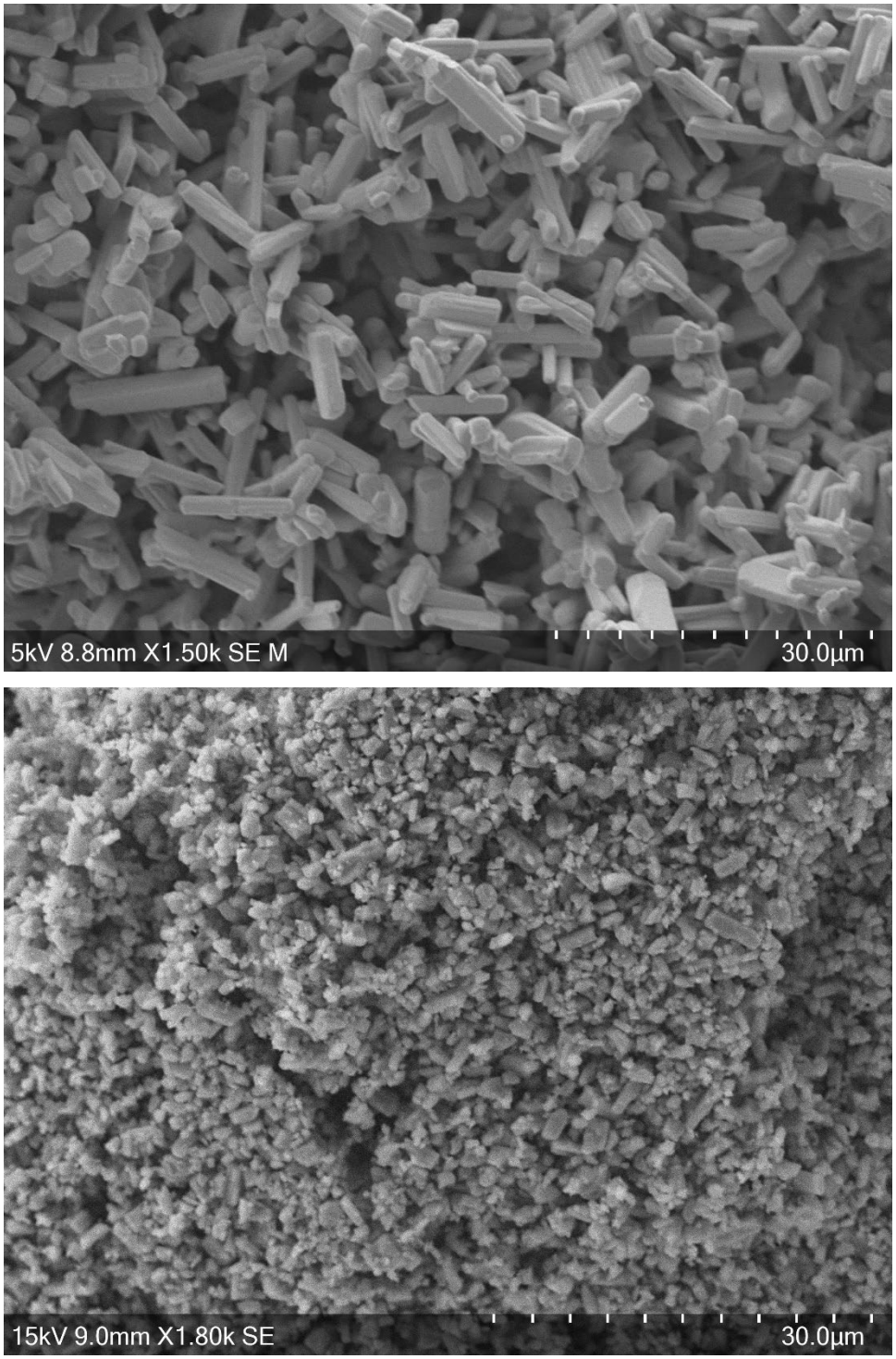

Figure 4. 12: SEM images of the as prepared $Nb_9Ti_{1.5}W_{1.5}O_{30}$ (top) and the powder after ball milling for 15 mins at 350 rpm (bottom).

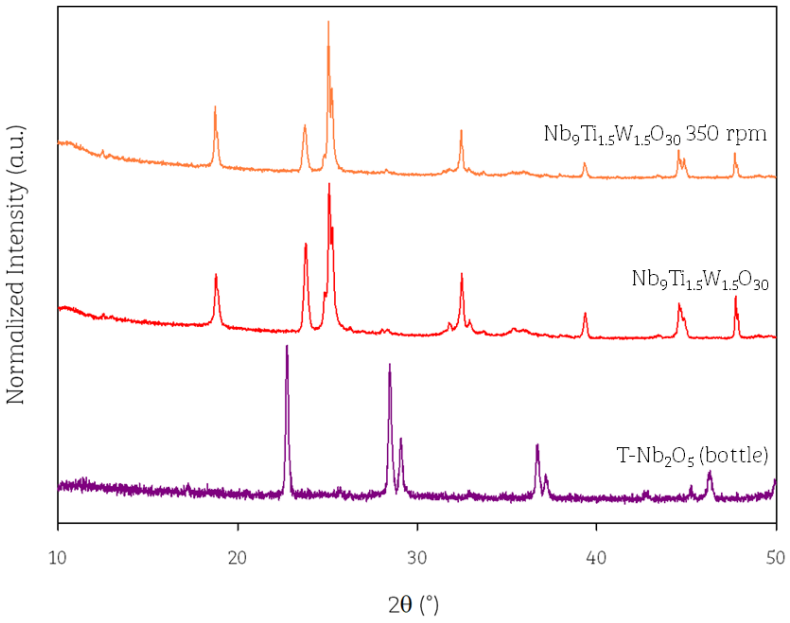

Figure 4. 13: XRD patterns from bottom to top of: T-Nb_2O_5 (orthorhombic phase; from bottle), $Nb_9Ti_{1.5}W_{1.5}O_{30}$ as prepared and the sample after ball milling at 350 rpm 15 mins (Cu Ka).

The unit cell parameters for the pristine and ball milled samples have been determined and compared to T-Nb_2O_5 in (**Table 4. 4**). The 350 rpm $Nb_9Ti_{1.5}W_{1.5}O_{30}$ sample appears to have a larger unit cell than the pristine equivalent, the difference may be attributed to reduction in preferred orientation allowing for a better fit (as shown in **Figure 4. 14**). The cell volume for the 700 rpm milled phase is within error of the T-Nb_2O_5 unit cell albeit the errors are large due to the broad nature of the peaks. Taking the empirical formula of $Nb_9Ti_{1.5}W_{1.5}O_{30}$ to give $Nb_{1.5}Ti_{0.25}W_{0.25}O_5$ and considering the ionic radii of the ions (**Table 4. 5**) it would be expected the unit cell volume to reduce to account for the substitution of Nb^{5+} with smaller ions.

Table 4. 4: Unit cell parameters of the resulting $Nb_9Ti_{1.5}W_{1.5}O_{30}$ phase after ball milling.

Composition	Crystal Symmetry	a (Å)	b (Å)	c (Å)	β (°)	Cell Volume (Å^3)
T-Nb_2O_5	Orthorhombic P b m a	6.220(2)	29.254(7)	3.948(2)	90	718.3(5)
$Nb_9Ti_{1.5}W_{1.5}O_{30}$	Monoclinic C2/m	28.43 (1)	3.814 (2)	17.265 (6)	125.23 (1)	1530 (1)
$Nb_9Ti_{1.5}W_{1.5}O_{30}$ 350 rpm	Monoclinic C2/m	28.546 (6)	3.829 (1)	17.519 (4)	125.04 (1)	1567.8 (7)
$Nb_9Ti_{1.5}W_{1.5}O_{30}$ 700 rpm	Orthorhombic P b m a	6.233 (3)	29.5 (1)	3.93 (2)	90	722 (6)

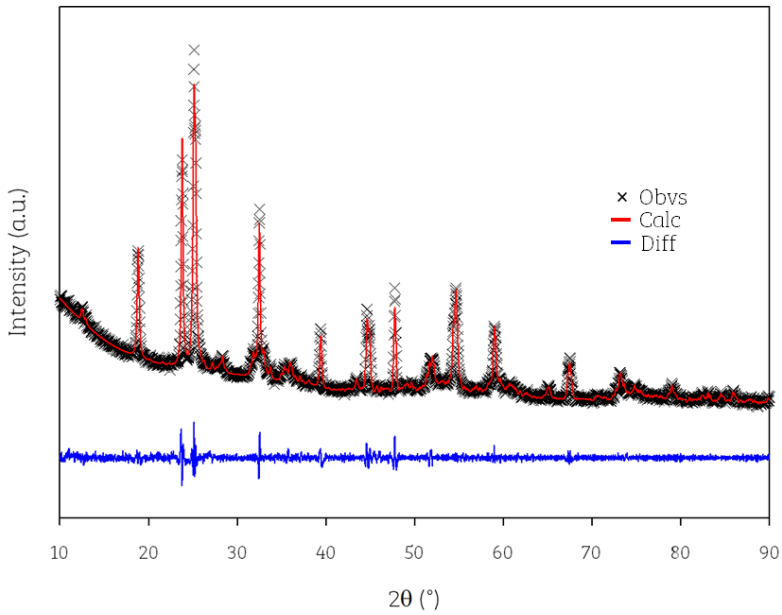

Figure 4. 14: Observed, calculated and difference XRD profiles for $Nb_9Ti_{1.5}W_{1.5}O_{30}$ (R_{wp} – 2.91 %, R_p – 2.14%) (Cu Kα).

Table 4. 5: Ionic radii of Nb^{5+}, Ti^{4+} and W^{6+} with respect to the co-ordination present in the T-Nb_2O_5 phase.

Ion	Co-ordination No.	Ionic Radii (Å)
Nb	6	0.64
	7	0.69
Ti	6	0.605
W	6	0.6

The effect of the milling on the electrochemical performance were then investigated. When cycling symmetrically at 600 mA g^{-1} (after formation of 10 mA g^{-1}) (**Figure 4. 15**), the none ball-milled sample (labelled pristine) returned overall higher capacities than both ball mill samples, with the 700 rpm sample (T-$Nb_9Ti_{1.5}W_{1.5}O_{30}$) showing the poorest of performance, which is consistent with the change in structure to a non-Wadsley Roth phase. While the aim of reducing particle size was to aid lithium diffusion and hence performance, the 350 rpm is found to perform worse than the pristine material. Potentially introducing the ball-milling step may have introduced some of the T-phase character within the particle, e.g. on the surface.

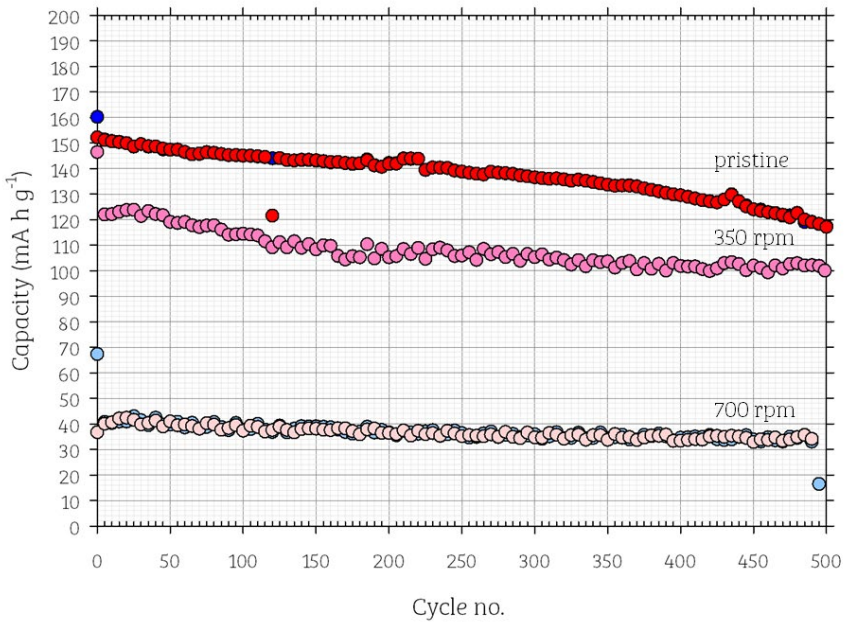

Figure 4. 15: Capacity (mA h g^{-1}) vs. cycle plot of the two $Nb_9Ti_{1.5}W_{1.5}O_{30}$ polymorphs in Li half coin cell set-up. A current density of 600 mA g^{-1} was applied.

4.3.3.3 H-Nb_2O_5 – 700 rpm

For completion, the H-Nb_2O_5 phase was taken and also ball milled at 700 rpm to check for any potential phase changes with this procedure. The resulting change in particle morphology is shown in **Figure 4. 16**, where ball milling has resulted in the similar loss of the rod-like character to deliver larger agglomerates with the "fluffy" size particles.

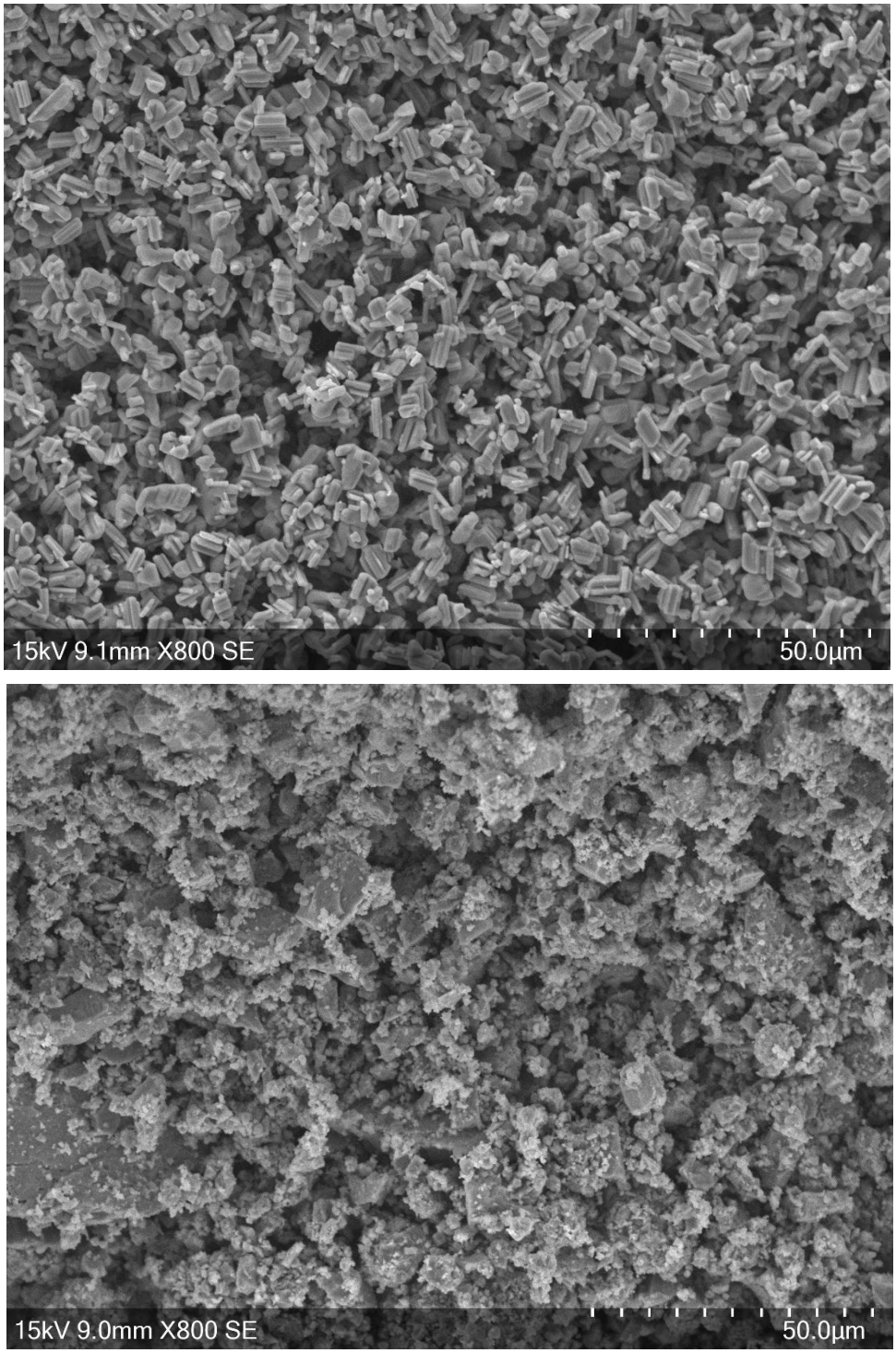

Figure 4. 16: SEM images of H-Nb_2O_5 (top) and the sample after ball milling for 1hr at 700 rpm (bottom).

The morphology change can be attributed back to the phase change observed with the PXRD patterns (**Figure 4. 17**), such that the H-Nb_2O_5 phase is lost and the T-Nb_2O_5 is noticeably re-formed with peak broadening due to the small particle size.

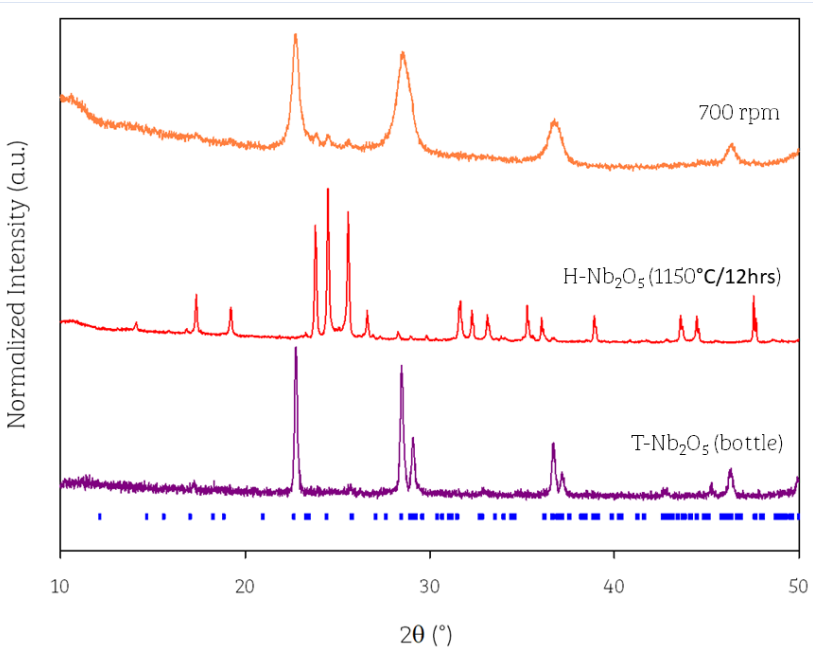

Figure 4. 17: XRD patterns of T-Nb_2O_5 from the bottle (bottom), H-Nb_2O_5 (middle) and the reverted T-Nb_2O_5 through ball milling H- Nb_2O_5 at 700 rpm. The blue dashes represents the T-Nb_2O_5 orthorhombic phase.

The unit cell parameters of this transition are presented in **Table 4. 6**, with the 700 rpm cell volume within error of the original T-Nb_2O_5 unit cell Pawley fit.

Table 4. 6: Unit cell parameters of Nb_2O_5, after heating to 1150°C (H-polymorph) before ball milling to 700 rpm to reform T-polymorph.

Composition	Crystal Symmetry	a (Å)	b (Å)	c (Å)	β (°)	Cell Volume (Å^3)
T-Nb_2O_5	Orthorhombic P b m a	6.220(2)	29.254(7)	3.948(2)	90.0	718.3(5)
H-Nb_2O_5	Monoclinic P2	21.166(7)	3.8229(9)	19.148(5)	118.03(1)	1367.7(7)
700 rpm	Orthorhombic P b m a	6.24(1)	29.19(8)	3.93(1)	90.0	716(3)

The same phase change was observed for the $Nb_{22}CuO_{56}$ system.

In attempting to understanding why the phase transformation is occurring with the introduction of this additional step, the literature regarding the impact on high temperature – high pressure environments were considered. Griffith *et al.* have suggested the phase transformation to H-Nb_2O_5 is irreversible.[3] However, this is contradictory to previous reports which showed H-Nb_2O_5 can transform to either B-Nb_2O_5 or T-Nb_2O_5 with increasing temperature and pressure, with the T-phase being the more stable phase at high pressures/temperatures.[4] Zibrov *et al.* conducted a temperature/pressure study which suggested that H-Nb_2O_5 converts T-Nb_2O_5 at either 1250°C/ 7.5 GPa or 1300°C /8.0 GPa.[5] Although the introduction of the ball-milling step has a negative effective on cell performance, this result itself can be viewed as serendipitous, such that there is an awareness of the effect of ball-milling (which is commonly used within the battery/materials field) which can trigger phase transformations which should only be possible at both high temperature/pressures.

4.3.4 Advanced Testing

4.3.4.1 Tap Density

Using Quantachrome Instrument AUTOTAP and applying a series of 1,000 taps to the sample, the sample's tap density was found to be 1.06 g cm^{-3}.

Based upon the thickness and mass of the electrode disc (excluding the current collector foil), the initial density of the material was determined to be 1.03 g cm^{-3}, and using the theoretical density (4.12 g cm^{-3}) the initial porosity was found to be ca. 75%. The process of calendaring reduces the porosity, such that ideally it should be between 30 – 40 %.

4.3.4.2 Formation Cycling

The electrodes were investigated and tested in a Li-half coin cell set-up. From previous DSC analysis (**Figure 4. 8**), no redox processes are observed above 2.5 V, with this in mind, the voltage limits were amended for the cells to cycle between 1 V and the new upper limit of 2.5 V (**see appendix for plotted formation data**). On formation cycling, the lithiation and delithiation capacities, were found on average to be 248 ± 10 and 241± 4 mA h g^{-1}, respectively, as shown in **Table 4. 7**.

Table 4. 7: Specific capacities of the four cells from formation cycling at 10 mA g^{-1}.

Cell/ Electrode No.	Mass (mg)	Process	OCV (V)	Lithiation Time (hrs)	Capacity (mA h g^{-1})		
					1	2	3
1	3.92	Lithiation	2.44	31.1	266.4	251.9	249.1
		Delithiation			247.5	246.3	244.7
2	4.32	Lithiation	1.96	31.1	232.8	241.6	239.3
		Delithiation			238.1	236.5	235.3
3	4.00	Lithiation	2.52	31.1	261.9	245.7	242.0
		Delithiation			240.3	239.1	237.5
4	4.48	Lithiation	2.39	31.1	256.9	246.1	243.5
		Delithiation			242.1	240.9	239.7

4.3.4.3 Long term – constant current cycling

Cells (electrode no.) 1 and 2, after formation cycling were set to cycle for 500 further times, as shown in **Figure 4. 18,** at a higher rate of 600 mA g^{-1} (full description of testing procedure see **2.2.5.1.4 Advanced Testing Procedures**). After 500 cycles, both cells had a capacity retention (lithiation) of 71.4 (1) % (**Table 4. 8**).

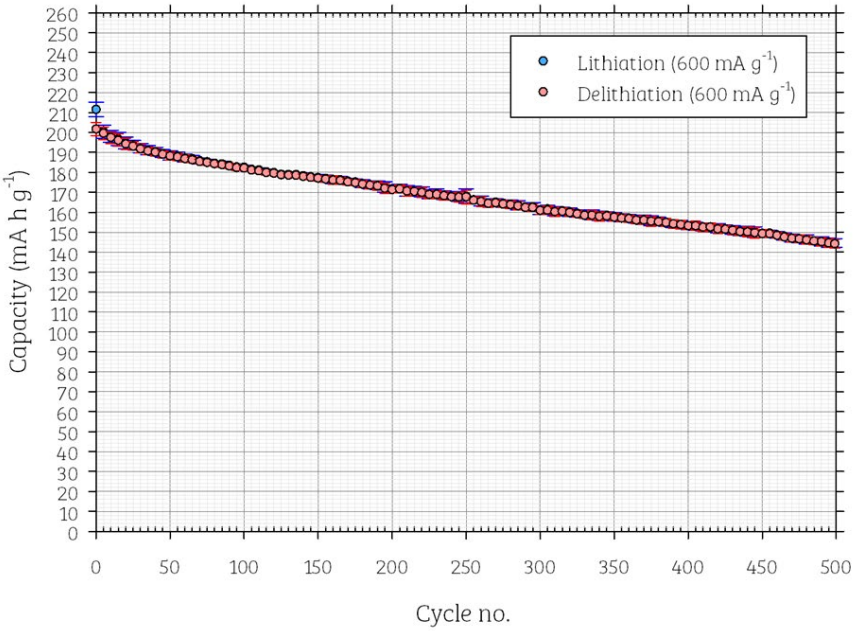

Figure 4. 18: The average specific capacities of $Nb_9Ti_{1.5}W_{1.5}O_{30}$ vs. Li metal, between limits of 2.5 V to 1 V, using the calendered electrodes 1 and 2, at a capacity of 600 mA g^{-1} over 500 cycles, with error bars included.

Table 4. 8: Resulting lithiation capacities of electrodes 1 and 2 ($Nb_9T_{i1.5}W_{1.5}O_{30}$ vs. Li metal), which underwent continuous cycling at 600 mA g^{-1} for 500 cycles.

Electrode No.	Mass (mg)	Lithiation Capacity (mA h g^{-1})		Capacity
		1	500	Retention (%)
1	3.92	205.8	146.7	71.3
2	4.32	199.0	142.2	71.5

4.3.4.4 Asymmetric Cycling (Lithiation Rate Increasing)

The second test applied to half of the conditioned cells (no. 3 and 4) involved asymmetric cycling between the limits 1 V to 2.5 V, where the delithiation rate was kept constant at approximately 100 mA g^{-1}. The lithiation rate was gradually increased from: 20 mA g^{-1} up to 4 A g^{-1} (see appendix for raw data plots) with 5 cycles at each rate. This style of testing is supposed to mimic application conditions such that the lithiation (i.e. charging if in a full cell architecture) would cope with the consumers' demands of high charge rates.

Figure 4. 19 summarises the final capacity after each cycle for this testing procedure. The constant voltage step was accidentally set to be applied on the delithiation step, rather lithiation – this is more detrimental to a cathode material under test. At the highest current density of 4 A g^{-1}, an average specific capacity of 102.2(8) mA h g^{-1} was returned with lithiation time from rest to the lower voltage limit taking 1 minute and 43 seconds.

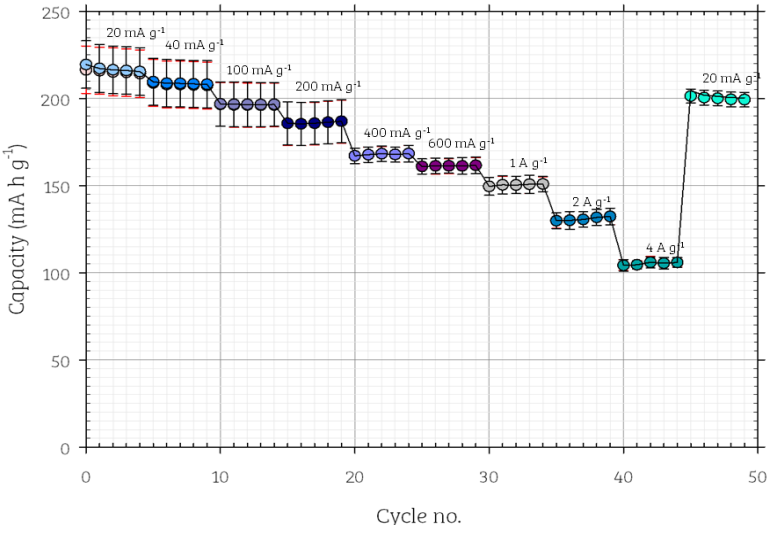

Figure 4. 19: Average specific capacities of electrodes 3 and 4 ($Nb_9Ti_{1.5}W_{1.5}O_{30}$ vs. Li metal) at each charging step. Black error bars are for lithiation, red are for the delihiation. CV applied on the delithiation step.

The constant voltage step, when testing an anode material, should be applied on the lithiation step (for a cathode, this is on the delithiation step). A further two cells were made and re-tested, with a corrected testing procedure to mitigate this mistake – as shown in **Figure 4. 20**. If the 600 mA g^{-1} data points are considered now (cycles 25 to 30) the average capacity is ca. 180 mA h g^{-1} – higher than the previous set of data where the CV step was applied incorrectly (160 mA h g^{-1}), and are in closer value to the average specific capacities found in the 600 mA g^{-1} long term cycling testing procedure (ca. 195 mA h g^{-1}) in **Figure 4. 18**. At the highest current density (4 A g^{-1}), lithiation was returning on average 134 (2) mA h g^{-1}, within a lithiation time to 1 V of 1 minute 35 seconds $\pm$ 12 seconds and a total lithiation time (which correlates to the returned reported capacity, including the CV step) was 2 minutes 20 seconds $\pm$ 7 seconds. The average and error within these reported values were deduced from both cells over the 5 cycles at the highest current density. The average specific capacities of the cell data plotted in **Figure 4. 20**, with the associated capacity retention (based upon the average capacity at 20 mA g^{-1}) are reported in

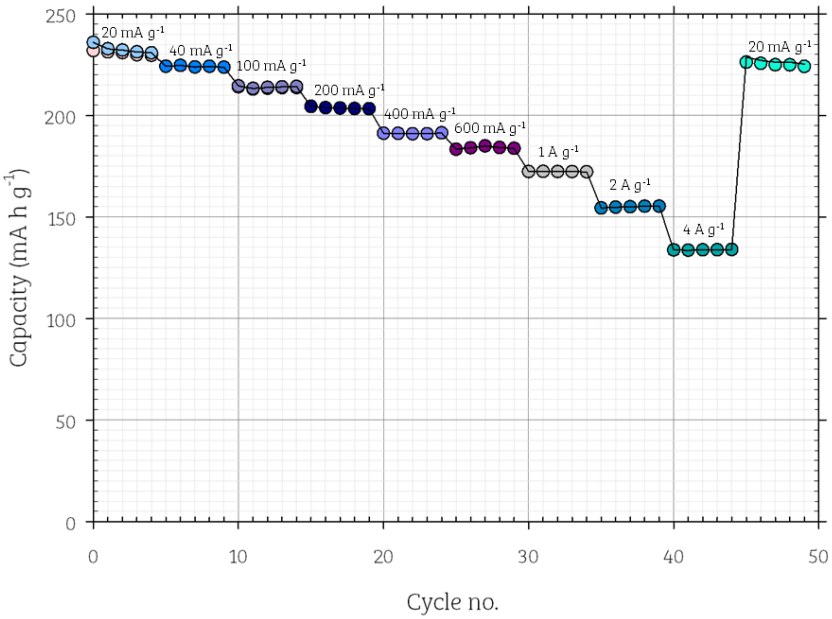

Figure 4. 20: Average specific capacities of a further two electrodes ($Nb_9Ti_{1.5}W_{1.5}O_{30}$ vs. Li metal), with CV applied on the delithiation step. The error bars are included, but are within the data point marker.

Table 4. 9: Average specific capacities of the cell data plotted in Figure 4. 20, with the capacity retention determined from the average value at 20 mA g^{-1}.

Lithiation Current Density ($mA\ g^{-1}$)	Capacity ($mA\ h\ g^{-1}$)		Capacity Retention (%)	
	Lithiation	Delithiation	Lithiation	Delithiation
20	233 (2)	231 (1)	99	99
40	224 (1)	223 (1)	96	97
100	214 (1)	214 (1)	92	93
200	203.7 (9)	203.4 (9)	87	88
400	191.1 (9)	190.8 (9)	82	83
600	184 (1)	184 (1)	79	80
1000	172.3 (8)	172.2 (7)	74	75
2000	155 (2)	155 (2)	67	67
4000	134 (2)	134 (2)	58	58
20	227 (1)	225.1 (9)	97	97

4.3.4.5 Asymmetric Cycling (Delithiation Rate Increasing)

Another asymmetric study was conducted with one cell, with the lithiation step set at 100 mA g^{-1}, while this time the delithiation rate increased. This additional test was done to evaluate whether on the previous asymmetric testing (**Figure 4. 21**), the obtained capacity was the result of lithium plating – as lithium metal is not an appropriate high power electrode. The inverse asymmetric results are presented in **Figure 4. 21,** and interestingly, the obvious current rate steps seen previously are no longer, and instead show a constant decreasing gradient up until the higher current densities. Beyond cycle 45 there is no correlation with the (de)lithiation capacities. Ultimately, this study does show the high capacity previously seen isn't a result of lithium plating, due to the high current densities forcing lithium deintercalation from the niobium electrode and returning a high delithiation capacity. With the application of 4 A g^{-1}, a capacity retention of 83% (delithiation) within approximately 2 minutes and 30 seconds – full capacity retention details are provided in **Table 4. 10**.

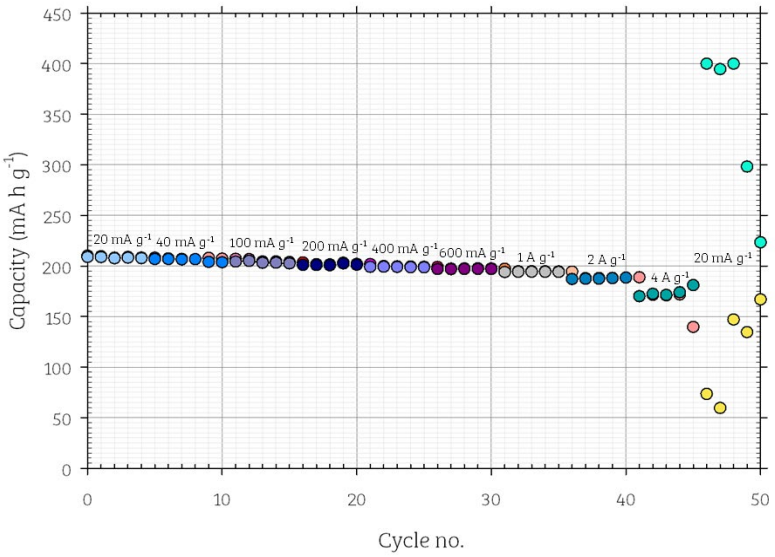

Figure 4. 21: Specific capacity of a cell undergoing an asymmetric testing ($Nb_9Ti_{1.5}W_{1.5}O_{30}$ vs. Li metal), where the lithiation rate is kept constant at 100 mA g^{-1} (blues, green, grey and purple data points), while the delithiation rate gradually increases (pinks,orange and yellow data points).

Table 4. 10: Average specific capacities of the cell data plotted in Figure 4. 21, with the capacity retention determined from the average value at 20 mA g^{-1} for lithiation and delithiation.

Delithiation Current Density (mA g^{-1})	Capacity (mA h g^{-1})		Capacity Retention (%)	
	Lithiation	Delithiation	Lithiation	Delithiation
20	209.0 (7)	208.1 (5)	100	100
40	207.3 (5)	206 (1)	99	98
100	205 (1)	203.6 (9)	98	97
200	202.3 (8)	201.2 (6)	97	97
400	199.9 (9)	198.9 (2)	95	95
600	197.8 (6)	196.9 (1)	94	95
1000	195 (1)	194.1 (1)	93	93
2000	189 (3)	187.6 (5)	90	90
4000	169 (16)	174 (4)	67	87
20	116 (42)	343 (71)	80	107

Because of the cell failure towards the end of this study, two cells previously measured in the asymmetric lithiation (lithiation increasing in rate, delithiation constant at 100 mA g^{-1}) study (**Figure 4. 20**) were tested again but with the asymmetric delithiation test – these results are shown within **Figure 4. 22**. (values tabulated in **Table 4. 11**). While the 4 A g^{-1} capacity results drop dramatically compared to the previous cell, the specific capacity does return at 20 mA g^{-1} – linear to the first 5 cycles at this rate.

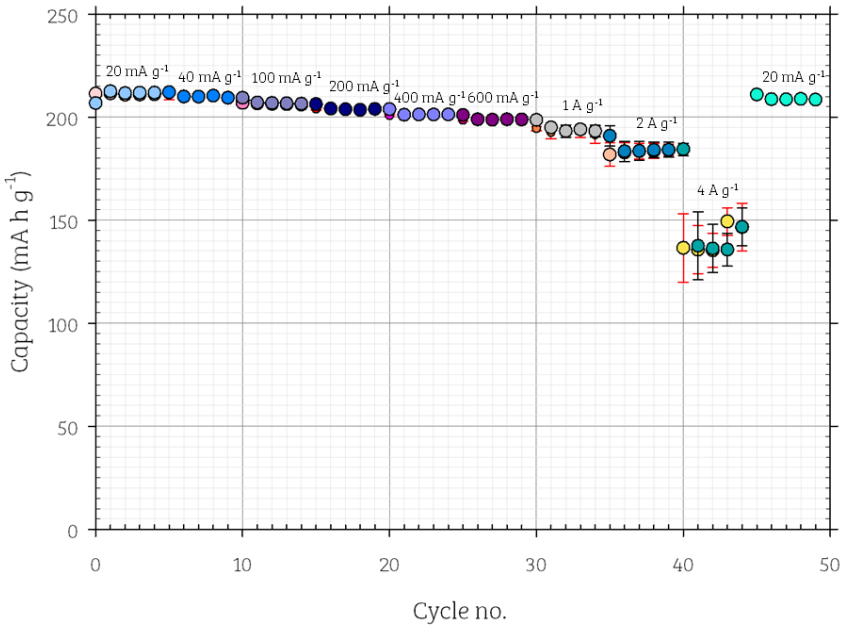

Figure 4. 22: Specific capacity of a cell undergoing an asymmetric testing ($Nb_9Ti_{1.5}W_{1.5}O_{30}$ vs. Li metal), where the lithiation rate is kept constant at 100 mA g^{-1} while the delithiation rate is increased.

Table 4. 11: Average specific capacities of the cell data plotted in Figure 4. 22, with the capacity retention determined from the average value at 20 mA g^{-1} for lithiation and delithiation.

Delithiation Current Density (mA g^{-1})	Capacity (mA h g^{-1})		Capacity Retention (%)	
	Lithiation	Delithiation	Lithiation	Delithiation
20	211 (2)	211 (0)	100	100
40	210 (1)	209 (1)	100	99
100	207 (1)	206.4 (5)	98	98
200	204 (1)	203.5 (5)	97	96
400	202 (1)	200.8 (4)	96	95
600	199.3 (10)	198.4 (5)	94	94
1000	195 (3)	193 (3)	92	91
2000	185 (5)	183 (4)	88	87
4000	148 (21)	141 (12)	70	67
20	196 (28)	209 (1)	93	99

4.3.5 Full Cell Performance

4.3.5.1 Electrode Preparation

The coatings of both electrodes need to be such the capacity (mA h cm^{-2}) is balanced. In the case of these full cells of NMC 532-$Nb_9Ti_{1.5}W_{1.5}O_{30}$, to balance effectively, the NMC 532 electrodes were required to be cut to a diameter of 11 mm with the target capacity of 1 mA h cm^{-2}, while the anode would need to be 12 mm in diameter with the aim of 1.1 mA h cm^{-2}, such that the ratio of cathode to anode is 1 : 1.1 in terms of the capacity (mA h cm^{-2}).

From previous coatings of NMC 532 using method 2, the electrode discs (12 mm) weighed in the region, on average, of 7.56 mg (electrode coating only, exclusive of the current collector mass), which would produce a capacity per area of 0.828 mA h cm^{-2}.

To achieve our aim of 1 mA h cm^{-2}, adjustments in the bar coater height was made from 200 μm up to 225.2 μm, to produce a coating of greater thickness. The thickness (pre-calendered) was slightly out and a re-attempt was made at set height of 260 μm. The electrode coatings were then calendered.

An example of electrode pairings, with the determination of capacity with respect to area, are shown in **Table 4. 12**. The capacity for NMC 532[6] is taken to be 166 mA h g^{-1}, while the anode – from our previous studies – is taken to be 250 mA h g^{-1} (where the average lithiation capacity was found to be 248 ± 10 mA h g^{-1}).

Table 4. 12: An example of determining the capacity (mA h cm^{-2}) to allow for a successful pairing and thus electrode balancing for full cell architecture.

	Diameter (cm)	Area (cm^2)	Mass of foil disc (mg)	Mass of coated disc (mg)	Mass of coating (mg)	Thickness of foil disc (mm)	Average thickness of coated disc (mm)	Average thickness of coating (mm)	Coat Weight (mg cm^{-2})	Capacity (mA h g^{-1})	Capacity (mA h)	Capacity (mA h cm^{-2})
NMC 532 Electrode 2	1.1	0.95	4.1	11.1	7.0	0.015	0.063	0.048	7.37	166	0.93	0.979
$Nb_9Ti_{1.5}W_{1.5}O_{30}$ Electrode 1	1.2	1.13	10.1	16.5	6.4	0.01	0.038	0.028	5.66	250	1.28	1.132

4.3.5.2 Electrochemical Performance

The applied current was based upon the current loading of the NMC 532. While it was intended for the full cells to be cycled initially at 10 mA g^{-1} for formation and then at increased rates, for either asymmetric cycling or constant C-rate cycling, it is notable (and is included) on the plots the current densities (mA g^{-1}) are out. This is due to error relating to the mass of the aluminium foil not being correctly updated within the spreadsheet to correlate with the reduction of the diameter of the electrodes cut from 12 mm (from initial coating runs) down to 11 mm. The small difference in mass of foil only becomes more severe at higher current loadings. Like before, where the cells produced are used for multiple testing procedures, for simplicity, the formation of the sets of cells have been split up (**Figure 4. 23** and **Figure 4. 24**), such that cells which experienced similar advanced testing (i.e. high constant C-rating) are combined to allow for ease of correlation. For all 4 full cells, the first charging cycle sees a significant reduction in capacity from above 300 to below 180 mA h g^{-1} (formation capacities presented in **Table 4. 13**). Typically a loss on the first few cycles, hence the need for formation cycle, is expected, but this is larger than ideal. Future work will consider mitigating this significant loss through further optimization. Nevertheless these preliminary full cell tests do demonstrate that the new $Nb_9Ti_{1.5}W_{1.5}O_{30}$ anode can be used in a full Li-ion cell.

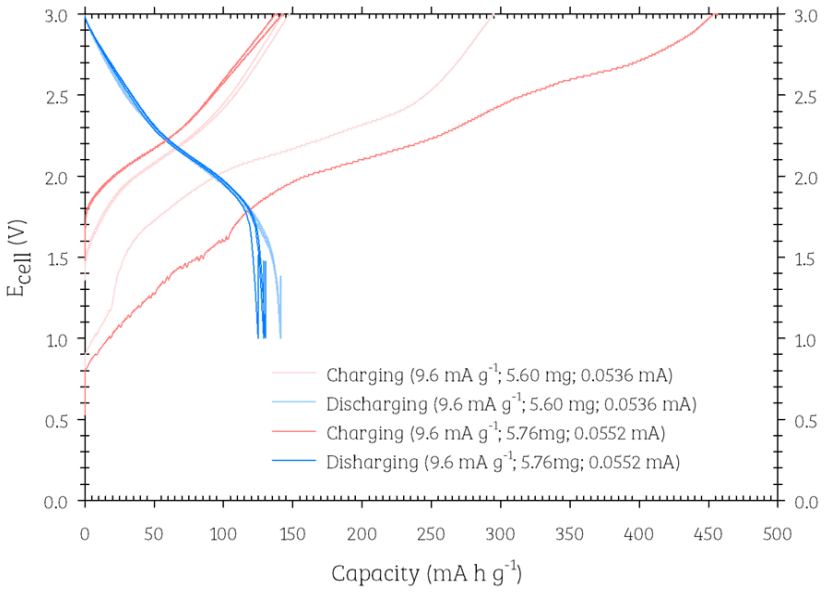

Figure 4. 23: Capacity plot of the full cells (1 and 2; $Nb_9Ti_{1.5}W_{1.5}O_{30}$ vs. NMC532) during the formation cycling, at ca. 10 mA g^{-1}, cycling 3 cycles between 3 V and 1 V.

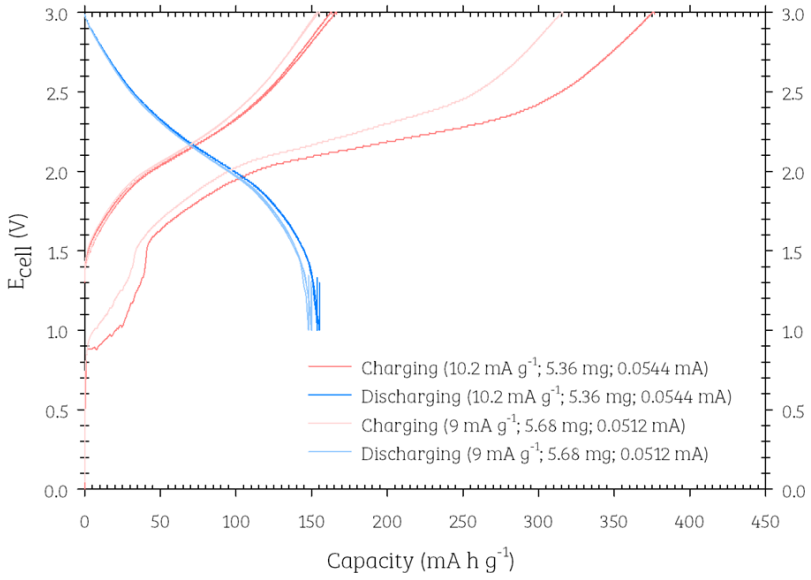

Figure 4. 24: Capacity plot of the full cells (3 and 4; $Nb_9Ti_{1.5}W_{1.5}O_{30}$ vs. NMC532) during the formation cycling, at ca. 10 mA g^{-1}, cycling 3 cycles between 3V

Table 4. 13: Electrode masses of the cathode and anode discs within the full cell, and the corresponding current applied and the returned capacity values upon charging during formation.

Full cell no.	Anode AM (mg)	NMC-532 AM (mg)	Applied Current (mA)	mA g^{-1}	Capacity on charging (mA h g^{-1})		
					1	2	3
1	5.12	5.60	0.0536	9.6	308.58	154.48	149.51
2	5.12	5.76	0.0552	9.6	476.18	149.46	144.54
3	5.28	5.68	0.0512	9.0	316.01	155.39	153.89
4	5.04	5.36	0.0544	10.2	376.55	166.39	163.28

4.4 Conclusions

A baseline procedure for coating and testing these materials has been established, with the ink formulation consisting of subsequent solid steps rather than a preliminary ball mill step. Due to the testing of this material ($Nb_9Ti_{1.5}W_{1.5}O_{30}$) occurring concurrent with the $Nb_{22}CuO_{56}$, the coating methodologies (1 and 2) shown previously in Chapter 3 have been equally experienced within this chapter too.

Towards optimising this material and using high speed ball milling, a phase transformation from $Nb_9Ti_{1.5}W_{1.5}O_{30}$ to the T- $Nb_9Ti_{1.5}W_{1.5}O_{30}$ phase was observed. The cell performance with this additional milling was found to be poor, which was attributed to the known low capacity of this T-phase. Nevertheless, the discovery that ball-milling can be used to cause such a phase change which normally requires high-pressure/temperature conditions is interesting, and suggests further work on the effect of ball milling battery materials is warranted. The preliminary work on the $Nb_9Ti_{1.5}W_{1.5}O_{30}$ material has shown favourable cell performance. With the asymmetric cycling with the increase in the lithiation rate, at the highest current density (4 A g^{-1}), lithiation was returning on average 134 (2) mA h g^{-1}, within a lithiation time to 1 V of

1 minute 35 seconds ± 12 seconds and a total lithiation time (which correlates to the returned reported capacity, including the CV step) was 2 minutes 20 seconds ± 7 seconds. However, one of the challenges with assessing rate performance in Li metal half cells is the fact that Li metal has some issues at high rate, particularly related to the Li stripping process. Therefore, in order to overcome this issue, the inverse test was ran such that lithiation rate was kept constant and delithiation gradually increased (in this way the rapid process at the Li electrode is plating rather than stripping). This showed improved performance, highlighting the issues noted above with the Li stripping process. The results showed that with the application of 4 A g^{-1}, a capacity retention of 83% (delithiation) was observed within approximately 2 minutes and 30 seconds, with an average lithiation of 169 (16) mA h g^{-1}.

Overall the results are very promising, however it is difficult to compare these results against literature reports, given the differences in methodology and quite commonly, the lack of electrode information with respect to current densities applied and the cell thickness – which serve as an important marker to cell performance (as previously reviewed in Chapter 1 with respect to the differences in reports regarding $Nb_{16}W_5O_{55}$). However, the added advantage of the $Nb_9Ti_{1.5}W_{1.5}O_{30}$ material revolves around the lower W content and the introduction of Ti into the material – it is both cheaper and lighter than both Nb and W, while the material has shown very good performance at high charge rates.

4.5 Future Work

Given the preliminary study in developing the coating and testing methodology, further work to enhance the performance of this material will involve ensuring electrodes are effectively calendered such that the porosity is in an acceptable range (porosity to be 30-40%). In addition, given the reports on Nb-W-O materials, it would be worthwhile to prepare electrodes of thickness ca. 2.1 mg – to allow for an effective comparison to Griffith *et al.* work on the Nb-W-O systems in order to illustrate the promising potential of the $Nb_9Ti_{1.5}W_{1.5}O_{30}$ material.

4.6 References

1 K. J. Griffith, K. M. Wiaderek, G. Cibin, L. E. Marbella and C. P. Grey, *Nature*, 2018, **559**, 556–563.

2 K. J. Griffith, Y. Harada, S. Egusa, R. M. Ribas, R. S. Monteiro, R. B. Von Dreele, A. K. Cheetham, R. J. Cava, C. P. Grey and J. B. Goodenough, *Chem. Mater.*, 2021, **33**, 4–18.

3 K. J. Griffith, A. C. Forse, J. M. Griffin and C. P. Grey, *J. Am. Chem. Soc.*, 2016, **138**, 8888–8899.

4 J. L. Waring, R. S. Roth and H. S. Parker, *J. Res. Natl. Bur. Stand. Sect. A Phys. Chem.*, 1973, **77A**, 705.

5 I. P. Zibrov, V. P. Filonenko, P. E. Werner, B. O. Marinder and M. Sundberg, *J. Solid State Chem.*, 1998, **141**, 205–211.

6 Targray NMC Powder for Battery Manufacturers, https://www.targray.com/li-ion-battery/cathode-materials/nmc, (accessed 21 May 2022).

Chapter 5: Alternative ink formulation and coating approaches for novel Nb-based anode materials: Ti and W doping

This chapter will focus on alternative coating formulations, with the focus nominally on water-soluble binders for enhanced recyclability, which eliminates the use of PVDF and so the avoidance of the use of the solvent NMP. Following on from **Chapter 4's** initial study on $Nb_9Ti_{1.5}W_{1.5}O_{30}$ from the initial characterisation and electrochemical testing stand point, this material will again be considered in these alternative approaches.

Given the limited number of cell channels available for this study, the electrochemical testing repeats are limited, however, the methodology developed and discussed provides opportunities for future development and optimisation.

Figure 5. 1: Graphical abstract representing the 'organic' origins of the binders used within these chapters – such as iota-carrageenan and carboxymethyl cellulose (CMC).

5.1 Background: Context and Aims

As presented within the previous chapter, and as is quite common within Li-ion battery manufacture, polyvinylidene fluoride (PVDF) and N-Methyl-2-pyrrolidone (NMP) are dominant components in the preparation of electrode coatings.

While it is advantageous to distance manufacturing processing from the use of NMP primarily on safety reasons, due to the substance's well-known teratogen, sensitizer and toxic properties, there are other environmental benefits too. With respect to the PVDF binder, issues arise when considering the recyclability of the electrode, when considering a full circular economy in the battery landscape. In efforts to recycle Li-ion batteries, there are multiple routes ranging from highest to lowest energy intensive processes of: pyrolysis, hydrometallurgy and direct recycling to name a few. Of the pyrolysis process, the implication of PVDF within the composite is that it has potential to fluorinate the active material within the composite electrode[1], while also risking the formation of hazardous hydrofluoric acid [2] (HF; which through digestion, contact or inhalation can be fatal[3]). In addition, with respect to the use of physical processing techniques within the recycling domain, the hydrophobicity of the binder[4] surrounding the active material can affect the hydrophobicity of the substances and hence affect the efficiency of separation.

Alternatives to PVDF include the use of dual system: sodium carboxymethyl cellulose (CMC) and emulsified styrene butadiene rubber (SBR), a water soluble route.

The use of carrageenan as a binder for Li-ion batteries, to date, has only been described once within the literature. This substance, is instead, often associated with use within the electrolyte. The first instance for binder use has been reported for a Li-S battery, to seek an alternative to PVDF which struggled with the mechanical stress during electrode cycling for this type of Li-ion battery.[5] The ink formulated with (iota-/lambda-)carrageenan consisted of a ratio of AM:CB:B of 60:30:10, with the slurry deposited onto aluminium foil.

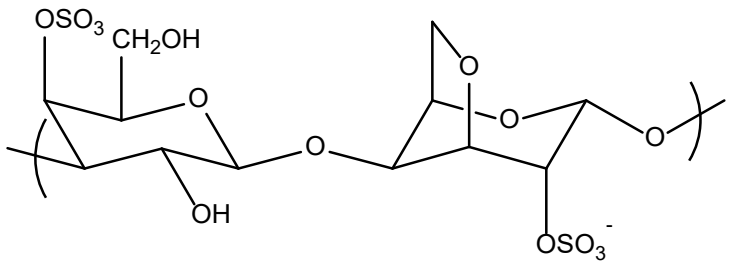

Figure 5. 2: Simplest molecular repeating unit of iota-carrageenan.

5.2 Experimental

5.2.1 Synthesis of Active Material

The synthesis of the active material: niobium titanium tungsten oxide ($Nb_9Ti_{1.5}W_{1.5}O_{30}$) materials is outlined in section **4.2.1.1**.

5.2.2 Coating Methods

5.2.2.1 Alternative Binders

At the time of this body of work, no SOP existed for the ink formulation using alternative green binders, such as the CMC-SBR combination. Instead 2 individuals: Alex Sargent, School of Chemistry and Dr Yazid Lakhdar, School of Metallurgy and Materials, within the battery research groups at the University of Birmingham, had varying methodologies – this was based on their own research experiences.

Alex Sargent made use of a ratio of AM:CB:CMC:SBR of 90:2:5:3, with the order of additions of solids set as: CMC, CB, AM and SBR. Apart from the SBR addition experiencing a mix of 5 mins/ 1300 rpm, the other solids were mixed for 10 mins. The degas step remained consistently 3 mins/ 1800 rpm. The solids to water content were approximately 0.5 g and 0.8 g. respectively.

Yazid Lakhdar made use of a ratio of AM:CB:CNT:CMC:SBR of 90:4.5:0.5:2:3, with the order of additions of solids set as: AM, CB, CMC, CNT and SBR. The AM, CB and CMC were mixed for 3 mins/ 1300 rpm. The addition of CNT and further water were mixed for 3 mins/2000 rpm, before a degas stage of 4 mins/2000 rpm. The SBR was the final addition to be made with a comparatively gentle mix of 3 mins/500 rpm.

From these two methods, there are variations in the ratio of solids and in the addition of solids. The most notable variation is for the addition of SBR – Alex Sargent added this before the degas stage, while the Yazid Lakhdar added it afterwards but with a lower rpm.

Aspects of each of these methodologies have been considered to investigate the use of water soluble binders with $Nb_9Ti_{1.5}W_{1.5}O_{30}$.

5.2.2.1.1 CMC and SBR

5.2.2.1.2 Method 1

The ratio of AM:CB:CMC:SBR was 90:2:5:3, with the total solid content to be 0.5 g.

The initial step involved mechanochemical mixing of the AM and CB together for a total time of 30 mins at 350 rpm (using a Fritsch planetary ball mill Pulverisette 7).

The binder – sodium carboxymethyl cellulose (CMC) – was weighed and added to the THINKY mixer pot, with the following addition of ca. 0.4 g of water, before mixing for 4 mins/1300 rpm. The AM:CB were added next and mixed for a further 5 mins/1300 rpm. Note – the carbon black type is specified in the results section (i.e. whether it was "Super P" or "C45"). Two further subsequent water additions were made with ca. 0.2 g and then ca. 0.1 g, with a mixing step of 3 mins/1300 rpm for both additions. (The steps to reduce the viscosity can be combined, such that 0.3 g of water can be added in one-go; nominally these slow and individual additions are precautionary measures so as not to reduce the solid contents down too drastically.) The mixture was degassed for 3

mins/2000 rpm, before the addition of a 50% aqueous styrene-butadiene rubber (SBR) solution and a final mix of 3mins/500 rpm.

5.2.2.1.3 Method 2

The ratio of AM:CB:CMC:SBR was 90:2:5:3, with the total solid content to be 0.5 g.

The binder – sodium carboxymethyl cellulose (CMC) – was weighed and added to the THINKY mixer pot, with the following addition of ca. 0.4 g of water and the inclusion of 6 small balls (ca. 5 mm) before mixing for 5mins/1300 rpm. The CB was added next and mixed for a further 5 mins/1300 rpm. The AM and ca. 0.4 – 0.5 g of water were added to the mixture, with a mix of 10mins/1300 rpm. The next stage considered the importance of varying when the SBR should be added to the mixture.

5.2.2.1.3.1 Variation in SBR addition

Before degas: The 50% aqueous SBR solution was added to the mixture and mixed for 3 mins/1300 rpm, before the removal of the balls. The final degas stage was made at 3 mins/1800 rpm.

After degas: The 6 small balls were removed and the mixture set to degas at 3 mins/1800 rpm. The 50% aqueous SBR addition was added and a final mix of 3mins/500 rpm was made.

Method 2 of the CMC and SBR addition was devised to replicate as best as possible the standard recipe used for the PVDF systems. The additional variable in this method considers the effect of the SBR point of addition.

Figure 5. 3 shows a visual representation of the differences of additions for both methods, and with the variation in the SBR addition.

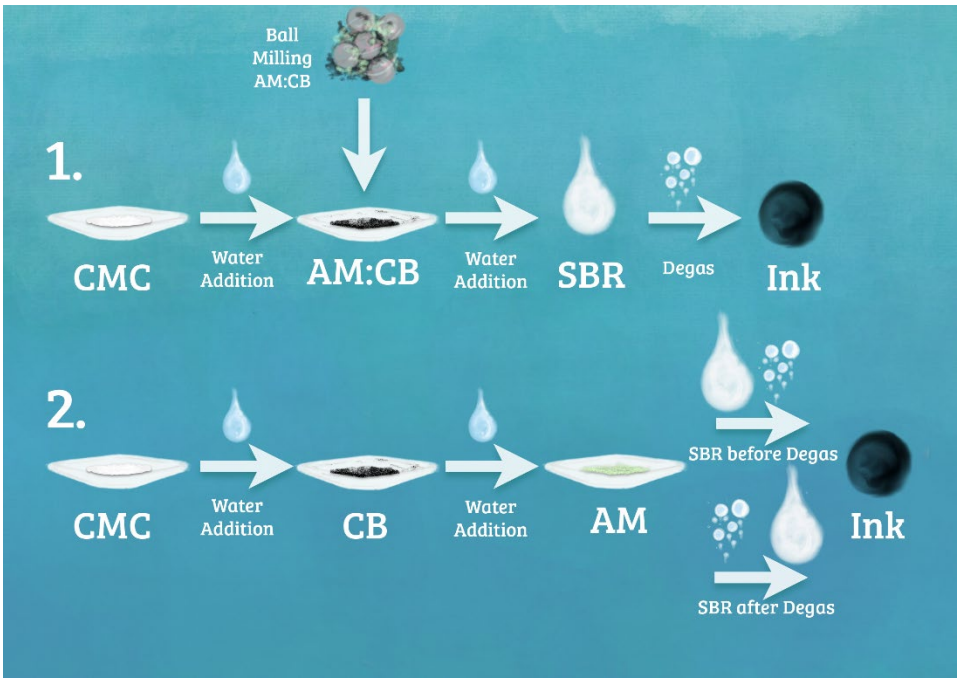

Figure 5. 3: Representation of the coating process described with the variations in the methods and material addition steps.

Unless explicitly stated the electrode coatings should be assumed to be not calendered. This additional process step was typically implemented when the electrochemical performance was showing promising results.

5.2.2.1.4 Iota-carrageenan

The ratio of AM:CB:B was 90:2:8, with the total solid content of 0.5 g.

The binder – iota-carrageenan – was weighed and added to the THINKY mixer pot, with the following addition of ca. 0.4 g of water and 6 small balls (ca. 5 mm), before mixing for 5 mins/1300 rpm. The CB (C45) addition was made followed with ca. 0.3 g of water and mixing for 5 mins/1300 rpm. It was observed after this step that the mixture was quite paste like and possibly more water was required in this step, but this is open to future optimisation work. The AM was the final solid addition to be made with 0.2 g of water, for 5 mins/1300 rpm. Due to consistency, a final addition of water was made of ca. 0.4 g to reduce the consistency of the coating and mixed for 5mins/1300 rpm. Although the observable consistency was noted to be good – the final water addition should have been less, but was from fault of a pipetting error. The mixture was degassed at 3 mins/1300 rpm.

For all coating recipes: the resulting slurry was cast onto copper foil using a draw-down coater, where the bar height was set to 200 μm. The resulting coating was dried for up to 2 hours at 80°C before being transferred for overnight drying in a vacuum oven pre-set at 110°C.

5.2.3 Coin Cell Assembly

5.2.3.1 Li-Half Cell

The fabrication of coin cells were previously described **Chapter 2: Coin Cell Assembly**.

5.2.4 Electrochemical Testing

As standard, the electrochemical properties were measured using a BioLogic BCS805 battery tester in galvanostatic mode between 3.0 V and 1.0 V, unless explicitly stated in later testing studies within this chapter.

As this body of work was happening in conjunction with the initial work of the $Nb_9Ti_{1.5}W_{1.5}O_{30}$ through optimising the performance, the cells considering CMC-SBR would have made use of method 1 – where the c-rating is deduced from the level of intercalation expected, rather than applying a standard 10 mA g^{-1}. For this reason, although the cells were likely to have been set to cycle at "C/20", the resulting figures of the testing data will include the actual mA g^{-1} of the procedure.

5.3 Results and Discussion

5.3.1 Coating Methodology 1

The initial work, commencing the use of CMC-SBR followed the 2.2.1 Coating Formulations: Method 1, such that the AM and the CB were pre-mixed beforehand in a ball mill. In addition, the use of different CB sources were trialled: Super P and C45 (a further CB source common in electrode fabrication is C65, but this wasn't considered here). Both cells with the differing carbon additive were cycled between 1 V and 3 V, and the resulting charge-discharge curves plotted in Figure 5. 4 and Figure 5. 5, respectively for Super P and C45. Both cells show improvements in the achievable specific capacity with the number of cycles, but ultimately C45 CB shows better performance. The difference in cell performance with variation in carbon additive has also been reported in the literature, e.g. red phosphorus for use as a Na-ion cathode material delivered slightly higher capacities with the use of C45 over Super P.[6] The difference in performance potentially may be attributed to the level of impurities; C45 has lower metal traces in comparison to Super P.[7] While reversible cycling was achieved, ultimately the PVDF coatings explored previously are out-performing these cells significantly, which suggests further optimisation is required.

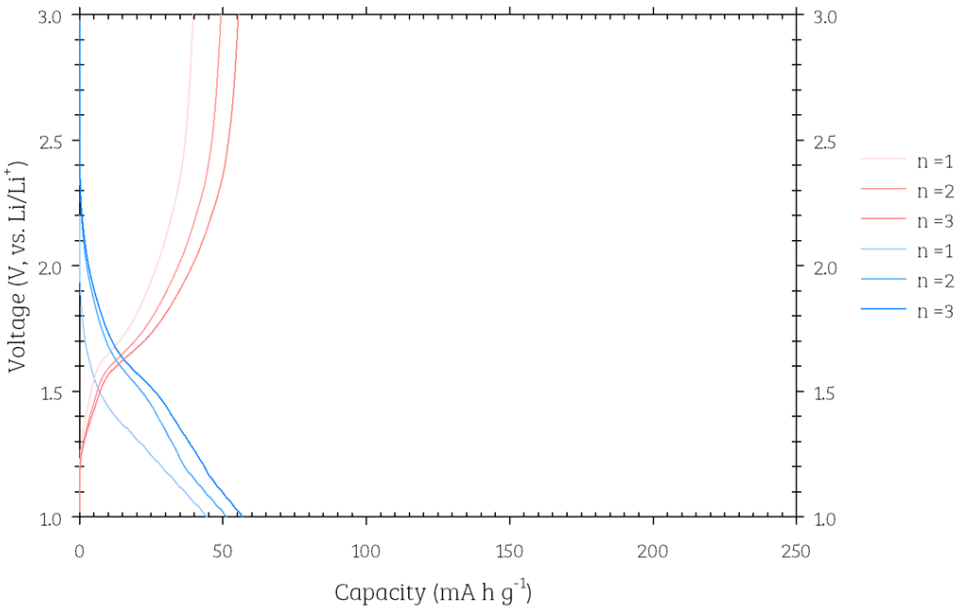

Figure 5. 4: Galvanostatic discharge-charge curves of $Nb_9Ti_{1.5}W_{1.5}O_{30}$ vs. Li metal, where the coating is produced via coating method 1 and the carbon black is Super P. Current density applied 9.7 mA g^{-1}.

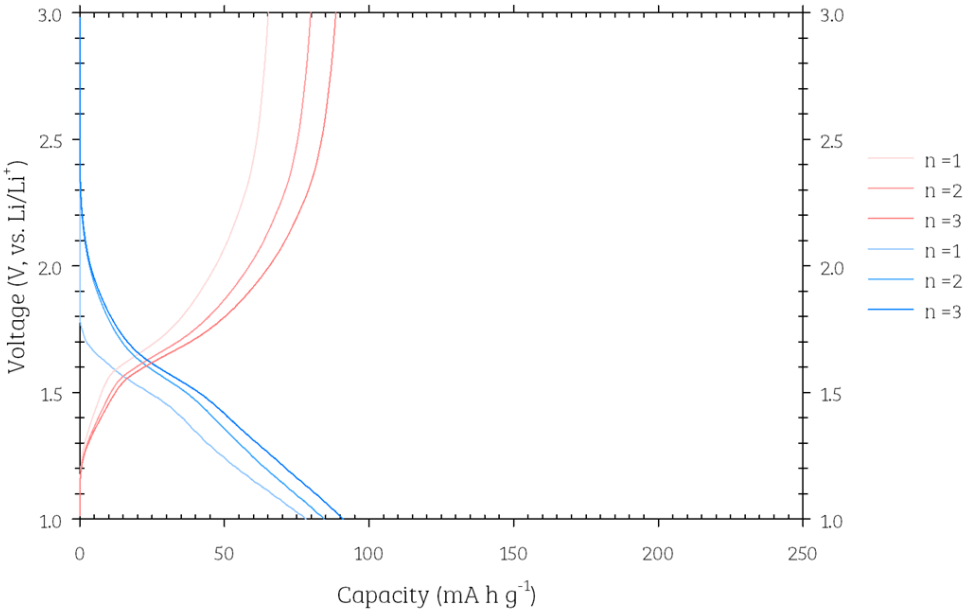

Figure 5. 5: Galvanostatic discharge-charge curves of $Nb_9Ti_{1.5}W_{1.5}O_{30}$ vs. Li metal, where the coating is produced via coating method 1 and the carbon black is C45. Current density applied 9.7 mA g^{-1}.

5.3.2 Coating Methodology 2 –variation in SBR addition

Towards optimising a coating method for use of CMC-SBR, one variation that had been noted regarded the addition of the SBR. Therefore, as outlined in **Figure 5. 3**, this difference was considered. The resulting charge-discharge curves from altering the SBR addition with respect to the final degas stage, are shown respectively in **Figure 5. 6** and **Figure 5. 7**, for the addition of SBR before degas and then SBR after degas – with a current density of 9.7 mA g^{-1} applied to both cells. Significantly, the variation in coating methodology has improved upon the initial testing.

Further cells will be required to confirm whether the variation in the SBR addition is significant, there is a slight increase in capacity by adding the SBR before degassing.

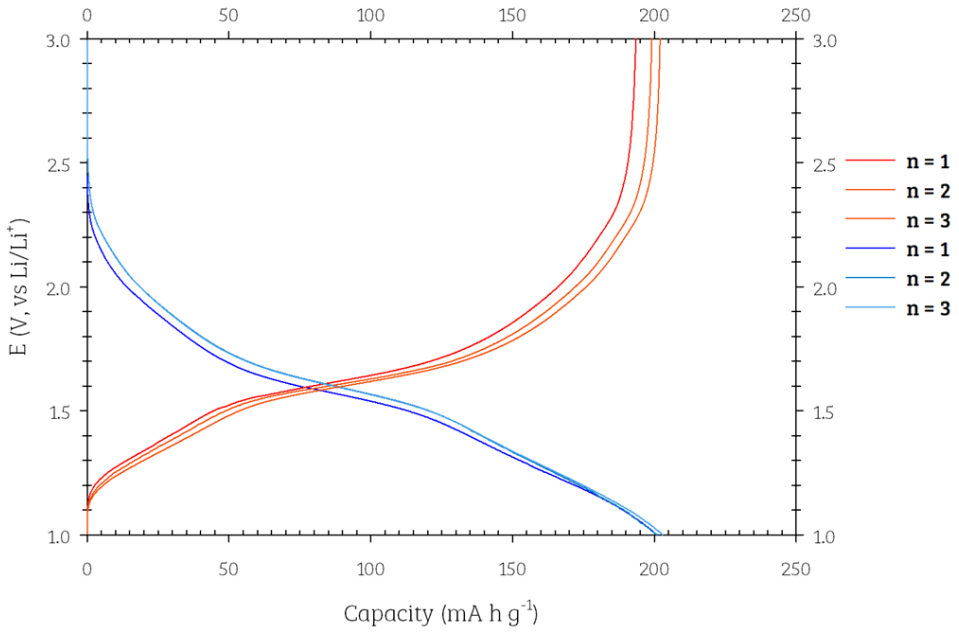

Figure 5. 6: Galvanostatic discharge-charge curves of $Nb_9Ti_{1.5}W_{1.5}O_{30}$ vs. Li metal, where the coating involved the SBR component added before the degas step. The electrodes were fabricated with a Super P conductive additive.

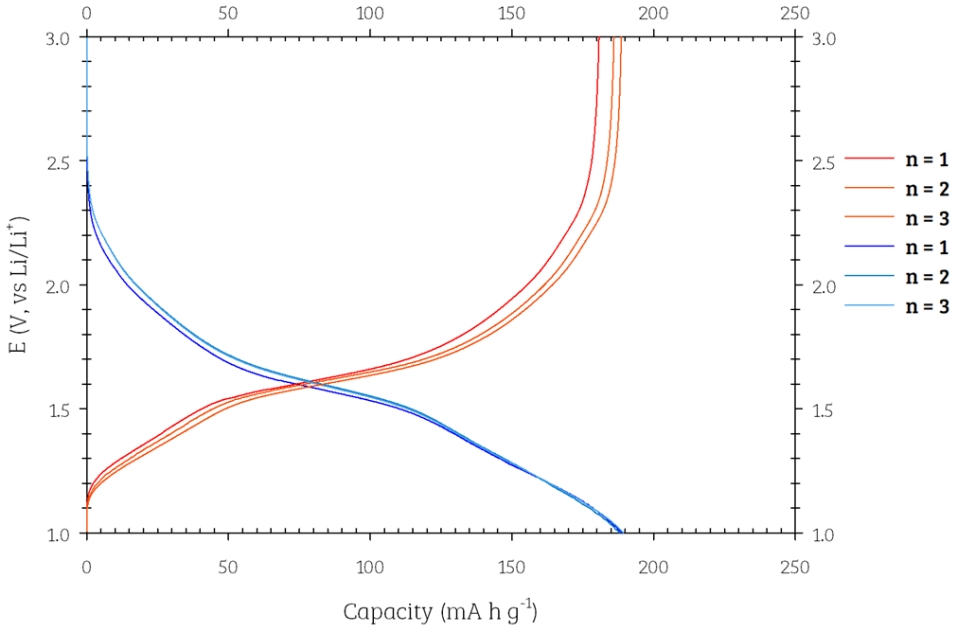

Figure 5. 7: Galvanostatic discharge-charge curves of $Nb_9Ti_{1.5}W_{1.5}O_{30}$ vs. Li metal, where the coating involved the SBR component added after the degas step. The electrodes were fabricated with a Super P conductive additive.

Significantly, the alteration in mixing formulation has improved the obtainable specific capacities. When considering the use of Super P, for both coating methodologies, by removing the ball milling step, the first cycle alone is improved by four times as much.

5.3.3 Iota-Carrageenan

Before considering the electrochemical performance of this electrode metal with carrageenan as a binder, a pristine electrode disc was imaged on the SEM. The SE image of the coating is shown in **Figure 5. 8**, with the image scaled at 30 µm showing the morphology of the surface to show the retention of the rod-like character of the $Nb_9Ti_{1.5}W_{1.5}O_{30}$ material and overall a quite fluffy texture. The coating was also mapped using the EDX attachment with the detection of S and Na being representative of the carrageenan binder (**Figure 5. 9**). In addition, signals (not included in the EDS image here) did highlight the presence of K and Al. When reviewing the specification sheet of the iota-carrageen (Alfa Aesar; product no.: J60603, lot. no.: Y15C021), 20% of the substance consists of 'Ash' – which would potentially account for the impurities visible on the EDS spectra.[8]

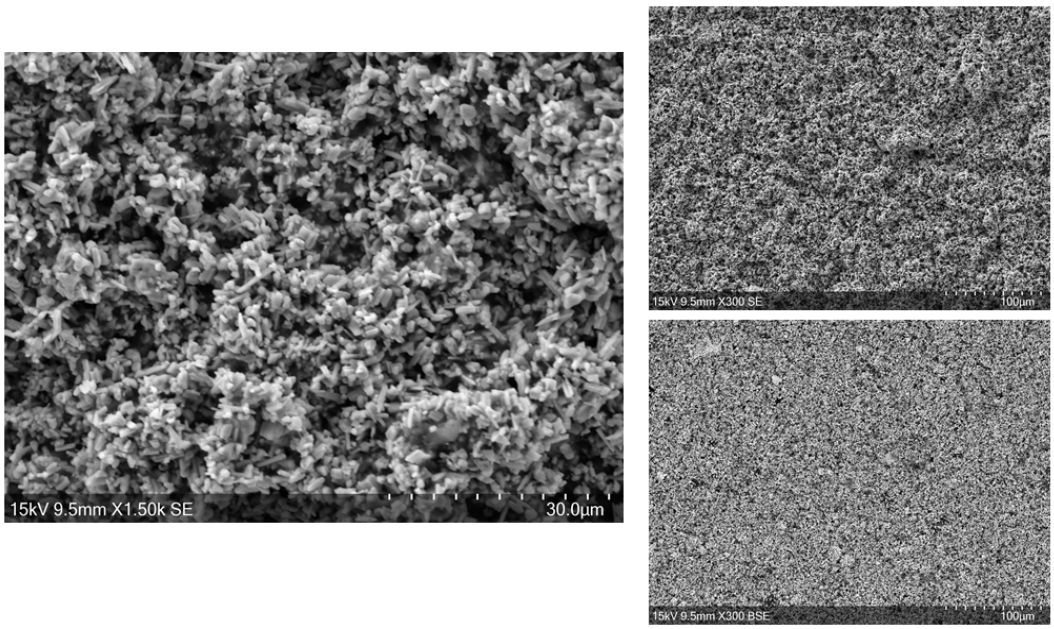

Figure 5. 8: SE imaging of the surface of the $Nb_9Ti_{1.5}W_{1.5}O_{30}$ electrode on Cu foil, with CB and iota-carrageenan at 30 µm (left) and 100 µm (top right), with the equivalent BSE image (bottom right).

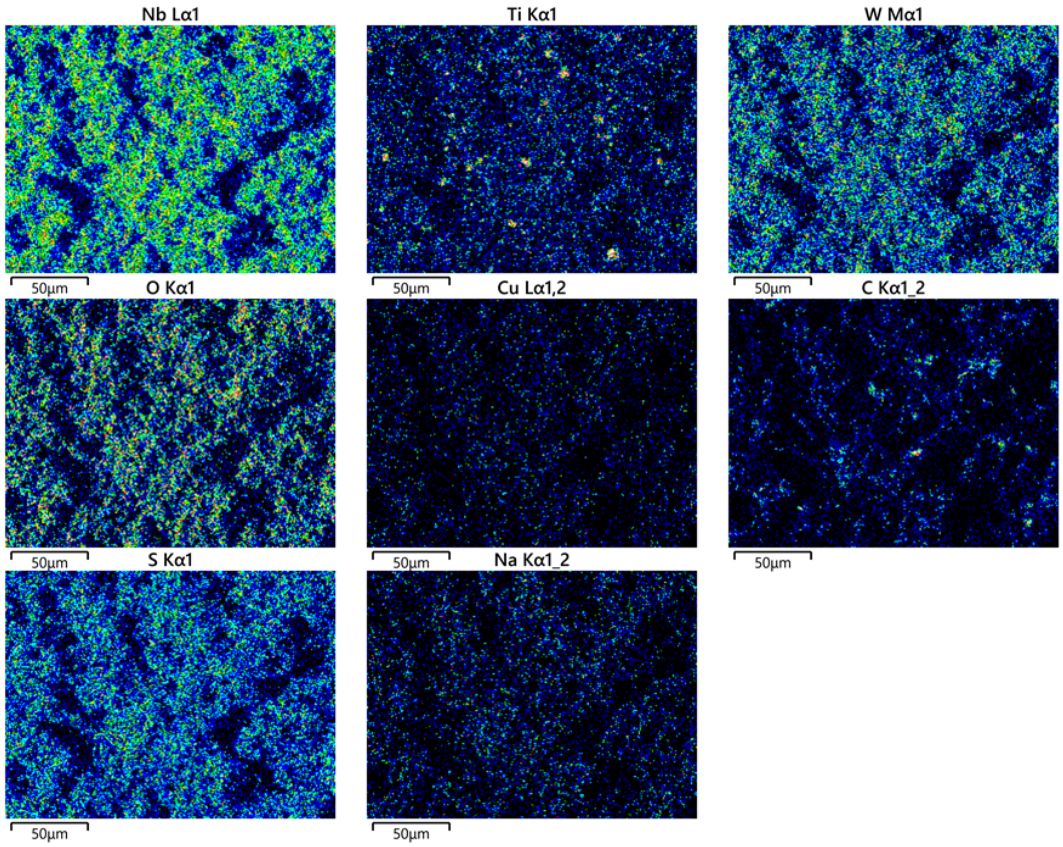

Figure 5. 9: SEM-EDS imaging of the carrageenan coating.

The carrageenan study occurred towards the end of the overall project time, thus the testing methodology reflects the developments within the **Electrochemical Testing: Method 2**, where fixed current densities were applied instead of a C-rate, for formation and the more advanced testing techniques. The initial formation cycles (**Figure 5. 10**) between 1 V to 3 V, on average for both cells and all 3 cycles, was found to be 238 (8) and 232 (6) mA g^{-1} for lithiation and delithiation, respectively– an improvement on the performance found for the CMC/SBR route.

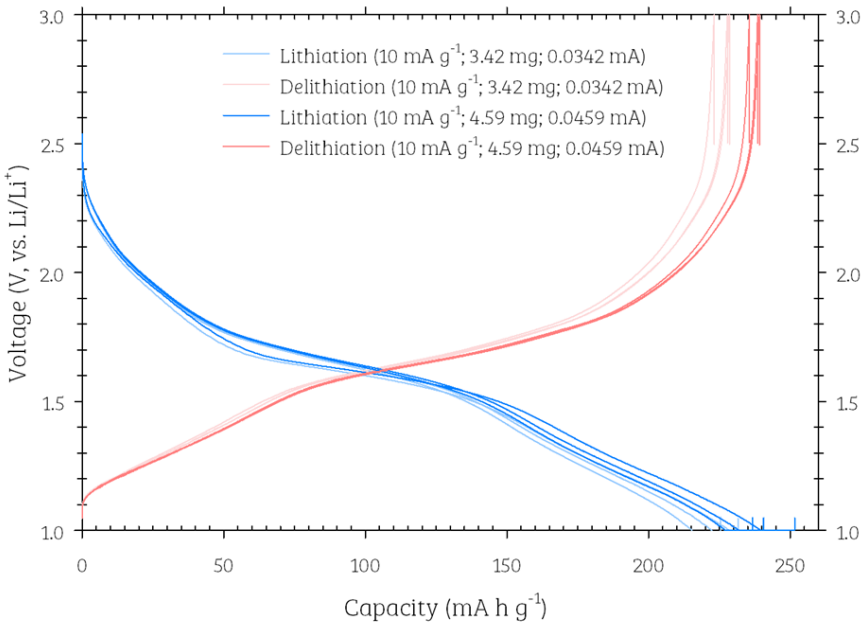

Figure 5. 10: Galvanostatic discharge-charge curves of $Nb_9Ti_{1.5}W_{1.5}O_{30}$ vs. Li metal, where the coating made use of iota-carrageenan as a binder system.

Two cells were studied, one cell (electrode AM of 3.42 mg) was considered for a repeated equivalent "3C-3C" measurement, where (de)lithiation involved the application of a current density of 600 mA g^{-1}, while the second cell was considered for lithiation-delithiation study. Rather than cycling up to 3 V, the upper limit for the more advanced testing was reduced to 2.5 V. The resulting capacities obtained in the former testing procedure (of 600 mA g^{-1}) over 500 cycles are plotted in **Figure 5. 11**, which on average was found to be 96 (6) mA g^{-1} for both lithiation and delithiation steps and overall the capacity retention was 68% from the 1st to the 500th cycle (this relates to the second testing procedure at 600 mA g^{-1}, and does not include the initial 3 formation cycles).

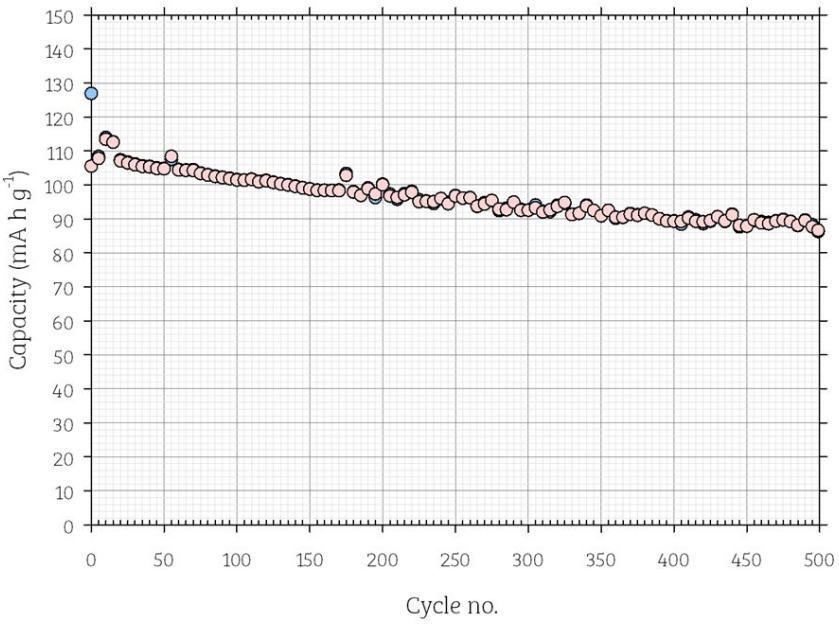

Figure 5. 11: Capacity (mA h g^{-1}) vs. cycle plot of the two $Nb_9Ti_{1.5}W_{1.5}O_{30}$ polymorphs in Li half coin cell set-up. A current of 600 mA g^{-1} (ca. "3C-3C") was applied.

The second cell was tested with asymmetric cycling, where the lithiation rate was gradually increased from 20 mA g^{-1} up to 4 A g^{-1} to represent fast charging of the $Nb_9Ti_{1.5}W_{1.5}O_{30}$ (**Figure 5. 12**). At the low current densities, the carrageenan cell demonstrated a slightly lower capacity than the PVDF cell – this disparity worsens with increasing current densities. Potential future work could also look to reduce the percentage of binder and increase the conductive additive. In the PVDF cell the ratio of AM:CB:B is 80:10:10, while this trial of the carrageen cell is 90:2:8, where the level of AM was chosen to be more representative of a commercial system.

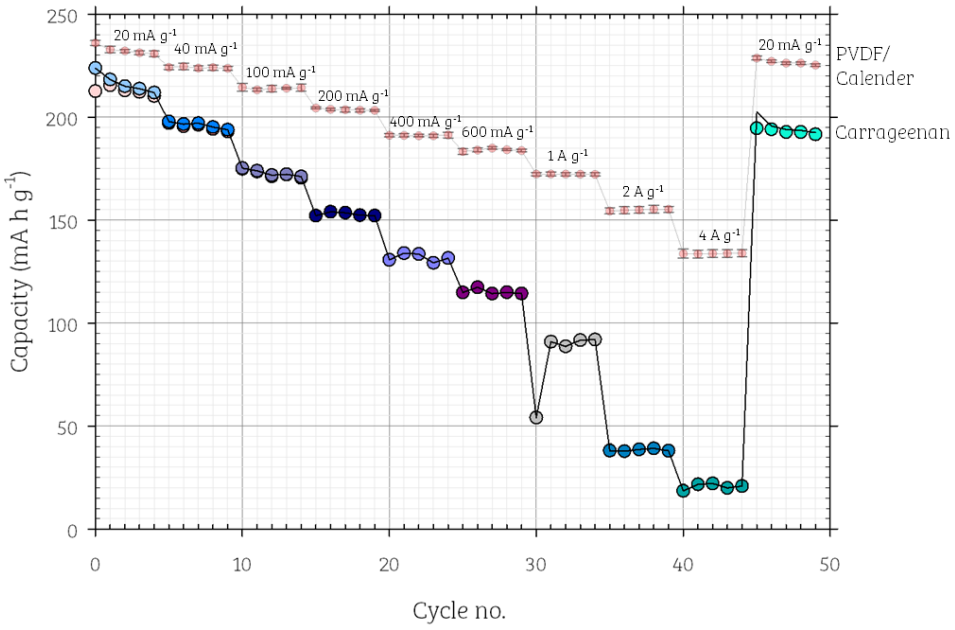

Figure 5. 12: Specific capacities of the cell with electrode AM weight of 4.59 mg, with CV applied on the lithiation step. For comparison, the PVDF/calendered cell series which underwent the same testing procedure has been added (red series).

5.4 Conclusions

This chapter has focused on preliminary work on different coating methodologies for the $Nb_9Ti_{1.5}W_{1.5}O_{30}$ aiming towards greener coating formulations. Initial work of the CMC-SBR formulation showed moving towards sequential solid additions (Coating Methodology 2) which led to improved performance upon previous mixing studies where the CB was ball milled with the AM ahead of the coating procedure. While the number of cells in this study were limited (and so further work is needed), the alteration in formulation step showed improvement in performance (varying the SBR addition), but in comparison to the PVDF cells within the previous chapter, still fell short.

The iota-carrageenan binder is a promising alternative to PVDF, with comparable performance achieved at the low current densities. However at high current densities, the disparity between this system and the PVDF binder system increases drastically, albeit the level of binder, conducting carbon used was higher for the latter.

5.5 Future Work

There are many more variables that can be explored within this body of work. As the green binder method was initially adapted to be as closed as possible to the procedure involving PVDF, future work would involve looking into refining the mixing procedure – such that the mixing duration could be reduced to reduce the amount of heat from mixing and hence, the heat's affect on the viscosity of the binders in use. Further work would also be required to evaluate the quantity of binder used as well as the amount of conductive additive i.e. the carbon black and assess performance, as well as considering the addition of carbon nanotubes, nominally in reference towards the iota-carrageenan study.

Because of the limited number of cells within this study, that mainly considered performance on formation cycling (i.e. 10 mA g^{-1}), repeats will be necessary and more advanced testing is required to consider the impact of applying high current densities, as well as long term cycling.

In addition, the ink was coated onto Cu foil and so future studies would consider the use of Al foil instead, however given prior work within the literature, this may result in a reduction of capacity[1].

While these greener alternatives are considered for improved safety and recyclability, a study assessing the improved recyclability of electrodes using iota-carrageenan could also be conducted.

5.6 References

1 F. J. Berry, X. Ren, R. Heap, P. Slater and M. F. Thomas, *Solid State Commun.*, 2005, **134**, 621–624.

2 J. E. Marshall, A. Zhenova, S. Roberts, T. Petchey, P. Zhu, C. E. J. Dancer, C. R. Mcelroy, E. Kendrick and V. Goodship, , DOI:10.3390/polym13091354.

3 Sigma-Aldrich, Hydrofluoric acid, https://www.sigmaaldrich.com/GB/en/sds/sigald/339261, (accessed 11 June 2022).

4 R. Sommerville, J. Shaw-Stewart, V. Goodship, N. Rowson and E. Kendrick, *Sustain. Mater. Technol.*, 2020, **25**, e00197.

5 T. Kazda, D. Capková, K. Jaššo, A. F. Straková, E. Shembel, A. Markevich and M. Sedlaříková, *Materials (Basel).*, , DOI:10.3390/ma14195578.

6 R. Wang, H. Mo, S. Li, Y. Gong, B. He and H. Wang, , DOI:10.1038/s41598-018-36797-z.

7 C-nergy C65 and C45, http://mtikorea.co.kr/web/smh/pdf/LeafletC-NERGYC65_45.pdf, (accessed 12 June 2022).

8 Certificate of Analysis: Carrageenan, iota-type, https://alfaaesar.com/certs/certsJ/J60603-Y15C021.pdf, (accessed 11 June 2022).

9 K. J. Griffith, K. M. Wiaderek, G. Cibin, L. E. Marbella and C. P. Grey, *Nature*, 2018, **559**, 556–563.

Chapter 6: Synthesis, characterization and application of novel Nb-based anode materials: Cu doping

Synthesis, characterization and doping studies of sodium (mixed) metal sulfates

The main body of this chapter has been reproduced from the publication: E. H. Driscoll *et al.*, "The importance of ionic radii in determining the structure obtained for sodium transition metal sulfates: Tuning structure through transition metal and selenate doping", with permission from *Journal of Solid State Chemistry*, 2020, **282**, 121080. Copyright 2019 Elsevier Inc. This chapter will focus on the synthesis of sodium mixed-metal sulfate-selenates and reinforcing the ionic radii-structure relationship found for these systems, before outlining an adapted method[1] from Driscoll *et al.* for the synthesis of a new sodium titanium sulfate system.

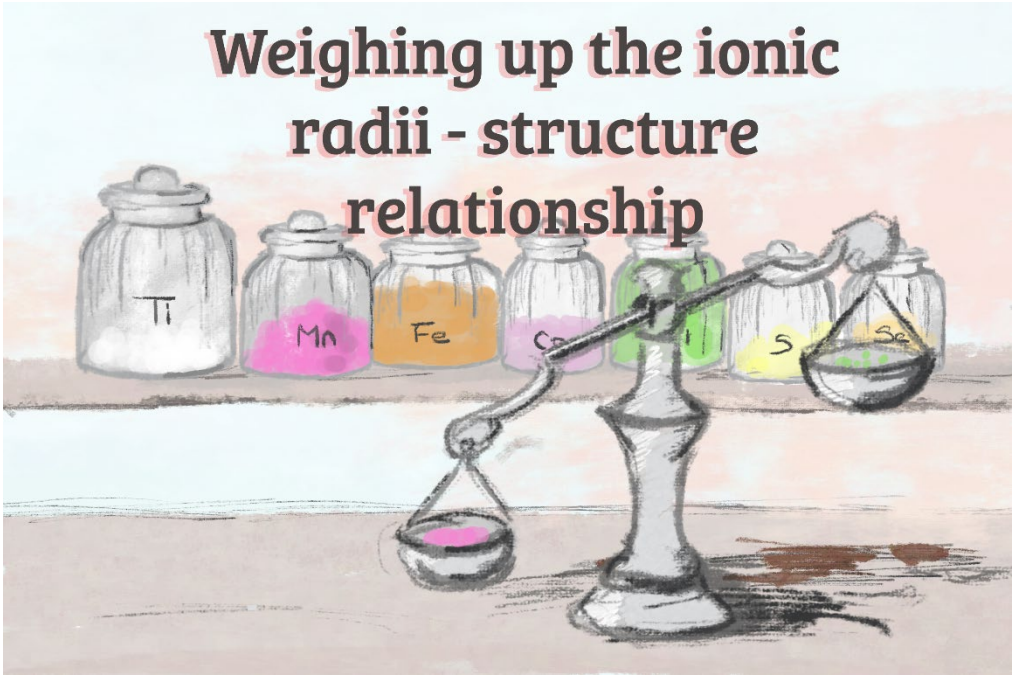

Figure 6. 1: Graphical abstract for this chapter focusing on the synthesis and doping studies of sodium (mixed) metal sulfates.

6.1 Background: Context and Aims

Considerable interest towards alluaudite-type structures for Na-ion cathodes still remains. The interest in these structures relates back to an alluaudite-sulfate system achieving the highest voltage of 3.8 V against Na metal[2] – a substantial feat given the SHE differences of Li and Na. Previous studies by Driscoll *et al.* highlighted an ionic size relationship to structure-type relationship, such that smaller metal ions (Ni, Co) had preference for the 2-1-2 bimetallic sulfate, while the larger metal ions (Mn and Fe) had preference for an alluaudite-type structure. Through selenate doping, a Ni alluaudite system was synthesized – the first of its kind.

Within the current literature, there are no reports of a fully-sulfate system for a sodium titanium system. Zhao *et al.* reported a hydrogen titanium phosphate sulfate system with a chemical formula of $H_{0.4}Ti_2(PO_4)_{2.4}(SO_4)_{0.6}$ for Li- and Na-ion battery application.[3] In keeping with the focus on Ti-based systems, NASICON $Na_3Ti_2(PO_4)_3$ has been reported.[4] To enhance electrochemical capacity the pursuit towards a sulfate-based system was considered. $Ti_2(SO_4)_3$ was synthesized through the reaction of Ti metal and concentrated sulfuric acid.[5] An alternative method makes use of the electrochemical reduction of titanyl sulfate in sulfuric acid, followed by a heat treatment under H_2.[5]

A reduction synthesis method has previously been shown by Driscoll *et al.* to access sodium vanadium sulfate systems for use in NIBs applications (**Figure 6. 2**).[1] Through the use of oxalic acid, a vanadyl oxalate intermediate can be prepared from the reduction of V_2O_5, with the subsequent additions of Na_2SO_4 and $(NH_4)_2SO_4$ to consequently form $Na_2VO(SO_4)_2$. A further reduction of vanadium from +4 down to +3 can be achieved through heating the precipitate under N_2 to form $NaV(SO_4)_2$ and

$Na_3V(SO_4)_3$. The further reduction is thought to be of carbothermal origin, due to the presence of carbon species in the resulting precipitate. This synthesis strategy is advantageous due to eliminating the complexity of previous routes, while being a facile low cost route. Therefore in avoiding the use of strong acids, this alternative method will be used to access the sodium titanium sulfate systems discussed within this chapter.

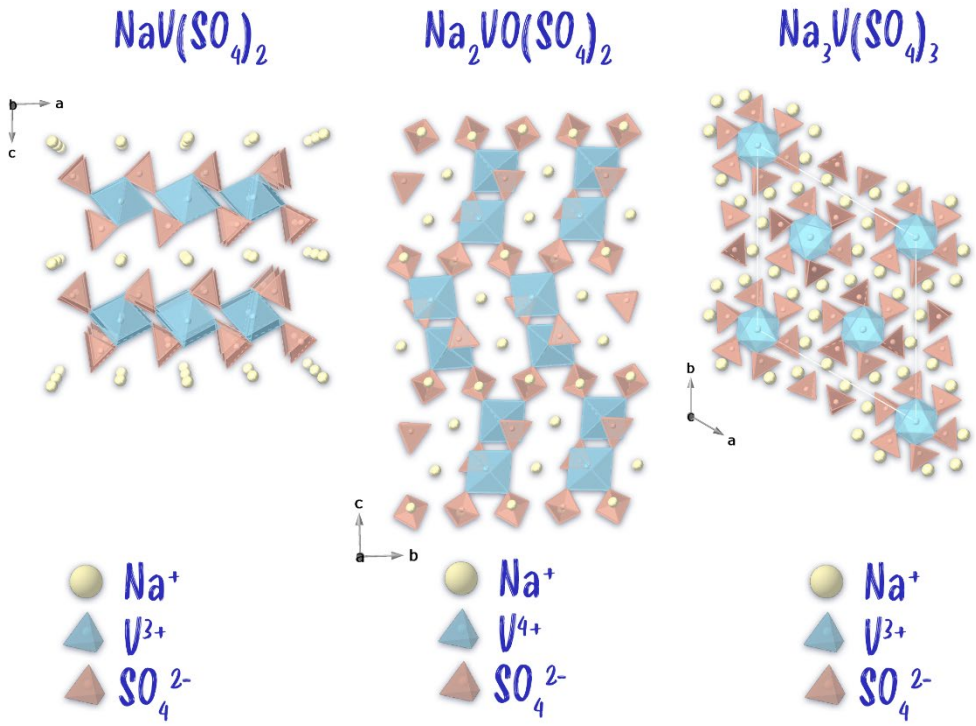

Figure 6. 2: Crystal structures (left to right) of: $NaV(SO_4)_2$, $Na_2VO(SO_4)_2$ and $Na_3V(SO_4)_3$.

Therefore the overall aims of this chapter is to explore the size relationship within the alluaudite-bimetallic sulfate/selenite relationship, through the synthesis of mixed-metal (Ni, Mn, Co and Fe) systems. Consideration towards sodium copper/zinc sulfates will be considered, in addition to the synthesis of a Ti equivalent, thus exploring the majority of the first row of transition metals.

6.2 Experimental

6.2.1 Na – M-M' – SO_4/SeO_4 systems (M = M' = Co, Ni, Mn, Fe, Cu and Zn)

This synthesis method was the same as that used previously, involving the formation of $Na_2M(SO_4)_{2-y}(SeO_4)_y.2H_2O$ before subsequent heating to dehydrate.[6] For the formation of 0.5 g (mixed-metal) $Na_2M_{1-x}M'_x(SO_4)_{2-y}(SeO_4)_y.2H_2O$ phases, stoichiometric amounts of Na_2SO_4, Na_2SeO_4 and $MSO_4.\boldsymbol{x}H_2O$ (M / M' = Co, Ni, Fe and Cu; $\boldsymbol{x}$ being equal to: 1 for Mn; 6 for Ni, and 7 for Fe and Co, and 5 for Cu) were weighed accurately and dissolved in 20 mL of deionised water and stirred at 60°C for 30 min. To prevent the oxidation of Fe^{2+}, 20 mg of L-ascorbic acid was added to the mixtures. Samples were heated overnight at either 100-110**℃** (compositions without Ni) or 130**℃** (Ni containing compositions) to obtain the dihydrate precursor.

For the dehydration of these $Na_2M_{1-x}M'_x(SO_4)_{2-y}(SeO_4)_y.2H_2O$ phases, samples were heated in alumina crucibles up to 350**℃** (300°C for Cu) in air at a rate of 0.5**℃** min^{-1} and held at this temperature for 12 hours, with the exception of the Fe and Cu containing samples, where a dry N_2 atmosphere was used instead.

The sample purity and structure determination were evaluated using powder X-ray diffraction. Structure refinements were carried out using the GSAS suite of programs using structural models from our previous study[6].

6.2.2 Na – M – SO_4 systems (M = Ti)

For the synthesis of the Na-Ti-SO_4 systems, an adapted method from Driscoll *et al.* used in the synthesis of Na-V-SO_4 systems was used.[1] $TiOSO_4$ (0.3949 g) and oxalic acid dihydrate (0.4469 g) were dispensed and added to 20 mL of deionised water. The $TiOSO_4$ and oxalic acid dihydrate was set at a molar ratio of 0.66:1. The mixture was left to stir at 60°C for 30 minutes to ensure the Ti precursor was fully dissolved (notable from the initial white cloudy mixture turning to a clear and colourless solution). The subsequent additions of Na_2SO_4 and $(NH_4)_2SO_4$ were added to the mixture and left to stir for a further hour at temperature. The samples were heated overnight at 110°C, followed by a subsequent heat treatment at 350°C at a rate of 0.5 and held at this temperature for one hour. The atmosphere used will be discussed within the results section.

The sample purity and structure determination were evaluated using powder X-ray diffraction. Structure refinements were carried out using the GSAS and TOPAS suite of programs.

6.3 Results

6.3.1 Na – M-M' – SO_4/SeO_4 systems (M = M' = Co, Ni, Mn, Fe, Cu and Zn)

Through a low temperature heat treatment, the resulting dehydrated products of $Na_2M(SO_4)_{2-y}(SeO_4)_y.2H_2O$ systems have been previously shown to form a 2-1-2 $Na_2M(SO_4)_2$ system, an alluaudite-type phase, or a mixture of these two phases dependent on the transition metal size and the selenate content. Thus, with no selenate doping, the 2-1-2 structure is adopted by the smaller transition metals ions (Co and Ni), while the alluaudite structure is adopted for the larger transition metals (Mn, Fe). Through selenate doping, a structure transformation from the 2-1-2 to the alluaudite-type is observed for both Co and Ni with higher levels of selenate doping required for the smaller Ni. Here the results for the mixed transition metal systems are presented and discussed.

6.3.1.1 Phases formed on dehydration of $Na_2Fe_{1-x}Ni_x(SO_4)_2.2H_2O$

The dehydration of Ni-doped $Na_2Fe_{1-x}Ni_x(SO_4)_2.2H_2O$ was the first system to be investigated and the resulting XRD patterns are presented in **Figure 6. 3** with cell parameters and phase fractions from Rietveld refinement shown in **Table 6. 1**. Due to issues with the stability of the Fe^{2+} in conjunction with selenate[6], only the sulfate endmember samples were investigated. The XRD data for the lowest level of Ni-doping (x = 0.1) were best fit using the off-stoichiometric alluaudite $Na_{2+2x}M_{2-x}(SO_4)_3$ phase, with Na rich vanthoffite ($Na_6M(SO_4)$) impurity phase and a small fraction of a 2-1-2 phase, thus suggesting no incorporation of Ni at this dopant level. A similar scenario was obtained for the x = 0.25 sample, albeit with a reduced alluaudite phase fraction and

potentially a low level of Ni incorporation into this phase when considering the obtained unit cell parameters. With increasing Ni content, the 2-1-2 phase fraction increases as expected, such that for x > 0.5, a phase pure 2-1-2 sample is obtained. Thus, this doping strategy shows that a range of mixed Ni/Fe systems with the 2-1-2 structure can be obtained, which may offer interesting electrochemical properties as Na-ion cathode materials.

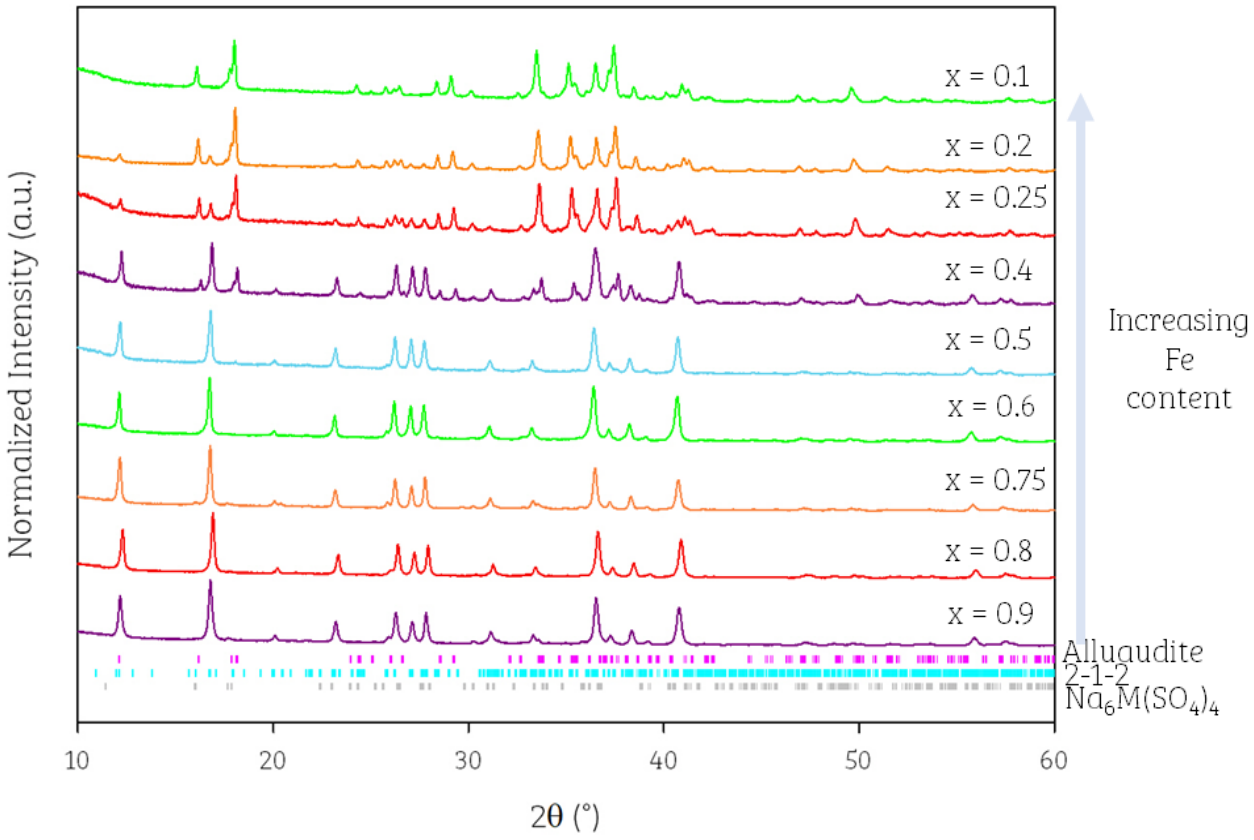

Figure 6. 3: XRD patterns obtained after dehydration of $Na_2Fe_{1-x}Ni_x(SO_4)_2.2H_2O$ (Co Kα) showing a change from mainly alluaudite ($0.1 \leq x \leq 0.25$; low Ni content) to 2-1-2 phase ($0.5 \leq x \leq 0.9$; high Ni content).

Table 6. 1: Unit cell parameters and phase fractions of the phases formed on dehydration of $Na_2Fe_{1-x}Ni_x(SO_4)_2.2H_2O$.

Dopant Level (x)	a (Å)	b (Å)	c (Å)	α (°)	β (°)	γ (°)	Cell Volume (Å^3)	Phase	% Wt fraction	Ref.
0	12.65027(15)	12.76546(14)	6.51011(7)	90.0	115.5394(4)	90.0	948.573(19)	Alluaudite	N/A	7
	23.30(4)	10.31(2)	17.35(3)	90.0	99.4(1)	90.0	4111(6)	2-1-2	3	
0.1	12.6592(5)	12.7685(5)	6.5176(2)	90.0	115.506(2)	90.0	950.83(8)	Alluaudite	80	
	9.9699 (2)	9.265(2)	8.251(2)	90.0	113.45(1)	90.0	680.2(2)	$Na_6M(SO_4)_4$	17	
	23.301(5)	10.280(2)	17.396(4)	90.0	99.15(2)	90.0	4114(8)	2-1-2	17	
0.25	12.6394(5)	12.7372(5)	6.5022(2)	90.0	115.417(2)	90.0	945.49(8)	Alluaudite	70	
	9.697(2)	9.257(2)	8.242(2)	90.0	113.48(1)	90.0	678.6(2)	$Na_6M(SO_4)_4$	13	
0.5	23.320(1)	10.2927(5)	17.409(1)	90.0	99.172(3)	90.0	4125.1(4)	2-1-2	97	
	12.648(5)	12.732(4)	6.502(2)	90.0	115.26(4)	90.0	947.0(5)	Alluaudite	3	
0.75	23.265(1)	10.275(6)	17.381(1)	90.0	99.059(4)	90.0	4103.2(4)	2-1-2	100	
1	23.196(2)	10.2577(9)	17.339(2)	90.0	98.932(6)	90.0	4075.6(7)	2-1-2	100	6

6.3.1.2 Phases formed on dehydration of $Na_2Co_xMn_{1-x}(SO_4)_{2-y}(SeO_4)_y.2H_2O$

6.3.1.2.1 x = 0.25

The XRD patterns for the lowest Co doping (M = $Co_{0.25}Mn_{0.75}$) level examined are shown in **Figure 6. 4**. For all selenate contents, the alluaudite structure was observed, with some $Na_6M(SO_4)_4$ impurity observed for the sulfate endmember (y = 0). The resulting refined unit cell parameters are shown in **Table 6. 2**.

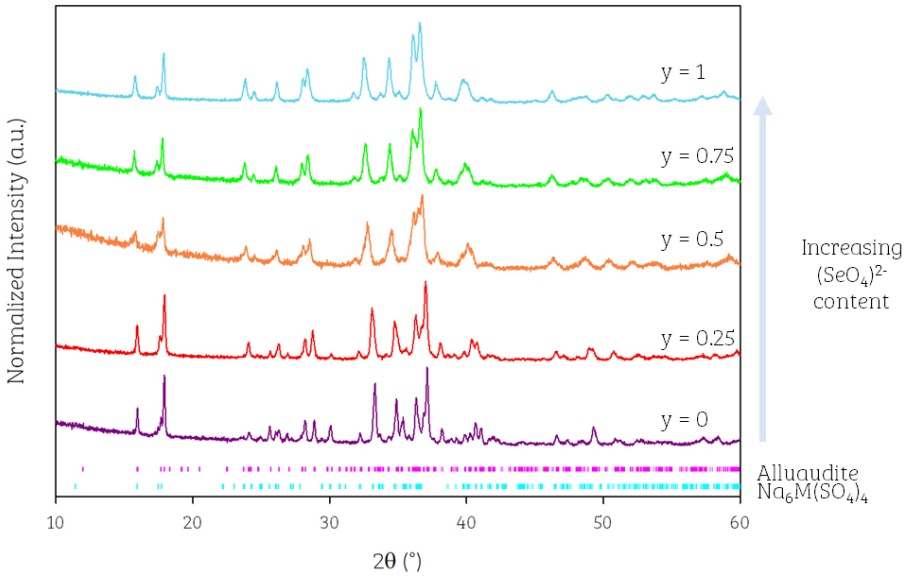

Figure 6. 4: XRD patterns obtained after dehydration of $Na_2Co_{0.25}Mn_{0.75}(SO_4)_{2-y}(SeO_4)_y.2H_2O$ (Co Kα) showing the formation of an alluaudite phase for all selenate doped compositions.

Table 6. 2: Unit cell parameters and phase fractions of the phases formed on dehydration of $Na_2Co_{0.25}Mn_{0.75}(SO_4)_{2-y}(SeO_4)_y.2H_2O$.

Dopant Level (y)	a (Å)	b (Å)	c (Å)	α (°)	β (°)	γ (°)	Cell Volume (Å^3)	Phase	%
0	9.767(1)	9.294(1)	8.297(1)	90.0	113.371(8)	90.0	691.4(1)	$Na_6M(SO_4)_4$	16
	11.5299(8)	12.8853(8)	6.5532(4)	90.0	95.186(5)	90.0	969.6(2)	Alluaudite	84
0.25	11.575(1)	12.955(1)	6.6061(5)	90.0	95.504(6)	90.0	986.1(2)	Alluaudite	100
0.5	11.632(3)	13.045(3)	6.660(1)	90.0	95.69(1)	90.0	1005.6(5)	Alluaudite	100
0.75	11.638(2)	13.079(2)	6.686(8)	90.0	95.855(9)	90.0	1012.4(3)	Alluaudite	100
1	11.663(1)	13.137(1)	6.7258(7)	90.0	96.086(7)	90.0	1024.7(3)	Alluaudite	100

6.3.1.2.2 x = 0.5

For 50:50 Co:Mn, the alluaudite phase was also shown to be present for all selenate contents. The resulting XRD data and refined unit cell parameters are shown in **Figure 6. 5** and **Table 6. 3**, respectively.

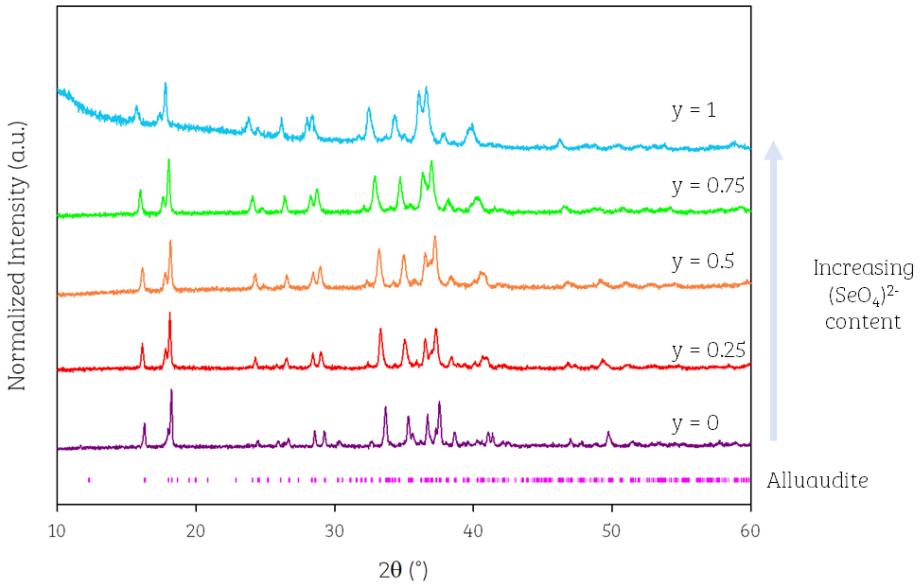

Figure 6. 5: XRD patterns obtained after dehydration of $Na_2Co_{0.5}Mn_{0.5}(SO_4)_{2-y}(SeO_4)_y.2H_2O$ (Co Kα) showing the formation of an alluaudite phase for all compositions.

Table 6. 3: Unit cell parameters of the alluaudite phase formed on dehydration of $Na_2Co_{0.5}Mn_{0.5}(SO_4)_{2-y}(SeO_4)_y.2H_2O$.

Dopant Level (y)	a (Å)	b (Å)	c (Å)	α (°)	β (°)	γ (°)	Cell Volume (Å^3)	Phase	%
0	11.490(2)	12.815(1)	6.5281(8)	90.0	95.37(1)	90.0	957.0(3)	Alluaudite	100
0.25	11.529(2)	12.889(2)	6.5808(8)	90.0	95.66(1)	90.0	973.1(3)	Alluaudite	100
0.5	11.560(2)	12.949(2)	6.6189(8)	90.0	95.84(1)	90.0	985.6(3)	Alluaudite	100
0.75	11.605(1)	13.019(1)	6.6637(7)	90.0	96.05(1)	90.0	1001.2(3)	Alluaudite	100
1	11.634(2)	13.083(2)	6.704(1)	90.0	96.24(2)	90.0	1014.4(5)	Alluaudite	100

6.3.1.2.3 x = 0.75

Increasing the level of cobalt further also led to the alluaudite phase being obtained. In this case, the sulfate endmember (x = 0) showed the presence of some $Na_6M(SO_4)_4$ impurity, while this impurity was eliminated on selenate doping (**Figure 6. 6**, **Table 6. 4**).

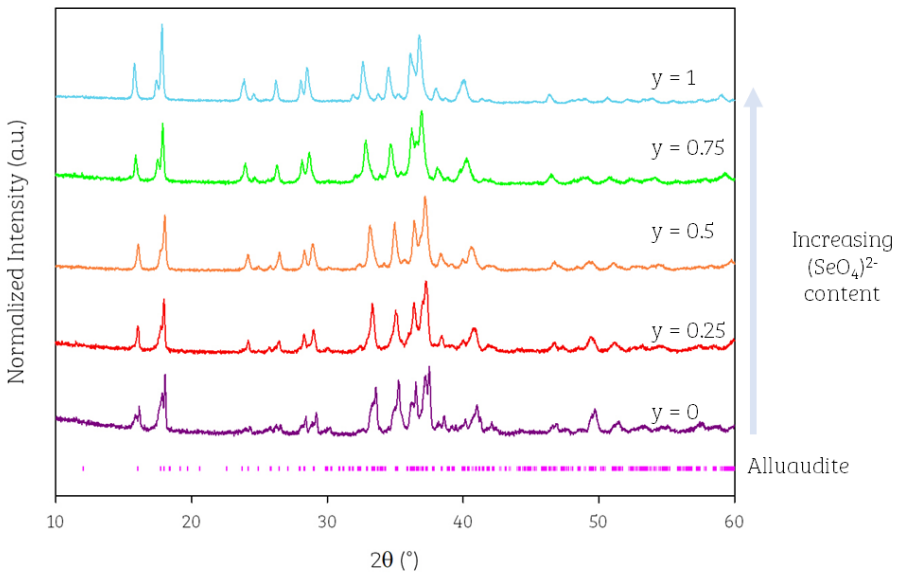

Figure 6. 6: XRD patterns obtained after dehydration of $Na_2Co_{0.75}Mn_{0.25}(SO_4)_{2-y}(SeO_4)_y.2H_2O$ (Co Kα) showing the formation of an alluaudite phase for all compositions.

Table 6. 4: Unit cell parameters of the alluaudite phase formed on dehydration of $Na_2Co_{0.75}Mn_{0.25}(SO_4)_{2-y}(SeO_4)_y.2H_2O$.

Dopant Level (y)	a (Å)	b (Å)	c (Å)	α (°)	β (°)	γ (°)	Cell Volume (Å^3)	Phase	%
0	11.492(1)	12.761(1)	6.5305(7)	90.0	95.827(8)	90.0	952.8(3)	Alluaudite	80
	9.749(2)	9.250(5)	8.286(4)	90.0	113.18(2)	90.0	686.9(4)	$Na_6M(SO_4)_4$	20
0.25	11.522(2)	12.830(2)	6.5532(8)	90.0	95.69(1)	90.0	964.0(3)	Alluaudite	100
0.5	11.551(1)	12.890(1)	6.5950(6)	90.0	95.898(8)	90.0	976.8(3)	Alluaudite	100
0.75	11.587(1)	12.961(2)	6.388(7)	90.0	96.10(1)	90.0	991.3(3)	Alluaudite	100
1	11.6122(9)	13.0112(10)	6.6729(5)	90.0	96.255(7)	90.0	1002.2(2)	Alluaudite	100

6.3.1.3 Phases formed on dehydration of $Na_2Ni_xMn_{1-x}(SO_4)_{2-y}(SeO_4)_y.2H_2O$ (x = 0.25, 0.5, 0.75)

6.3.1.3.1 x = 0.25 and 0.5

For Ni contents, x = 0.25 and 0.5, the sulfate endmember was shown to consist of a phase mixture, with the alluaudite-type phase becoming more dominant with increasing selenate content, as shown by the XRD data (**Figure 6. 7** and **Figure 6. 8**). In particular, for the lower Ni content (x = 0.25), a phase pure alluaudite was obtained for y ≥0.5 (**Table 6. 5**). However, for the higher Ni content (x = 0.5), mixed (alluaudite and 2-1-2) phases were obtained throughout, with the phase fraction of the alluaudite phase increasing as the selenate content increased, such that for y = 1 the PXRD pattern shows mainly alluaudite (**Table 6. 6**).

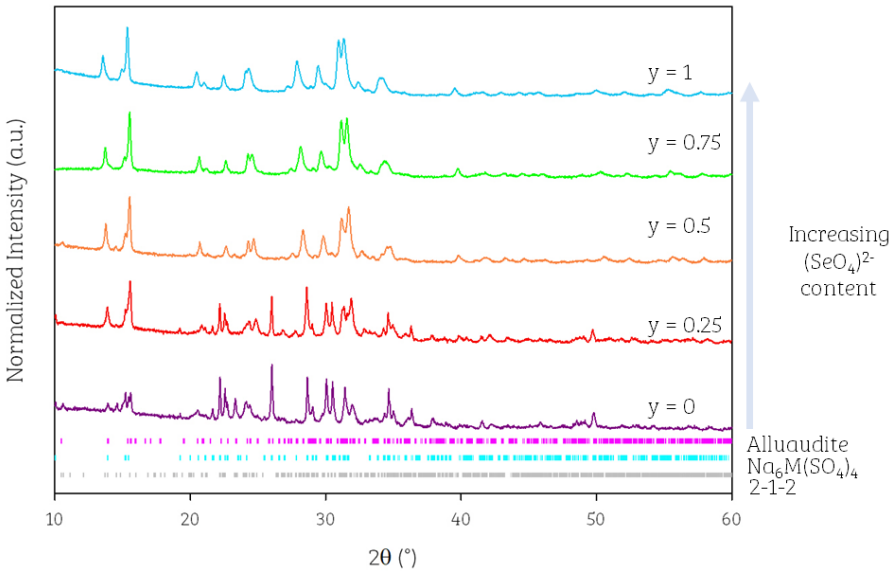

Figure 6. 7: XRD patterns obtained after dehydration of $Na_2Ni_{0.25}Mn_{0.75}(SO_4)_{2-y}(SeO_4)_y.2H_2O$ (Cu Kα) showing formation of phase pure alluaudite for y≥0.5.

Table 6. 5: Refined unit cell parameters of the phases formed on dehydration of $Na_2Ni_{0.25}Mn_{0.75}(SO_4)_{2-y}(SeO_4)_y.2H_2O$

Dopant Level (y)	a (Å)	b (Å)	c (Å)	α (°)	β (°)	γ (°)	Cell Volume (Å^3)	Phase	% Wt fraction
0	23.34(4)	10.32(1)	17.35(3)	90.0	98.33(9)	90.0	4135(5)	2-1-2	13
	9.741(2)	9.300(1)	8.278(1)	90.0	113.207(7)	90.0	689.2(2)	$Na_6M(SO_4)_4$	64
	11.532(5)	12.875(6)	6.562(4)	90.0	95.26(7)	90.0	970.2(8)	Alluaudite	23
0.25	9.747(2)	9.320(2)	8.287(1)	90.0	113.153(7)	90.0	692.2(2)	$Na_6M(SO_4)_4$	40
	11.574(2)	12.937(3)	6.589(1)	90.0	95.51(3)	90.0	982.1(4)	Alluaudite	60
0.5	11.597(1)	13.015(1)	6.6444(7)	90.0	95.75(1)	90.0	997.8(3)	Alluaudite	100
0.75	11.629(2)	13.096(2)	6.6952(8)	90.0	95.94(1)	90.0	1014.2(3)	Alluaudite	100
1	11.648(1)	13.124(1)	6.7182(6)	90.0	96.11(1)	90.0	1021.1(3)	Alluaudite	100

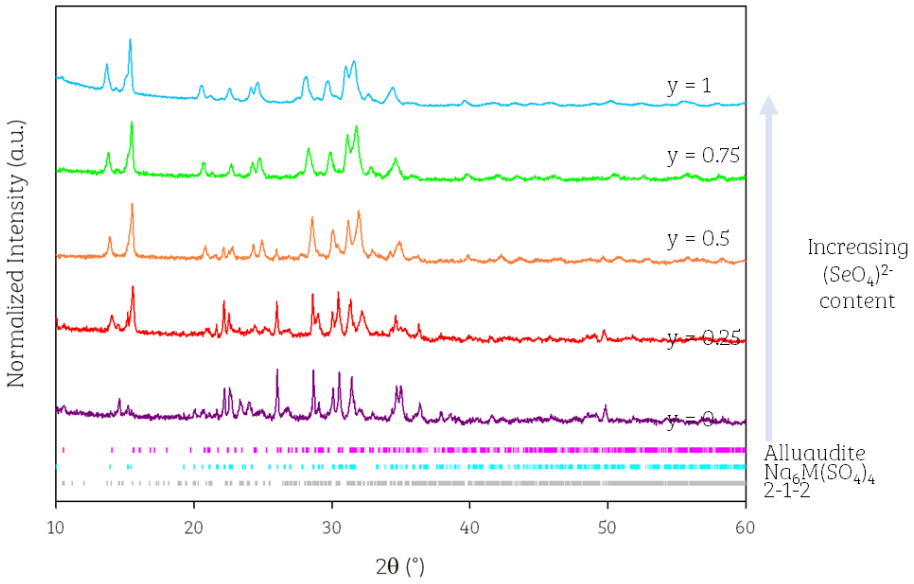

Figure 6. 8: XRD patterns obtained after dehydration of $Na_2Ni_{0.5}Mn_{0.5}(SO_4)_{2-y}(SeO_4)_y.2H_2O$ (Cu Kα) showing increasing alluaudite phase fraction with increasing selenate content.

Table 6. 6: Refined unit cell parameters of the phases formed on dehydration of $Na_2Ni_{0.5}Mn_{0.5}(SO_4)_{2-y}(SeO_4)_y.2H_2O$.

Dopant Level (y)	a (Å)	b (Å)	c (Å)	α (°)	β (°)	γ (°)	Cell Volume (Å^3)	Phase	% Wt fraction
0	23.231(5)	19.283(2)	17.350(3)	90.0	99.20(1)	90.0	4111(1)	2-1-2	12
	9.733(2)	9.289(3)	8.273(2)	90.0	113.19(1)	90.0	688.5(1)	$Na_6M(SO_4)_4$	85
	11.499(5)	12.759(5)	6.461(4)	90.0	95.49(6)	90.0	943.6(7)	Alluaudite	3
0.25	9.747(2)	9.319(2)	8.281(1)	90.0	113.180(8)	90.0	691.5(2)	$Na_6M(SO_4)_4$	48
	11.554(3)	12.762(3)	6.511(2)	90.0	95.79(4)	90.0	955.2(5)	Alluaudite	52
0.50	9.746(3)	9.333(4)	8.288(3)	90.0	113.19(2)	90.0	693.0(4)	$Na_6M(SO_4)_4$	21
	11.588(2)	12.876(2)	6.584(1)	90.0	95.90(2)	90.0	977.1(4)	Alluaudite	79
0.75	23.456(5)	10.295(2)	17.533(3)	90.0	98.96(2)	90.0	4182(1)	2-1-2	4
	11.615(1)	12.958(1)	6.6342(6)	90.0	96.13(1)	90.0	992.8(2)	Alluaudite	96
1	23.270(2)	10.339(7)	17.43(1)	90.0	97.85(6)	90.0	4153(4)	2-1-2	2
	11.652(1)	13.016(1)	6.6767(7)	90.0	96.27(1)	90.0	1006.6(5)	Alluaudite	98

6.3.1.3.2 x = 0.75

On increasing the Ni content further (x = 0.75), the 2-1-2 phase was shown to be present for lower selenate levels (y ≤ 0.25), with the alluaudite-type structure observed for higher selenate levels (y ≥ 0.5) (**Figure 6. 9, Table 6. 7**). For the sulfate endmember, an $Na_6M(SO_4)_4$ impurity phase was found to be present.

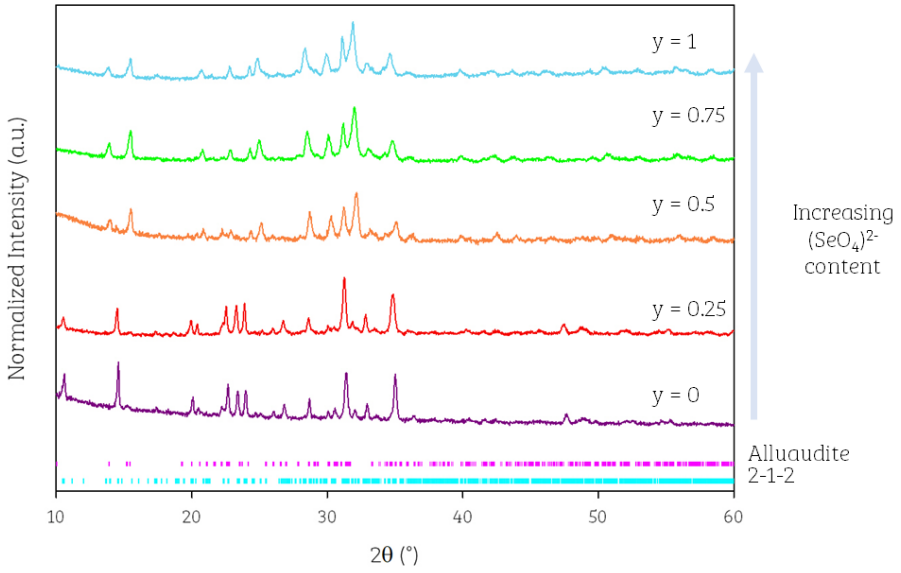

Figure 6. 9: XRD patterns obtained after dehydration of $Na_2Ni_{0.75}Mn_{0.25}(SO_4)_{2-y}(SeO_4)_y.2H_2O$ (Cu Kα) showing the phase change from 2-1-2 to alluaudite with increasing selenate.

*Table 6. 7: Refined unit cell parameters of the phases formed on dehydration of $Na_2Ni_{0.75}Mn_{0.25}(SO_4)_{2-y}(SeO_4)_y.2H_2O$. * denotes refinement whereby the main phase has been refined only and does not take into account secondary phases.*

Dopant Level (y)	a (Å)	b (Å)	c (Å)	α (°)	β (°)	γ (°)	Cell Volume (Å^3)	Phase	%
0	23.286(4)	10.285(2)	17.386(4)	90.0	99.14(1)	90.0	4111(1)	2-1-2	74
	9.738(4)	9.284(6)	8.279(4)	90.0	113.15(3)	90.0	688.1(4)	$Na_6M(SO_4)_4$	26
0.25*	23.380(5)	10.306(3)	17.457(6)	90.0	98.95(1)	90.0	4155(2)	2-1-2	*
0.5	11.560(3)	12.780(3)	6.538(1)	90.0	96.04(2)	90.0	960.6(6)	Alluaudite	100
0.75	11.593(3)	12.847(3)	6.584(1)	90.0	96.21(2)	90.0	974.7(6)	Alluaudite	100
1	11.566(1)	12.857(1)	6.6023(9)	90.0	96.45(2)	90.0	975.4(2)	Alluaudite	100

6.3.1.4 Alternative Structure Systems

6.3.1.5 Phases formed on dehydration of $Na_2M(SO_4)_{2-y}(SeO_4)_y.2H_2O$, M = Cu and Zn

6.3.1.5.1 M = Cu

Oxoanion studies involving the intermediate dihydrate products were previously investigated by Driscoll *et al.* for the metals Mn, Fe, Co, Ni and Cu[8], with the corresponding dehydration products and structure types studied albeit without the successful determination of the Cu-analogue structure[6]. At the time, the resulting structure of the Cu product remained unresolved, although a recent report by Kovrugin *et al.* has now successfully identified the structure of this phase (**Figure 6. 10**)[9]. Therefore, using this structural model, we have reinvestigated the phases obtained from dehydration of $Na_2Cu(SO_4)_{2-y}(SeO_4)_y.2H_2O$. The resulting XRD patterns (**Figure 6. 11**) indicate that all phases are isostructural with the previously reported $Na_2Cu(SO_4)_2$, illustrating no change in structure on selenate doping for this system. The refined unit cell parameters for all phases are given in **Table 6. 8,** and show, as expected, increasing unit cell parameters with increasing selenate content. The different structure adopted by this system is most likely related to the fact that Cu^{2+} is a Jahn Teller ion. This leads to the adoption of a tetragonal pyramidal coordination with an additional two longer bonds (**Figure 6. 10**).[9]

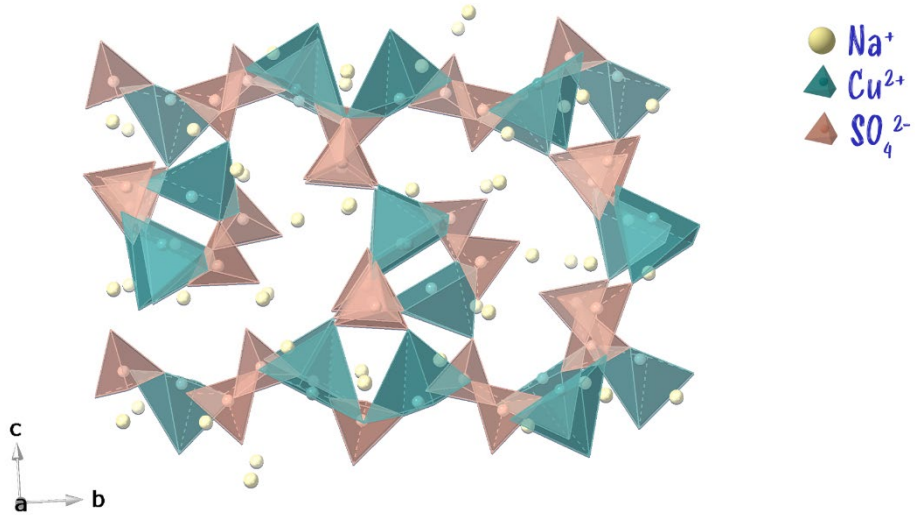

Figure 6. 10: Crystal structure of $Na_2Cu(SO_4)_2$.

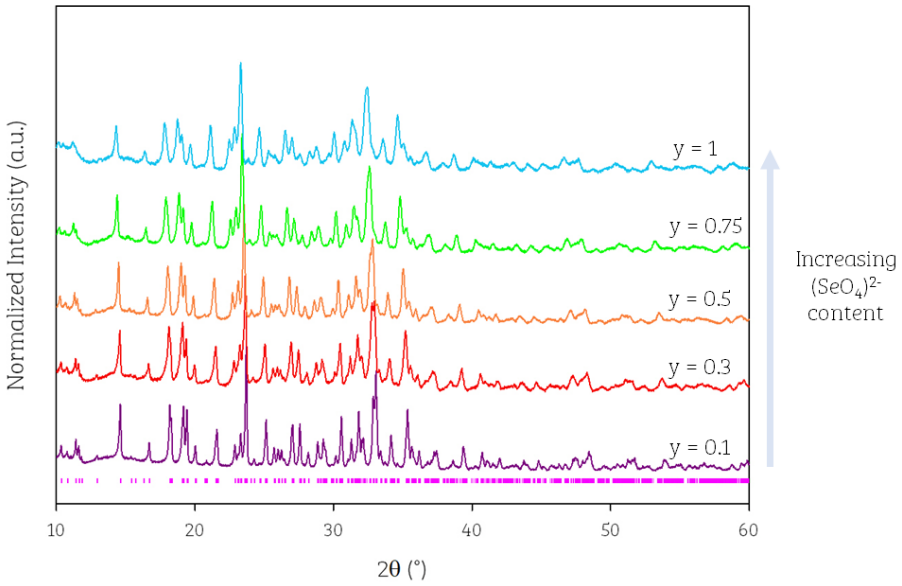

Figure 6. 11: XRD patterns of $Na_2Cu(SO_4)_{2-y}(SeO_4)_y$ (y = 0.1 upto 1) (Cu Kα).

Table 6. 8: Refined unit cell parameters of $Na_2Cu(SO_4)_{2-y}(SeO_4)_y$ (x = 0.1 upto 1) using the structural mode reported by Kourugin et al.[9]

Dopant Level (y)	a (Å)	b (Å)	c (Å)	α (°)	β (°)	γ (°)	Cell Volume (Å^3)
0.1	8.9808(3)	15.5684(4)	10.1634(3)	90.0	107.087(2)	90.0	1358.30(9)
0.3	9.0023(7)	15.615(1)	10.2026(9)	90.0	107.117(6)	90.0	1370.7(3)
0.5	9.0307(4)	15.6667(7)	10.2455(4)	90.0	107.149(5)	90.0	1385.12(8)
0.75	9.0698(8)	15.739(1)	10.3016(9)	90.0	107.175(6)	90.0	1405.0(3)
1	9.112(1)	15.816(2)	10.360(1)	90.0	107.171(9)	90.0	1426.5(4)

6.3.1.5.2 M = Zn

The equivalent Zn series was also investigated with the gradual selenate doping into the system. Although on inspection, the resulting XRD patterns (**Figure 6. 12**) appear to emulate the same patterns shown previously from 2-1-2 to alluaudite, including showing a phase transformation, the XRD patterns could not be fitted with the current model used for the other metal series. It is suspected the difference originates from the Zn having preference for a co-ordination of 5 (**Figure 6. 13**), rather than 6 seen for the previous metals (Ni, Co, Mn and Fe) and further work is needed to evaluate the structure of these materials.

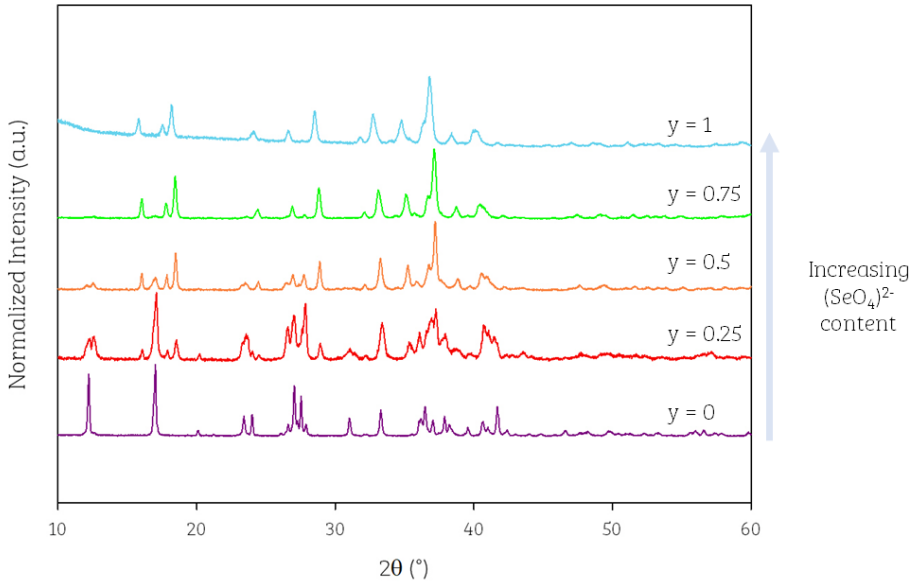

Figure 6. 12: XRD patterns of $Na_2ZnSO_4)_{2-y}(SeO_4)_y$ (y = 0.1 upto 1) (Cu Kα).

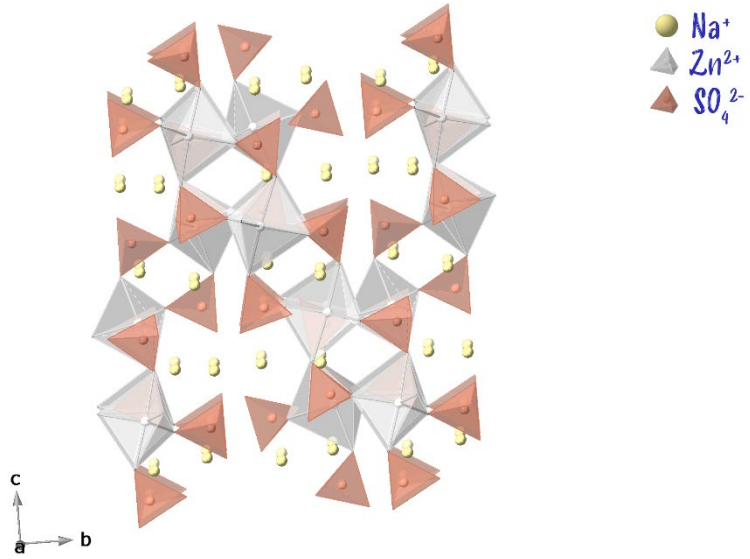

Figure 6. 13: Crystal structure of $Na_2Zn(SO_4)_2$ - ICSD collection code 170139.

6.4 Discussion

6.4.1 Na – M-M' – SO_4/SeO_4 systems (M = M' = Co, Ni, Mn, Fe, Cu and Zn)

Previous work had shown that the metal ionic radii and selenate content influenced the structure obtained on dehydration of $Na_2M(SO_4)_{2-y}(SeO_4)_y.2H_2O$ (M = Mn, Co and Ni) samples: in particular the 2-1-2 phase was observed for the smaller transition metals ions, while the alluaudite-type structure for the larger ions. On selenate doping, there was a tendency for all systems to adopt the alluaudite structure, with the selenate content required to obtain this structure depending on the size of the transition metal. This led to a proposed relationship based on the combined ionic radii of the metal ion and weighted average S/Se ionic radii. In this work, these studies have been extended to mixed transition metal systems, allowing the size relationship plot to be updated, as shown in Figure 6. 14. The results from these new mixed systems further confirms the ionic radii sum relationship, as the compositions from this study fit within the boundaries reported previously. Thus, this work confirms that structure-type formation preference can be predicted using this relationship plot, and so it can be potentially exploited to design new alluaudite or 2-1-2 phases. However, it must be noted this ionic structure relationship is limited to metals which prefer octahedral geometry, as the Cu series does not form the alluaudite-type structure upon selenate doping but rather adopts a different structure altogether, most likely correlated with the fact that Cu^{2+} is a Jahn Teller ion. In addition, Zn which has preference for a co-ordination of 5, could not be refined with the current structural model and has not been included in the relationship plot.

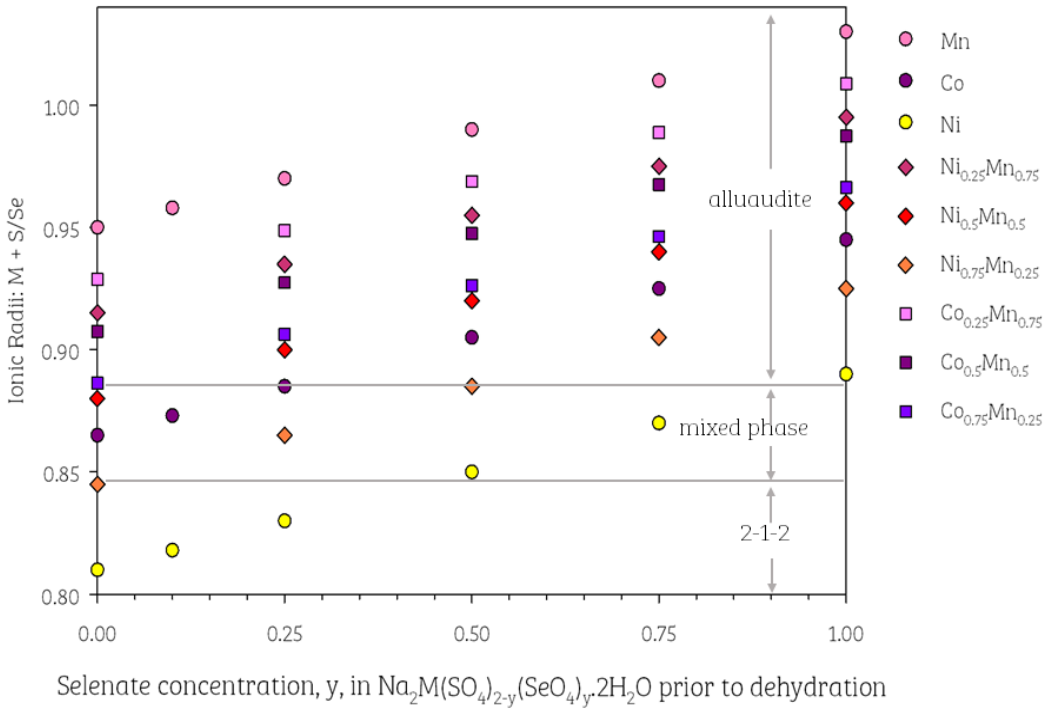

Figure 6. 14: Revised plot of sum of the weighted average ionic radii of M and the weighted average ionic radius of S/Se (where M = Mn, Fe, Co and Ni) vs selenate content. Increasing the transition metal ionic radii, and/or increasing the selenate content, leads to the alluaudite-type structure becoming more favoured.

The variation of cell volumes for both the alluaudite and 2-1-2 phases against level of selenate doping are shown in **Figure 6. 15** and **Figure 6. 16**. Both plots show a general increase in cell volume with the increase in selenate content. The alluaudite cell volumes show similar cell parameter increase in gradients for all series, consistent with a uniform increase in cell size on selenate doping. For the 2-1-2 (**Figure 6. 16**) and Cu series (**Figure 6. 17**), a similar percentage increase is also observed, confirming the selenate incorporation.

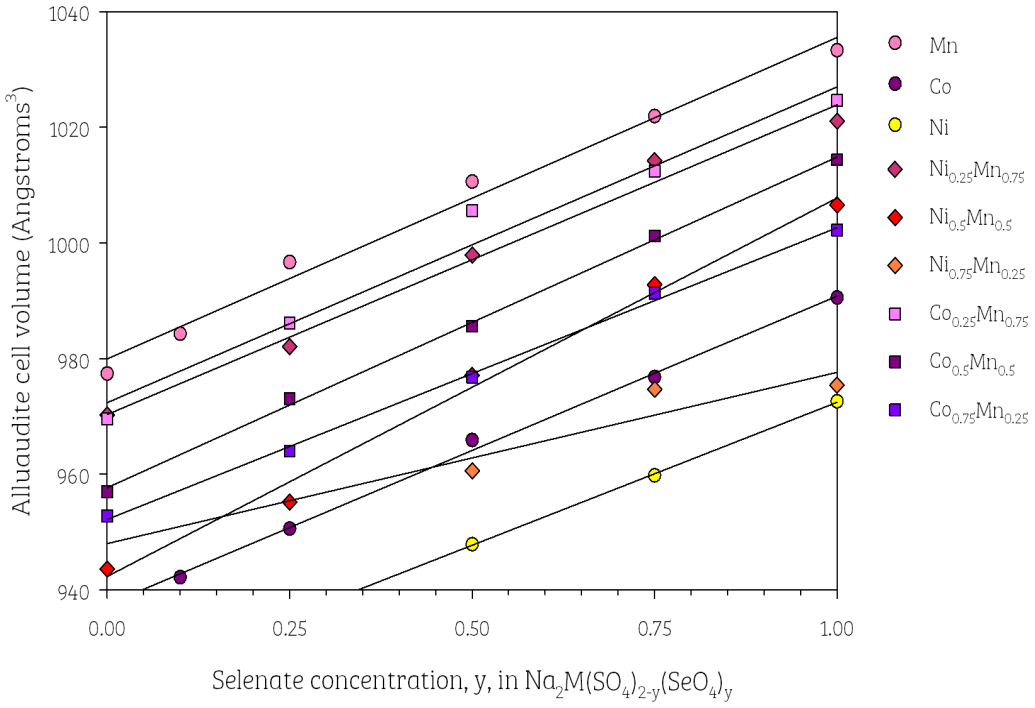

Figure 6. 15: Variation in cell volumes with selenate content for the alluaudite phases.

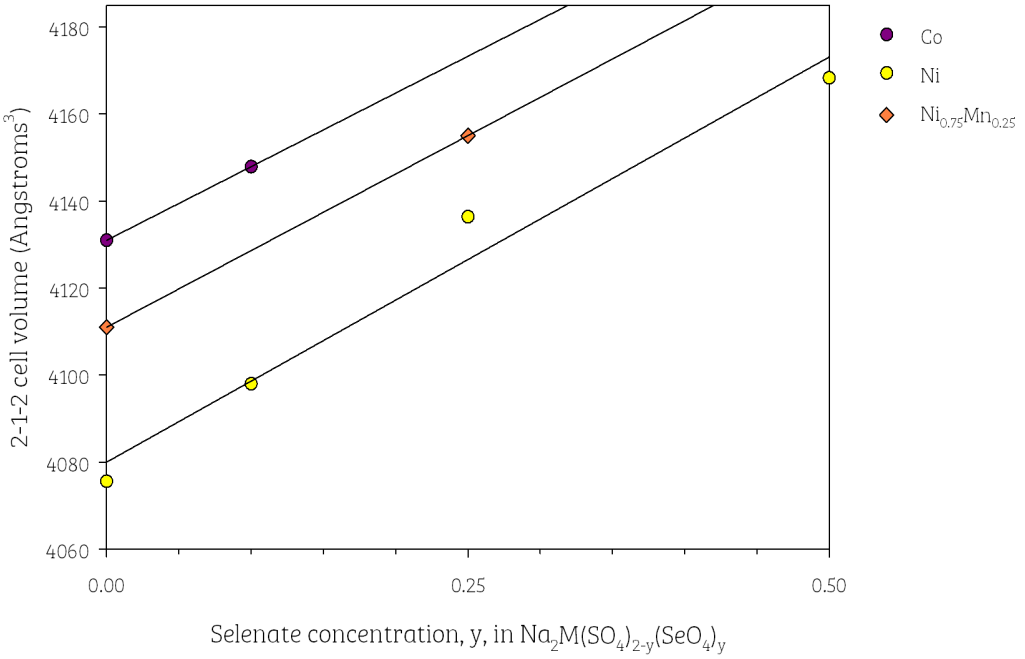

Figure 6. 16: Variation in cell volumes with selenate content for 2-1-2 samples. (Refined unit cell parameters with a phase weight percent less than or equal to 4% have not been included in this plot).

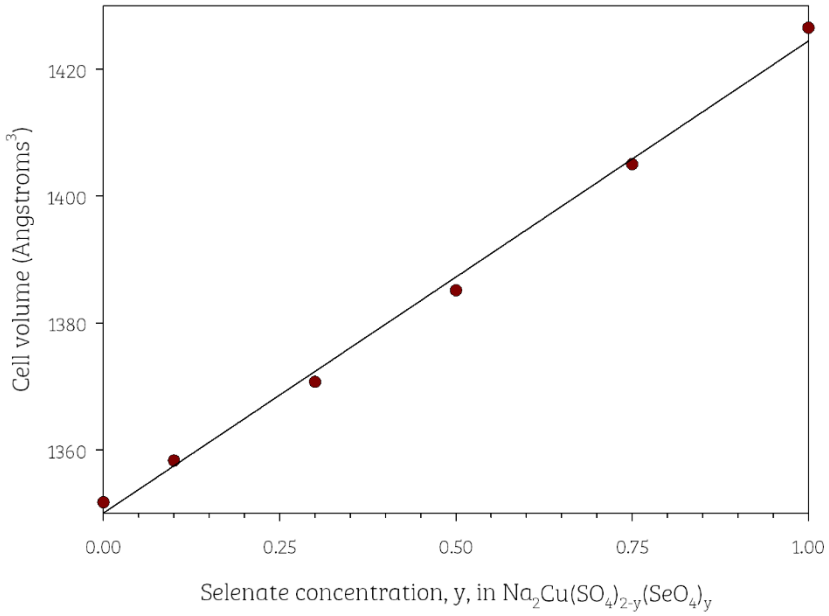

Figure 6. 17: Variation in cell volumes with selenate content for $Na_2Cu(SO_4)_{2-y}(SeO_4)_y$. Sulfate endmember cell volume value from ref [9].

6.5 Results and Discussion

6.5.1 Na-Ti-SO_4 Systems

Using Driscoll *et al.*'s method, the synthesis of $Na_3Ti(SO_4)_3$ was attempted. In the vanadium reduction, the ratio of V_2O_5 and oxalic acid was 1:3. For the titanium reduction, the ratio was altered to be 2:3 with respect to $TiOSO_4$ and oxalic acid. This ratio reflects the stoichiometries required to form titanium (III) oxalate ($Ti_2C_6O_{12}$). Within the procedure, the titanium oxysulfate is fully dissolved with the oxalic acid before any further additions of the sodium sulfate and ammonium sulfate. The solution was left to evaporate overnight and a white precipitate was observed to form and collected. The resulting sample, after a N_2 treatment, appeared as a light brown/beige with respect to the colour (**Figure 6. 18**). Titanium (III) complexes are usually observed to be violet in colour, while titanium (IV) compositions remain white due to no electron occupation of d-orbitals, and so the observed colour is inconclusive of the Ti oxidation state.

Figure 6. 18: Photo of the white precipitate (left) and the beige appearance of $Na_3Ti(SO_4)_3$ after heating under N_2.

The resulting XRD pattern was found to match quite closely to the $Na_3V(SO_4)_3$ phase (SG: R -3 h), as shown in the resulting profile from attempting to the fit data on GSAS

(**Figure 6. 19**). The fractional co-ordinates and occupancies were not refined at this stage, only the unit cell.

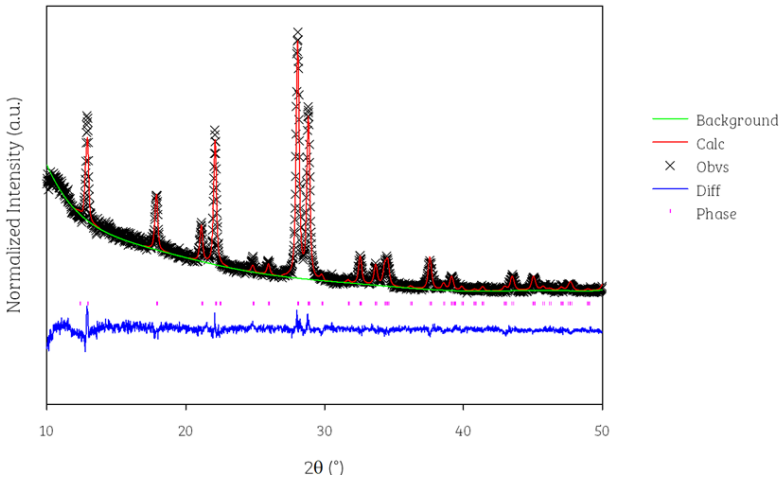

Figure 6. 19: Observed, calculated and difference XRD profiles for $Na_3Ti(SO_4)_3$ (R_{wp} - 6.68%, R_p – 5.22%) (Cu Kα).

The obtained unit cell parameters were obtained for the Ti system and compared against the known V equivalent system, as shown in **Table 6. 9**. The greater cell volume observed for the titanium equivalent system would suggest, based upon the ionic radii (**Table 6. 10**), the synthesis route has resulted in the reduction of Ti^{4+} to Ti^{3+}, given the larger ionic radius of the latter.

Table 6. 9: Unit cell parameters of $Na_3V(SO_4)_3$ [ref. 1] and $Na_3Ti(SO_4)_3$.

Sample	a (Å)	b (Å)	c (Å)	α (°)	β (°)	γ (°)	Cell Volume ($Å^3$)	Ref.
$Na_3V(SO_4)_3$	13.4460(6)	13.4460(6)	9.0781(5)	90.0	90.0	120.0	1421.4(2)	1
$Na_3Ti(SO_4)_3$	13.769(2)	13.769(2)	9.022(1)	90.0	90.0	120.0	1481.3(5)	

Table 6. 10: Ionic radii of selected metal ions of interest for this system.[10]

Ion	CN	Ionic Radii (Å)
Na^+	6	1.02
V^{3+}	6	0.64
Ti^{3+}	6	0.67
Ti^{4+}	6	0.605

However to confirm the oxidation state of the Ti, the sample was heated also under ambient atmosphere. The resulting XRD patterns for both conditions are shown in Figure 6. 20, and regardless of the differences of atmosphere, the same XRD pattern is returned. From this, it can be inferred the oxidation state of Ti remains as +4. With this result, the original formula of $Na_3Ti(III)(SO_4)_3$ would now be invalid and not be charge balance with the change in Ti oxidation. In addition, with the differences in synthesis atmospheres used, the resulting colours of the samples are different – the sample heated under air was white (Figure 6. 21).

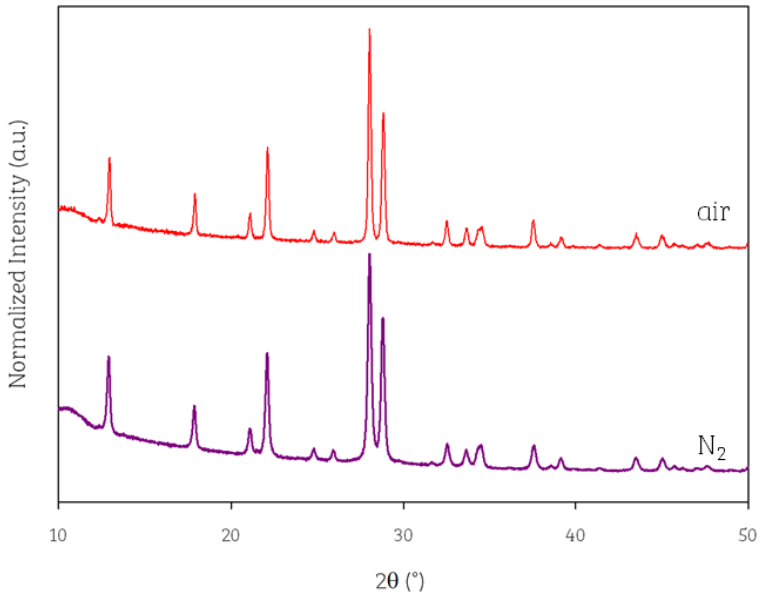

Figure 6. 20: Comparison of the XRD pattern of $Na_3Ti(SO_4)_3$ heated under different atmospheres N_2 (purple; bottom) and air (red; top) to 350°C/1hr/0.5°C min^{-1} (Cu Kα).

Figure 6. 21: Photograph of the $Na_3Ti(SO_4)_3$ after half the sample was heated in air (top) and the other half under N_2 (bottom).

Thus to determine the correct chemical formula, samples were produced with off-stoichiometric sodium and sulfate content to charge balance, in addition to reducing

the amount of titanium to reflect the new oxidation state (**Figure 6. 22**). However all variations to charge balance were not phase pure compared to the original stoichiometry used.

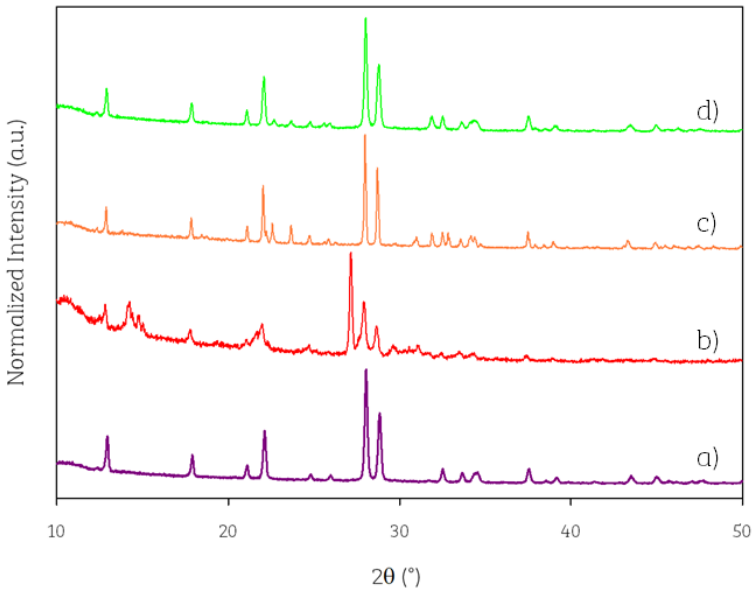

Figure 6. 22: Resulting XRD patterns of a) $Na_3Ti(SO_4)_3$, b) $Na_2Ti(SO_4)_3$, c)$Na_3Ti_{0.66}(SO_4)_3$ and d)$Na_4Ti(SO_4)_{3.5}$. All samples heated to 350°C/1hr/0.5°C min^{-1} under air (Cu Kα).

To deduce the oxidation state of the titanium, samples synthesized both under N_2 and air, with the same heating programme, were submitted to Diamond Lightsource Ltd Energy Materials Block Allocation Group SP14239, with reference samples of Ti_2O_3 and $TiOSO_4$.

Sample Composition	Amount of Sample (mg)	Amount of Avicel® cellulose (mg)
$Na_3Ti(SO_4)_3/N_2$	15	50
$Na_3Ti(SO_4)_3$/Air	15	50
$TiOSO_4$	6	50
$Ti2O_3$	3	50

The resulting absorption data confirmed the oxidation state to be Ti^{4+} (**Figure 6. 23**), where regardless of the different synthesis conditions (air/N_2), both $Na_3Ti(SO_4)_3$ samples overlap and the bands resemble closely to the Ti^{+4} reference of $TiOSO_4$.

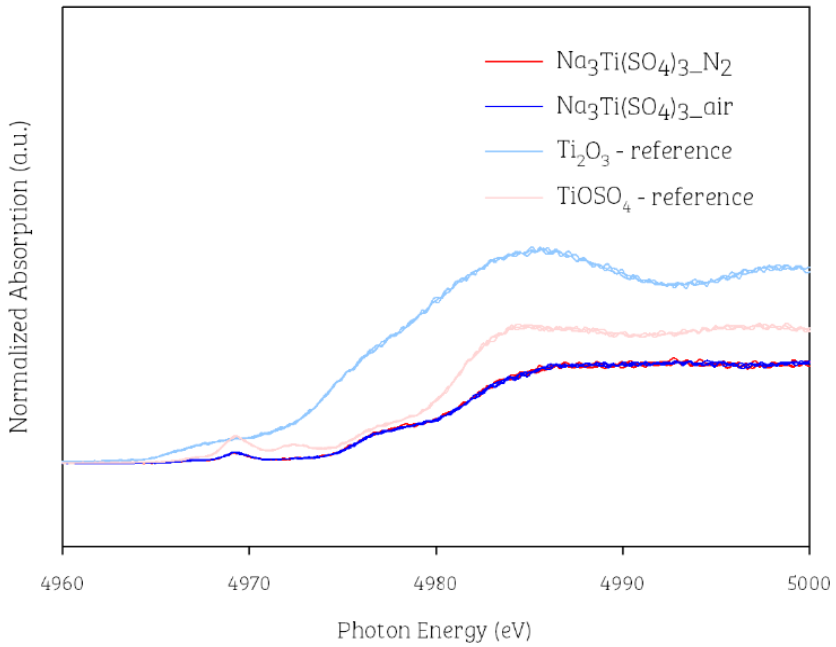

Figure 6. 23: Resulting absorption data of $Na_3Ti(SO_4)_3$-N_2 (red), $Na_3Ti(SO_4)_3$-air (blue), Ti_2O_3 -reference (light blue) and $TiOSO_4$ – reference (pink), collected by the Energy Materials BAG.

The slight colour difference between samples under the different atmospheres may suggest a small amount of Ti^{3+}.

The sodium-titanium-sulfate sample produced under air was run on TGA-MS to help elucidate the sample's chemical formula, given the confirmation of the titanium oxidation state. The sample was heated up to 700°C/5°Cmin^{-1} under N_2 in an attempt to decompose the sample. After heating, the sample was found to have melted into the crucible, but a small amount of sample was obtained to run a PXRD – where the

diffraction pattern consisted of Na_2SO_4 and TiO_2. In the TGA-MS run, up to 100°C there is m/z loss of 17 and 18, which can be attributed at this stage to surface water. At ca. 400°C there is an apparent increase for these currents once again. No loss of SO_4 (m/z = 96) was apparent throughout the run. From the change in stoichiometries study (**Figure 6. 22**), the potential of hydroxide within the structure was not considered, but may provide suitable charge balancing for the Ti^{+4}.

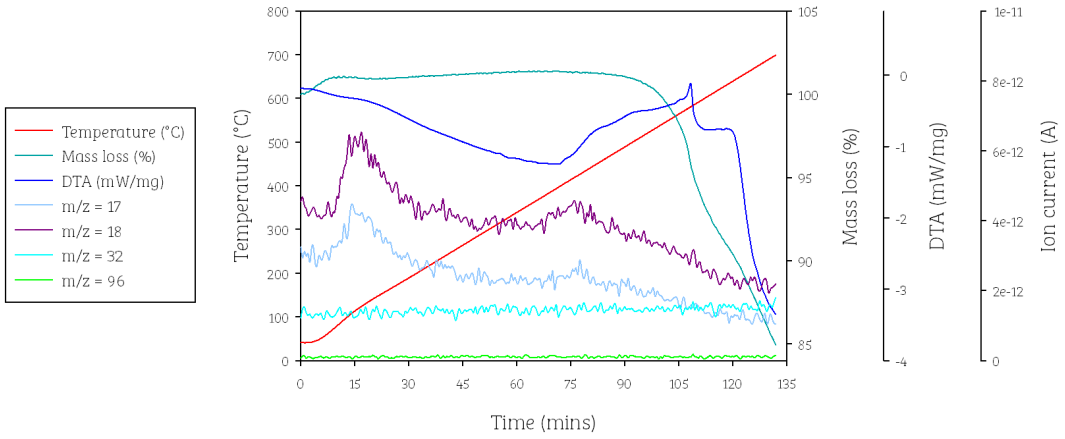

Figure 6. 24: TGA-MS plot of sample $Na_3Ti(SO_4)_3$-air heated up to 700°C/5°Cmin^{-1}/N_2.

With the structure potentially being of the formula $Na_3Ti(SO_4)_{2.5}((OH)_4)_{0.5}$ (RMM = 390.991 g mol^{-1}), the mass loss of 15% observed would result in the final mass of the sample to be 29.0 mg. The loss of mole of water would equate to 1.6 mg. Through determining the amount of Na_2SO_4 and TiO_2 remaining within the sample (based upon a molar ratio of 1.5 and 1, respectively), at the end of the study, this would summate to 25.5 mg. Thus, it would suggest another component is being lost on heating, but equally there is 3.42 mg unaccounted for in the final mass remaining.

Returning to the original .cif of $Na_3V(SO_4)_3$ with SG of R-3h, the fit was once again quite good. Small impurities were noted which are likely from the age of the sample rather than the initial synthesis conditions (left for 1 month before re-scanning for higher quality data for refinement).

Initially the sulfate occupancy was refined to ascertain whether some of the SO_4 units were instead $(OH)_4^{4-}$ tetrahedrons (based upon the postulation this material was similar to a hydrogarnet). Rather than reducing in value, the sulfate occupancy value crept above 1. This refinement was re-trialled with the introduction of constraints to prevent all occupancies (if set to be refined) from creeping above 1 and setting the condition for the occupancy on all of the oxygen sites to be equivalent. This resulted in the chemical formula to not be charge balance. Further iterations involved allowing the occupancy of the titanium sites to be refined, along with the sulfur and oxygen sites – in this case the titanium occupancy would reduce to ca. 0.75. Again, when checking the chemical formula, there were issues of: charge balancing, the suggestion of the titanium ion having an oxidation of less than +3, or in some cases not enough oxygen within the overall formula (after the deduction of oxygen required for the sulfate units) and not having any remaining oxygen to be suggested for the proposed.

The refinement was reattempted, but with the sulfate occupancy pre-set at 5/6 to give the overall no. of SO_4 units to be 2.5 in the overall formula. The resulting fit is shown in **Figure 6. 25** albeit with some intensity mismatch, the fit was still reasonable. The corresponding refined atomic co-ordinates are given in **Table 6. 11** and the resulting crystal structure shown in **Figure 6. 26**. Comparing the refined unit cell parameters to the original Pawley fit (**Table 6. 12**), there is a slight increase in the cell volume but with

reduced error – likely a consequence from refining with the higher quality data. Further work involves the use of Neutron diffraction techniques to locate H^+ and to confirm the $[(OH)_4]^{4-}$ group – as at this stage, given the evidence of Ti^{4+} and presence of water, the overall formula is postulated.

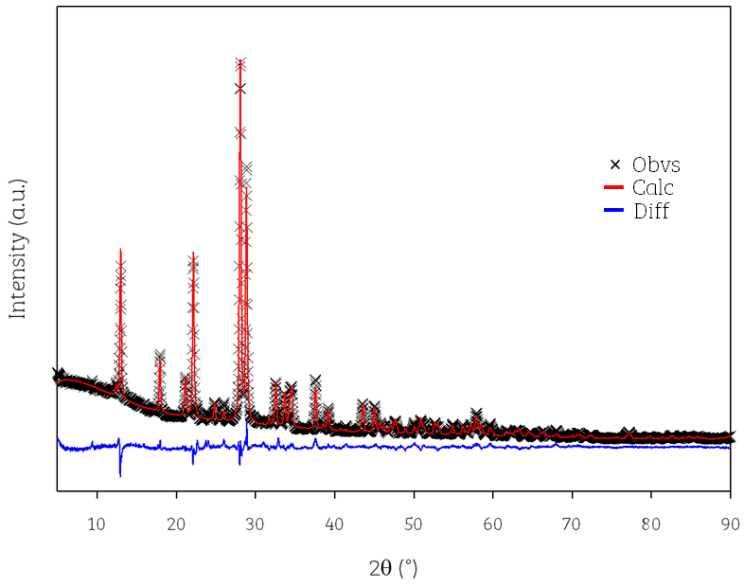

Figure 6. 25: Observed, calculated and difference XRD profiles for $Na_3Ti(SO_4)_{2.5}((OH)_4)_{0.5}$ (R_{wp} – 5.74 %, R_p – 4.39%) (Cu Kα).

Table 6. 11: Structural parameters and coordinates for $Na_3Ti(SO_4)_{2.5}((OH)_4)_{0.5}$. Cell parameters: a = 13.7714 (3) Å, c = 9.0375 (4) Å, cell volume = 1484.33 (9) Å^3.R_{wp} = 5.74% and R_p = 4.39%

Atom type	Site Multiplicity	x	y	z	occ	beq
Ti1	3	0	0	0	1.00 (2)	4.6 (4)
Ti2	3	0	0	0.5	1.00 (3)	2.4 (4)
S1	18	-0.0313 (5)	0.1637 (5)	0.2646 (7)	5/6	1.1 (2)
Na1	18	0.7346 (4)	0.1077 (6)	0.46050 (7)	1.00 (2)	2.7 (3)
O1	18	0.0161 (7)	0.1252 (8)	0.376 (1)	1.00 (4)	1.9 (4)
O2	18	0.8552 (1)	0.1004 (10)	0.2834 (10)	1.00 (3)	1.4 (4)
O3	18	0.0132 (8)	0.279 (1)	0.290 (1)	1.00 (3)	2.6 (5)
O4	18	0.0085 (8)	0.1574 (9)	0.142 (1)	1.00 (4)	3.0 (5)

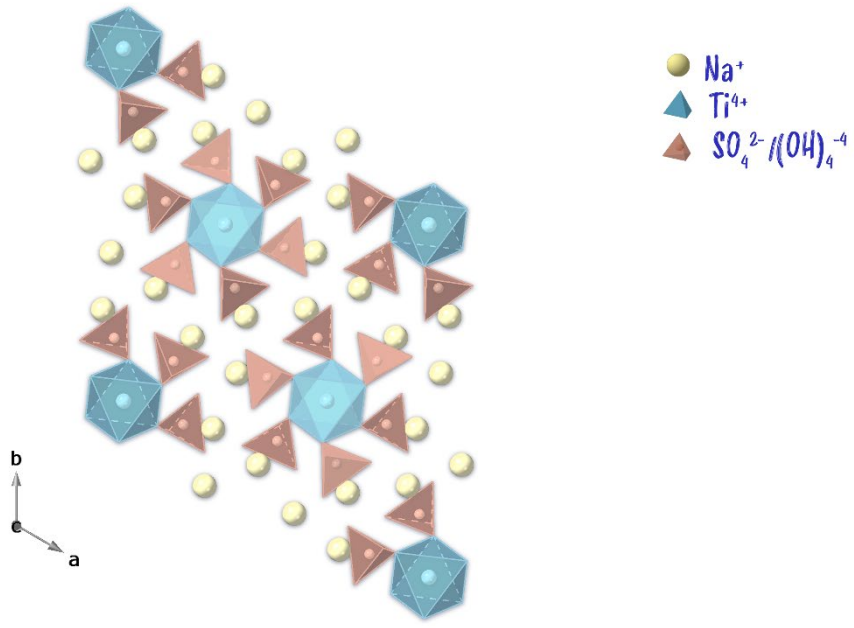

Figure 6. 26: Resulting crystal structure from the Rietveld refinement of $Na_3Ti(SO_4)_{2.5}((OH)_4)_{0.5}$.

Table 6. 12: Unit cell parameters comparing $Na_3V(SO_4)_3$ to the Ti-analogue ($Na_3Ti(SO_4)_3$) and the revised formula of $Na_3Ti(SO_4)_{2.5}((OH)_4)_{0.5}$.

Sample	a (Å)	c (Å)	Cell Volume (Å^3)	Ref.
$Na_3V(SO_4)_3$	13.4460(6)	9.0781(5)	1421.4(2)	1
$Na_3Ti(SO_4)_3$ (Pawley fit)	13.769(2)	9.022(1)	1481.3(5)	
$Na_3Ti(SO_4)_{2.5}((OH)_4)_{0.5}$ (Rietveld Refinement)	13.7714 (3)	9.0375 (4)	1484.33 (9)	

6.6 Conclusions

6.6.1 Na – M-M' – SO_4/SeO_4 systems (M = M' = Co, Ni, Mn, Fe, Cu and Zn)

The results validate our earlier proposal of the relationship between structure of $Na_2M(SO_4)_{2-y}(SeO_4)_y$ samples and the sum of the transition metal and weighted average S/Se ion radius, showing that this relationship extends to mixed transition metal systems (Figure 20). In particular the alluaudite structure is obtained for large ionic radii sums, while the 2-1-2 structure forms for small ionic radii sums. Thus the former can be obtained by either increasing the transition metal site size (e.g. Fe, Mn incorporation) and/or selenate doping, while smaller transition metals (e.g. Ni incorporation) and no selenate doping favours the latter. Overall, this established size relationship within these sodium transition metal (Fe, Mn, Co, Ni) sulfate systems provides the ability to effectively tune the material to the desired structure. However, it must be noted the relationship only applies to metal ions in the octahedral geometry, since the related Cu containing systems are shown to adopt a different structure, most

likely related to the Jahn Teller nature of Cu^{2+}, where Cu adopts a tetragonal pyramid geometry with the addition of two elongated bonds to oxygen below the base. In this system, no change in structure is observed on selenate doping.

6.6.2 Na-Ti-SO_4

Building on Driscoll *et al.*'s reduction method to access lower transition metal oxidation states found to be most stable in acidic solution, an attempt at making an equivalent sodium titanium sulfate was made with the following formula of $Na_3Ti(SO_4)_3$ – isostructural to $Na_3V(SO_4)_3$. Although the sample was found to be phase pure and have increased unit cell parameters suggesting a Ti^{3+} was successfully formed, the same phase can be formed under air which rather suggest the presence of Ti^{+4}. In further experiments to deduce the actual chemical formula, the amounts of Na, Ti and SO_4 content were altered, which resulted in impure samples. Samples were submitted to Diamond Lightsource Ltd for XAS to conclude the oxidation state of the Ti – which was found to be Ti^{+4}. To deduce the chemical formula, TGA-MS was ran on the air sample – where obvious mass losses of m/z = 17 and 18 were found initially and at a higher temperature of 400°C.

To our current knowledge, no other Na-Ti-SO_4-OH systems have been reported within the literature, thus making this system the first of its kind.

6.7 Future Work

6.7.1 Na – M-M' – SO_4/SeO_4 systems (M = M' = Co, Ni, Mn, Fe, Cu and Zn)

To evaluate the potential of these new compositions, electrochemical testing needs to be conducted, with the hope of mapping structure to performance in terms of electrochemical testing. The next challenges with these materials revolve around the solubility of the sulfate within the electrolyte and thus the breakdown of the material. Thus with such testing, either large amounts of binder need to be used or the material is coated before hand (potentially through the ball mill of a binder) to act as a protective coating.

6.7.2 Na-Ti-SO_4

To finalise efforts on this system, future work would consider the use of neutron diffraction and infrared spectroscopy to confirm the structural model.

6.8 References

1 L. L. Driscoll, A. J. Wright and P. R. Slater, *Dalt. Trans.*, 2018, **47**, 13535–13542.

2 P. Barpanda, G. Oyama, S.-I. Nishimura, S.-C. Chung and A. Yamada, *Nat. Commun.*, 2014, **5**, 4358.

3 R. Zhao, D. Mieritz, D. K. Seo and C. K. Chan, *J. Power Sources*, 2017, **343**, 197–206.

4 P. Senguttuvan, G. Rousse, M. E. Arroyo y de Dompablo, H. Vezin, J.-M. Tarascon and M. R. Palacín, *J. Am. Chem. Soc.*, 2013, **135**, 3897–3903.

5 P. Senguttuvan, G. Rousse, H. Vezin, J. M. Tarascon and M. R. Palacín, *Chem. Mater.*, 2013, **25**, 2391–2393.

6 L. L. Driscoll, E. Kendrick, K. S. Knight, A. J. Wright and P. R. Slater, *J. Solid State Chem.*, 2018, **258**, 64–71.

7 S. Nishimura, Y. Suzuki, J. Lu, S. Torii, T. Kamiyama and A. Yamada, *Chem. Mater.*, 2016, **28**, 2393–2399.

8 L. L. Driscoll, E. Kendrick, A. J. Wright and P. R. Slater, *J. Solid State Chem.*, 2016, **242**, 103–111.

9 O. Mentré, C. Masquelier, O. I. Siidra, M. Colmont, D. O. Nekrasova, S. Y. Stefanovich and V. M. Kovrugin, *Cryst. Growth Des.*, 2019, **19**, 1233–1244.

10 R. D. Shannon, *Acta Cryst*, 1976, **A32**, 751–767.

Chapter 7: Inspiring the Next Generation of Battery Researchers

The main body of this chapter, nominally the "Battery Jenga" section has been reproduced from the publication: E. H. Driscoll *et al.*, "The Building Blocks of Battery Technology: Using modified tower block games set to explain and aid the understanding of rechargeable Li-ion batteries", with permission from *J. Chem. Educ.* 2020, 97, 8, 2231–2237.Copyright 2020 American Chemical Society.

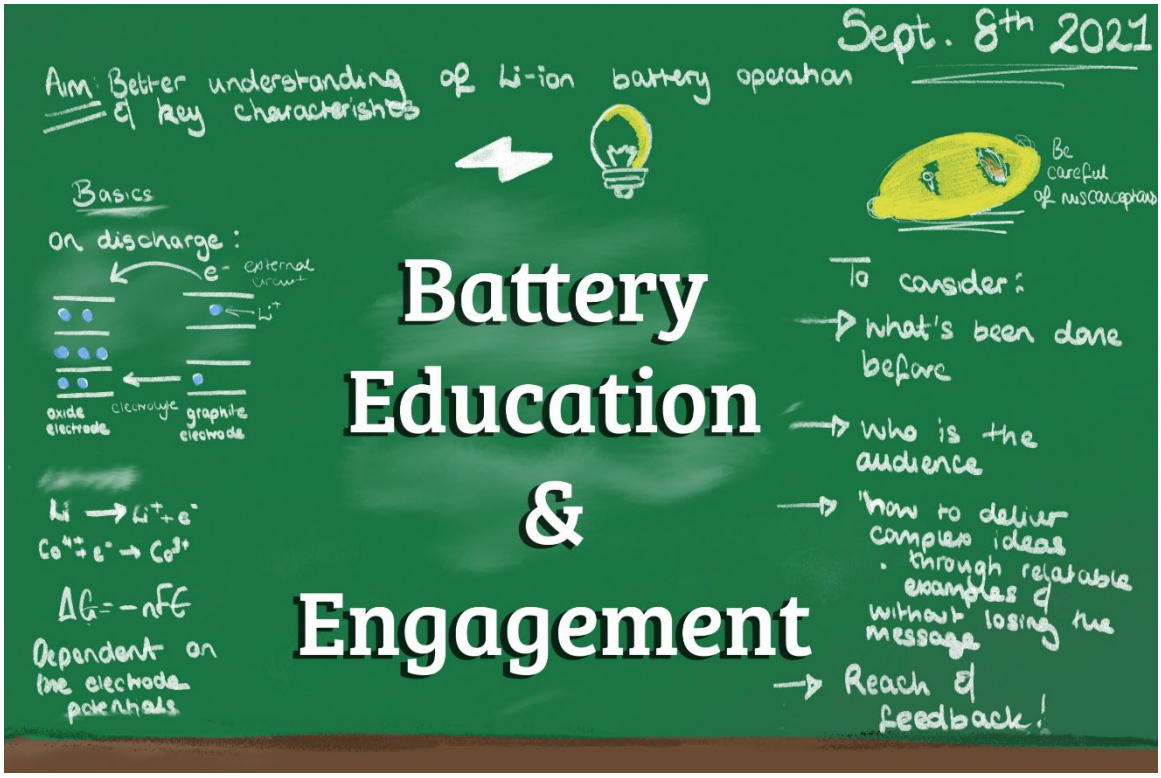

Figure 7. 1: Graphical abstract for this chapter focusing on 'Battery Education and Engagement'.

7.1 Background: Context and Aims

Li-ion batteries have become a modern staple within our society, influencing our social infrastructure initially, through the portable electronic industry (smart phones and tablets use), but in more recent years within the automotive sector with the manufacture of fully electric vehicles. Thus, it is paramount the underlying chemical concepts and theory can be widely understood by a range of audiences and backgrounds so as to allow consumers to make effective decisions, children to appreciate the science within their lives, and in some cases to appreciate what research funding supports.

To this end, very limited educational resources are available to explain Li-ion batteries operation, and in particular their rechargeable nature. Within this section, various resources created to explore Li-ion battery research will be illustrated, with feedback discussed along with further exploration into making these activities accessible.

7.2 The Building Blocks of Battery Technology: Using Modified Tower Block Game Sets to Explain and Aid the Understanding of Rechargeable Li-Ion Batteries

7.2.1 Introduction

The lack of demos to explain Li-ion batteries has been our motivation to design a suitable activity in using tower block sets, such as Jenga, which can complement the non-rechargeable demos. The archetypal Li-ion battery with electrode materials $LiCoO_2$-graphite are layered systems, and hence the stacking of blocks in a normal tower block game makes this traditional set ideal to customise into the appearance of this battery set-up.

This isn't the first instance of this tower block game being used in an educational setting. They have been used to explore risk management concepts to senior nursing students whereby the student had to identify risks to patients without the tower toppling over[1]. In addition, they have been used for teaching institutional oppression, whereby the game is played normally but rules are introduced to make the game play increasingly difficult.[2] Both authors comment on how the use of the tower block game acts to promote engaging learning and reinforce/fortify the students new understanding. A more recent case study involving a tower block game for educational purposes has been the 'Scientific Scissors: Genetic Jenga' game, whereby laboratory tongs are used to remove or replace the blocks representing gene code, and allows resultant discussion of how genes are connected and how displacements can affect surrounding genes.[3]

A rechargeable Li-ion battery consists of two electrodes, such as a layered lithium transition metal oxide electrode ($LiCoO_2$, or Ni, Mn, Al doped analogues) and a graphite electrode. The electrodes are separated with an electrolyte. A simplified schematic is shown in **Figure 7. 2**. On charging, the lithium ions traverse via the electrolyte, from the oxide electrode to the graphite electrode. An electron will move via the current collectors through an external circuit. On discharging, the reverse process will occur and hence the electron will do 'work' and power our application.

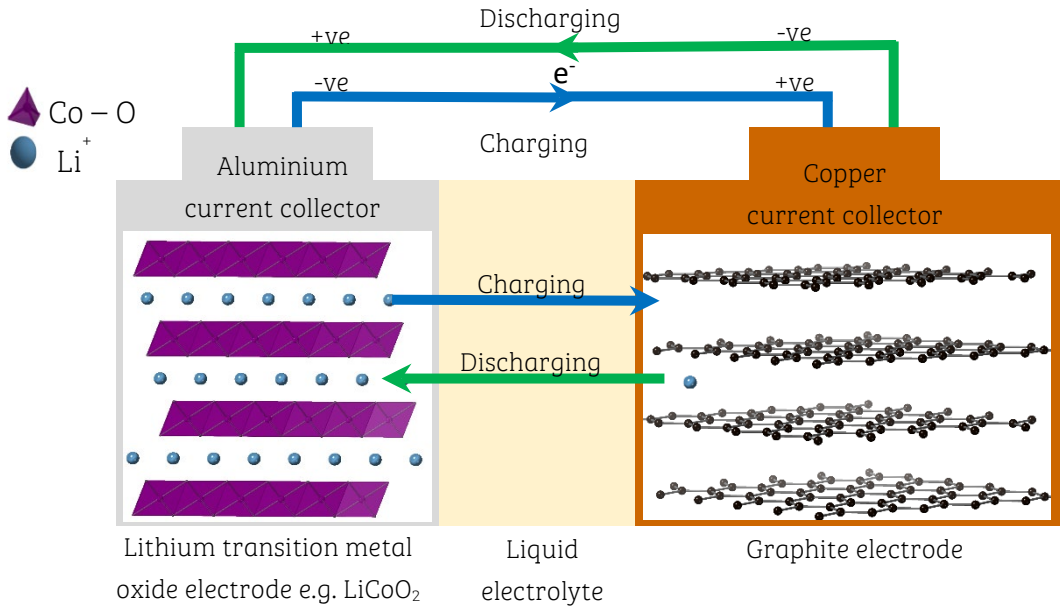

Figure 7. 2: Diagram depicting the charge mobility on charging and discharging between the two electrodes.

The redox processes in the discharging diagram, i.e. when our battery is powering a device, can be described with the following equations: **Equations 7. 1 - 7. 2**, such that the (negative) graphite electrode is being oxidized (losing an electron) and the (positive) oxide electrode is being reduced (gaining the electron). Through this redox process, the Li-ion from the graphite will migrate through the electrolyte back into the oxide electrode, whilst the electron traverses the external circuit powering the device.

Equation 7. 1: Negative Electrode (Graphite) – Oxidation.

$$CLi_x \rightarrow C + xLi^+ + xe^-$$

Equation 7. 2: Positive Electrode (LCO) – Reduction.

$$xLi^+ + Li_{1-x}CoO_2 + xe^- \rightarrow LiCoO_2$$

Earlier batteries made use of lithium metal (Li) as the negative electrode and these equations: **7. 3** and **7. 4** are given in the AQA Chemistry A level specification[4,5], although in a real battery not all the Li can be removed from $LiCoO_2$ (hence it should be more accurately represented with equations: **7. 1** and **7. 2**.

Equation 7. 3: Negative Electrode (Li metal) – Oxidation.

$$Li \rightarrow Li^+ + e^-$$

Equation 7. 4: Positive Electrode (LCO) – Reduction.

$$Li^+ + CoO_2 + e^- \rightarrow Li^+[CoO_2]^-$$

7.2.2 Activity

Two tower blocks sets were purchased, with each set consisting of 58 blocks and before use, set-up each of the towers which reached a height of 0.6 m.

One set was designated to be the LCO material (oxide electrode; cathode; positive electrode) and the second as the graphite electrode (anode; negative electrode). Note, battery chemists name the electrodes (cathode/anode) based on the **processes occurring on discharging**; from here on in, the positive (cathode) and negative (anode) will be referred to what they are on discharge and be simplified to oxide and graphite electrode respectively. The proposed design of the electrodes on their respective current collectors is shown in **Figure 7. 3**.

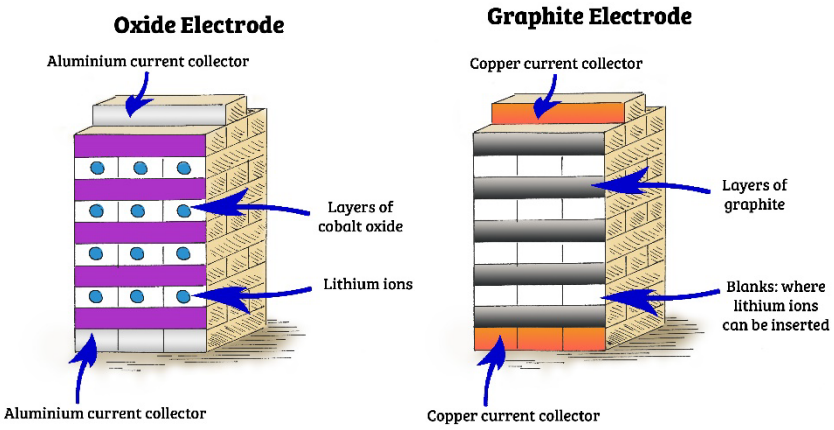

Figure 7. 3: Illustration of the tower sets with the proposed plan on how the oxide and graphite electrodes will be illustrated, on their respective current collector.

For our initial two sets we opted to paint the sets as follows: cobalt oxide layer/purple and red spheres (16); graphite layer/gradient grey (8); lithium/blue dots (42); white blanks (24); copper/orange (1); aluminium/grey (4); orange/grey dual side (1) with additional spares of 16 blocks (7 blanks, 1 orange, 8 lithium). The two tower sets at their full height are shown in **Figure 7. 4** without the additional spare blocks.

Figure 7. 4: Two of the battery towers set up with the oxide electrode (left) and graphite electrode (right).

The two tower block game sets in this form allowed us to show intercalation processes that occur on charging through the removal of the lithium ion blocks between the longitudinal cobalt-oxide blocks and insertion of them between the longitudinal layers of the graphite in our second tower set (**Figure 7. 5**). The reverse motion with the removal of the lithium from the graphite electrode back to the oxide electrode shows the processes that occur on discharging.

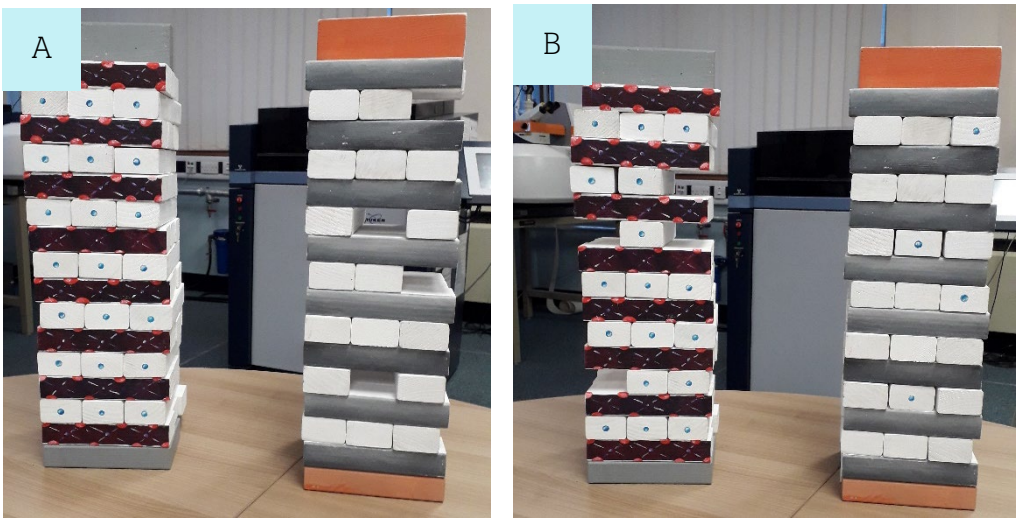

Figure 7. 5: Painted tower block game sets with the electrodes set-up. A) The graphite electrode shows vacancies where the lithium blocks can be inserted, as shown in B) on charging from the oxide electrode.

One aspect of battery chemistry is that it is not possible to remove all the Li from between the CoO_2 layers. Typically, only half of the lithium ions present in $LiCoO_2$ can be removed, which we can visually show with the tower block sets. When running the demo of charging, participants select specific lithium ion blocks, but never 3 lithium ions in one row; when students are asked why, they explained that this is to prevent the tower from collapsing. This is synonymous with this material, whereby overcharging (removing more than x = 0.5 Li from $Li_{1-x}CoO_2$) can result in the breakdown of the material, as CoO_2 is an unstable intermediate and there is a resultant oxygen release, which can oxidise the electrolyte and result in the danger of a battery fire.

In addition, the battery tower block game sets can show the capacity fade concept (why the performance of the battery reduces over continued use) due to the degradation of the battery, through showing how the blocks become slightly displaced (**Figure 7. 6**)

when removing and inserting the lithium blocks into the electrodes, illustrating distortions in the structure on removal/reinsertion of lithium.

Figure 7. 6: The oxide electrode tower block set showing cobalt oxide layers have become displaced through the (de)intercalation of the lithium during cycle, thus showing degradation.

With our original graphite electrode set, on the reverse side, the blocks were painted in the same way as our oxide electrode. Through turning our graphite set round by 180° and placing it adjacent to our initial oxide electrode, the two oxide electrodes (Figure 7. 7) could be used to show what happens with the varying rates of charges applied (i.e. fast or slow removal of the lithium ions). In running this activity, two students were invited to participate, with one student operating at slow charge with slow removal of the lithium blocks, whilst the other student would be representing fast charge and remove the lithium blocks as fast as they could; this invariably leads to the eventuality of structure collapse, as the displacement of the blocks become more severe.

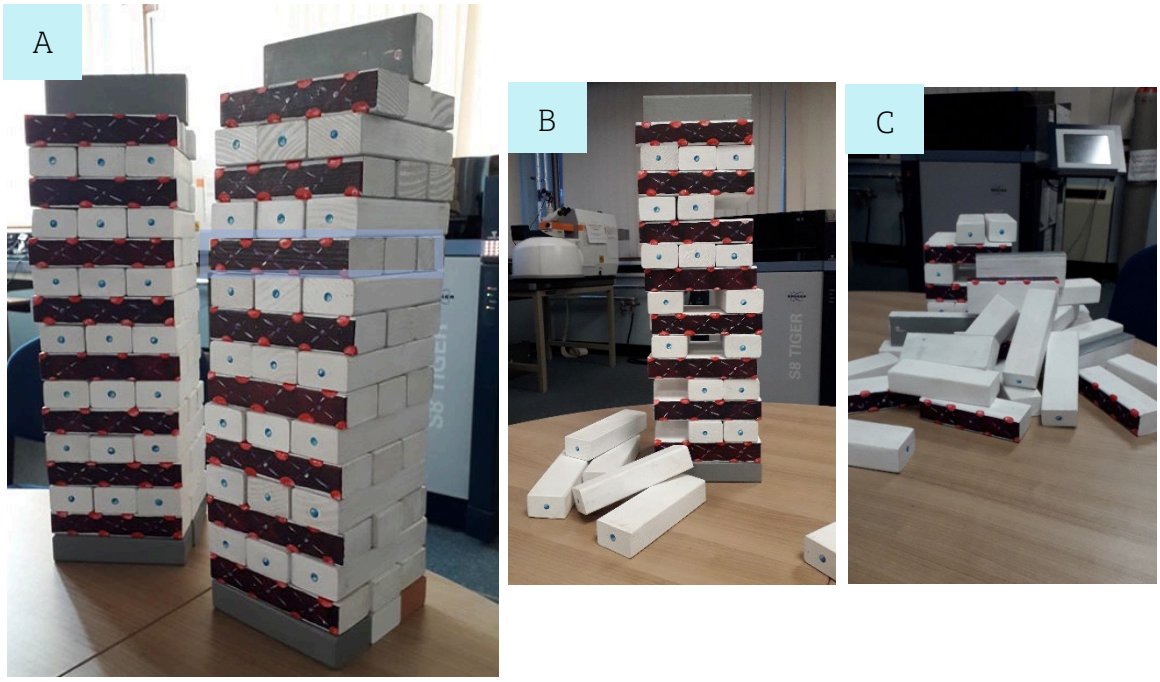

Figure 7. 7: A) Painting some of the blanks in the graphite layer to be like the cobalt oxide layer in the graphite electrode, allowed us to have two oxide electrode sets. The two oxide electrode towers can be used to show the differing rates of charges with volunteers: slow charge (B) and fast charge (C) which has resulted in structure collapse.

7.2.2.1 Tactile Battery Tower Block Set

The initial painted tower block sets were further developed to enable the activity to be more inclusive, nominally for students who are blind or partially-sighted. Therefore this set needs to have a good contrast in colours, in addition to having distinct shapes and textures. For this version, one tower set was purchased and divided in two, with each tower having a lithium cobalt oxide electrode face and a graphite electrode on the rear to make multiple use of the sets (**Figure 7. 8A**). For the oxide electrode, the lithium ions are represented by blue painted wooden buttons and the cobalt oxide layers with purple glitter paper with embossed plastic gems. The graphite electrode was produced with painted grey cardboard albeit without the top layer, to leave a ridged texture akin to the layered structure of this material. The aluminium current collector was decorated

with aluminium foil, whilst the copper current collector was painted orange and had 1 pence pieces affixed to the surface. The total no. of pieces represented are as follows: cobalt oxide layers (10), graphite layers (10), lithium pieces on one end with a white blank on the opposite end (24), white blanks (8), orange copper one square face and aluminium foil on the opposite end (6), longitudinal 50:50 orange copper: aluminium foil (2).

As with the painted tower block set discussed previously, the different activities can be visualized with the tactile equivalent. To allow the lithium ion insertion path to be more clearer, vacancies in the graphite electrode can be removed before hand, as shown in Figure 7. 8B, before charging (Figure 7. 8C). Degradation (Figure 7. 8D) and charging rates (Figure 7. 8F) can also be demonstrated, as previously mentioned with our initial painted set. Producing a demonstration that is tactile benefits all learners, not just students who are blind or partially sighted.

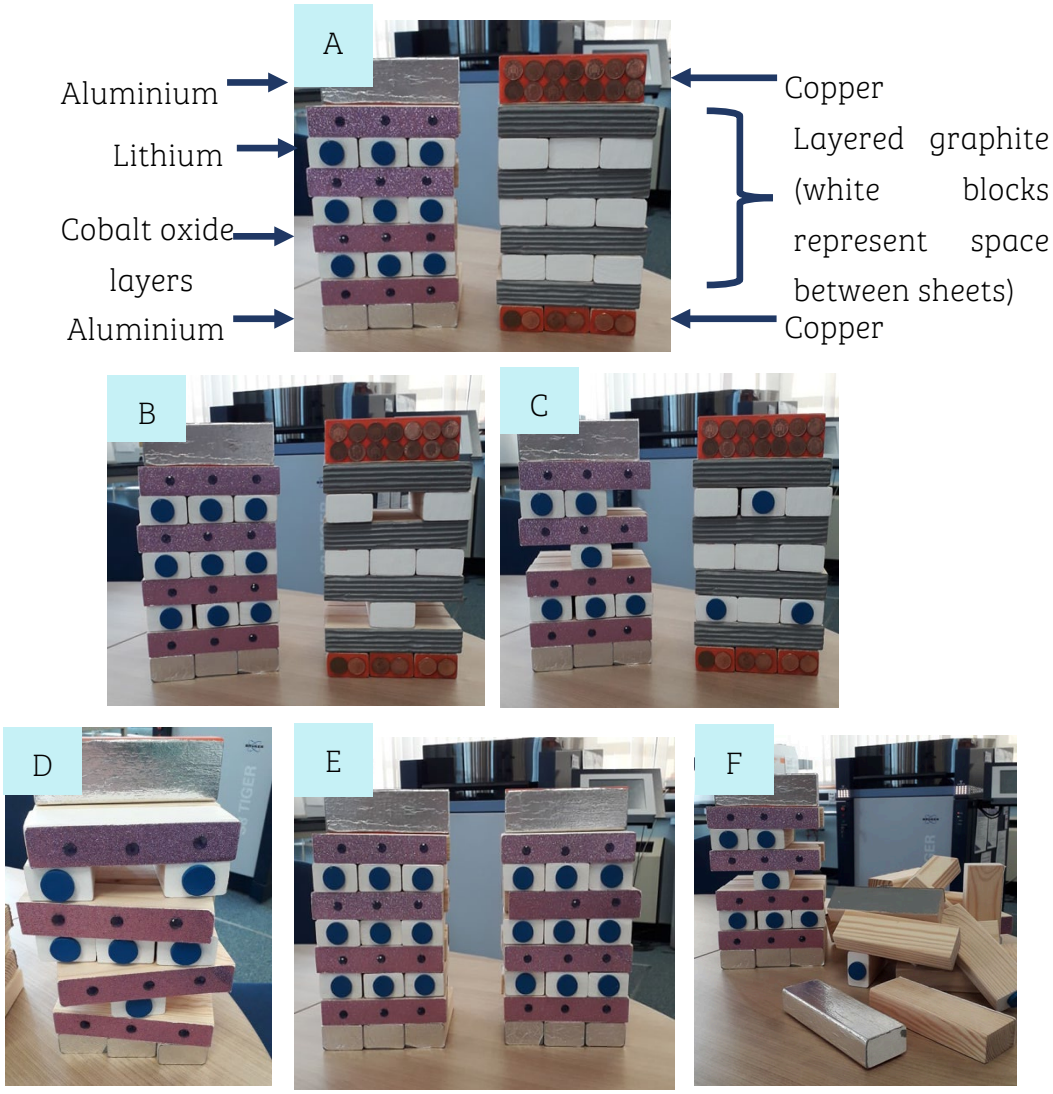

Figure 7. 8: A) Tactile tower block electrodes set-up (note each tower has the opposite electrode on the reverse). B) Showing vacancies where the lithium blocks can be inserted, as shown in C). D) shows how the blocks don't remain in the exact positions and hence degradation can be shown. E) Two oxide electrodes presented in preparation of the rate-charge activity. F) The aftermath of the rate-charge activity, the left tower had a slow charge applied, whilst the right tower has collapsed from too fast of a charge i.e. too fast removal of the lithium blocks.

7.2.3 Feedback

The demonstration has been used with multiple age groups since March 2019, from secondary school students having an introduction to rechargeable batteries to University level undergraduates receiving the demonstration to reinforce learning and key concept for this type of battery, as well as to the wider public at a range of museums and other events. From these earlier events, we received a range of positive comments on post-it note feedback (Figure 7. 9).

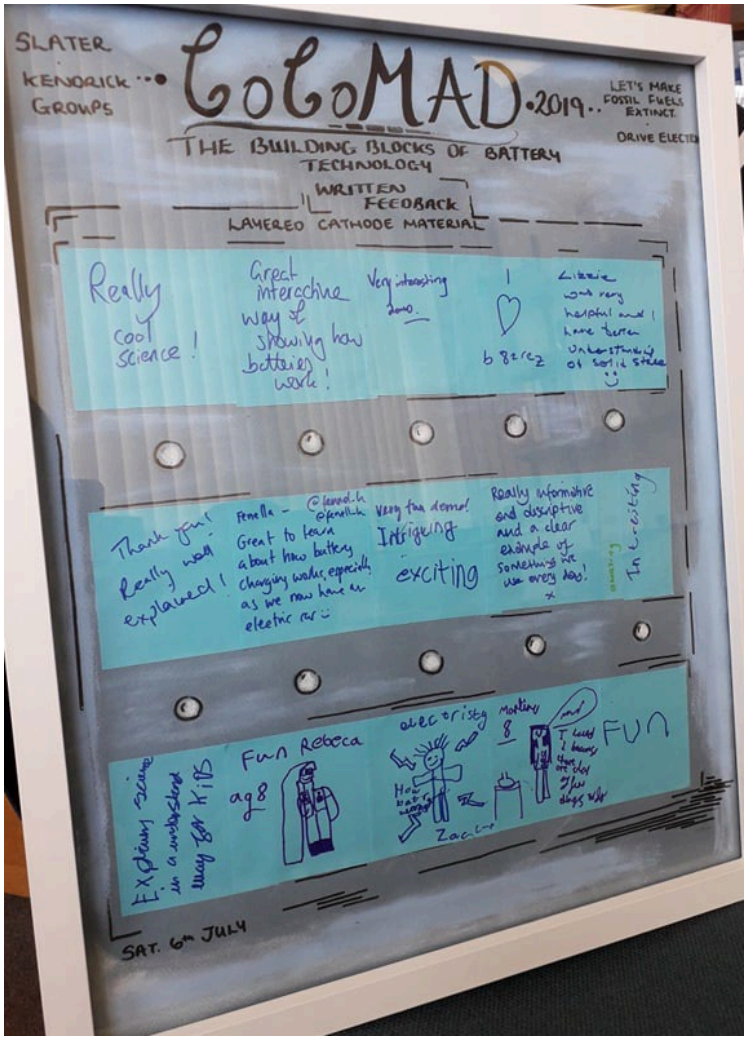

Figure 7. 9: Initial feedback collected via post-it note at the CoCoMAD 2019 festival.

In order to assess the usefulness of this activity in more detail, a survey was handed out before and after the battery tower blocks demonstrations, during a week period in January 2020. The first two questions asked for words associated with 'Rechargeable batteries' and 'Li-ion batteries'. The following two questions (no. 3 and 4) in the pre-survey were presented with choices on the Likert scale with "I am confident in explaining which electrode is which in a $LiCoO_2$-graphite cell for a Li-ion battery" and "I am confident in explaining how Li-ion batteries operate", with a tick box option of: not at all, a little, not sure, some and greatly. All of these initial questions were asked again after the use of the battery tower blocks demonstration in a post activity survey with the additional question of "The battery tower blocks are a useful prop in explaining how Li-ion batteries operate" with a final open feedback box on how the activity could be improved in understanding.

Responses were gathered from year 3 chemistry undergraduate students (n = 13) who were receiving an introductory lecture to rechargeable batteries. The survey was then open to other Chemistry undergraduates, who came along to a separate session (n = 16). Responses were then collected from Year 9 to Year 11 secondary school children before an energy-based demo lecture, where the battery tower blocks were used to explain the operation of Li-(and Na-)ion batteries (n = 49). Finally, the painted and tactile tower block game sets were shown to a small group of adults who specialise in public engagement and work with children with special educational needs (n = 3).

The following section will consider these responses, with the generation of the word plots considering the frequency of associated words for the first question and tabulated answers for questions 3-5.

The Year 9 – Year 11 school children word-chart responses are presented for question 1 in **Figure 7. 10** and **Figure 7. 11,** with pre- and post-demonstration answers, respectively These responses are shown in particular, due to this group being the larger cohort and the least experienced in terms of chemistry. The word chart responses for question 2 for this group, along with the University students answers for both initial questions are provided in the supporting information of the original publication.[6] The initial responses to the word associated with 'Rechargeable batteries' appear to be words connected to electricity and the topic's physical quantities, in addition to the name of applications of where this type of battery can be found i.e. phones and electric vehicles.

Pre-demonstration

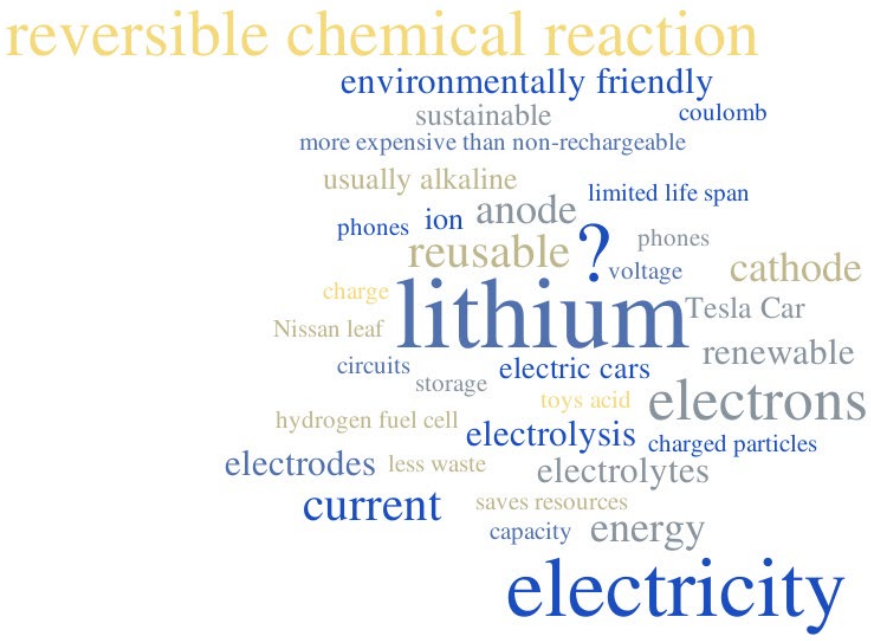

Figure 7. 10: Generated word chart from collected responses from Year 9 – Year 11 School Children pre-demonstration for the question of "words associated with 'Rechargeable batteries' ".

Post-demonstration

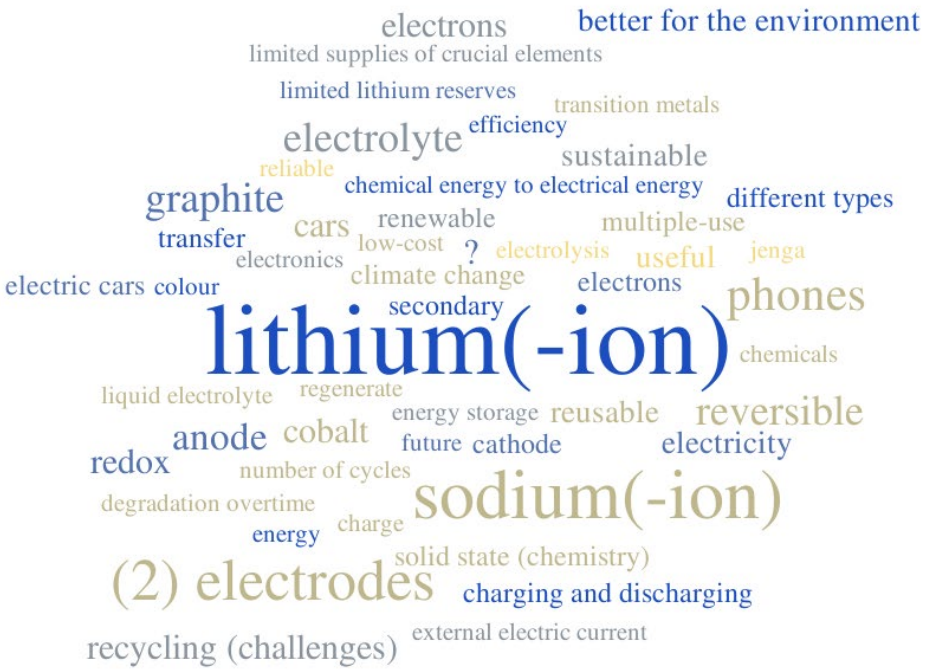

Figure 7. 11: Generated word chart from collected responses from Year 9 – Year 11 School Children post-demonstration for the question of "words associated with 'Rechargeable batteries' ".

The pre-survey answers for question 2 of words associated with Li-ion batteries, again, had applications stated, however, electrode terminology was stated i.e. cathode and anode. The post-survey answers for this question are presented in the supporting information.

The post-demonstration responses for both questions appear to consider more technical information on what these batteries consist chemically of and greater concerns for the environment.

If no responses were given to either of the associated word questions, a question mark was counted as that response. The frequency of an unsure answer reduced after the post-demonstration. Note in the energy lecture, Na-ion batteries were mentioned and hence this is why some students have written this as an answer.

The Likert responses from all groups: University students, adults and Year 9 – 11 school children, pre- and post-demonstration, will now be considered collectively for the following questions within Table 7. 1:

- Question 3: I am confident in explaining which electrode is which in a $LiCoO_2$-graphite cell for a Li-ion battery.
- Question 4: I am confident in explaining how Li-ion batteries operate.
- Question 5: The battery tower block game is a useful prop in explaining how Li-ion batteries operate.

Table 7. 1: Responses from the three different audiences: University students, adults and Year 9 – Year 11 school children in response to question 3, 4 and 5, with the pre- and post-survey results recorded on the Likert scale.

		Responses				
Audience	*Question*	*Not at all*	*A little*	*Not sure*	*Some*	*Greatly*
University students	3 (pre)	8	4	8	8	1
	3 (post)		1		17	11
	4 (pre)	5	8	4	11	1
	4 (post)		1		14	14
	5 (post)				2	27
Adults	3 (pre)	3				
	3 (post)	1	1		1	
	4 (pre)	3				
	4 (post)		2		1	
	5 (post)		1		1	1
Year 9– Year 11 school children	3 (pre)	41	2	4	2	
	3 (post)	3	15	4	25	2
	4 (pre)	26	15	3	5	
	4 (post)		9	2	32	6
	5 (post)		2	2	21	24

The general trend for question 3 and 4 in the post-survey all show a positive response of students finding they would be more confident in answering these questions. The responses from the adult group seems to be a small improvement from the demonstration, but this could be due to being a small sample size, as well as not having a chemical background and receiving only a 10 minute overview (since this was done in a session, where a range of tactile chemistry resources were being discussed), thus requiring more time to grasp the concept.

The responses on whether the battery tower blocks demonstration is useful for explaining Li-ion batteries operation all had extremely positive responses, with no-one stating it was not useful at all. The University students appear to have found the battery tower block sets the most useful, but this may be due to the fact that battery science is

a University module. Overall, the results from these surveys, and general feedback from our prior use at a range of events, support the conclusion that the battery tower block game is a useful tool to explain Li-ion battery concepts.

More in depth written feedback was received from some students within the Undergraduate group covering how the battery tower block game sets can support their learning from an assessment standpoint. The students comments centred around the demonstration offering a clear visualization of the structural chemistry of the electrodes, how the demonstration helped support the topic of redox reactions and from the application view point, the rechargeable nature of these batteries and how they degrade with time.

From a structural point of view, the students commented that the tower block set was useful in showing "a visual differentiation of the [electrodes] that isn't always as clear from just diagrams", in addition that the battery tower block sets do "an excellent job of showing the distinct layers present in the electrodes" and showing "lithium exists in different layers to the cobalt oxide in one electrode and the graphite in another". This student went on further to comment how the "white 'blanks' between the graphite layers [was] really useful in defining the layers and showing exactly where and how the lithium ions intercalate". Another commented on the movement of the lithium ions which "helped [the] understanding of how a lithium-ion battery works" and "it was clear that not all lithium ions from one layer could be removed as then the lithium cobalt oxide would not be able to retain its structure".

In terms of the topics, which the demonstration can support, redox reactions and (electrochemical) potentials were cited. “Although the activity itself didn’t explicitly detail the reduction potentials of the processes”, when put “into the context of charging and discharging an electrical device, it became clear where work was being done”. In addition, another student commented on “an understanding of the redox processes alone means that these scenarios are a bit difficult to visualize effectively and that’s where the demo has its real strength; a visual representation which accurately mirrors concepts that are potentially difficult to grasp otherwise”.

In terms of explaining battery characteristics with operation, rates of charges and degradation, the students praised the demo highly for the ease of visualizing these different aspects. “This is a really useful tool for showing lithium charge and discharge, which is a really important concept in the batteries course I have taken this year. I also like how this introduces some important aspects of battery chemistry such as high rate of charge (balancing a fast rate for applications such as charging cars/portables quickly vs. avoiding collapse of the structure when too many lithium ions are removed at once)”. “The demonstration involving many charge/discharge cycles is useful in demonstrating that batteries are rechargeable but that their structure will degrade over time” and highlights the “down fall of fast charge cycles and the dangers of over-extraction of Li-ions which damage the structure of electrodes”.

Connecting the tower block set activities to real life observations when explaining these mechanisms to students can reinforce learning, such that one student drew a connection by commenting on the “degradation of the cobalt structure happens due to charging and discharging of the lithium ions, causing the cobalt oxide to become

degraded and this is the reason the battery on my phone worsens with the more I charge and use it". Another commented on having a physical representation helped support their lecture material, such that "being told in lectures that many cycles of charge and discharge can result in a breakdown of structure is difficult to visualise. However, moving the lithium blocks in and out of the structure repeatedly resulting in loss of alignment gives a really nice visual aid that I can use in my revision."

Finally, with the multiple scenarios the tower block sets can show, one student "was surprised how many concepts the set could introduce and it's interesting to see how it could be used as an interactive demonstration taking up an entire exercise in class, or as the starting point for much more complex chemistry in later years, leading into discussion of how removal of lithium is accompanied by a change in cobalt oxidation state and what this means for the battery setup."

A suggested improvement to this demonstration was to show the external circuit with the movement of electrons; to show this, a pipe cleaner attached to the current collector tops with moveable beads to represent the electrons was suggested.

The tactile set has been reviewed by two teachers who specialize in the education of visually impaired students. The feedback we have received was extremely positive, where the set was praised for its use of textures, contrasting colours and the highly interactive nature of the set, such as when the tower block set is collapsed when performing fast charging. From this feedback and to ensure suitability, the suggested improvements related to a modification of the reversible set which was used to show the effect of different charge rates: in this set, the blocks were constructed so that the graphite electrode was on one side and the oxide electrode on the other side, as

mentioned previously (**Figure 7. 7**). The feedback suggested that having both electrodes on the same tower (one at front, the other at the back) may confuse students, who rely heavily on exploring the textures. Thus the recommendation was to have each tower represent a single electrode, with no decoration on the reverse. With this amendment, the only activity which will be impacted with this modification will be the rate-charging demonstration, where two students are required. Instead of running the activity simultaneously, one student should operate as a slow charge such that the structure remains intact and after resetting, a second student uses the same tower block set operating at fast charge. The second recommendation, following this alteration, would be for the educator to play a sounding beep to set the contrasting paces of lithium ion removal from the tower sets. This will help support the students in timing the block removal and prevent any confusion in what they should be aiming for. This addition would benefit sighted students also.

We acknowledge feedback directly from blind and visually impaired students will be most beneficial and we plan to conduct this survey at a later date and make suitable adjustments based on student's feedback to ensure the activity is the most beneficial it could possibly be for them.

From the original and tactile tower block set, the oxide electrode made use of a purple cobalt-oxide layer. Our original colour palette for the tactile set with the pink, blue and grey colours was selected based on information on the RNIB's 'Colour Vision Deficiency' information web page, which provides examples of the colours visible with the different impairments.[7] Further research by E. C. Hayward (University of Birmingham, UK) found the colours most appropriate for colour blind students are blue and yellow[8,9], hence this was accounted for in our updated sticker template within the supporting information

of the original publication.[6] **Figure 7. 12** highlights the tower block game set with the updated colour palette and the associated key guide for students.

Figure 7. 12: A further modification of the tower block set's colour palette to account for the research by E. C. Hayward, University of Birmingham, UK.

The tower block game set has been shown to not be limited to the layered crystal systems as shown with the $LiCoO_2$ set, and through further work, an additional cathode material used in commercial cells, lithium iron phosphate ($LiFePO_4$;LFP) has been produced by E. Hanover (University of Birmingham, UK) into a tower block game set (**Figure 7. 13**). The adaption allows for comparison between the electrode materials (LFP and $LiCoO_2$) structure stability while lower energy density of LFP can be illustrated to the original $LiCoO_2$.

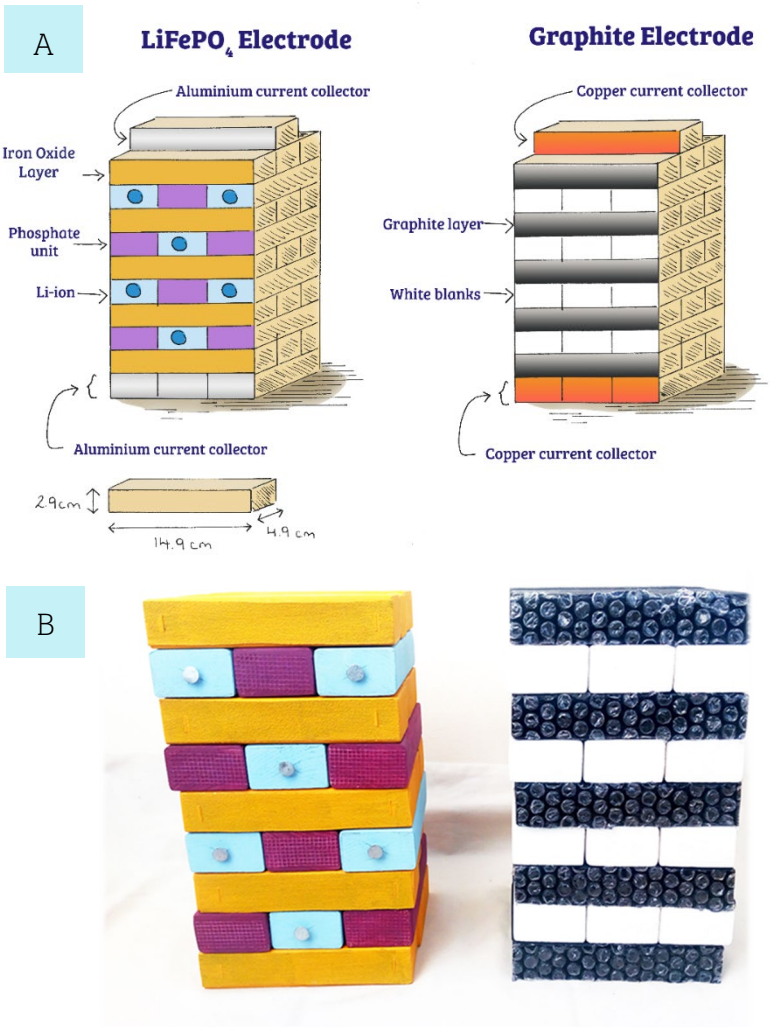

Figure 7. 13: The illustration of the LFP-graphite battery jenga (top) and the demonstration set (bottom). LFP set designed by E. Hanover, University of Birmingham, UK.

7.2.4 Reach

In terms of public engagement work, although social media has multiple benefits of accessing wider audiences through these platforms, resource reach is particularly difficult to achieve – and necessarily this is down to the limitation in the network associated with your media account.

Coinciding with the date of the publication of the paper, a gif describing the full demonstrations of the tower block set was designed and published (Figure 7. 14). To assess reach, Twitter analytics (which are used by the Journal's altmetric system) can be easily accessed. To date (23 August 2021), the gif alone has had: 46,872 impressions, 11,312 media views, 3,326 total engagements. The journal altmetric can offer further insights in terms of the demographic and geographic details of those accessing the resource. The altmetric at the time of writing has recognised 200 tweets from 152 users, with an upper bound of 443,305 followers. Of particular interest, relates to the (Twitter) demographic breakdown, where 52% of access originates from scientists, but more impressive is with 47% of the members of public accessing the resource, and 1% from science communications. Thus, with any publication taking advantage of the different social media platforms and news outlets associated with your institution, can allow for a greater dissemination of resource. As a result, the news outlets which have featured this work are shown in Figure 7. 15.

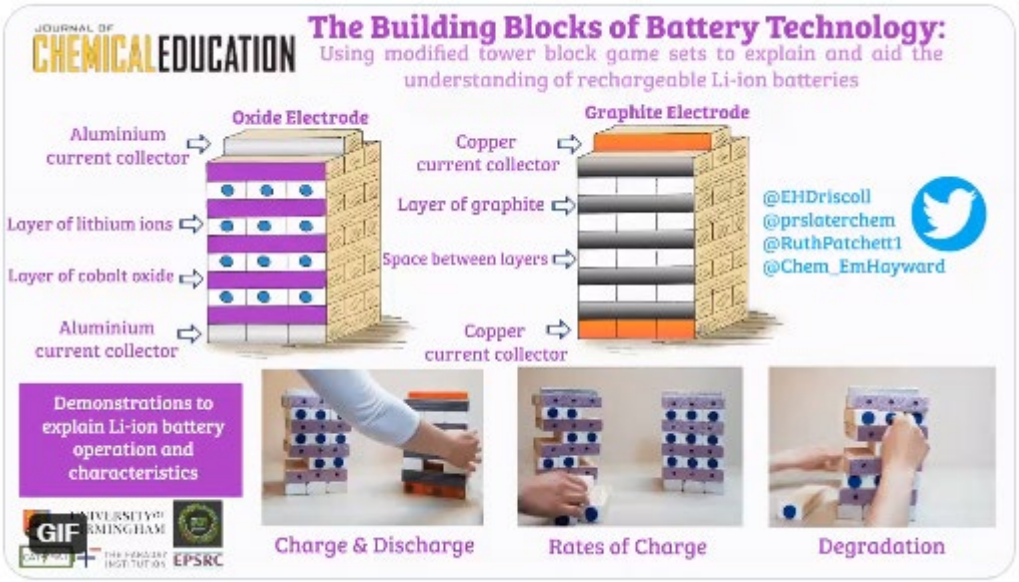

Figure 7. 14: To increase reach of this piece, a gif designed for the Twitter platform was published. The gif highlights the illustrated tower block game model with the associated demonstrations of: charge and discharge, rates of charge, and degradation.

Figure 7. 15: News outlets and articles which have featured this work.

7.2.5 Supporting Content

The supporting information contains a list of items and instructions to reproduce the battery tower block game sets, with the associated components of the battery of the correct dimensions, which can be printed directly onto the recommended sticker paper and affixed to the tower blocks. Additional results from the surveys are also presented in the form of word charts. In addition, demonstration videos with both sets: painted (Video A) and tactile (Video B) have been produced to explain the activities, with an additional voice over (Video C) which provides further points for the educators.

7.3 The Lithium Shuffle Project: Producing Educational Videos to explore Li-ion battery operation and characteristics

7.3.1 Introduction

The second activity to be highlighted within this body of work is the creation of an educational video showing the inner workings of a Li-ion battery as an education tool nominally for public engagement, which can also be used in the classroom setting to support battery education.

The use of educational videos offers an alternative learning platform[10,11] and is regarded as an important learning tool, whereby this media allows for the bridging of knowledge gaps[12,13] and can serve within active-learning strategies, such that content is incorporated into question and answers sessions, which allows for students to evaluate the content they have just observed.

In terms of chemical education, there are a wealth of examples where produced content has been effective in disseminating information. Of particular relevance in the year gone-by (the challenges of limited social contact with the COVID19 pandemic), through the production of images and videos across the social media platform Instagram, Ye *et al.* allowed for the retention of engagement of students and staff.[14] Through the use of this media, complex chemical concepts can be considered. In particular, some notable examples, make use of use of anthropomorphism, the attribution of human characterisations to non-human entities. Using the art of dance, the 'DanceChemistry' video series explored fundamental chemistry concepts, which allowed for students to visualize chemistry in a new and memorable way.[15] The 'DanceChemistry' series portrayed chemical interactions at the molecular level using dancers to represent the

chemical species.[15] 'ChemCloutChallenge' involved students to act out principles, such as gas law relationships and electrolyte solubility.[16] Although the production of quality content is important, the reach of the resource for public engagement activities is equally challenging. The use of social media platforms are brilliant tools in disseminating chemical information to a wide (international) audience with a range of different backgrounds.[14,15,17,18] Hayes *et al.* reported the use of TikTok to create fun, exciting and engaging chemistry outreach educational videos, but were limited in terms of advertising the content to non-followers of the social media account.[17] However, the suggestion of using alternative media platforms to raise awareness may reach a greater audience[17], but again, may still be limited in terms of account following.

7.3.2 Activity

At the time of the Lithium Shuffle project, limited resources were available in exploring the Li-ion battery operation and taking inspiration from a fellow research group, who used anthropomorphism to explore polymer chemistry (videos are currently not available to the public), an outreach grant was submitted for the funding of the props for a Li-ion battery video to the Royal Society of Chemistry outreach fund.

The previous example of the tower block game set focused primarily on the electrodes, neglecting the external circuit and the electrolyte, however in this example, the full battery make-up is used. Volunteers at the University of Birmingham from the School of Chemistry and School of Materials and Metallurgy re-enacted the processes that occur on charging and discharging. As before with the archetypal $LiCoO_2$ – graphite cell architecture was used, in this case in the human demonstration of the working of this battery. To remain consistent, the colours selected to represent the lithium, graphite

(carbon) and the cobalt in the (initial) tower block game set was retained for the Lithium Shuffle Project.

Before filming, a key of the T-shirt and prop guide was sent to all participants, this is shown in Figure 7. 16. The additions upon the tower block game set, includes the following components: such as the electrolyte, current collectors, the oxygen and the electrons. The electrolyte nominally being a lithium-based salt was simplistically represented with volunteers in the colour coded lithium shirts, but being in a liquid state of motion, compared to the lithium within the oxide electrode, would have the ability to move. The oxygens were presented by inflatable arm bands, which would be held between the cobalt ions. The oxygen component was represented in the tower block game set in the first painted model, but in later representations this detail was lost. The external circuit consists of the foils used to deposit the electrode coatings on, the aluminium foil for the oxide electrode and the copper foil for the graphite electrode, represented respectively by the grey and orange T-shirts respectively. Within the external circuit, the electrons will have mobility from the consequential redox reactions. In this demonstration, the electrons were represented by the beach balls. When the electrons are doing work, a lightbulb (painted cardboard) prop held by a volunteer in the yellow T-shirt would be flipped from off (white background) to on (yellow background) on discharge of the battery.

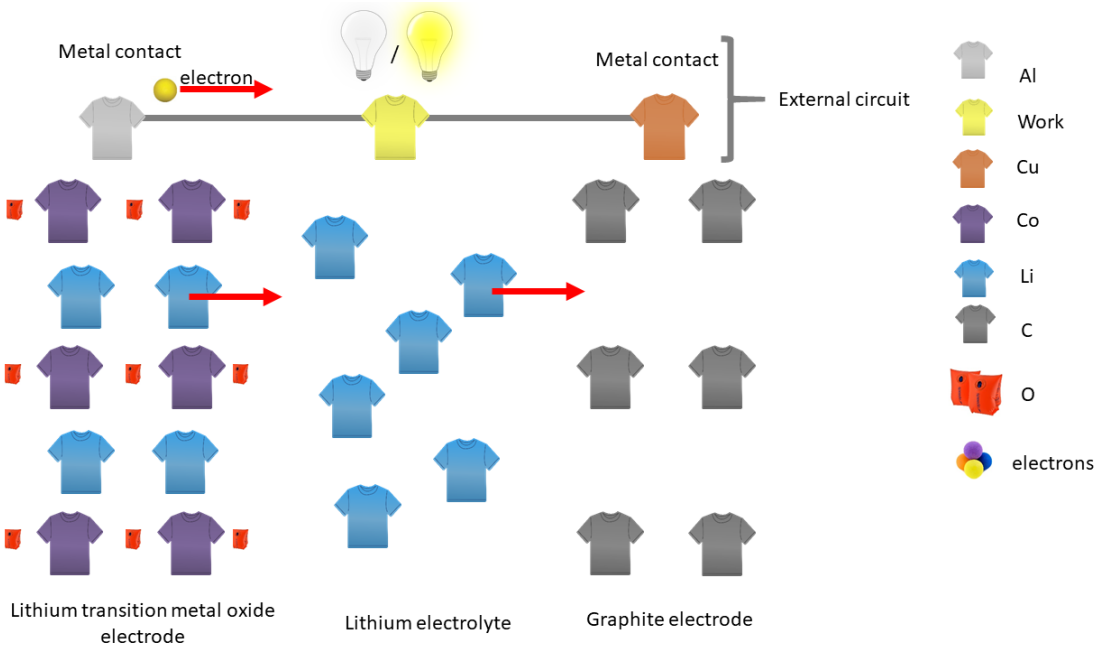

Figure 7. 16: A key of the demonstration produced for the participants to under the processes of a Li-ion battery and its components. The arrows within the diagram depict the status of the battery to be charging.

The set-up on the day of the filming, closely reassembles the key sent ahead of time to the participants, as shown in **Figure 7. 17A**. Within the video, labels associated with the different components i.e. liquid electrolyte, are labelled (**Figure 7. 17A).** The second video-still depicts what happens to the battery upon the first charge, where one lithium transverses from the oxide electrode into the liquid electrolyte, before intercalating into the graphite electrode, simultaneously with the movement of the electron in the external circuit from the aluminium current collector to the copper current collector (**Figure 7. 17B**). The reverse process is shown in the **Figure 7. 17C**.

A

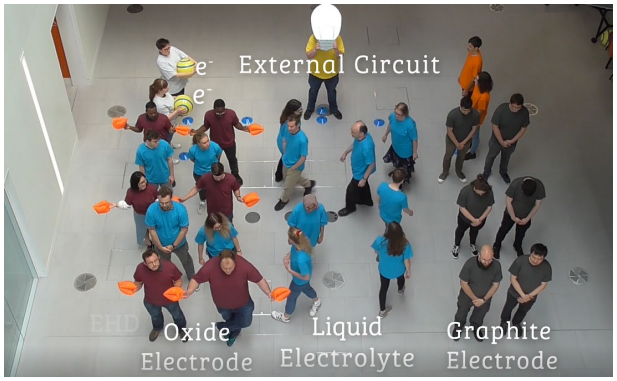

B

C

Figure 7. 17: The Lithium Shuffle Project video output available on YouTube. The first (A) still shows the human Li-ion battery demonstration set-up, with the overlay titles. The second still (B) shows the motion happening upon charging the battery, while the third still (C) shows the reverse in discharging.

To support the video content, the Li-ion battery operation demonstration is introduced with a key of the components. The example of the oxide electrode represented through volunteers is shown in **Figure 7. 18**.

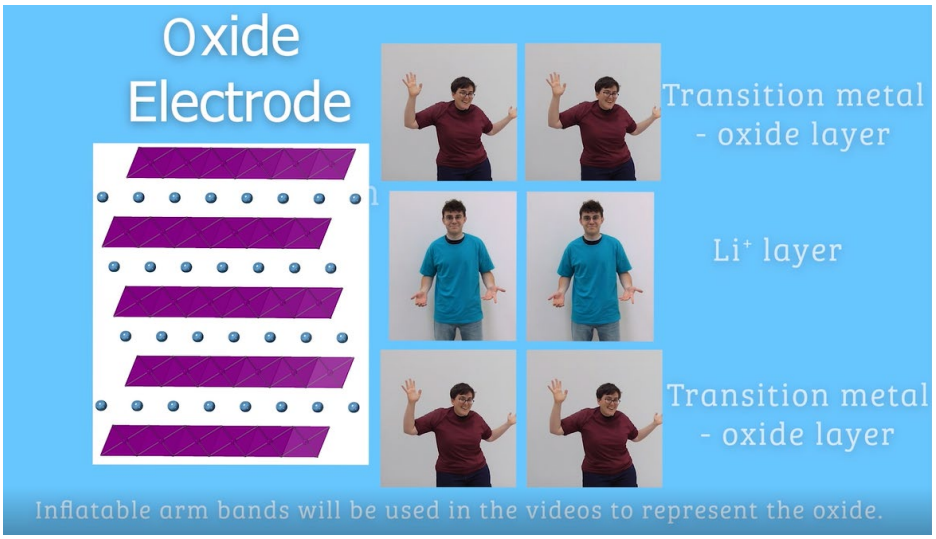

Figure 7. 18: Video-still showing the oxide electrode key with the crystal structure and the anthropomorphism form of the transition metal-oxide and lithium ion layer.

To reiterate key information from the demonstration with the volunteers, cardboard props produced for the activity, including a giant lightbulb and battery with moveable charging bars (**Figure 7. 19**), were recorded and overlayed with text highlighting qualitatively the process within the battery upon discharge, and adding a relatable application with the smart phone.

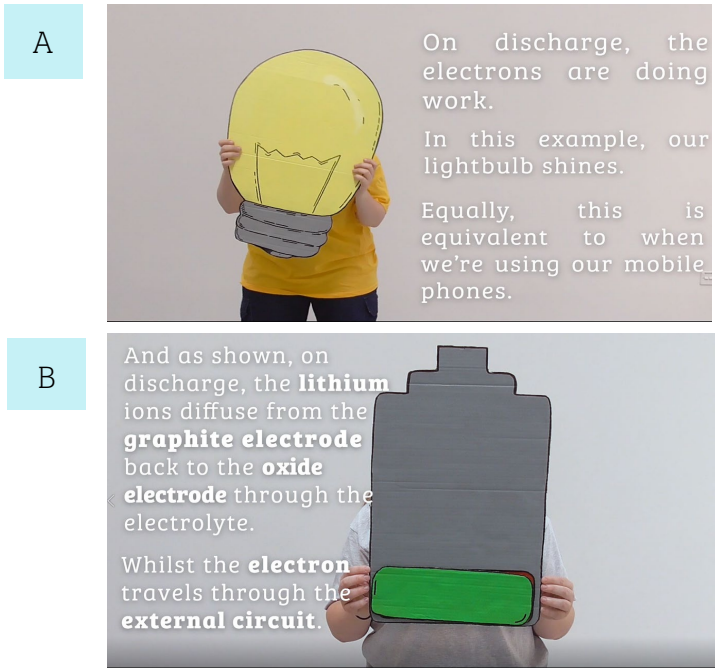

Figure 7. 19: Video stills from the video showing the use of cardboard props, a cheap and effective method, for adding a visual aid. Video still A) shows the use of the lightbulb with a description of work done by the electron upon discharge, while video still B) makes use of battery with decreasing green bars to signify what happens to the percentage of charge on discharge.

After the initial introduction of charging and discharging, the educational video explored more advanced topics including the solid-electrolyte interface (SEI) and when it forms. To the best of our knowledge, there are no known representations of the SEI layer within the education literature. The SEI is known to behave as a protection layer for the graphite electrode and it is vital for the operation of the battery, as such, the SEI was portrayed through the use of a security outfit, as shown in Figure 7. 20A. Experimentally, the SEI layer forms on the first few initial cycles within the Li-ion battery. Within our educational video, the SEI formation was visualized through the first charging step, where the volunteer acting as a lithium ion within the electrolyte region changes into the security outfit and holds onto the beach ball (electron; this

represent the fact that some lithium and electrons are lost forming the SEI layer) and cannot be utilised I later cycling, before policing this boundary between the electrolyte and graphite electrode (Figure 7. 20B).

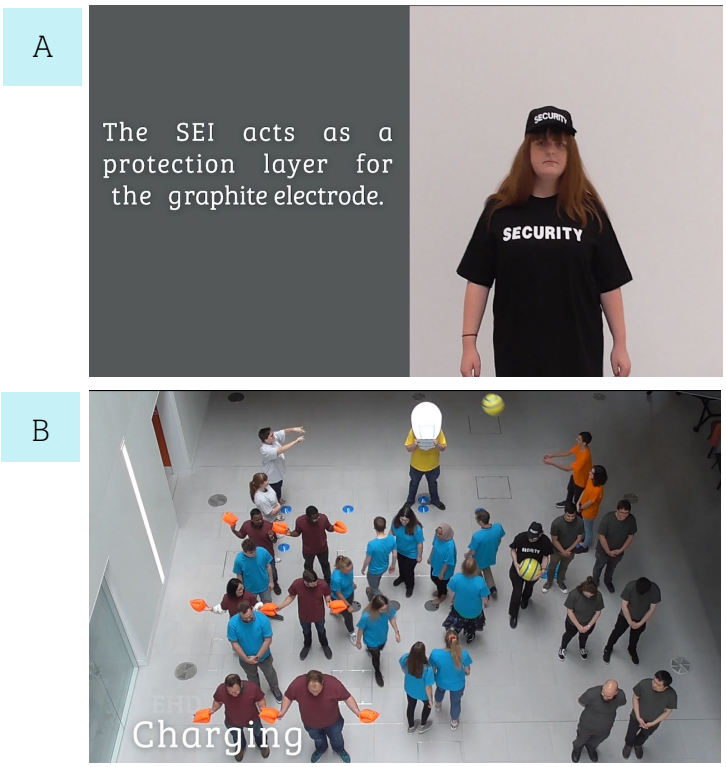

Figure 7. 20: Video-stills taken from the completed video highlighting the solid-electrolyte interface (SEI), with the initial notes on the SEI function and associated outfit key (A) and the SEI forming upon the initial cycles (B).

7.3.3 Reach

The hardest aspects to achieve with regards to engagement work are: reach and obtaining feedback. Both consequently are time-based activities, with maximum interaction on a limited timescale.

With regards to the Lithium Shuffle, from the time of publication (19th December 2019) on YouTube to the time of writing (23rd August 2021), the video had received 1,103 views

since publication, with the average view duration of 2:08 minutes (the video total length in terms of content 3:46 minutes). With regards to the average view durations, the average viewer would have viewed the initial battery set-up, the charging-discharging demonstration, and the written description of the Li-ion battery operation.

The importance of using a variety of different platforms to increase awareness of the resource is reflected in the traffic source. The external traffic sites accounted for 656 views, with the breakdown shown within Table 7. 2.

Table 7. 2: External traffic data from the "Lithium Shuffle Project" video uploaded onto YouTube[19].

Domain	Views	%
rsc.org	171	26.1
Twitter	159	24.2
Facebook	50	7.6
Google Search	43	6.6
YouTube	40	6.1
bham.ac.uk	27	4.1
Linkedin.com	24	3.7

Without the breakdown of the demographics, it is very difficult to ascertain whether the resource, targeted nominally at non-battery scientists (the wider public) and school students, is reaching the desired audience. From the traffic sources of the external traffic, the most interesting domains which can be discussed further are: rsc.org, bham.ac.uk and Twitter.

The high proportion of viewer share from the rsc.org would originate from the publication of the article titled "Lithium shuffle" to highlight the RSC IYPT2019 funded project.[20] Consequently, the YouTube viewer statistics show a huge spike in viewers in March 2020, coinciding with the publication of the article. Thus nominally this domain would represent those in the chemical societies, from students to professionals including those within education sector.

The second domain of interest is bham.ac.uk, which signifies the undergraduate (and potentially postgraduate) community are making use of this resource.

External traffic source via Twitter was also flagged in the YouTube analytics. The Twitter analytics relating to the piece are only available to the original post's account holder. Of the two posts to advertise the piece, the initial post after the publication of the video of YouTube achieved: 11,272 impressions, 169 media views and 486 total engagements were made.

Of the limited feedback received for this resource, the audio was flagged as not being "the best quality and the speaker didn't seem too enthused", however, the model was well received and the viewer appreciated "linking the model to mobile phones, something all post-16 students know how to use!". To become more in-line with engagement videos used on YouTube, the main video was re-edited to produce two individual videos. Each video contained a new key using only coloured coded symbols to represent the components, rather than the previous anthropomorphism. One video focused primarily on charging and discharging. The average view timing correlates with the bulk of the content of the visual charge and discharge demonstration being

watched. The second video focused solely on the SEI. Interestingly, of the two short videos, the SEI video has 3 x the views of the initial charging-discharging video. Upon commencing a YouTube search "solid electrolyte interface lithium ion battery", the Lithium Shuffle SEI shortened video appears third in the list. With the lack of educational literature exploring the SEI, this most likely explains the greater views for those attempting to understand this interface. To raise awareness of the shortened videos, and following on from the success of the gif produced for 'Battery Jenga' (**Figure 7. 14**), an equivalent was produced for the Lithium Shuffle Project (**Figure 7. 21**). The analytics show the gif resulted in a total of 3,008 impressions, 1,217 media views and 242 total engagements.

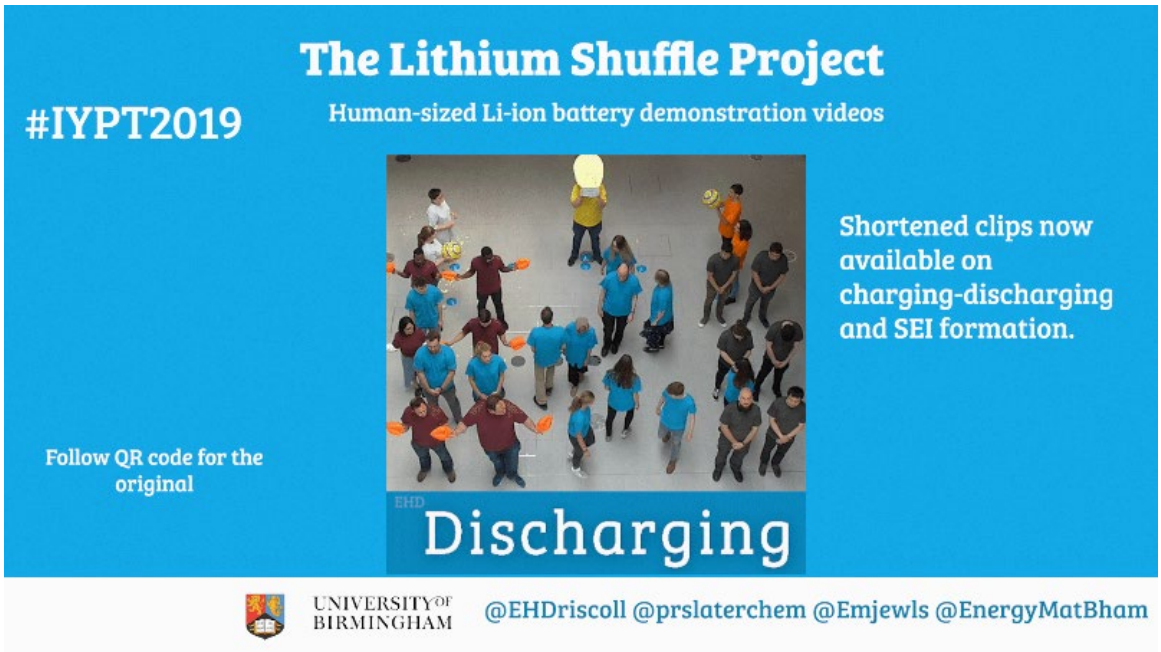

Figure 7. 21: To gain further reach, a gif for the Twitter social media platform was produced and published.

The second aspect to this project involved running equivalent school workshops of the Lithium Shuffle Project. The RSC outreach grant allowed for the funding of sport bibs

to allow for the creation of the playground games to communicate battery operation. The charging-discharge processes were re-enacted in the playground, however, the activity seemed limited in engaging through this form. Making this activity more engaging and worthwhile in this form, will be discussed within the 'The Electric Workshop'.

7.4 An Electric Workshop

As discussed previously, there are numerous activities for exploring non-rechargeable batteries but limited resources for the equivalent rechargeable types. From the previous sections in this body of work – there are now 2 further resources to explain the equivalent rechargeable type with Li-ion batteries. Both types of batteries are used by all demographics of the UK, thus the next challenge was to bring together both activities and highlight the different types of batteries i.e. (non)rechargeable.

7.4.1 Combining Activities

Thus, a workshop was designed for school students which would gradually lead them through the topics of circuits to non-rechargeable batteries and finally to rechargeable ones.

The workshop was first conducted at St Nicholas' CE First School, Codsall, Wolverhampton, UK as part of the school's celebration of science in June 2021, with the target audience of Years 3 and 4 (ages 7-8 and 8-9, respectively). Within this age group, the topics of electricity are taught at Year 4.

To start the workshop, firstly the children were asked to be an electrical circuit. To do this, 2 props from the Lithium Shuffle Project were re-used – the giant lightbulb and the battery with adjustable charge bars. The students were directed to form a giant open circle and then instructed to turn so they were facing the back's of their fellow classmate. Two individuals within the group were elected to be in charge of the battery and the lightbulb. With the battery being fully charged the students were directed to run as fast as possible, but not to overtake anyone. When passing the lightbulb, students were told to jump or hop on the spot. This action was to represent a potential difference going through the lightbulb. This initial activity can be shown in a re-enactment photo in **Figure 7. 22A**. To represent a change in current flow, at times the battery direction would flip, and the students would then have to run in the opposite direction (**Figure 7. 22B**). Although the current flow rate would not change and hence electron flow with the students movement should remain constant, to allow the activity to remain engaging, the students were told to look at the battery's charging bars. With the depleting battery bars, the energy overall would be decreasing and thus the students would gradually slow down until the battery was completely discharged (**Figure 7. 22C**). From an observational perspective, the students enthusiasm was starkly different from the beginning of the activity to the end. At the mention of the activity, students seemed impassive to the idea of becoming an electrical circuit. At the end of the activity and asked whether they enjoyed the game, the resounding 'Yes!' was evidence enough the students found the activity fun and engaging.

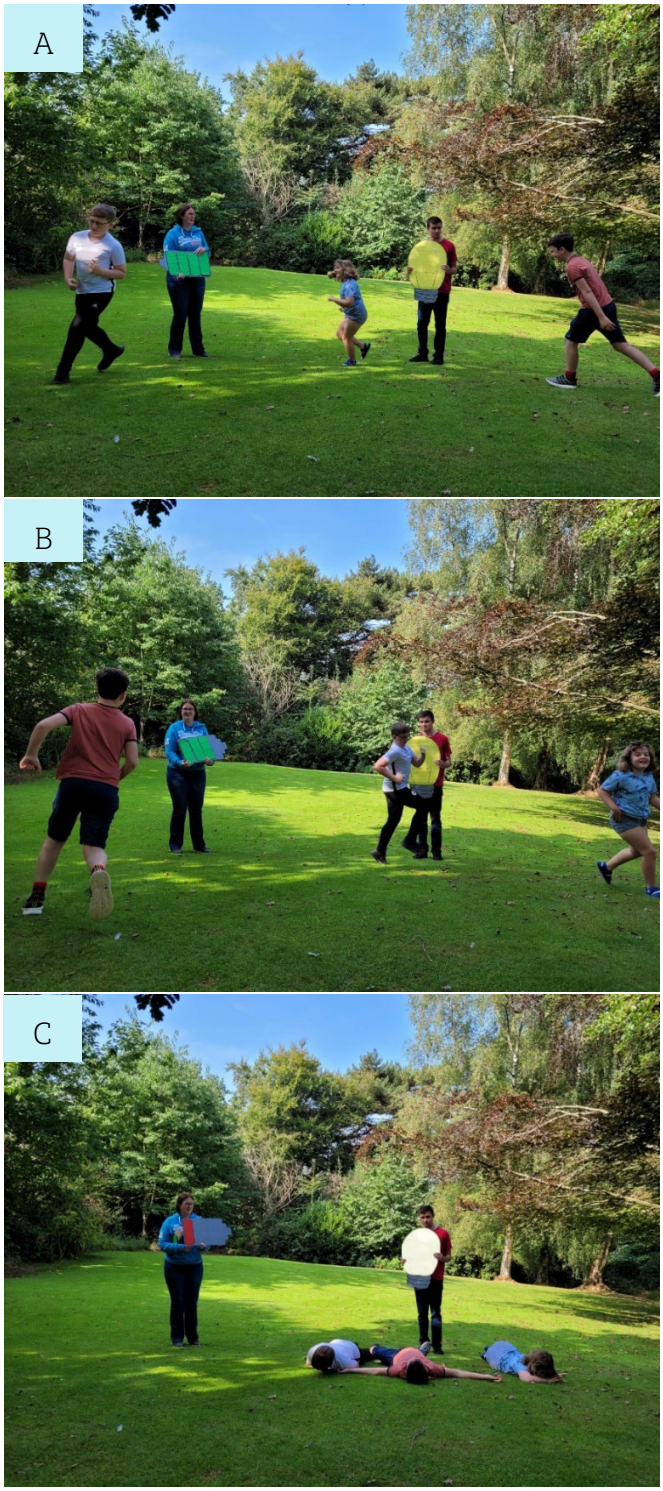

Figure 7. 22: Re-enacting of the "Becoming an electric circuit". Image A shows the students, behaving as electrons, running round in an anti-clockwise fashion in the same direction of the fully charged battery. The lightbulb remains on. Image B shows the students, running slightly slower but in a clockwise-fashion, while the light bulb remains on. Image C shows the students have collasped as a result of the battery running out of charge and thus the light bulb is now off.

After becoming an electrical circuit, the next activity would focus on batteries. Initially the students are asked about where they can find the batteries and provide examples – at this question - numerous answers of both non-rechargeable and rechargeable batteries were given.

To introduce the non-rechargeable battery topic, the students (within pairs) were provided with: a lemon with the Zn nail already inserted (for safety purposes for this age group), 2 wires with crocodile clips, a red LED and a copper 2 p coin. With the previous activity, where the students were themselves the wires and had the 2 props acting as components, the students could then account for the additional pieces (lemon, nail and copper coin) which would allow for the creation of their lemon cells. In some cases, some students would bypass the use of wires and would insert the coin and LED directly into the lemon with the nail already previously inserted. When this occurred, the students were reminded what property of the circuit they were when becoming an electric circuit in the playground. With one single lemon, the red LED wouldn't be able to light up due to the generated voltage being too low for this component, but it allows for the correction of the single circuits if students are struggling to assemble, before moving on. To light the red LED up, two pairs would need to connect their lemon cells up in series. It is possible to light the blue LEDs up with a further two lemons.

To introduce the notion of rechargeable batteries, an adapted playground game of the Lithium Shuffle was ran. The students were put into pairs, with one student wearing a purple bib to represent the oxide electrode, while the second student would be wearing a black sports bib to represent the graphite electrode, as shown respectively in **Figure 7. 23A** and **Figure 7. 23B.** Each pair would then face each other, and with the full class

form two lines of students. The student in the purple bib would have a sports bean bag or a small ball.

Figure 7. 23: Image A shows our 2 students representing oxide electrodes in the purple bibs holding tennis balls, which will represent the lithium ion. Image B shows our teacher and student pairing representing the graphite electrodes.

With this age group, the class leaders needs to be explicit in making sure the students are aware they should be aiming for their pairs hands and not anywhere else. On charging, the student in the purple bib would throw their bean bag or small ball to their partner (Figure 7. 24A). In the event where one of the students have not caught their bean bag, the pair are asked to sit down. This concept brings about the safety of charging/discharging rates, such that when students are asked to throw the bean bag at a faster rate, they are more likely to drop the bean bag and have to sit down, such that it is synonymous with the 'Battery Jenga' rate of charge demonstration. In the case

of the Lithium Shuffle project, where the SEI layer is introduced, this concept was also involved within this game. While the SEI is there to act as a protection layer, this was included in this game to add an extra life to the pairs who dropped the bean bag or ball (Figure 7. 24B). Overall the main purpose of this game, termed by students an adaption of 'hot potato', is to allow students to become familiar of there being two electrodes and what happens to the lithium (bean bag/ball) on charging and discharging. The idea of additional protection from the SEI layer was introduced too, to allow the game to continue.

Figure 7. 24: Image A shows the hot potato lithium game in action, where the oxide electrodes are throwing the tennis ball to the graphite electrodes. Image B shows the involvement of the SEI providing the pair who have dropped their lithium a further chance to play the game.

With the students now being familiar with the Li-ion battery set-up, the final activity involved the use of 'Battery Jenga' set to reiterate the concepts of charging-discharging and rate of charge, as well as introduce the concept of degradation. When discussing Li-ion battery technology, making the activities to be relatable, engaging and visually stimulating allows the students to make connections, i.e. getting students to think what they do when their tablet devices run out of charge – they charge them, thus we can link this to lithium-ion motion.

7.4.2 Feedback

The following feedback was collected from the teachers leading Year 3 and Year 4 respectively:

7.4.2.1 Mr Ryan Gough

"To describe the activities hosted by Lizzie as inspiring, engaging and exceptional would be an understatement. From the very moment she stepped into the room, Lizzie's passion for Science as a subject and her interest in batteries shone through vividly. The multi-sensory activity of children becoming a circuit brought the concept of electricity to life in a child-friendly and age-appropriate manner and supported the understanding of how electricity is energy which powers components; this was moved a step further whereby she explored the association between the level of battery-charged power and the impact on components in a circuit. This helped all children, regardless of their background or ability to engage with the session and motivated them fully. This was complimented by a follow-up activity focusing on how lemons could help power a circuit - this engaged children's natural curiosity for learning and was an

exceptional link between the practical outdoor activity and putting a real circuit together. Without doubt, we would welcome Lizzie back into school to further inspire our children (and staff!)."

7.4.2.2 Miss Lucy Abbis

"Because the activities were practical, the children were instantly engaged! The children could visualise the teaching that was occurring and are more likely to remember the process. The activities linked to electricity were targeted perfectly for the children's ability and age…The children could link the activities to previous learning. You took on board the behaviour policy (we clap to get the children's attention) and that helped the children to remain on task when you needed their attention. You walked around the children to support, question and challenge the children whilst they completed their activities. This was lovely as they had the opportunity to ask questions and you could scaffold learning accordingly."

7.5 Conclusions

7.5.1 The Building Blocks of Battery Technology: Using Modified Tower Block Game Sets to Explain and Aid the Understanding of Rechargeable Li-Ion Batteries

To summarise and conclude, we have illustrated a standard tower block set to be akin to the two electrodes that are found in a Li-ion battery. The battery tower block sets allow us to show the intercalation chemistry of the lithium ions, through the removal of the blocks from the oxide electrode to the graphite electrode upon charging, with the reverse process occurring on discharging. A range of other battery chemistry effects can be considered through comparing the rate of charge, with an activity involving two

students who remove the blocks at different rates. The lack of ability to remove three lithium ion blocks from one layer also helps reinforce structural aspects of the $LiCoO_2$ material, whereby not all of the lithium can be removed. Finally, when removing and reinserting blocks into the tower sets, the longitudinal blocks of the purple/red cobalt oxide layers or the grey graphite layers are gradually knocked off centre. This effect can help to explain the degradation effects Li-ion batteries can experience from repeated cycling. A survey was undertaken and n = 81 responses were collected. The responses consisted of University students, a specialist adult group and secondary school children for pre- and post-demonstration. Overall, the battery tower block game received positive feedback for its use in reinforcing battery education. The tower block set has been received further iterations to make the set as accessible as possible, in addition to another cathode chemistry being adapted into the game set. Furthermore, we believe that additional activities can also be developed using this resource, including multiple sets to help to explain how the battery management system of a full EV pack operates, and this is the subject of our future development in this area.

7.5.2 The Lithium Shuffle Project: Producing Educational Videos to explore Li-ion battery operation and characteristics

The Lithium Shuffle Project saw the creation of an educational video resource making use of anthropomorphism to explore how Li-ion batteries operate. The resource builds upon the 'Battery Jenga' resource, such that the electrolyte and the external circuit are also visualised. Included in this resource was the illustration of the formation of the SEI layer. To our knowledge there are no resources highlighting this formation through a creative media. The lack of resources for this characteristic has proved the individual shortened SEI clip to be quite popular. The resource itself seems to be viewed by

scientific audiences – those within the chemical sector (as shown by the RSC external traffic of the resource) – and likely undergraduate students. The resource itself obtained very little feedback, thus it is difficult to ascertain how well the resource is as an educational tool. Within the RSC funding, sports bibs were purchased to allow for equivalent playground games to be ran with school children. This aspect will be discussed further within the next section in making this activity more engaging.

7.5.3 An Electric Workshop

Through the electric workshop, both activities of 'Battery Jenga' and the 'Lithium Shuffle Project' can be brought together in the introduction of batteries and circuits. Although battery chemistry features in the A-level specification, with reference to Li-ion battery teaching, and circuits are touched upon in KS2, it is evident through our workshop that Li-ion batteries can be introduced at a much earlier age group. Thus, with the increasing interest in the electrification of vehicles, the topics surrounding battery chemistry can and should be taught at much younger age groups.

7.6 Future Work

7.6.1 The Building Blocks of Battery Technology: Using Modified Tower Block Game Sets to Explain and Aid the Understanding of Rechargeable Li-Ion Batteries

The paper and the associated content, which includes the educator makers guide and the questions, is currently only available in English.[2] To gain a greater reach with the resource, with a global technology, future work includes translating the piece into other languages.

In terms of the battery education, primarily only the UK curriculum was considered in this body of work. Future work would involve looking into other curriculums across the globe, specifically in countries which have had a significant uptake in the electrification of vehicles, such as China. The research would hopefully justify a need for change with regards to the UK's curriculum surrounding battery education, which is only briefly touched on for the A-level qualification. The main bulk of battery education is found at higher education towards the latter years in undergraduate programmes.

7.6.2 The Lithium Shuffle Project: Producing Educational Videos to explore Li-ion battery operation and characteristics

Additional footage was recorded for the Lithium Shuffle to explore overcharging. Future efforts will look to release this content when discussing battery safety.

7.6.3 An Electric Workshop

The practical set-ups of batteries currently makes use of the non-rechargeable types, nominally due to ease, handling and safety. Future work would look to see whether a practical creating a Li-ion battery suitable for the classroom, where students can assemble themselves is possible.

7.7 References

1 T. Brown, *J. Nurs. Educ.*, 2018, **57**, 765.

2 S. Lichtenwalter and P. Baker, *J. Soc. Work Educ.*, 2010, **46**, 305–313.

3 Genome Editing Public Engagement Synergy (GEPES), https://www.publicengagement.ac.uk/sites/default/files/publication/gepes_taster_case_studies_august_2019_0.pdf (accessed February 2020).

4 AQA, AQA AS (7404) and A-level (7405) Chemistry, https://filestore.aqa.org.uk/resources/chemistry/specifications/AQA-7404-7405-SP-2015.PDF, (accessed 1 March 2020).

5 M. Falkner, F. Emily, C. Kitts, A. Park and S. Pattison, Eds., *A-Level Chemistry Exam Board: AQA Complete Revision & Practice*, CGP, Cumbria, 2018.

6 E. H. Driscoll, E. C. Hayward, R. Patchett, P. A. Anderson and P. R. Slater, *J. Chem. Educ.*, 2020, **97**, 2231–2237.

7 RNIB:Colour Vision Deficiency, https://www.rnib.org.uk/nb-online/colour-vision-deficiency, (accessed 1 May 2020).

8 NHS: Colour vision deficiency (colour blindness), https://www.nhs.uk/conditions/colour-vision-deficiency/?fbclid=IwAR059wK0s3MJZIp4QaG8QWSnxKxK5TZsR_NzkMde_dpNmvKTpx1q7GDh6m8, (accessed 1 May 2020).

9 Colour Blind Awareness: Types of Colour Blindness, http://www.colourblindawareness.org/colour-blindness/types-of-colour-blindness/?fbclid=IwAR2ctnWIjpcIsUe8QyqNjct1dQSgKhiRy7iq_g0RdMWJUV0gxXjX-87NvVw, (accessed 1 May 2020).

10 D. Zhang, L. Zhou, R. O. Briggs and J. F. Nunamaker, *Inf. Manag.*, 2006, **43**, 15–27.

11 P. J. Guo, J. Kim and R. Rubin, *ACM Press*, 2014, 41–50.

12 Y. He, S. Swenson and N. Lents, *J. Chem. Educ.*, 2012, **89**, 1128–1132.

13 S. A. Lloyd and C. L. Robertson, *Teach. Psychol.*, 2012, **39**, 67–71.

14 S. Ye, R. W. Hartmann, M. Söderström, M. A. Amin, B. Skillinghaug, L. S. Schembri and L. R. Odell, *J. Chem. Educ.*, 2020, **97**, 3217–3222.

15 G. C. Tay and K. D. Edwards, *J. Chem. Educ.*, 2015, **92**, 1956–1959.

16 M. O. Hight, N. Q. Nguyen and T. A. Su, *J. Chem. Educ.*, 2021, **98**, 1283–1289.

17 C. Hayes, K. Stott, K. J. Lamb and G. A. Hurst, *J. Chem. Educ.*, 2020, **97**, 3858–3866.

18 D. K. Smith, *J. Chem. Educ.*, 2014, **91**, 1594–1599.

19 Driscoll, E. H. Lithium Shuffle - Battery Operation https://www.youtube.com/watch?v=r1fXpQdqHgE (accessed March 2020.

20 E. H. Driscoll, Lithium shuffle, https://www.rsc.org/news-events/community/2020/mar/lithium-shuffle/, (accessed 23 March 2020).

Chapter 8: Conclusions, Future Work, Funding Acknowledgements and Contributions

8.1 Conclusions

The thesis set out to describe novel materials for both Li- and Na-ion battery applications, including the development of novel educational resources to support the teaching of this topic.

Focus was initially given to two novel materials for high power anode application for Li-ion batteries: $Nb_{22}CuO_{56}$ and $Nb_9Ti_{1.5}W_{1.5}O_{30}$. Niobium-based systems are of interest due to advantages associated with not only improved inherent safety but increased theoretical gravimetric capacities, due to the dual redox couple of the niobium, for fast charging.

With the apparent differences in the literature surrounding the performance of niobates, the methodology (and materials) developed within this thesis were initially benchmarked against H (monoclinic) - Nb_2O_5 – the high temperature polymorph consisting of a 3 x 5 Wadsley-Roth block structure. The work on this polymorph offers a baseline on expectation on the redox couples occurring within the voltage window and thus associated gravimetric capacity, such that the Nb^{5+}/Nb^{4+} redox was found to be occurring in full with some of the Nb^{4+}/Nb^{3+} thereafter, based upon the level of lithiation.

$Nb_{22}CuO_{56}$ is the second niobium copper oxide to have been assessed for high power Li-ion anode applications, where the Cu doping was proposed for improved electronic

conduction. Due to the novelty of this material, there were challenges associated with refining the crystal structure, but with the discovery of a suitable cell ($Na_{0.77}Nb_{1.88}Fe_{0.038}O_{4.808}$) with C2/m symmetry a full Rietveld refinement was completed and the Cu doping was deduced to be occurring on the Nb2 site. Further characterisation techniques are required to confirm the structure, due to some apparent intensity mismatches.

To improve the electrical conductivity, the material was heated in a reducing atmosphere to produce metallic Cu nanoparticles on the surface (evidenced by SEM) and denoted X-$Nb_{22}CuO_{56}$ (for ex-solved) within this work. Preliminary studies showed the pristine $Nb_{22}CuO_{56}$ to have a higher average capacity than the X-$Nb_{22}CuO_{56}$, and thus work on this sample was ceased. The additional step to ex-solve the Cu from within the structure was likely inhibiting the performance of the material overall, due to the likely reduction of Nb^{5+} occurring.

Conducting advanced testing on the pristine material ($Nb_{22}CuO_{56}$) led to improved performance (239 ± 45 and 209 ± 18 mA h g^{-1} for lithiation and delithiation respectively, while cycling at a current density of 10 mA g^{-1}) – similar to the benchmark values for the H-Nb_2O_5. Unfortunately, during advanced testing, the material delivered less than satisfactory performance at the higher current densities, but was able to return on its linear trajectory at the lower ratings. Future work will consider further asymmetric electrochemical testing (such that the lithiation rate is kept constant, while the delithiation rate increases – the contrary to what was trialled within this body of work on this material).

The second novel niobate to be discussed within this thesis was $Nb_9Ti_{1.5}W_{1.5}O_{30}$ – a material of the same crystal symmetry of the $Nb_{22}CuO_{56}$ (C2/m) – however characterisation here was limited to Pawley fits to determine the unit cell parameters alone, due to the increased complexity of the material with Ti and W doping.

Coinciding with previous work, a baseline considering two different coating methodologies (method 1 and 2) using PVDF as a binder, allowed for the resulting electrochemical performance to be assessed, and ultimately as before, removing the initial ball mill step of CB with the AM was found to beneficial in the form of improved performance and consistency in capacity retention.

The preliminary work on the $Nb_9Ti_{1.5}W_{1.5}O_{30}$ material has shown favourable cell performance. With the asymmetric cycling with the increase in the lithiation rate, at the highest current density (4 A g^{-1}), lithiation was returning on average a capacity of 134 (2) mA h g^{-1}, within a lithiation time to 1 V of 1 minute 35 seconds ± 12 seconds and a total lithiation time (which correlates to the returned reported capacity, including the CV step) was 2 minutes 20 seconds ± 7 seconds.

However, it was commented on the challenges associated with high performance testing against Li metal – as this electrode is not necessarily suitable in the incidences of metal stripping. Therefore to mitigate against this issue, the inverse test was ran such that lithiation rate was kept constant and the delithiation rate was gradually increased (in this way the rapid processes occurring at the Li electrode would be undergoing plating rather than stripping). This showed improved performance, highlighting the issues noted above with the Li stripping process. The results showed

that with the application of 4 A g^{-1}, a capacity retention of 83% (delithiation) was observed within approximately 2 minutes and 30 seconds, with an average lithiation of 169 (16) mA h g^{-1}.

Towards optimising this material and using high speed ball milling, a phase transformation from $Nb_9Ti_{1.5}W_{1.5}O_{30}$ to the T- $Nb_9Ti_{1.5}W_{1.5}O_{30}$ phase was observed, which can be akin to high pressure effects. The cell performance with this additional high speed milling was found to be poor, which was attributed to the known low capacity of the associated T-phase (tungsten bronze structure type instead of Wadsley-Roth block structures).

This material was also tried in the green formulation coatings, with binder systems of CMC/SBR and iota-carrageenan considered, with the development of appropriate mixing methodology. The purpose of using water soluble binders will ease future recycling challenges. The cell testing within this chapter was limited, but offers methodology to develop upon to improve cell performance – in particular the iota-carrageenan showed promise through delivering comparable performance to PVDF at low current densities, however further work is required to improve the high rate performance.

Overall the results are very promising, however it is difficult to compare these results against literature reports, given the differences in methodology and quite commonly, the lack of electrode information with respect to current densities applied and the cell thickness – which serve as an important marker to cell performance (as previously

reviewed in Chapter 1 with respect to the differences in reports regarding $Nb_{16}W_5O_{55}$; p28).

However, the added advantage of the $Nb_9Ti_{1.5}W_{1.5}O_{30}$ material revolves around the lower W content and the introduction of Ti into the material – it is both cheaper and lighter than both Nb and W, while the material has shown very good performance at high charge rates.

The latter part of this thesis explored a range of sulfate-based Na-ion cathode materials. Building on prior work of the established ion-size relationship influencing structure preference of alluaudite-type and bimetallic sulfate systems, mixed-metal substitutions were considered to exploit this relationship further to mitigate the use of toxic dopants (i.e. selenate). The mixed metal substitutions were of the form of dehydrated $Na_2M_{1-x}M'_x(SO_4)_{2-y}(SeO_4)_y.2H_2O$, where M = M' = Ni, Fe, Mn, and Co, and showed the structure type can be tuned based on the metal ionic radii, thus adding extra design control with these materials.

For completion, other metals from the first transition metal row were considered: Cu and Zn, however the former was shown to adopt a different structure likely as a result of the Jahn-Teller distortion associated with Cu^{2+} and evidenced with the 2 elongated bonds within the tetragonal pyramidal geometry adopted. With increased selenate doping, no phase changes were observed. The Zn system, although showing similarities to the alluaudite structure-type could not be fitted against the current alluaudite model. On review of $Na_2Zn(SO_4)_2$ – Zn is found to occupy a 5 co-ordinate geometry. Thus,

with both these metals, it can be deduced the ionic-size relationship is limited to metals which are present in the octahedral geometry.

In a separate synthesis strategy, a $Na_3Ti(SO_4)_3$ system was targeted based upon a previous synthesis strategy of forming $Na_3V(SO_4)_3$ via an acid reduction of the V_2O_5, in addition to the knowledge Ti^{3+} shown to have a greater stability than Ti^{4+} in acidic conditions. Although the phase formed pattern matched to the V system, ultimately the sample could be produced under air and thus alluding to the presence of Ti^{4+}. This oxidation state was reinforced with XAS measurements at Diamond Lightsource Ltd. To compensate this difference in oxidation state and to ensure the formula was charged balanced, $Na_3Ti(SO_4)_{2.5}((OH)_4)_{0.5}$ was proposed to be the likely formula – further characterisation is required to confirm this.

The final part of this work described a series of engaging educational resources to explore and aid the understanding of Li-ion batteries – most notably the development and impact of 'Battery Jenga'. The resource stands as the first of its kind to effectively explore the operation of this type of battery, while remaining accessible and hands-on to a range of different audiences. The demonstration itself while showing charging and discharging processes with the movement of blocks, can also open up discussion on battery degradation and rate of charges with respect to structure stability.

The second resource to showcase Li-ion battery operation was an educational video resource labelled as the "Lithium Shuffle Project" – an online video resource adopting anthropomorphism to explore operation, in addition to highlighting the formation and purpose of the solid-electrolyte interface (SEI).

Through the electric workshop, both activities of 'Battery Jenga' and the 'Lithium Shuffle Project' were brought together in the introduction of batteries and circuits to School children. The workshop began with allowing children to become an electric circuit through a playground game, where the children represent the electrons within the wires, while volunteers have roles of circuit components such as: light bulb, battery, and in some cases a switch (suggested based on curriculum learnings). The workshop then made use of traditional resources, such as lemon cells, to reinforce circuit set-up previously seen in the playground. These activities then supported discussion around rechargeable batteries, and thus allowing 'Battery Jenga' and 'Lithium Shuffle Project' to be introduced, with the latter activity making use of a 'hot potato' style game with just the electrodes.

These activities, while proven to be successful, through consideration on feedback and reach, allow for innovative ways to inspire the next generation – be it students or the wider public, when aiming for a greener future.

8.2 Acknowledgements: Contributions, Awards and Funding

8.2.1 Chapter 3 – 5

I'd like to thank firstly Prof. Peter Slater for providing the initial starting point with this work – with the material itself. I'd also like to thank Dr Laura Driscoll and Dr Yazid Lakhdar, for both their patience's and support in initially getting this material to cycle and the more advanced procedures respectively. Finally, I'd like to thank Dr Tzu-Yu (Evin) Chen for her support and knowledge in using TOPAS and to credit Evin for finding an appropriate starting crystal model.

8.2.2 Chapter 6

I'd like to thank Prof. Alan Chadwick (University of Kent, UK), Dr. Giannantonio Cibin (Diamond Lightsource) and Dr. Diego Gianolio (Diamond Lightsource) for the award of beam time as part of the Energy Materials Block Allocation Group SP14239, to help deduce the oxidation state of the titanium within the Na-Ti-SO_4 samples.

8.2.3 Chapter 7

I'd like to thank Prof. Peter Slater for being a positive driving force behind this work and nominating me for the following awards:

With thanks to The Faraday Institution Engagement/STEM Outreach Community Awards 2021 for recognising the effort and resources for inspiring the next generation, nominally the resources mentioned in this thesis.

With thanks to the University of Birmingham's College of Engineering and Physical Science society awards recognising the outreach efforts in battery education and accessibility.

With thanks to the Royal Society of Chemistry for recognising efforts during the COVID-19 with supporting the local section with outreach work and the Solid State interest group.

With thanks to the British Crystallographic Association – Young Crystallographers Group for the award of the Parkin Prize lecture – where these outreach resources were highlighted.

8.2.3.1 The Building Blocks of Battery Technology: Using Modified Tower Block Game Sets to Explain and Aid the Understanding of Rechargeable Li-Ion Batteries

I'd like to thank the following funding bodies/individuals who have supported this work:

- EPSRC JUICED Hub; EP/R023662/1.
- The Faraday Institution's CATMAT (FIRG016), ReLiB (FIRG005) and Nextrode (FIRG015) projects.
- Northrop Grumman for funding the initial tower block set for Year 10's Forge your Futures (April 2019) and The Green Heart Festival, University of Birmingham for funding for the larger festival tower block set.

- Ellie Mestle for liasing with the initial tower block set funding body, and Joseph Davies (summer intern 2019 for ChemBAM, University of Birmingham) for supporting the fabrication of the tactile set with Emily.
- Thank you to the undergraduate students at The University of Birmingham for assisting the additional feedback round.
- Thank you to both Will Stark from New College Worcester, Worcestershire, UK and Robyn Watson from Thomasson Memorial Sensory Support Service, Bolton, UK for providing invaluable feedback for our tactile battery tower block sets.

The Faraday Institution (FUSE) for funding Emily Hanover's summer internship.

8.2.3.2 The Lithium Shuffle Project: Producing Educational Videos to explore Li-ion battery operation and characteristics

I'd like to thank the following funding bodies/individuals who have supported this work:

- Royal Society of Chemistry IYPT2019 fund for supporting this project.
- All volunteers from the School of Chemistry and School of Materials and Metallurgy who willing gave their time to become an element within a Li-ion battery.
- My supervisor, Prof. Peter Slater, for wonderfully showing how the SEI layer forms on the initial cycles and how the interface acts a protection barrier to the graphite electrode.

8.2.3.3 An Electric Workshop

I'd like to thank Mr Joshua Piggott, the science lead at St Nicholas' CE First School, Codsall, Wolverhampton, UK for allowing us to join the school for science week and trial

our battery activities. I'd like to extend the thanks to the other teachers in the school who welcomed us and who took part in being an electrical circuit! All year groups in the academic session of 2020-2021 were truly brilliant to work with.

I'd like to once again thank Dr Ruth Patchett for introducing me to Joshua and starting this collaboration between us.

I'd like to also extend my thanks to my wonderful FUSE interns: Emily Hanover (2020, 2021), Zoe Wright (2021) and Hannah Blakiston (2021). In addition to Anton Zorin and Dr Pooja Goddard who helped support the Electric and Recycling workshops at St. Nicholas' CE First School.

Due to privacy issues surrounding photos taken at the School visit, the electric workshop activities were reproduced with the support of the Wood Lane Massive group (i.e. my amazing neighbours). Thank you to Nicola Barnes, Nick Barnes, Thomas Bamford-Barnes, Joshua Thompson and Alice Thompson for being great sports!

Chapter 9: Appendix

9.1 Chapter 3: Synthesis, characterization and application of novel Nb-based anode materials: Cu doping

To investigate whether metallic Cu was forming upon cycling of the $Nb_{22}CuO_{56}$ electrode, a study was conducted which involved the imaging of the electrodes from cells that had been cycled to a specific point. No metallic Cu was observed, as seen in the previous X-$Nb_{22}CuO_{56}$ system. There are interesting changes in morphologies witnessed when lithiating the material to 1 V – but these changes are reversible. If a study of this kind would be repeated in future, it must be ensured cells are dismantled straight away after cycling to a specific point (in circumstances where in-situ is not possible), this is to ensure the images are true to the environment we are considering. In addition, the likely change in morphology observed may be due to lithium on the surface reacting with surface moisture – thus electrodes should be imaged under inert atmosphere.

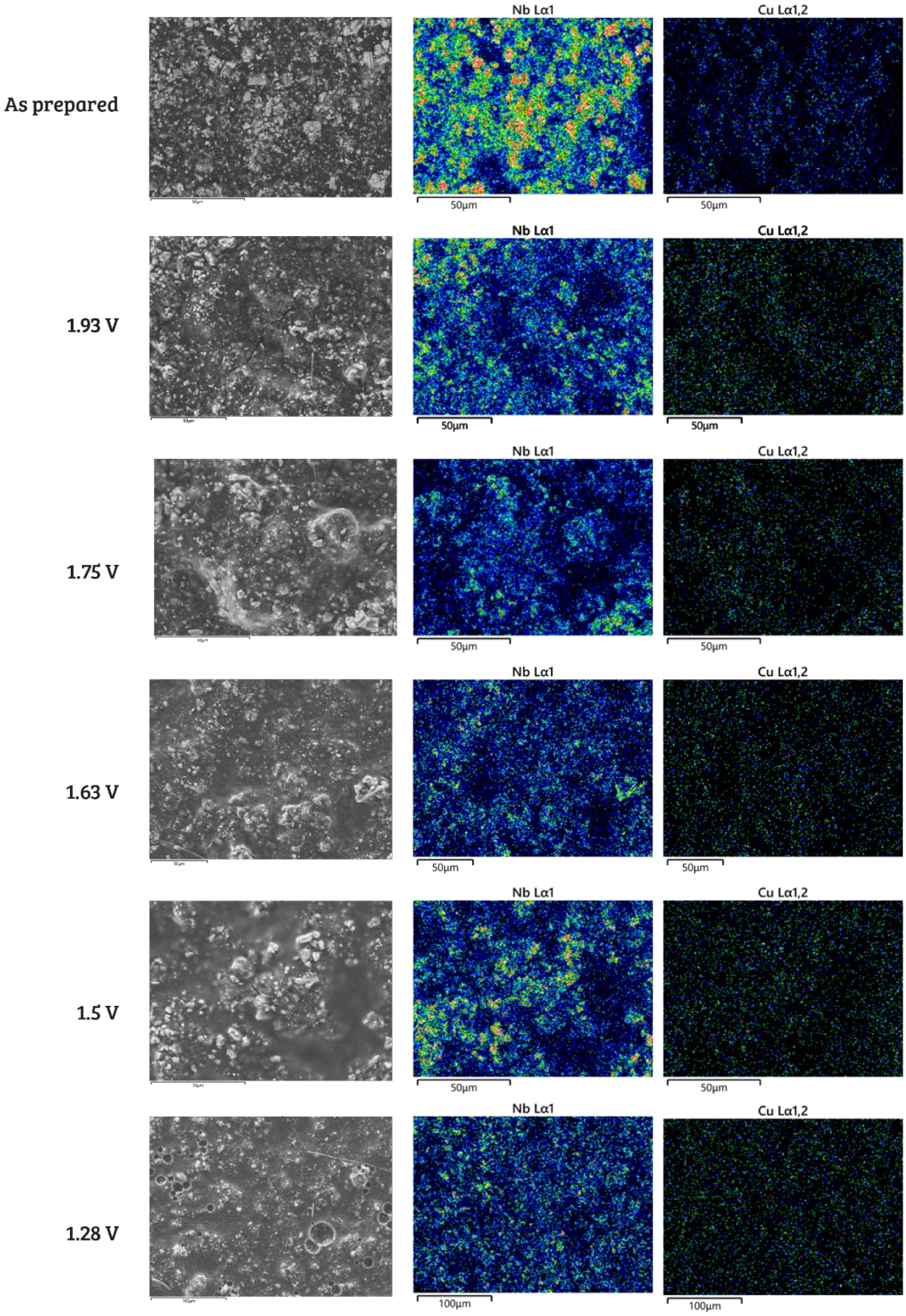

Figure 9. 1: SEM images of electrodes cycled to down to 1 V before returning to 3 V (which were identified from the DSC plot of potential phase changes) – part 1.

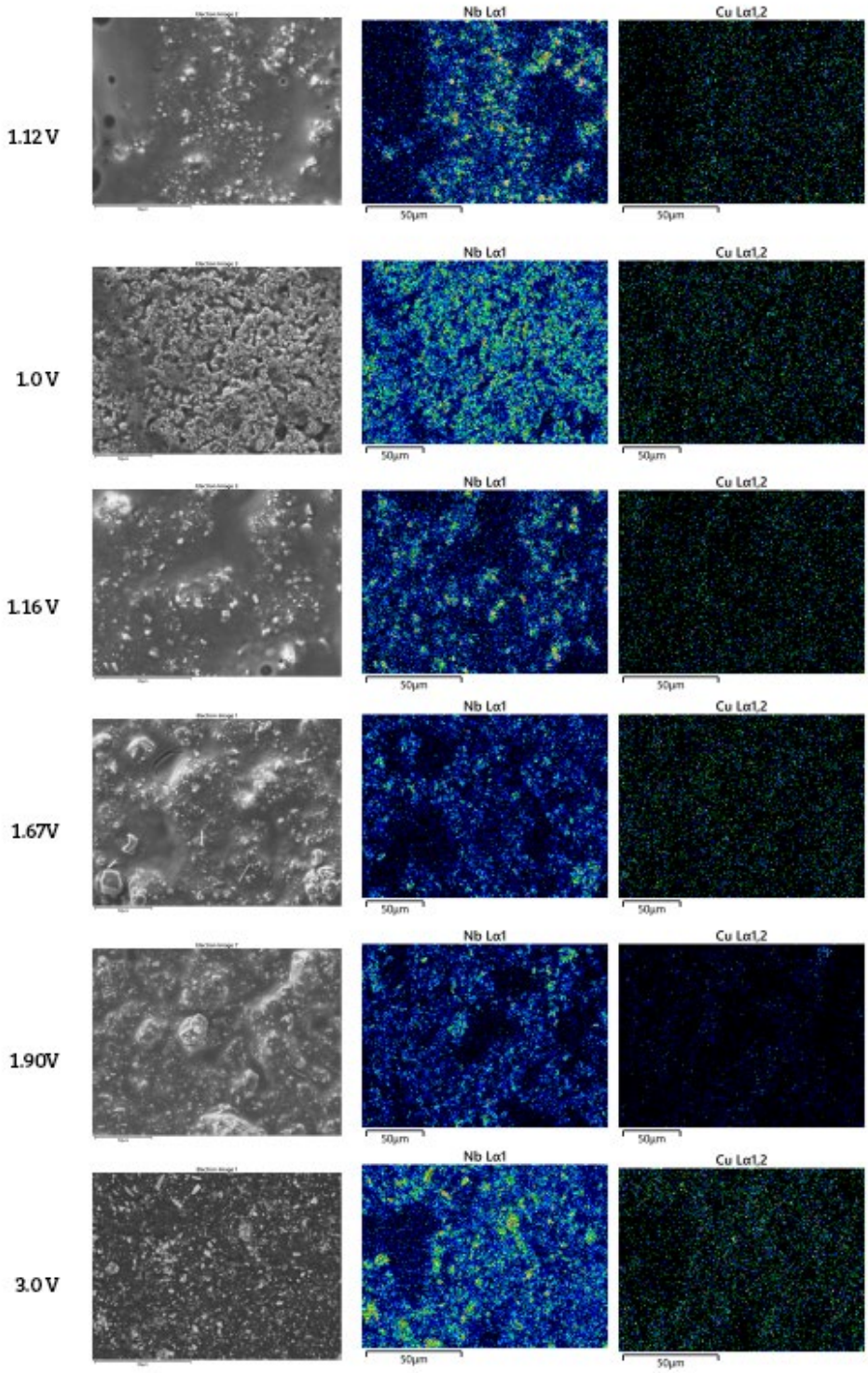

Figure 9. 2: SEM images of electrodes cycled to 1 V before returning to 3 V (which were identified from the DSC plot of potential phase changes) – part 2.

Determination of the theoretical density of $Nb_{22}CuO_{56}$:

$$Theoretical\ Density\ (g\ cm^{-3}) = \frac{16\big((1.91\ \times\ A_{Nb}) + (0.87\ \times A_{Cu}) + (4.87\ \times A_O)\big)\ (g\ mol^{-1})}{1578\ \times 10^{-24}\ (cm^3) \times 6.022\ \times 10^{23}\ (mol^{-1})}$$

$$Theoretical\ Density\ (g\ cm^{-3}) = \frac{4178\ (g\ mol^{-1})}{1578\ \times 10^{-24}\ (cm^3) \times 6.022\ \times 10^{23}\ (mol^{-1})}$$

$$Theoretical\ Density\ (g\ cm^{-3}) = 4.39\ g\ cm^{-3}$$

Table 9. 1: Density contributions within the composite electrode of $Nb_{22}CuO_{56}$:B:CB.

Material	Density	Wt %
$Nb_{22}CuO_{56}$	4.39	80
PVDF	1.78	10
Carbon Black	1.8	10

9.2 Chapter 4: Synthesis, characterization and application of novel Nb-based anode materials: Ti and W doping

Determination of the theoretical density of $Nb_9Ti_{1.5}W_{1.5}O_{30}$.

$$Theoretical\ Density\ (g\ cm^{-3}) = \frac{16\big((1.5\ \times\ A_{Nb}) + (0.25\ \times A_{Ti}) + (0.25 \times A_W) + (5\ \times A_O)\big)\ (g\ mol^{-1})}{1567.8 \times 10^{-24}\ (cm^3) \times 6.022\ \times 10^{23}\ (mol^{-1})}$$

$$Theoretical\ Density\ (g\ cm^{-3}) = \frac{4436\ (g\ mol^{-1})}{1567.8 \times 10^{-24}\ (cm^3) \times 6.022\ \times 10^{23}\ (mol^{-1})}$$

$$Theoretical\ Density\ (g\ cm^{-3}) =\ 4.70\ g\ cm^{-3}$$

Table 9. 2: The charging-rate study on a $Nb_9Ti_{1.5}W_{1.5}O_{30}$ vs Li half coin cell, with values of the experimental capacity and capacity obtained. The applied current and the related c-rating are also included. The AM of the electrode disc was 5.04 mg. Data corresponding to Figure 4.7.

Step	Applied Current (mA)	Capacity (mA g^{-1})		Experimental Capacity on each cycle (n) (mA h g^{-1})						Capacity retention (cycle n =2 to last cycle)
				1	2	5	10	15	20	
1.0	-0.0365	7.14	-I	233.22	227.80	223.35	219.846	214.59	211.06	92.7
	+0.0365		+I	227.49	226.09	222.91	219.35	214.61	211.07	93.4
1.1	-0.0731	14.48	-I	198.18	199.00	197.71				99.4
	+0.0731		+I	195.06	197.05	196.15				99.5
1.2	-0.1462	29.0	-I	189.09	185.10	186.00				100.5
	+0.1462		+I	186.35	184.29	185.05				100.4
1.3	-0.3655	72.62	-I	165.56	162.66	162.26				99.8
	+0.3655		+I	162.51	162.51	161.88				99.6
1.4	-0.731	145	-I	142.76	139.81	139.83				100.0
	+0.731		+I	139.73	139.74	139.72				99.9
1.5	-1.462	290	-I	118.35	114.73	118.61				103.4
	+1.462		+I	114.30	114.99	118.36				102.9
1.6	-0.0365	7.14	-I	193.40	186.44	204.53				109.7
	+0.0365		+I	203.52	184.40	201.70				109.4

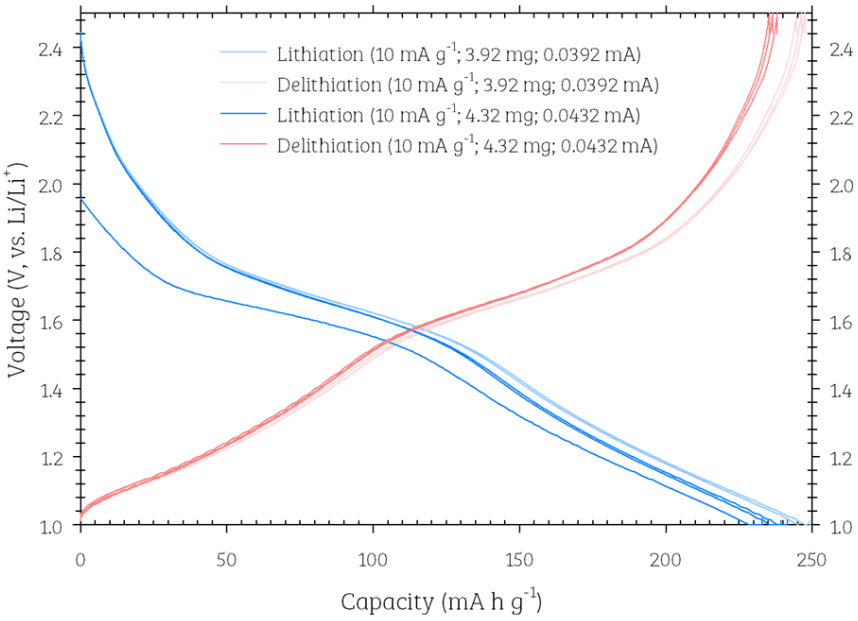

Figure 9. 3: Galvanostatic discharge-charge curves of $Nb_9Ti_{1.5}W_{1.5}O_{30}$ vs. Li metal, between reduced limits of 2.5 V to 1 V, using the calendered electrodes 1 and 2.

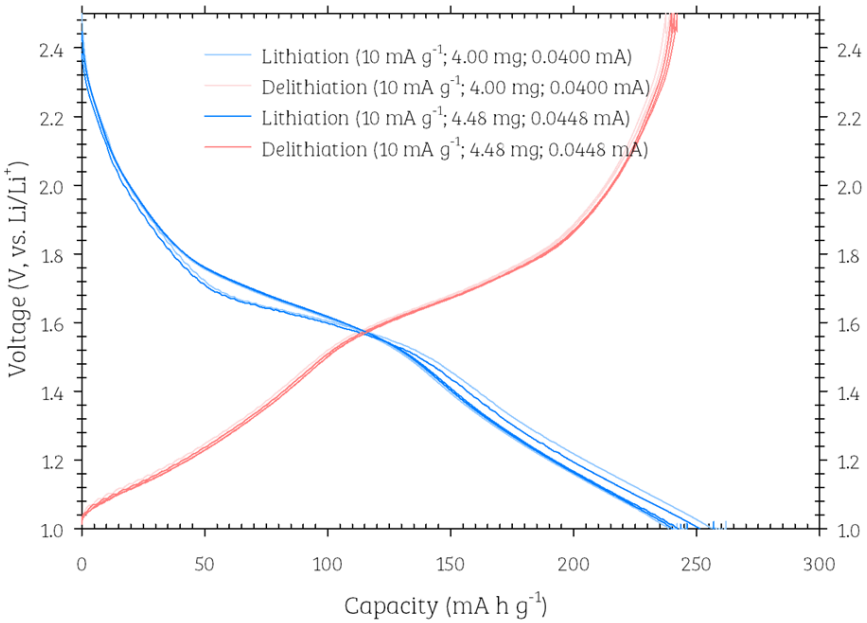

Figure 9. 4: Galvanostatic discharge-charge curves of $Nb_9Ti_{1.5}W_{1.5}O_{30}$ vs. Li metal, between reduced limits of 2.5 V to 1 V, using the calendered electrodes 3 and 4.

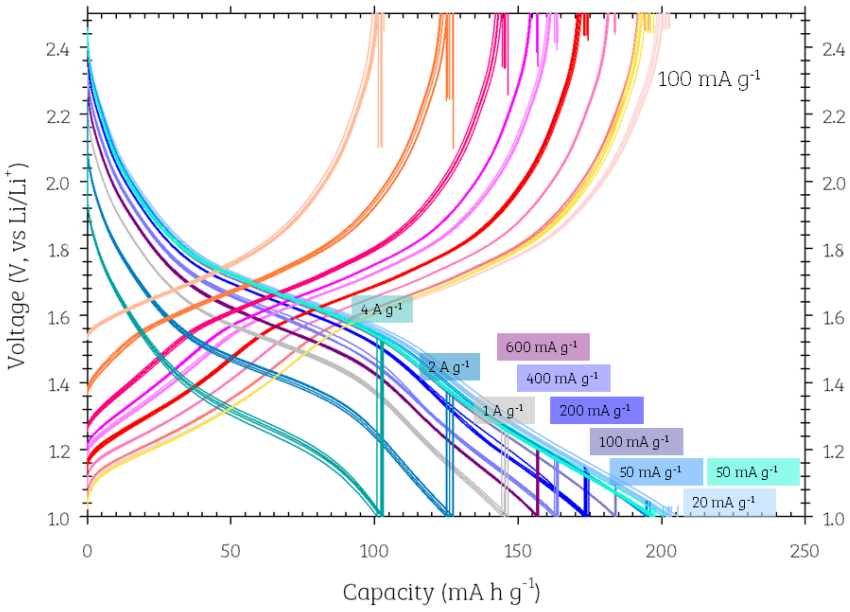

Figure 9. 5:Galvanostatic discharge-charge curves of $Nb_9Ti_{1.5}W_{1.5}O_{30}$ vs. Li metal, between reduced limits of 2.5 V to 1 V, using the calendered electrode 3.

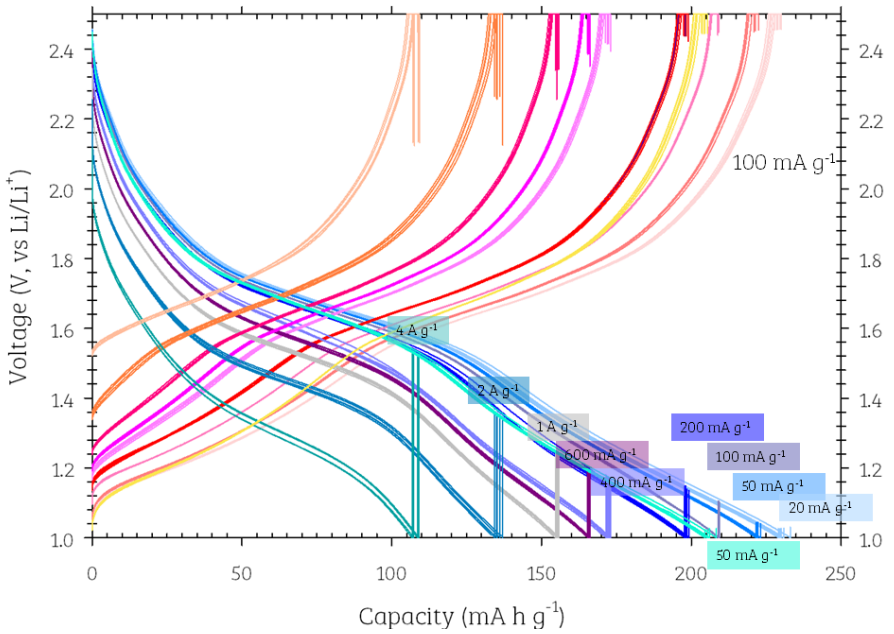

Figure 9. 6: Galvanostatic discharge-charge curves of $Nb_9Ti_{1.5}W_{1.5}O_{30}$ vs. Li metal, between reduced limits of 2.5 V to 1 V, using the calendered electrode 4.

9.3 Chapter 5: Alternative ink formulation and coating approaches for novel Nb-based anode materials: Ti and W doping

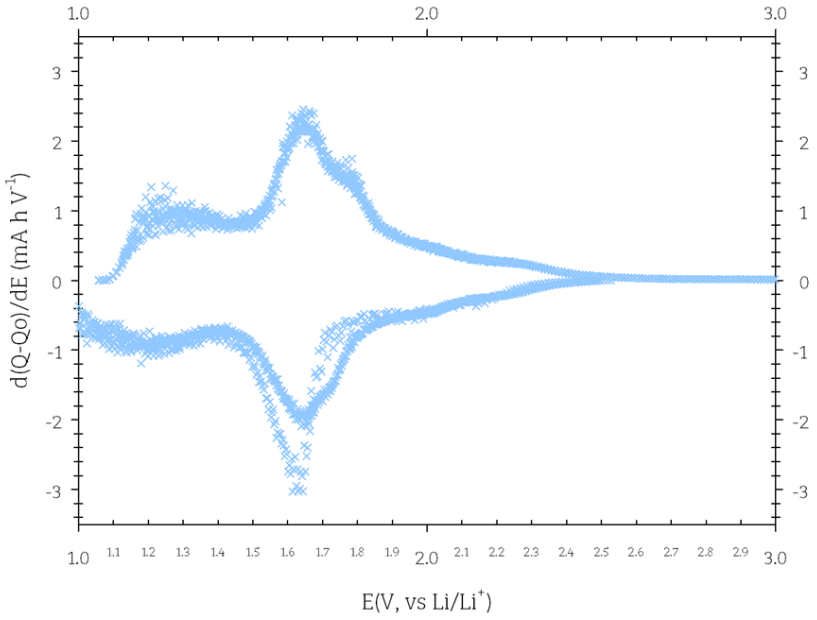

Figure 9. 7: Differential scanning calorimetry (DSC) plot derived from the galvanostatic discharge/charge profile of $Nb_9Ti_{1.5}W_{1.5}O_{30}$ at a rate corresponding to 10 mA g^{-1}.

Table 9. 3: Average capacity values of the $Nb_9Ti_{1.5}W_{1.5}O_{30}$ cells comparing the use of PVDF against iota-Carrageenan. Data corresponds to

Current Density (mA g^{-1})	Average Step Capacity (mA h g^{-1})			
	PVDF		Iota-Carrageenan	
	Lithiation	Delithiation	Lithiation	Delithiation
20	231 (2)	229.7 (9)	217 (4)	213 (2)
40	222.9 (2)	222.2 (2)	196 (1)	195 (1)
100	212.7 (4)	212.3 (4)	173 (1)	172 (2)
200	203.2 (9)	202.9 (9)	152.9 (8)	152.6 (8)
400	190.2 (2)	190.0 (2)	132 (2)	132 (2)
600	183 (1)	183 (1)	115 (1)	115 (1)
1000	171.52 (5)	171.43 (6)	83 (15)	84
2000	153.3 (3)	153.3 (3)	38.3 (5)	38.9 (5)
4000	131.9 (3)	131.9 (2)	21 (1)	21 (1)
20	226 (1)	224.6 (7)	196 (4)	193 (1)